UNIVERSIDAD CARLOS III DE MADRID

TESIS DOCTORAL

GENERIC SCALE INVARIANCE IN CONTINUUM MODELS OF TWO-DIMENSIONAL SURFACES

Autor:
Edoardo Vivo

Directores:
Rodolfo Cuerno Rejado
Matteo Nicoli

DEPARTAMENTO DE MATEMÁTICAS

Leganés, 2014

TESIS DOCTORAL

GENERIC SCALE INVARIANCE IN CONTINUUM MODELS OF TWO-DIMENSIONAL SURFACES

Autor: **Edoardo Vivo**
Director/es: **Rodolfo Cuerno Rejado**, **Matteo Nicoli**

Firma del Tribunal Calificador

		Firma
Presidente:		
Vocal:		
Secretario:		

Calificación :

Leganés, de de

GENERIC SCALE INVARIANCE IN CONTINUUM MODELS OF TWO-DIMENSIONAL SURFACES

Edoardo Vivo

July 2014

CONTENTS

INTRODUCTION

The study of interfacial phenomena has always constituted an integral part of condensed matter physics and materials science. Indeed, most properties of real materials depend crucially on the presence of imperfections, such as bulk vacancies, dislocations, surface roughness, etc. which derive from the non-equilibrium conditions under which the material has formed [1, 2]. In the last century, the increasing interest in systems with considerable surface to volume ratio, such as for instance devices at the nanoscale, has attracted scientists from different fields, from physics to chemistry, biology, or engineering [3]. This is due to the great amount of technological applications of such systems to a wide variety of situations. Moreover, the improvement of production and characterization techniques for the growth of surfaces at micro and nano-scale, such as Molecular Beam Epitaxy, or for surface etching, such as Ion Beam Sputtering , have unveiled unexpected interesting physical properties of the grown interfaces. From a technological point of view, the ability to control and predict the effect induced by disorder and the mechanisms of self-organization that ensue during the growth dynamics is of great interest [4]. For instance, the possibility to control the surface roughness could improve electric conductivity or the mechanical contact of certain devices, whereas the ability to control the formation of a pattern could change, for instance, the optical properties of the material.

Apart from its great technological significance, the study of interfacial phenomena is of a considerable fundamental interest. This is due to the fact that, as mentioned above, these are typical instances of non-equilibrium systems: the evolution of the surface is driven by a physical or chemical deposition (or etching) process that frequently prevents relaxation towards equilibrium [5]. Moreover, it is well known that many interfaces in nature display a statistically self-affine structure [6], implying irregularities at all length scales that cannot be treated within the framework of standard methods of mathematical analysis. Since the formation of these structures occurs spontaneously, with no need to tune any experimental parameter, such phenomenon is typically referred to as *generic scale invariance* [7,8]. A quantitative study of such systems is possible due to a powerful set of concepts borrowed from statistical mechanics, such as scale invariance, multiscaling, morphological instabilities, or pattern formation. An important observation arising in the study of these systems is that many of their features are *universal*, meaning that

such properties do not depend on the microscopic details of the system considered. The concept of universality has been extensively used in this context, since it enables the use of common tools to describe very diverse physical processes, which may take place even at length scales separated by many orders of magnitude [9].

In this Thesis we use continuum models of surface growth to study the scaling properties of surfaces evolving under conditions when generic scale invariance arises. More precisely, we focus our attention on the interplay between generic scale invariance and two different phenomena: the onset of morphological instabilities and the presence of anisotropic effects.

As for the first problem, we consider a paradigmatic example of an equation displaying generic scale invariance and morphological instabilities, namely the noisy Kuramoto-Sivashinsky equation. The asymptotic behavior of this model is yet to be understood for a two-dimensional substrate. In fact, a controversy exists regarding which universality class it belongs to. By means of large scale numerical simulations, we show that such equation in two-dimensional substrates belongs to the celebrated Kardar-Parisi-Zhang universality class.

Next, we focus on generically scale invariant models whose scaling exponents are different when measured along different substrate directions. When this happens, we say that the systems displays *strong anisotropy*. Despite the ubiquity of anisotropies in natural systems, relatively little attention has been dedicated to this phenomenon so far. This is perhaps due to the fact that most of the models studied in the context of surface dynamics take either an isotropic form, or, even when the form is completely anisotropic, still display a scaling behavior that does not change with the direction considered. After introducing a theoretical framework for the study of strongly anisotropic models, we test it against several anisotropic equations. Then, we perform a detailed numerical and analytical study of additional models, with the aim is of finding conditions for strong anisotropy. Our conclusion is that a rather peculiar form of the equation is required, along with a dynamics that is conserved. Finally, we present experimental evidence for the occurrence of strong anisotropy. We achieve this by considering experimental data from Ion Beam Sputtering under certain experimental conditions, and by applying our scaling hypothesis to the morphologies obtained.

The manuscript is divided into six chapters, each one with its own conclusions section. Lengthy calculations and minor results are collected into appendices. In the final chapter we summarize our conclusions from a unified perspective, and outline future research lines that follow naturally from the results of this Thesis. Let us now briefly explain the content of each one of the other chapters:

- In Chapter 1 we introduce most of the concepts used in the rest of the thesis. After a brief review on the concept of (generic) scale invariance in equilibrium and nonequilibrium systems, we focus our attention on surface growth models described by Langevin equations. We then define the observables that quantify the roughening process, and we describe their typical behavior for isotropic systems, which is encoded in the Family-Vicsek Ansatz.

We then introduce the notion of universality class and the concept of anisotropic scaling (strong anisotropy), and review some of the known results in this context. Finally, we briefly mention the phenomenon of morphological instability and, thus, pattern formation in the context of surface growth models.

- In Chapter 2 we present the numerical and analytical tools broadly used in this thesis. Namely, the dynamic renormalization group technique is introduced and discussed, and the numerical scheme used in the integration of stochastic equations is presented.
- In Chapter 3, we perform a numerical study of the noisy Kuramoto-Sivashinsky equation in two space dimensions. In the first part, we introduce the model and discuss its main properties and relevance; in the second part, we present the controversy on its universality class. Finally, we describe our numerical results in detail, and we present solid arguments which prove that this equation is in the Kardar-Parisi-Zhang universality class. The contents of this chapter have been published in (1).
- In Chapter 4 we start addressing the problem of the scaling properties of anisotropic equations. We first present an anisotropic scaling Ansatz that generalizes the Family-Vicsek hypothesis, and extends known anisotropic scaling relations to observables in momentum space. We then test this Ansatz by performing simulations of two anisotropic equations, a linear one and a nonlinear one, obtaining a good agreement with our theoretical predictions. In the process, we introduce a whole family of linear models displaying strong anisotropy. This analysis leads us to the identification of observables that do not scale as expected because of the finite size and finite lattice spacing used. The results of this chapter have been published in (2).
- In Chapter 5 we continue the study of anisotropic equations, by exploring the effect of anisotropic nonlinearities on several well-known models. In the first part of the chapter, we consider equations with conserved dynamics and non-conserved noise, while in the second part we study an equation with non-conserved dynamics. In both cases, we present the dynamic renormalization group analysis and the results from direct numerical integration of the equations. We find that strong anisotropy only ensues for conserved dynamics, and for non-generic parameter conditions. This analysis has been published in (3).
- In Chapter 6 we apply the anisotropic scaling Ansatz introduced in Chapter 4 to morphologies obtained from Ion Beam Sputtering experiments. After a brief historical review on this experimental technique and its theoretical modeling, we consider two experimental sets: one corresponding to a "clean" experiment in which contamination of the sample is carefully avoided, and another one where co-deposition of impurities gives rise to a morphological instability. In both cases we observe the presence of strong anisotropy and our results compare quite well with theoretical expectations.

The contents of this chapter have been published in (4).

Published articles

(1) M. Nicoli, E. Vivo, and R. Cuerno, "Kardar-Parisi-Zhang asymptotics for the two-dimensional noisy Kuramoto-Sivashinsky equation," Physical Review E, vol. 82, p. 045202(R), 2010.

(2) E. Vivo, M. Nicoli, and R. Cuerno, "Strong anisotropy in two-dimensional surfaces with generic scale invariance: Gaussian and related models," Physical Review E, vol. 86, p. 051611, 2012.

(3) E. Vivo, M. Nicoli, and R. Cuerno. "Strong anisotropy in two-dimensional surfaces with generic scale invariance: Nonlinear effects." Physical Review E, vol. 89, p. 042407, 2014.

(4) E. Vivo, M. Nicoli, M. Engler, T. Michely, L. Vázquez, and R. Cuerno, "Strong anisotropy in surface kinetic roughening: Analysis and experiments," Physical Review B, vol. 86, p. 245427, 2012.

1

GENERIC SCALE INVARIANCE AND SURFACE GROWTH EQUATIONS

It is possible to find many systems in nature that display *scale invariance*. Examples are abundant, such as river networks, fault lines, coastlines, blood and pulmonary vessels, etc. There exist several ways to define scale invariant (or self-similar) objects. One possibility is to say that such systems do not change if subject to a rescaling of coordinates, which intuitively corresponds to performing a "zoom in" or "zoom out" on them. It is also possible to define and construct objects that are self-similar in a *statistical* sense. This would mean that the rescaling mentioned above would produce a different object, whose statistical properties are nonetheless the same as the original one. One can then distinguish several cases based on the nature of the rescaling and on the deterministic or statistic nature of the similarity, and introduce a variety of concepts such as fractals, self-affine transformations, etc. [5].

In Statistical Physics, the phenomenon of scale invariance has been found to be typically related to an *algebraic* (power law) decay of the *correlation functions* of the system, which, in turn, corresponds to a diverging *correlation length*. This implies the lack of a characteristic length (and/or time) scale [10]. On the other hand, it is also well known that the correlation functions for a wide class of equilibrium systems actually decay *exponentially* fast, rather than algebraically, thus implying that these systems are *not* scale invariant. However, in the presence of a continuous phase transition and only at the critical point, the system will also display scale invariance due to the divergence of the correlation length [9]. Nevertheless, a great number of natural processes occur far from equilibrium, thus implying that quantities such as e.g. the temperature, cannot be tuned to their critical values. In fact, in general such quantities cannot even be defined far from equilibrium. However, also

for these kind of systems scale invariance seems to be quite ubiquitous. It is then natural to search for systems displaying scale invariance without parameter tuning. If this happens, we say that the system displays *generic* scale invariance [7, 8]. A more precise definition for this behavior states that a system is generic scale invariant whenever its correlation function presents an algebraic decay in a macroscopic region of the phase space [11]. Scale-invariant behavior without parameter tuning immediately suggests Self-Organized Criticality (SOC) systems [12, 13]. Examples are given by granular systems, such as a pile of rice [14], in which grains are deposited at times between successive avalanches. These kinds of systems are thus characterized by an *infinite* time-scale separation between their characteristic relaxation time (through avalanches) and the external driving force (addition of the next grain). However, in this Thesis we consider systems where this time-scale separation does not hold, the random driving force acting independently of the state of the system. This would be the case, for instance, of growth of a thin film by deposition, where particles are allowed stick to the substrate at any time and place.

In the following, we briefly review how the concept of scale invariance emerges from the theory of phase transitions and the Ginzburg-Landau formalism, by considering a paradigmatic example of equilibrium system, the Ising model. Next, we extend the Ginzburg-Landau theory to non-equilibrium systems, focusing on surface growth equations, and we consider the conditions under which generic scale invariance occurs. In the remainder of this chapter, we review the most commonly used tools in the study of surface growth equations, namely the Family-Vicsek Ansatz and the concept of universality classes. We then consider another phenomenon that is found to occur in the context of surface growth, namely the onset of instabilities that give rise to the formation of *patterns* on the surface. In some sense this situation is opposite to generic scale invariance, since a characteristic length scale of the system is spontaneously selected.

1.1 Scale invariance in equilibrium systems

The Ising model is an important example of an equilibrium system, which was introduced to describe magnetic systems in a simple fashion. This is one of the simplest models displaying a second order phase transition. Its simplicity, combined with a rich behavior and a wide range of applications, have made it a paradigm in the study of complex systems [15, 16]. In fact, it has had an enormous impact not only in physics, but also in other areas of science, including biology, neuroscience, economics, or sociology. Here, we focus on a coarse-grained representation of this discrete model, namely the one given by the well known Ginzburg-Landau-Wilson (GWL) free energy functional [9],

$$\mathcal{H}[\{h(\mathbf{r})\}] = \int_V d\mathbf{r} \left[\frac{K}{2} (\nabla h)^2 + f(h) - Bh \right]. \tag{1.1}$$

The so-called *order parameter*, h, represents the coarse-grained magnetization of the system, and B is the external magnetic field. The double-well potential

$$f(h) = \frac{1}{2}ah^2 + \frac{1}{4}bh^4 \tag{1.2}$$

depends on parameters a and b, which are proportional to the temperature difference $\tau = (T - T_c)/T_c$, with T_c being the critical temperature. Finally, the parameter K is related to the interaction energy between spins [17]. At a given temperature and neglecting fluctuations, the spatial configuration of the order parameter will be the one that minimizes the free energy, that is, the one satisfying the equation

$$\frac{\delta \mathcal{H}}{\delta h} = 0. \tag{1.3}$$

From this starting point, one could address the more complete question of how the Ising model evolves in time. For instance, it is natural to expect that, starting out from some initial condition, the order parameter will relax back to its equilibrium configuration. A common assumption [9] is that this rate of relaxation is proportional to the deviation from equilibrium. This assumption leads to the following equation for the rate of change of the order parameter,

$$\partial_t h = -\Gamma \frac{\delta \mathcal{H}}{\delta h}, \tag{1.4}$$

where Γ is a phenomenological parameter usually called *mobility*. This equation is known as the *time-dependent Ginzburg-Landau equation*. However, it may not describe correctly the evolution of the system towards the equilibrium state. In fact, depending on the initial conditions, it may cause h to evolve to a *local* minimum of $\mathcal{H}$, while the equilibrium state should correspond to a *global* one.

To ensure that the system approaches its global minimum, we need to take into account the fact that the dynamics of the order parameter is not purely relaxational, but may exhibit fluctuations due to the microscopic degrees of freedom. These fluctuations will sometimes cause h to move away from equilibrium during its time evolution. However, they also prevent the system from being trapped in any metastable minimum of $\mathcal{H}$ that may exist. These fluctuations can be modeled by introducing a noise term in Eq. (1.4), giving

$$\partial_t h = -\Gamma \frac{\delta \mathcal{H}}{\delta h} + \eta, \tag{1.5}$$

where η is a Gaussian random function satisfying

$$\begin{aligned} &\langle \eta(\mathbf{r}, t) \rangle = 0, \\ &\langle \eta(\mathbf{r}, t) \eta(\mathbf{r}', t') \rangle = 2D\delta^d(\mathbf{r} - \mathbf{r}')\delta(t - t'). \end{aligned} \tag{1.6}$$

Equation (1.5) is an example of a *stochastic partial differential equation*, also known as a *Langevin equation*. The constant $2D$ represents the variance of the

noise, and it is not difficult to see that, for equilibrium systems, it must be proportional to the temperature [9]. Indeed, it is possible to verify that the choice

$$D = \Gamma k_B T \tag{1.7}$$

leads to the correct probability distribution for the order parameter, namely,

$$P(\{h(\mathbf{r})\}) = \exp\left(-\frac{\Gamma\mathcal{H}}{D}\right) = \exp\left(-\frac{\mathcal{H}}{k_B T}\right), \tag{1.8}$$

as the stationary solution of the Fokker-Planck equation associated with the model defined by Eqs. (1.5)-(1.6).

If we consider the GWL functional for the Ising model (1.1), the evolution of h reads explicitly

$$\partial_t h = \Gamma\mathcal{K}\nabla^2 h - a\Gamma h - b\Gamma h^3 + \eta, \tag{1.9}$$

Equation (1.9) is difficult to solve analytically due to its non-linear character. However, it is possible to study the behavior of averaged quantities in the asymptotic state ($t \to \infty$), which can provide useful informations about the system. One of these is the *correlation function*, defined as

$$C(\mathbf{r}) = \left\langle \frac{1}{L^d}\sum_{\mathbf{x}} h(\mathbf{x}+\mathbf{r})h(\mathbf{x}) \right\rangle, \tag{1.10}$$

where L and d denote the lateral size and dimension of the substrate, respectively. The bracket $\langle\cdot\rangle$ denotes the average over the distribution of the noise. Another important observable is the *power spectral density* (PSD), defined as

$$S(\mathbf{k}, t) = \langle h_{\mathbf{k}} h_{-\mathbf{k}} \rangle \tag{1.11}$$

where $h_{\mathbf{k}}(t)$ is the Fourier transform of the deviation of h with respect to its mean value $\bar{h}$,

$$h_{\mathbf{k}} = \frac{1}{L^d}\int_\Omega d\mathbf{r}\, e^{-i\mathbf{k}\cdot\mathbf{r}}[h(\mathbf{r}) - \bar{h}], \tag{1.12}$$

where $\Omega = [0, L]^d$ and, for a system with periodic boundary conditions, $\mathbf{k} = 2\pi\mathbf{n}/L$, $\mathbf{n} = (n_1, \ldots, n_d)$, with $n_i \in \mathbb{Z}$. It is not difficult to verify that, substituting (1.12) into (1.11), one can find a relation between the correlation function and the PSD, namely,

$$C(\mathbf{r}) = \frac{1}{L^d}\sum_{\mathbf{k}} S(\mathbf{k})\cos(\mathbf{k}\cdot\mathbf{r}). \tag{1.13}$$

The analysis of the correlation function shows that, far away from the critical temperature ($\tau \neq 0$), and for any dimension $d \geq 2$, this quantity decays exponentially [9],

$$C(\mathbf{r}) \sim e^{-r/\xi}\left(\frac{\xi}{r}\right)^{\frac{d-1}{2}}. \tag{1.14}$$

In this equation, $r = |\mathbf{r}|$, and ξ is the so-called *correlation length* of the system, which is a measure of the distance over which spins are correlated with probability $\mathrm{O}(1)$, thus defining a characteristic length scale in the system.

As the system approaches the critical temperature ($\tau \to 0$), the correlation length diverges, and the correlation function displays a power law behavior,

$$C(\mathbf{r}) \sim \frac{1}{(r/\xi)^{d+2-\eta}}, \tag{1.15}$$

where η is the so-called *anomalous dimension*. The corresponding behavior for the PSD is

$$S(\mathbf{k}) \sim \left(\frac{|\mathbf{k}|}{|\mathbf{k}_0|}\right)^{-(2-\eta)}, \tag{1.16}$$

where $|\mathbf{k}_0|$ is a constant with units of wave vector. The difference between equations (1.14) and (1.15) lies in the fact that, even if both laws involve the same length scale ξ, this plays completely different roles in the two equations. In order to understand this, let us consider two functions, $f_1 = (r/\xi)^\alpha$ and $f_2 = \exp(r/\xi)$, and measure f_1 and f_2 on fixed intervals centered, e.g., in ξ, 10ξ, and 100ξ. The ratio of largest to smallest values changes for the exponential law f_2, while it remains unchanged for the power law. Then, by measuring a physical quantity obeying an exponential law, we can infer at which length scale we are working with respect to ξ, whereas for an observable following a power law, all length scales are equivalent and, in this sense, no characteristic length scale can be found for the system. Thus, in Eq. (1.14), ξ sets a *physical* characteristic length scale, while in Eq. (1.15), ξ is just a parameter with physical dimensions of length. In this sense, Eqs. (1.15) and (1.16) are equivalent mathematical expressions of *scale invariance* of the system. More details on this analysis can be found in [9, 10, 15].

This is how the concept of scale invariance emerges from the theory of phase transitions in statistical physics. If we go back to the interpretation of the order parameter h for the Ising model, then the lack of a characteristic length scale implies that, at T_c, one cannot find any typical size for the spin clusters. It is important to stress that for the Ising model, and many more systems which can be described similarly, scale invariance is achieved by tuning a parameter to a certain value (in this case, $T = T_c$). In this work, as explained in the following section, we will address systems whose scaling properties do not depend on the choice of any parameter.

1.1.1 Generic scale invariance in equilibrium

It is quite difficult to find equilibrium systems displaying generic scale invariance [8]. The reason for this can be seen by considering only the quadratic part of the function f in Eq. (1.2), obtaining a functional of the form

$$\mathcal{H}[\{h\}] = \int_V d\mathbf{r} \left[\frac{K}{2} (\nabla h)^2 + a h^2 \right], \tag{1.17}$$

which is also known as the "Gaussian approximation" [9] to the full GLW functional. The corresponding Langevin equation is

$$\partial_t h = \frac{\Gamma K}{2} \nabla^2 h - a h + \eta, \tag{1.18}$$

which, being linear, can be solved analytically. The power spectral density in the long time limit reads

$$S(\mathbf{k}) \sim \frac{1}{|\mathbf{k}|^2 + a}, \tag{1.19}$$

which, in turn, produces an exponential decay for the correlation function, unless a is set to zero. This shows that a possible way to obtain generic scale invariance would be to suppress the ah^2 term in Eq. (1.17) [or, equivalently, the linear term in Eq. (1.18)]. This can in principle be achieved in two ways: by invoking a symmetry of the system, or by considering a conserved dynamics for the order parameter. The former situation is given for instance by the XY model, where a global rotational symmetry is present, giving rise to scale invariant behavior at any temperature below the critical one [18]. However, this case is rather different from the situations we consider in this work, since the order parameter of the XY model is a *vector*, rather than a scalar quantity. Another example is given by systems whose order parameter satisfies a translational symmetry of the type

$$h(\mathbf{r}) \longrightarrow h(\mathbf{r}) + c, \tag{1.20}$$

like for instance the interface separating two different phases, for which a term of the form ah cannot appear in the Langevin equation [7, 8].

As far as conservation laws are concerned, it turns out that such a constraint may not be sufficient in order to get generic scale invariance in equilibrium. To illustrate this, let us consider the same functional as in Eq. (1.17). Imposing a conserved dynamics on the order parameter amounts to writing the corresponding Ginzburg-Landau equation as

$$\partial_t h = -\nabla \cdot \mathbf{J} + \eta_c, \tag{1.21}$$

where η_c is a conserved noise, which means that its variance D will no longer be a constant, but will depend on the wave vector $\mathbf{k}$. The current $\mathbf{J}$ is usually written as

$$\mathbf{J} = \nabla \mu, \tag{1.22}$$

$$\mu = -\Gamma \frac{\delta \mathcal{H}}{\delta h}, \tag{1.23}$$

with μ being a chemical potential. The equilibrium condition is thus analogous to the one in Eq. (1.7), but in this case both the noise variance and the mobility depend on the wave vector, i.e.

$$D(\mathbf{k}) = k_B T\, \Gamma(\mathbf{k}), \tag{1.24}$$

and the resulting Langevin equation takes the form

$$\partial_t h = -\Gamma \frac{K}{2} \nabla^4 h + a\Gamma \nabla^2 h + \eta_c. \tag{1.25}$$

The PSD will then behave as

$$S(\mathbf{k}) \sim \frac{|\mathbf{k}|^2}{|\mathbf{k}|^4 + a|\mathbf{k}|^2}, \tag{1.26}$$

and the correlation function will decay exponentially [7, 8], rather than algebraically, as happens for the non-conserved case. The difference between the conserved and non-conserved scenarios lies in the fact that, because of the constraints imposed by the conservation law, the relaxation of the field is more difficult and slower in the case of conserved dynamics [19]. In any case, it seems clear that introducing a conservation law for an equilibrium system *does not* necessarily lead to a generically scale invariant behavior.

1.2 Height equations and generic scale invariance

The Ginzburg-Landau theory goes way beyond the Ising model. It can be applied to a wide variety of systems, provided that we can identify a good order parameter, and write an appropriate Landau functional $\mathcal{H}$. However, still there are many systems that display some kind of scaling behavior but for which Eq. (1.5) does not hold, since it is not possible to write a coarse-grained free energy functional for them.

A large class of such non-equilibrium systems is provided by growing interfaces, like for example the wet-dry interface developing when a fluid flows through a porous medium, the burned-unburned interface in a forest fire, or the surface that develops when material is deposited onto a substrate [5]. In these cases, the "order parameter" h is interpreted as the height of the surface over a substrate. Actually, growing interfaces do include cases in which a GWL functional exists — such as e.g. thermal fluctuations of a liquid-vapor interface in a gravity field [19], see below — and other which cannot be described within this framework. Nevertheless, the dynamics of the latter systems can still be cast into a continuum stochastic differential equation for the height field $h(\mathbf{r}, t)$ [5,20]. This equation takes the general form

$$\partial_t h = -\Gamma\, \Xi + \eta, \tag{1.27}$$

where Γ is again a mobility, $\Xi(\mathbf{r}, t, h)$ is a deterministic function that depends on h and its spatial derivatives, while $\eta(\mathbf{r}, t)$ is a noise term analogous to the one appearing in (1.5). If growth occurs far from equilibrium, Eq. (1.27) cannot be derived

from a Landau functional. Then, the deterministic term Ξ has to be obtained directly from the properties of the system, like its symmetries [5]; alternatively, it can be derived taking e.g. the continuous limit of atomistic models [21], or else from phenomenological constitutive laws [22]. Another consequence of far-from-equilibrium growth is that in such a case the noise amplitude can no longer be related to the temperature; rather, it models random driving forces that keep the system out of equilibrium. Note, noise terms characterized by Eq. (1.6) cannot provide a description for e.g. Self-Organized Criticality (SOC) systems, since the random driving forces act at all length and time scales, independently of the state of the system. Descriptions of SOC systems based on Langevin equations with different noise properties are also available [23], but their analysis is outside the scope of this Thesis.

We will now address the problem of finding conditions for the occurrence of generic scale invariance in systems described by Eq. (1.27) [7, 8]. Let us start by considering a very simple system, namely thermal fluctuations of a liquid-vapor interface in a gravity field. The field h describes the height of the surface with respect to the bottom of the container. As it turns out, such a system can indeed be studied within the GLW formalism. It is not difficult to see [19] that a small slope expansion of the surface-tension contribution to the energy will give rise to a gradient-square term in the GLW functional, whereas gravity will contribute with a h^2 term. By performing the functional derivative, one then obtains

$$\Xi = ah - b\nabla^2 h, \tag{1.28}$$

and the resulting Langevin equation is actually the same as Eq. (1.18), thus giving rise to an *exponential* decay for the correlation function $C(\mathbf{r})$. Analogously to the case presented in Section 1.1.1, the reason for this behavior is the presence of the linear term ah on the right hand side of the Langevin equation. Due to its interpretation as the gravitational contribution to the energy, this is typically referred to as a "mass" term, even for systems in which gravity does not play any role. Again, there are then two ways to suppress this term without tuning any parameter: by invoking a symmetry, or imposing local conservation laws. In the following, we will briefly discuss these possibilities. A third option is also considered, namely equations with conserved dynamics but non-conserved noise. Generic scale invariance is established also in the latter case, as explained by heuristic arguments.

Symmetries

In the context of growing interfaces, the most common symmetry one can invoke is the translational invariance of the height field under a global shift, like that in Eq. (1.20). This symmetry implies that Ξ can only depend on spatial derivatives of h, thus suppressing the linear term ah in Eq. (1.28). It turns out that the only relevant terms in the renormalization group sense can be written as

$$\partial_t h = \nu \nabla^2 h + \frac{\lambda}{2}(\nabla h)^2 + \eta. \tag{1.29}$$

Equation (1.29) is the celebrated Kardar-Parisi-Zhang (KPZ) equation, which is known to produce scale invariant interfaces [24]. Analogously to the case of critical dynamics in equilibrium, the exponents characterizing the scale invariant behavior of this model are non-trivial and depend on the dimension of the substrate, provided it is smaller than the critical dimension d_c. However, in this context, the precise value for d_c remains unclear, with $d_c > 4$ quite likely applying [25, 26].

Conservation Laws

Contrary to the equilibrium case, it turns out that imposing conservation laws for the order parameters does lead to a generically scale invariant behavior for out-of-equilibrium systems. The only requirement is that the condition (1.24) is *not* verified [7], which actually makes explicit the true non-equilibrium nature of the system.

Conserving systems with non-conserving noise

An important class of models we will be dealing with in the remainder of this thesis, are those for which the dynamics is conserved but the noise is not, in such a way that the evolution equation can be written as

$$\partial_t h = \nabla \cdot \mathbf{J} + \eta. \tag{1.30}$$

In such cases, generic scale invariance can be reasonably expected to occur, as explained by the following heuristic argument [8]. The $\mathbf{k} = \mathbf{0}$ Fourier mode of the field h executes a random walk described by the equation,

$$\partial_t h_{\mathbf{k}=\mathbf{0}} = \eta_{\mathbf{k}=\mathbf{0}}, \tag{1.31}$$

implying that $S(\mathbf{k} = \mathbf{0}, \mathbf{t}) \sim \mathbf{t}$, which diverges at large times. The assumption that $S(\mathbf{k}, t)$ is continuous near $\mathbf{k} = \mathbf{0}$ then implies that spatial correlations will fall off more slowly than exponentially, typically giving rise to power laws.

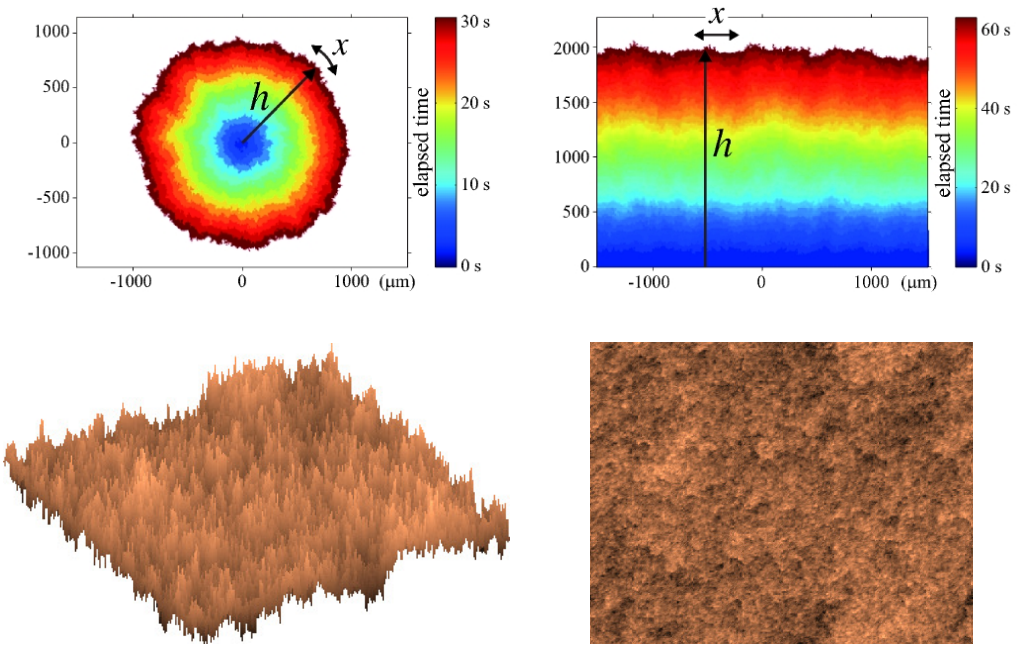

Figure 1.1: Examples of rough interfaces in experiments and numerical simulations. Top panel: experiments by Takeuchi *et al.* [27]. The depicted interfaces establish between two different phases of a turbulent liquid crystal. Their kinetic roughening properties have been proven to be in the celebrated Kardar-Parisi-Zhang universality class (see Table 1.1). The left and right panels show two different geometrical conditions under which the experiment was performed: circular and planar, respectively. Bottom panel: three-dimensional (left) and top (right) views of a morphology obtained from numerical simulations of the generalized Hwa-Kardar equation (see Chapter 5).

1.3 Kinetic Roughening

Starting from an ideally flat interface, under conditions for generic scale invariance, Eq. (1.27) produces a rough surface. The interplay between fluctuations and the deterministic part of the equation creates correlations among different points in the surface, in such a way that the correlation length grows in time until the whole system is correlated. Then, the system reaches a scale invariant stationary state, also referred to as *saturation*. This time evolution of the statistical features of rough interfaces is also known as *kinetic roughening* [5]. Examples of rough interfaces are presented in Figure and 1.1.

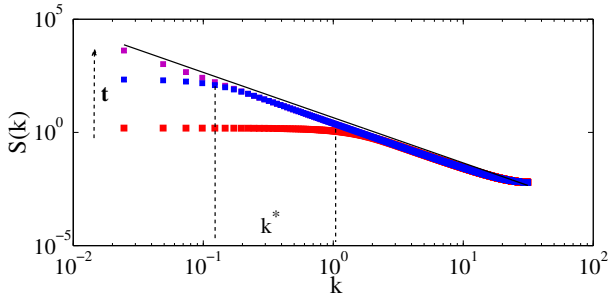

Figure 1.2: Example of power spectral density as a function of k for an equation of the type (1.27) in logarithmic scale. As time goes by (red to blue squares), the crossover happens at smaller values of k^*. For long times (violet squares) the scaling is clear in the whole range of k considered. This picture has been obtained form a numerical simulation of the Edwards-Wilkinson equation in two space dimensions. The solid black line is a guide for the eye with slope -2. Note that, for the EW equation in two dimensions, $\alpha = 0$ (see Table 1.1).

1.3.1 The Family-Vicsek Ansatz

Kinetic roughening can be characterized quantitatively by several observables; one of the most important ones is the power spectral density, defined as in Eq. (1.11). The typical behavior of the PSD of a rough surface is shown in Figure 1.2. Analytically, this behavior can be described by the so-called *Family-Vicsek* (FV) Ansatz [5, 28]

$$S(\mathbf{k}, t) = |\mathbf{k}|^{-(2\alpha+d)} s_1(|\mathbf{k}|^z t), \tag{1.32}$$

where

$$s_1(u) = \begin{cases} u^{(2\alpha+d)/z} & u \ll 1, \\ \text{const.} & u \gg 1. \end{cases} \tag{1.33}$$

Namely, at a given time t, the PSD decays as a power law for large values of $|\mathbf{k}|$, whereas it is approximately a constant (white noise) for small $|\mathbf{k}|$. The crossover happens when $|\mathbf{k}| = |\mathbf{k}^*|$, setting a *correlation length* $\xi \sim 1/|\mathbf{k}^*|$ for the system, to be understood as in Eqs. (1.15) and (1.16). Typically, the value $|\mathbf{k}^*|$ gets smaller as time increases. More precisely, $|\mathbf{k}^*| \sim t^{-1/z}$, meaning that the correlation length is growing in time as a power law. At long times, the system will be completely correlated (saturation) and the PSD will display only a clear power law behavior as a function of $|\mathbf{k}|$. The exponent α in Eq. (1.32) is called the *roughness exponent* of the system, while z is the *dynamic exponent*. The roughness exponent turns out to be related to the *fractal dimension* D of the surface via the relation $\alpha = d + 1 - D$, where d is the dimension of the substrate [29], the interface being a so-called *self-affine* fractal. A typical behavior for the PSD is shown in Figure 1.2.

There are other important observables which also exhibit scaling behavior in the context of kinetic roughening. One of them is the height-difference correlation

function, defined as

$$G(\mathbf{r},t) = \left\langle \sum_{\mathbf{x}} [h(\mathbf{x}+\mathbf{r},t) - h(\mathbf{x},t)]^2 \right\rangle . \tag{1.34}$$

By replacing $h(\mathbf{x}+\mathbf{r},t)$ and $h(\mathbf{x},t)$ with their representation in terms of the inverse Fourier transform, it is not difficult to find a relation between $G(\mathbf{r},t)$ and $S(\mathbf{k})$,

$$G(\mathbf{r},t) = \frac{1}{L^d} \sum_{\mathbf{k}} [1 - \cos(\mathbf{k}\cdot\mathbf{r})]\, S(\mathbf{k},t). \tag{1.35}$$

Then, plugging the function (1.32) for the power spectral density into Eq. (1.35), we can obtain a Family-Vicsek Ansatz for $G(\mathbf{r},t)$,

$$G(\mathbf{r},t) \sim |\mathbf{r}|^{2\alpha} f_c(t/|\mathbf{r}|^z), \tag{1.36}$$

where

$$f_c(u) = \begin{cases} u^{2\beta} & u \ll 1, \\ \text{const.} & u \gg 1, \end{cases} \tag{1.37}$$

and $\beta = \alpha/z$ is called the *growth exponent*. At a given time t, this observable will display a power-law growth with $|\mathbf{r}|$ (with exponent 2α) for distances below the correlation length ($|\mathbf{r}| \ll t^{1/z}$), and it then saturates to a certain value G_{sat}, which increases with time as $t^{2\beta}$.

Another important observable defined in real space is the *roughness* of the surface,

$$W(L,t) = \left\langle \left[\frac{1}{L^d} \sum_{\mathbf{r}} [h(\mathbf{r},t) - \bar{h}(t)]^2 \right]^{1/2} \right\rangle , \tag{1.38}$$

where $\bar{h}(t)$ is the mean height of at time t. As for the height-difference correlation function, we can write a relation between W and the PSD,

$$W^2 = \frac{1}{L^d} \sum_{\mathbf{k}\neq 0} S(\mathbf{k},t). \tag{1.39}$$

From this relation it is possible to derive the Family-Vicsek Ansatz for the roughness

$$W(L,t) \sim L^{\alpha} f_1(t/L^z) \sim t^{\beta} f_2(L/t^{1/z}), \tag{1.40}$$

where

$$f_1(u) = \begin{cases} u^{\beta} & u \ll 1, \\ \text{const.} & u \gg 1, \end{cases} \tag{1.41}$$

$$f_2(u) = \begin{cases} u^{\alpha} & u \ll 1, \\ \text{const.} & u \gg 1. \end{cases} \tag{1.42}$$

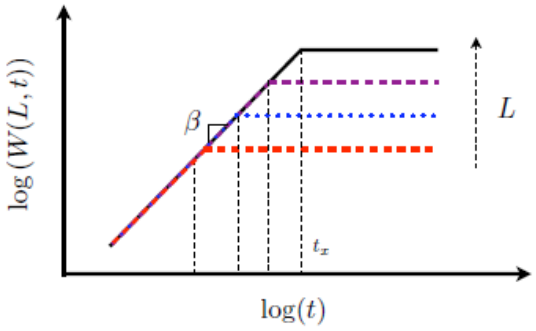

Figure 1.3: Example of roughness as a function of time for an equation of type (1.27). At relatively short times, the roughness grows in time as a power law with exponent β, while at a certain crossover time t_x, it reaches a saturation value. When the system size is increased (red to black squares), the saturation time and the saturation value also increase as power laws (see text). The picture has been taken from [5].

Hence, for a fixed system size L, the roughness grows in time as a power law with exponent β, and then, at a certain crossover time t_{sat}, it saturates to a value W_{sat}. The saturation value increases as a power law of L with the roughness exponent α, whilst the saturation time grows as L^z, with z being the dynamical exponent. A typical behavior of the roughness of a kinetically roughened interface is shown in Figure 1.3.

It is worth noticing that the Family-Vicsek Ansatz is usually only valid in certain regimes, neglecting transients and subdominant effects. Frequently, the growth exponent is estimated from the power law behavior of the roughness W, whereas the roughness exponent is obtained from the power spectral density S. In any case, the consistency of the estimated exponents can be easily checked by means of data collapses of the W and S curves.

1.3.2 Universality

The set of exponents (α, z) characterizes the behavior of the most important statistical observables of the system and, thus, the dynamics of the surface. Actually, growing surfaces can be classified according to the values of these exponents and their dependence on system dimension, into *universality classes*. Universality is an attractive feature in statistical physics. Even if the microscopic processes that result into a given morphology can be very different, there are many example of surfaces originated by different mechanisms which display the same critical exponents. For instance, it has been found that under certain conditions, thin films grown by Chemical Vapor Deposition (CVD) display the same statistical properties as the surface of cauliflowers plants [30]. Thus, systems that are separated by several orders of magnitude in length scales can be described by a common

	Equation	α	β	z	d
EW	$\partial_t h = \nu\nabla^2 h + \eta$	$(2-d)/2$	$(2-d)/4$	2	
LMBE	$\partial_t h = -\mathcal{K}\nabla^4 h + \eta$	$(4-d)/2$	$(4-d)/8$	4	
KPZ	$\partial_t h = \nu\nabla^2 h + (\lambda/2)(\nabla h)^2 + \eta$	$1/2$	$1/3$	$3/2$	1
		0.39	0.25	1.61	2
cKPZ	$\partial_t h = -\nabla^2\left[\nu\nabla^2 h + (\lambda/2)(\nabla h)^2\right] + \eta$	1	$1/3$	3	1
		$2/3$	$1/5$	$10/3$	2

Table 1.1: Summary of the most important universality classes for kinetic roughening systems. Due to their linear nature, the Edwards-Wilkinson (EW) and Linear Molecular Beam Epitaxy (LMBE) equations can be solved analytically and the values of the exponents can be calculated for all dimensions. For the Kardar-Parisi-Zhang (KPZ) equation, the exponents can be analytically calculated only for $d = 1$ [5], while the values shown for $d = 2$ result from numerical simulations [31, 32]. For the conserved KPZ (cKPZ) equation, the values of the exponents shown result from a one-loop dynamic renormalization group analysis [33]. Small corrections to these values have been found to appear in a two-loops analysis [34].

model that incorporates only the most important and fundamental phenomena taking place. The fact that the statistical properties of the surface are the same for different systems can be thought of as a manifestation of the same governing general principles. This occurs in spite of the different detailed physical mechanisms controlling the dynamics. Moreover, if two or more models are known to belong to the same universality class, this link between them can be exploited for further study. For instance, there are cases where a given model can be more efficiently studied with respect to another one in the same universality class. In the context of the Kardar-Parisi-Zhang universality class (see below), this happens for example for the restricted solid-on-solid (RSOS) and the ballistic deposition (BD) models, the former being easier to study numerically than the latter [5].

Historically, there are four important universality classes for kinetic roughening systems that will be important in this work: Edwards-Wilkinson (EW), Linear Molecular Beam Epitaxy (LMBE), Kardar-Parisi-Zhang (KPZ), and conserved Kardar-Parisi-Zhang (cKPZ). A summary of the corresponding equations and their exponents as a function of the substrate dimension is given in Table 1.1.

These universality classes, along with many others that are not mentioned here, have attracted much work in the kinetic roughening field. However, this approach is not immune to flaws one needs to be aware of. For instance, it has been shown [35] that it is possible to obtain a continuum range of exponent values. This can be done in several ways. The most common one is by changing the noise properties, for example by introducing conserved noise, power-law correlations, or power-law amplitudes for the fluctuations [36, 37]. Another possibility is to consider long range effects on the surface, in such a way that the resulting equations are non-local [38]. In both cases, the scaling exponents will depend *continuously* on the

parameters that characterize the noise properties or the decay of the integral kernels for the non-local equations. The existence of a continuum of exponent values questions the use of the concept of universality classes, in particular from a practical (experimental) point of view, especially if one is not able to connect the peculiar properties of the noise or the introduction of nonlocal interactions with actual physical mechanism that are relevant in the systems studied.

Other problems arising in this context are, for instance, the fact that there could be accidental or coincidental equalities among exponent sets. This occurs [39] for the roughness exponents of the KPZ and Edward-Wilkinson equations in one dimension, or when comparing the one dimensional LMBE equation with an EW type equation featuring a diffusion coefficient that is a random variable with a quenched columnar distribution [40]. In Reference [41] the authors construct a one-parameter family of models in such a way that, for a certain value of the controlling parameter, the model has the same scaling exponents as the one-dimensional Kardar-Parisi-Zhang equation. Thus, one is lead to think that it belongs to the KPZ universality class. However, it turns out that the model maintains the same exponents when increasing the spatial dimension. Since, in principle, universality classes in this context are defined by the values of the exponents *and* by their dimensional dependence, the proposed model is *not* in the KPZ universality class. However, experimental systems are limited to one or two-dimensional surfaces. Thus, if experimental data are only available for a given spatial dimension (as is almost always the case), it is not straightforward to assign such a system to a universality class, and a given choice can lead to an incomplete description of the system at hand.

In summary, the concept of universality is able to provide a simplified framework in which a great variety of systems can be studied. However, it is important to keep in mind the limitations of such an approach, especially when comparing the theory with experimental data.

1.3.3 Universality beyond the scaling exponents

It is well known from the theory of equilibrium critical phenomena that there exist universal quantities other than the critical exponents. The scaling functions for systems belonging to the same universality class, for instance, become identical at the critical point. Other well-known quantities in this context are the so-called *universal amplitudes*, typically expressed as a ratio between scaling functions [42]. Under appropriate circumstances, at the critical point these amplitudes are also shared by systems belonging to the same universality class.

As we have seen in the previous sections, a definition of universality classes based on the values of the "critical" exponents is also possible for out-of-equilibrium systems displaying generic scale invariance. Analogously to the equilibrium case, it would then be interesting to explore the existence of other universal quantities for such systems. Note, in this case no parameter needs to be tuned to its critical value.

Interestingly, many advances in this area have been produced in the context of the universality class of the Kardar-Parisi-Zhang (KPZ) equation, Eq. (1.29), which was put forward in 1986 within the framework of stochastic continuum models [24] (see Table 1.1). Since then, a great number of models have been proved to belong to this universality class, and a great effort has been put in order to exploit and extend this connection, beyond the values of the scaling exponents. The greatest advances so far have been obtained for the one-dimensional case. Note, in Eq. (1.29) the time evolution of the surface height depends essentially on three factors, namely

- A relaxation mechanism, provided by the linear operator (Laplacian).
- A growth speed that is rotationally invariant, and along the local normal direction of the surface. To lowest nonlinear order in a small-slope expansion, this is provided by the quadratic nonlinearity.
- An external random driving force.

Examples of physical phenomena modeled by the KPZ equation include turbulent liquid crystals [43], crystal growth on a thin film [44], bacteria colony growth [45], paper wetting [46], crack formation [47], and burning fronts [48], to cite a few. The values of the scaling exponents for the one-dimensional case are presented in Table 1.1.

Only a few years after the model was introduced, it was found by Krug, Meakin, and Halpin-Healy [49] that certain *universal amplitudes* exist for systems belonging to the KPZ universality class in one dimension. For example, the surface roughness W for an infinite system size was predicted to be of the form

$$W^2 = c_2 \left[\left(\frac{D}{\nu} \right)^2 |\lambda| t \right]^{2/3}, \tag{1.43}$$

with c_2 being a *universal* constant, independent of the specific model parameters; the exponent $2/3$ is exactly 2β (see Table 1.1). Thus, in order to check the universality hypothesis for a certain model, one needs to compute the surface roughness W and independently estimate the effective parameters ν, λ, and D. In certain cases, these can be computed analytically, while for the great majority of models they have to be estimated numerically [49].

The quantity c_2 provides an example of observable that is common to all models belonging to this universality class. By simple dimensional analysis, one also expects the rescaled height

$$\tilde{h} = \left[\left(\frac{D}{\nu} \right)^2 |\lambda| t \right]^{-1/3} h, \tag{1.44}$$

to have a universal distribution. Indeed, many universal properties of this distribution have been unveiled, such as amplitudes analogous to c_2 for the skewness (third order correlation function) and kurtosis (fourth order correlation function) [20,49].

Since then, the most important results for the universal features of the KPZ class have been actually obtained for *discrete models* that were conjectured to

belong to this class [50]. These results showed unexpected relations with combinatorial problems [51] and random matrix theory [52]. Johansson established a connection between the so-called discrete Total Asymmetric Simple Exclusion Process (dTASEP), a model which was already known to belong to the KPZ class, and random matrices [52]. Specifically, the author proved that the asymptotic probability distribution for the appropriately rescaled flux of particles was given by the so-called Tracy-Widom (TW) distribution [53], a well-known distribution in the context of random matrix theory. Prähofer and Spohn then extended this result to a wider class of models [54, 55]. More precisely, the authors considered the polynuclear growth model (PNG), an interacting particle system on the real line. Then, they mapped this model onto the combinatorial problem of the largest increasing subsequence of a random permutation of N integer numbers (also known as Ulam's problem), which in turn provides a link to the Tracy-Widom distribution [51]. The authors were able to confirm this connection for several system geometries. Subsequently, the same authors were able to characterize the *universal stochastic process* governing the fluctuations for the PNG model [56], whose single-point distribution is precisely the TW distribution mentioned above.

Interestingly enough, it was not until 2010 that analogous results for KPZ equation *itself* were obtained. This is due to the fact that such equation is mathematically ill-posed due to its nonlinearity. In fact, the function h is assumed to be locally Brownian and hence, in principle, it does not make sense to square its derivative [57]. This issue can be solved by means of a Cole-Hopf transform [58], upon which the KPZ equation turns into a linear equation with multiplicative noise, the latter being easier to treat mathematically than the former. In 2010, two groups (independently and in parallel) derived the exact formula for the one-point statistics for the solution to the KPZ equation [59, 60] for a wedge-type initial condition, and proved that this converges, at sufficiently large times, to the Tracy-Widom distribution. Later on, Calabrese and Le Doussal [61] derived an exact solution for a flat initial condition. For more details, we refer to the review in [57]. The fact that the exact solution depends on the geometry of the system and its initial conditions is not surprising. The quantity that does not depend on the initial conditions is the one-point probability distribution function, given by the TW distribution. However, this quantity does change for different geometries. More precisely, it has been shown that, in cases where the height profile is globally curved, such as growth from a seed or for wedge initial conditions, the corresponding probability distribution for the fluctuations of h is the same as the one of the largest eigenvalue of a random matrix in the Gaussian Unitary Ensemble (GUE) [53]. For flat initial conditions, the random matrices need to be extracted from another set, namely the Gaussian Orthogonal Ensemble (GOE). However, since both the GUE and GOE distributions are instances of the TW distribution, its universality is maintained in this context.

The results mentioned above provide a wide extension of the concept of universality in surface kinetic roughening. A remarkable example in this sense is given

by the experiments on turbulent liquid crystals by Takeuchi *et al.* [62], where one-dimensional KPZ behavior was assessed for the first time beyond scaling exponents values. In fact, this result was obtained by comparing also the probability distribution functions for the fluctuations of the interfaces, both for globally flat and curved interfaces (see Figure 1.1).

More recent years have witnessed an attempt to extend these results to two-dimensional systems in the KPZ universality class [63]. So far, no analytical prediction about the form of the probability distribution has been obtained. However, numerical simulations and experimental data are available, that also provide valuable confirmation of the universality of the probability distributions of the fluctuations in this case [64, 65].

As a word of caution, note that there may be cases related with the KPZ universality class in which a given model departs from it when increasing the substrate dimension, as it happens for instance for the models in Reference [41]. Issues of this type may play a role when arguing about the universality class of a given experimental system.

1.3.4 Anisotropic Surfaces

In the kinetic roughening context, to date most experimental and theoretical work has been devoted to characterize and understand scaling behavior that is isotropic in space. This is partly due to the fact that even the most natural anisotropic generalizations of the paradigmatic Kardar-Parisi-Zhang (KPZ) model and its conserved version, as we will see in more detail later on in this work, turn out to display isotropic behavior themselves. However, to some extent, this should strike us as unexpected. Considering the application of kinetic roughening to standard contexts, like epitaxial growth of thin films [44], or crystal growth from a melt [66], physical anisotropies are ubiquitous in energetic barriers for surfaces to relax by surface diffusion or in surface tension effects. Thus, it would be natural to expect the occurrence of anisotropic scaling properties in the asymptotic states of such systems. For instance, for thin films grown by molecular beam epitaxy (MBE) on surfaces that are vicinal to a high-symmetry orientation, the direction of the average surface tilt and the average orientation of the ensuing steps play very different physical roles, frequently leading to anisotropic behavior as for the step bunching and/or meandering instabilities in Si(001) [67–69]. Even under morphologically stable MBE growth conditions, as for growth of GaAs films [70, 71], spatial anisotropies may occur. Still with nanoscopic systems, erosion of thin films by ion-beam sputtering (IBS) induces space anisotropies related with the different roles played by the direction on the target that lies along the projection of the ion beam and the direction perpendicular to it [72, 73]. Reaching the realm of macroscopic spatially extended systems, fracture of solids provides still another instance for the occurrence of space anisotropies, in this case between the crack propagation and crack front directions [74]. Another class of systems where spatial anisotropies may occur is given by geological systems such as mountains, river basins or underwater

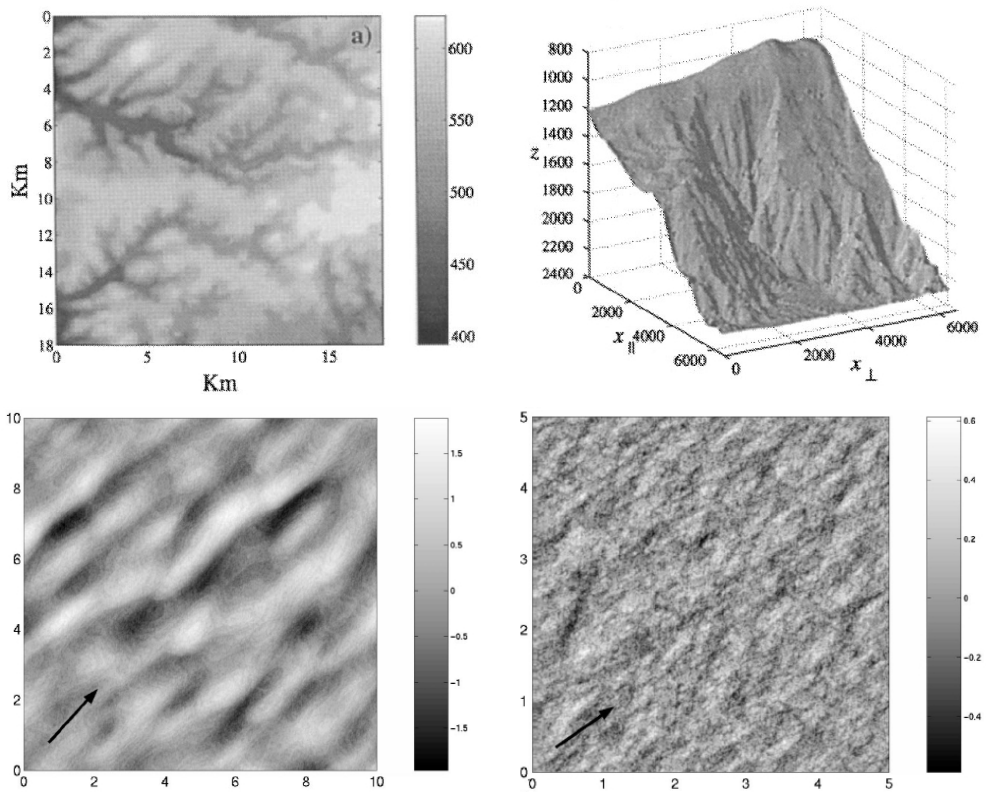

Figure 1.4: Examples of strongly anisotropic surfaces. Upper left panel: digital elevation map of an area of the Appalachian Plateau, in Northwest Pennsylvania. Elevations are given in meters. The spatial resolution is 90 m. Upper right panel: digital map of a submarine canyon off the coast of Oregon. The vertical axis represents the depth z below sea level. The spatial resolution is 50m. The pictures have been taken from [75]. Bottom panel: samples grown by molecular beam epitaxy onto a GaAs substrate. The arrows point along the $[1\,\bar{1}\,0]$ crystallographic direction. Left panel: growth occurs at $T = 600°$ on a thermally desorbed substrate. Right panel: growth at $T = 595°$ on a hydrogen etched substrate. The images have been taken from [71].

canyons (see Figure 1.4), where the eroding activity of the wind or water combines with a preferred direction for the transport of material, given by the gravity [75].

From a mathematical point of view, the surfaces that occur in these systems are self-affine fractals (as in the isotropic case) whose fractal dimension depends on the direction along which it is measured. Thus, for two-dimensional surfaces, we will define two different roughness exponents α_x and α_y such that $G_x(x) \sim |x|^{2\alpha_x}$ for correlations along fixed transects at $y = \text{const.}$, and $G_y(y) \sim |y|^{2\alpha_y}$ for correlations along fixed transects at $x = \text{const}$. Note that in general $\alpha_x \neq \alpha_y$. These

relations can be summarized in the following scaling form

$$G(x,y) \sim b^{2\alpha_x} G(b^{-1}x, b^{-\zeta}y), \tag{1.45}$$

where we have ignored the time dependence by performing the rescaling at saturation. In (1.45), b is an arbitrary positive real parameter and ζ is the *anisotropy exponent*, that can be related to α_x and α_y through

$$\zeta = \frac{\alpha_x}{\alpha_y}. \tag{1.46}$$

The scaling form (1.45) is not unique; in fact we can perform the rescaling along the y direction, obtaining the equivalent scaling form

$$G(x,y) \sim b^{2\alpha_y} G(b^{-1/\zeta}x, b^{-1}y), \tag{1.47}$$

where again b is arbitrary. Indeed, by setting $b = x$ and $b = y$ in equations (1.45) and (1.47) respectively, we get the desired scaling behaviors $G_x(x) \sim |x|^{2\alpha_x}$ and $G_y(y) \sim |y|^{2\alpha_y}$, while (1.46) is a consequence of the simultaneous occurrence of (1.45) and (1.47).

The anisotropy exponent ζ is a measure of the degree of anisotropy the system displays in its asymptotic state. When $\zeta = 1$ we will say that the system presents *weak anisotropy* (WA), while for $\zeta \neq 1$, the system displays *strong anisotropy* (SA). In the Renormalization Group language, anisotropy is said to be an irrelevant or a relevant perturbation of the isotropic behavior, respectively [9].

A classical example of an anisotropic equation is the so-called anisotropic Edwards-Wilkinson equation (aEW) which, in two dimensions, can be written as

$$\partial_t h = \nu_x \partial_x^2 h + \nu_y \partial_y^2 h + \eta, \tag{1.48}$$

simply accounting for the fact that the relaxation of the surface can occur at different scales for different directions. This equation arises in various physical contexts, like the Bradley-Harper theory for surface erosion by ion beam sputtering [76], or step dynamics in epitaxy [44]. Equation (1.48) can be solved analytically [77], giving equal scaling exponents α_x and α_y, resulting into an anisotropy exponent $\zeta = 1$. Thus, the aEW equation displays weak anisotropy, which can be interpreted in the following way: despite the fact that the diffusion coefficients ν_x and ν_y act at different length and time scales for the two directions, the difference between them is irrelevant in the asymptotic regime. One way to see that is to note that it is possible to perform a rescaling of the coordinates x and y in such a way that the equation becomes isotropic, and that the properties of the asymptotic state cannot depend on the units of length that are chosen.

Equation (1.48) is linear, so that one could think that a strong anisotropic behavior could be induced by an anisotropic non-linear term in the equation. Examples of the latter type are given by the anisotropic KPZ equation (aKPZ),

$$\partial_t h = \nu_x \partial_x^2 h + \nu_y \partial_y^2 h + \frac{\lambda_x}{2}(\partial_x h)^2 + \frac{\lambda_y}{2}(\partial_y h)^2 + \eta, \tag{1.49}$$

and by the conserved anisotropic KPZ equation (aCKPZ),

$$\partial_t h = -\nabla^2 \left[\nu_x \partial_x^2 h + \nu_y \partial_y^2 h + \mu \partial_x h + \frac{\lambda_x}{2} (\partial_x h)^2 + \frac{\lambda_y}{2} (\partial_y h)^2 \right] + \eta. \quad (1.50)$$

Equation (1.49) is not only important as a generalization of the KPZ equation, which is a prototypical model for generic scale invariance far from equilibrium [78]. It also appears in the description of physical phenomena like the growth of vicinal surfaces [79].

Equation (1.50) is widely used in describing many growing surfaces in the context of molecular beam epitaxy (MBE), in particular when the deposition occurs onto a crystal surface that has been miscut with respect to a high symmetry plane.

Equations (1.49), (1.50) cannot be solved analytically, but their asymptotic behavior has been studied using Renormalization Group techniques.

For the aKPZ equation, Wolf [79] found different behaviors depending on the relative signs of λ_x and λ_y, namely,

- For $\lambda_x = \lambda_y = 0$, Eq. (1.49) reduces to (1.48). It therefore behaves like the EW equation in two dimensions, see Table 1.1.
- For $\lambda_x \lambda_y < 0$, the nonlinear terms are irrelevant, and again Eq. (1.49) behaves like the isotropic EW equation in two dimensions;
- For $\lambda_x \lambda_y > 0$, the nonlinearities are relevant, but the asymptotic behavior is isotropic and in the $d = 2$ KPZ universality class (see table 1.1).

This results can be heuristically interpreted, as in the case of the aEW equation, in terms of a rescaling of the coordinates x and y. In the case $\lambda_x \lambda_y > 0$, such a rescaling can be performed so that the equation becomes the isotropic KPZ. On the other hand, when the nonlinearities have opposite signs, a similar rescaling does not exist, and the anisotropy can in principle have some effect on the asymptotics of the equation. However, it has been proved that the nonlinear contribution to the Fokker-Plank equation associated with Eq. (1.49) vanishes when $\lambda_x \lambda_y < 0$, thus implying that the asymptotic probability distribution for the height is the same as the anisotropic Edwards-Wilkinson equation [80]. Since, as mentioned above, the latter displays only *weak* anisotropy, the same conclusion holds for the aKPZ equation. The existence of solutions for which the nonlinearities cancel is typically referred to as the presence of *cancellation modes*. In the context of pattern formation (see Section 1.4 and Chapter 3), nonlinearities are important since they provide a smoothing mechanism that counteracts the linear instabilities. However, if the equation displays a cancellation mode that is unstable, then the nonlinearities cease to play any role, and small perturbation of a homogeneous configuration will blow up exponentially [81].

Thus, despite the richer behavior, we have seen that the aKPZ equation exhibits only weak anisotropy, as for the aEW equation. More recent works [78] showed that, for the aKPZ equation, anisotropies start to be relevant for $d > 2$, leading to rich phenomena that include new universality classes. This fact has also been verified by Barabasi *et al.* [82] by calculating the scaling exponents for the Toom

model. This is a discrete model believed to be described by the aKPZ equation. Its exponents are very close to those of the isotropic KPZ when the signs of the non-linearities are the same.

On the other hand, using dynamic renormalization group techniques, Kallabis showed that the asymptotic behavior of Eq. (1.50) is that of the isotropic conserved KPZ equation, independently of the relative sign of the nonlinearities [83] .

Thus, it appears that the most studied linear and non-linear anisotropic equations in the kinetic roughening literature do not display strongly anisotropic behavior. This advances the question whether it is possible or not to construct an equation (linear or not) displaying strong anisotropy in the physical $d = 2$ case. Indeed, some examples are available in the literature, but they have not been studied with much detail. In particular, the anisotropic scaling Ansatz for the PSD or for the correlation functions have not been verified in numerical simulations. Another issue is whether is it possible or not to infer a general criterion to discriminate equations with strong and weak anisotropy. In Chapter 5 we carry out a detailed analysis of some anisotropic equations, by extending the scaling Ansatz to other observables in momentum space and by verifying these hypothesis using analytical results obtained from Renormalization Group calculations.

1.4 Surface pattern formation

In the previous sections we have seen that generic scale invariance, i.e. the lack of a characteristic length scale, is quite a typical feature of surfaces subject to growth by deposition or erosion. However, in the context of surface growth phenomena, there exist many systems that do not display scale invariance. On the contrary, a particular length scale can be selected, which gives rise to several possible *patterns*, depending on the geometric constraints and the symmetries of the system. Examples of patterns in nature can span several orders of magnitude in typical length scales [84], ranging from the shape of galaxies, to the band structure of the atmosphere for some planets (like Jupiter), to dunes and ripples forming in the desert due to erosion of the wind, to patterns at the nanoscale obtained by various experimental techniques, such as ion beam sputtering (see Figure 1.5).

Mathematically, a pattern arises due to an *instability* that prevents the system from relaxing to its equilibrium state. More precisely, a (linear) instability occurs when small perturbations of the homogeneous state are exponentially amplified by the dynamics, thus originating a novel state with a well-defined spatial structure. Interestingly, it turns out that the framework of continuous equations of the form (1.27) also provides a good description of pattern forming systems in the context of surface growth.

In order to predict the behavior of the system, at least at early stages of the dynamics, a so-called linear stability analysis is usually performed. As explained below, this technique turns out to be a valuable tool in order to classify non-equilibrium systems regarding their pattern forming properties. For equations of

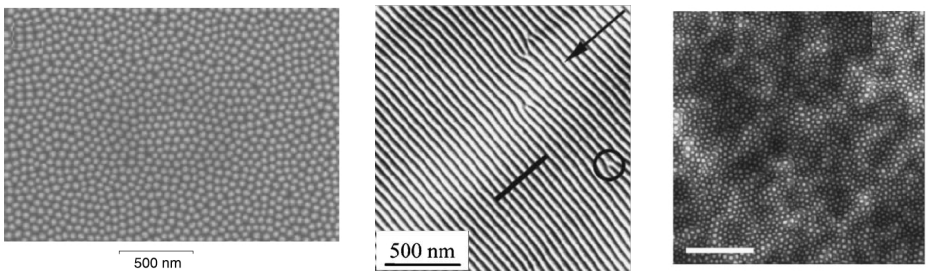

Figure 1.5: Examples of pattern formation in Ion Beam Sputtering experiments (see Sections 1.4 and 6.1). Left panel: highly ordered cones on a GaSb substrate irradiated with 420 eV Ar^+ ions at normal incidence. The picture has been taken from [85]. Central panel: ordered ripple structure produced by erosion of a silicon target with Kr^+ ions at 1200 eV, with incidence angle $\theta = 15°$. The arrow indicates the direction of the projection of the ion beam onto the substrate, while the circle shows a defect in the ripple structure. The picture has been taken from [86]. Right panel: short range order combined with long range disorder for a silicon sample irradiated with 1.2 keV Ar^+ ions at normal incidence. The bar represents 831 nm. The picture has been taken from [87]. The left and central panel are believed to provide examples of a Type I instability, while the right panel would constitute an instance of a Type II instability (see Section 1.4).

the type (1.27), the quantity of interest in this context is the real part of the dispersion relation $\sigma_{\mathbf{k}}$, which appears in the Fourier transform of Eq. (1.27),

$$\partial_t h_{\mathbf{k}} = \sigma_{\mathbf{k}} h_{\mathbf{k}} + \mathcal{N}[h]_{\mathbf{k}} + \eta_{\mathbf{k}}. \tag{1.51}$$

The quantity $\mathcal{N}[h]_{\mathbf{k}}$ is the Fourier transform of the nonlinear term of the equation, while $\sigma_{\mathbf{k}}$ is the Fourier transform of its linear operators. This quantity represents the rate of growth of an oscillatory perturbation to a homogeneous configuration with wave vector $\mathbf{k}$. The form of $\mathrm{Re}\,\sigma_{\mathbf{k}}$ as a function of $\mathbf{k}$ and of the other parameters in the system, provides us with a great deal of information. For instance, a local positive maximum of $\mathrm{Re}\,\sigma^*_{\mathbf{k}}$ at $\mathbf{k} = \mathbf{k}^*$ would suggest that the corresponding Fourier mode $h^*_{\mathbf{k}}$ will grow faster than all the others, thus selecting a preferred length scale for the system.

As stated above, a classification of linear instabilities is also available [84], that interestingly is akin to the statistical mechanics classification for phase transitions. Namely, consider an idealized one-dimensional pattern-forming system, that depends on a parameter p in such a way that the uniform state becomes linearly unstable when p exceeds a critical value p_c. The classification scheme is based on whether the maximum of σ_k passes through zero at a zero or a nonzero value of the wave number k as the control parameter p is varied, and on whether the instability is stationary or oscillatory at this point. Thus, linear instabilities can be classified as belonging to one of two classes that are traditionally referred to as type I and type II [84]. Each of these types can be further divided into two categories depending on

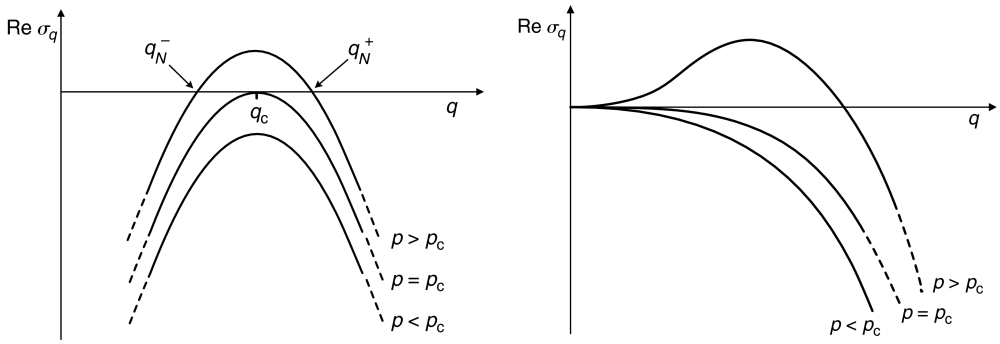

Figure 1.6: Growth rate $\mathrm{Re}\,\sigma_k$ as a function of k and for three values of p for the two main types of stationary linear instability. Upper left panel: type I instability. The value of p when the maximum of $\mathrm{Re}\,\sigma_k$ passes through zero identifies the critical parameter p_c and the wave number where this happens is the critical wave number k_c. The band of unstable modes is given by $k_N^- \leq k \leq k_N^+$. Upper right panel: type II instability. Note that the instability occurs first at $p = p_c$ at $k = 0$ but the wave number for the maximum growth rate occurs at a value of k that increases for $p > p_c$. The images have been taken from [84].

whether the *imaginary* part of the growth rate at onset given by a certain frequency ω_c is zero or not. If it is zero, we call the instability "stationary", whereas if it is nonzero, we call the instability "oscillatory". However, it turns out that stationary instabilities are the most relevant for the formation of time-independent patterns. The two main types are illustrated in Figure 1.6.

For a type-I instability, the instability occurs first at a nonzero wave number, i.e. the quantity σ_k first becomes positive at a critical wave number $k_c > 0$, so that the length $2\pi/k_c$ sets the characteristic scale of the patterns. For $p > p_c$, the uniform state is unstable to perturbations with wave vectors in a band between the neutral stability values, for which $\mathrm{Re}\sigma_k = 0$. These transitions are analogous to discontinuous (first order) phase transitions in that the typical length scale sets in abruptly at the critical point. Instabilities of this type give rise to morphologies characterized by well-ordered patterns. Examples can be found in the context of surface erosion by ion beam sputtering, where it is possible to produce extremely ordered arrays of quantum dots or ripples (see left and central panels of Figure 1.5). The qualitative behavior of the dispersion relation in this case is depicted in the left panel of Figure 1.6. For a type-II instability, the growth rate at $k = 0$ is always zero. This is often the case when one of the evolving fields obeys a conservation law so that the integrated value of the field over all space is constant over time. Typical curves of σ_k for p near p_c are shown on the right panel of Figure 1.6. Unlike a type I instability, this behavior implies that the characteristic length of the pattern diverges as $p \to p_c$, thus reminding of a second order (or continuous) phase transition for equilibrium systems, for which the correlation length diverges as the critical temperature is approached. These types of instabilities give rise to patterns

that typically tend to disorder at large length scales, due to the unstable modes at low k, see right panel of Figure 1.5.

2

ANALYTICAL AND NUMERICAL TOOLS

In this chapter, we provide an overview of the most important analytical and numerical techniques we will exploit throughout this thesis. We start out by considering the most important analytical tool we have used, the Dynamic Renormalization Group (DRG). After a short historical introduction and discussion about other analytical methods, we present an outline of the Forster-Nelson-Stephen procedure, which we will later on apply to several Langevin equations. We then turn to simulations, and briefly present and discuss the numerical (pseudospectral) method we have used to integrate all the models we have studied in this thesis.

2.1 Analytical tools: Renormalization group

Although great advances have been made in the search for exact solutions of nonlinear stochastic partial differential equations [61], e.g. for the Kardar-Parisi-Zhang equation in one spatial dimension, in general it is still beyond the current mathematical possibilities to exactly solve equations with other forms of nonlinearities and/or in higher dimensions. Moreover, while for linear stochastic equations such as, for example, the EW or LMBE equations, the values of the scaling exponents can be readily extracted from a simple rescaling of coordinates and fields [5], in general this is not the case in the presence of nonlinearities. In the latter, it is a non-trivial balance between the linear and the non-linear operators occurring in the equation which controls the asymptotic behavior. Thus, a variety of approximation methods has been put forward in order to elucidate the interplay among these terms, and to shed light on the asymptotic behavior of such systems. An example is given by the so-called mode-coupling theory, where appropriate evolution equation for the *correlation functions* are derived, and successively approximated by

various methods. Reference [88] provides a comprehensive review of this method, while in [89] the authors apply this technique to an equation we also study in this Thesis, namely the Hwa-Kardar equation. Another possibility is to consider approximations of the Fokker-Planck equation associated with the Langevin equation at hand, and then derive equations for the correlation functions. Such a procedure is usually referred to as *self-consistent expansion* [90].

Here, we focus on another approach, namely the renormalization group analysis. This procedure has been used quite successfully in the context of kinetic roughening, and has played a crucial role in 20th century physics in two apparently unrelated domains: the theory of fundamental interactions at the microscopic scale and the theory of continuous macroscopic phase transitions [91, 92]. In the former framework, it emerged in response to the necessity of renormalization to cancel infinities that appear in a straightforward interpretation of quantum field theory, while in the context of statistical physics, a more general procedure based on recursive averaging over short distance degrees of freedom was introduced to explain the universality properties of continuous phase transitions [9].

Several implementation of this method are available to study out-of-equilibrium systems. One possibility is to perform the coarse-graining and rescaling procedures (see Section 2.1.1) in real space, analogously to the Kadanoff block-spin transformation for the Ising model [9]. More details about this procedure are given in [93, 94] and references therein. However, the most common methods in this context have been put forward in momentum space. The field-theoretical approach pioneered by Martin, Siggia, Rose [95], Janssen [96] and de Dominicis [97], provides a systematic and controlled method for renormalization of stochastic parital differential equations [98], which moreover allows a systematic treatment of the symmetries of the problem, and can be modified in order to perform approximations that are non-perturbative [26, 99]. The basic idea, borrowed from quantum field theory [100], is to write the Langevin equations as a field theory formulated by using path integrals. In principle, this technique allows to write down equations for the correlation functions, that may be subject to several approximations in order to extract information on the asymptotic behavior of the system.

In this Thesis, we will use another approach in momentum space, the so-called dynamic renormalization group (DRG) method, which works directly on the Fourier-transformed Langevin equation [10], thus avoiding use of field-theoretical techniques. In the next section we present the Forster-Nelson-Stephen renormalization group scheme [101], which we will use in the remainder of this work in order to study the asymptotic properties of some anisotropic SPDEs. Originally, this method was developed in the context of fluctuating hydrodynamics [102] and, more recently, it has been successfully applied to understand e.g. the multiscale nature of fluctuating interfaces [21], kinetic roughening in surfaces controlled by unstable nonlocal interactions [103, 104], or the interplay between noise and morphological instabilities in anisotropic pattern-forming systems [105, 106], to cite a few examples.

2.1.1 The Forster-Nelson-Stephen theory

In this work we will address several equations in two spatial dimensions with different forms and number of nonlinearities. The most general way of writing such equations is in Fourier space, namely

$$\partial_t h_{\mathbf{k}} = \sigma_{\mathbf{k}} h_{\mathbf{k}} + \lambda_x \mathcal{N}_x[h, \nabla h]_{\mathbf{k}} + \lambda_y \mathcal{N}_y[h, \nabla h]_{\mathbf{k}} + \eta_{\mathbf{k}}, \tag{2.1}$$

where $\mathbf{k}$ is the wavevector in a two-dimensional Fourier space. The fluctuating term $\eta_{\mathbf{k}}$ is the space-Fourier transform of a Gaussian white noise with zero mean and variance equal to $2D$. For the sake of generality, we leave the dispersion relation $\sigma_{\mathbf{k}}$ unspecified. With respect to the nonlinear operators $\mathcal{N}_{x,y}$, they also remain generic, except for the fact that they are *bilinear* products of the height field and its derivatives - such as e.g. $(\partial_x h)^2$, $h\partial_x h$, etc. - with $\lambda_{x,y}$ being the coupling constants.

The first step of the DRG procedure consists in identifying the cut-off wavenumber of the problem $\Lambda = \pi/\Delta x$, with Δx being the lattice spacing in real space. Then, Eq. (2.1) is time-Fourier transformed as follows,

$$[-\sigma_{\mathbf{k}} - i\omega] h_{\mathbf{k},\omega} = \eta_{\mathbf{k},\omega} + \sum_{i=x}^{y} \lambda_i \int_{\mathbf{q}\in\mathcal{S}} \frac{d\mathbf{q}}{(2\pi)^2} \int_{-\infty}^{\infty} \frac{d\Omega}{2\pi} f_i(\mathbf{q}, \mathbf{k}) h_{\mathbf{q},\Omega} h_{\mathbf{k}-\mathbf{q},\omega-\Omega}, \tag{2.2}$$

where ω is the time frequency and the specific forms of the functions $f_{x,y}(\mathbf{q}, \mathbf{k})$ depend on those of the non-linear terms $\mathcal{N}_{x,y}$ in the equation. $\mathcal{S}$ is the region in momentum space such that both q_x and q_y are smaller than the cutoff Λ. Frequently, this square (or hypercubic) region is approximated by a circular (or spherical) one, so that the condition $\mathbf{q} \in \mathcal{S}$ can be written as $|\mathbf{q}| < \Lambda$. For simplicity, in the remainder of this section we will keep this approximation. However, it has to be noted that the form of $\mathcal{S}$ changes when dealing with anisotropic equations, and this introduces some complications that will be dealt with in Appendix A.

The next step is to split our integration region $\mathcal{S}$ into two parts, this separation being parametrized by a number $b = e^{\delta l} > 1$, in such a way that the height and noise fields are also divided into two disjoint intervals

$$h_{\mathbf{k},\omega} = \begin{cases} h^{<}_{\mathbf{k},\omega} & \text{for} \quad 0 < k < \Lambda/b, \\ h^{>}_{\mathbf{k},\omega} & \text{for} \quad \Lambda/b < k < \Lambda, \end{cases} \tag{2.3}$$

$$\eta_{\mathbf{k},\omega} = \begin{cases} \eta^{<}_{\mathbf{k},\omega} & \text{for} \quad 0 < k < \Lambda/b, \\ \eta^{>}_{\mathbf{k},\omega} & \text{for} \quad \Lambda/b < k < \Lambda, \end{cases} \tag{2.4}$$

where $k = |\mathbf{k}|$.

Now, in the FNS scheme we eliminate the high (or fast) modes by solving the growth equation perturbatively for $h^{>}_{\mathbf{k},\omega}$, and substitute the solution into the equation for $h^{<}_{\mathbf{k},\omega}$. To do this, we first define the *bare propagator* G_0 as

$$G_0(\mathbf{k}, \omega) = [-\sigma_{\mathbf{k}} - i\omega]^{-1}, \tag{2.5}$$

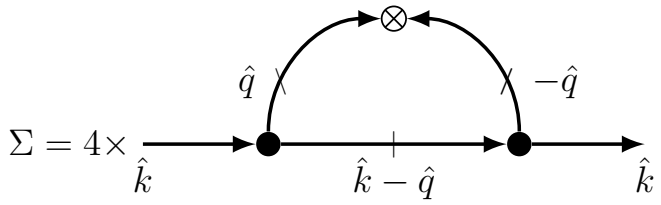

Figure 2.1: Diagram of the propagator renormalization $\Sigma(\mathbf{k},\omega)$. The arrows with vertical bars represent the bare propagators for fast modes.

so that, when the nonlinearities are set to zero, Eq. (2.2) reduces to

$$h_{0\mathbf{k},\omega} = G_0(\mathbf{k},\omega)\eta_{\mathbf{k},\omega}. \tag{2.6}$$

This is the starting point of a perturbative expansion, parametrized by the nonlinearities. For simplicity in the illustration of the procedure, let us consider a single nonlinearity λ_0. Then, the expansion for the fast modes would be

$$h^{>}_{\mathbf{k},\omega} = h^{>}_{0\mathbf{k},\omega} + \lambda_0 h^{>}_{1\mathbf{k},\omega} + \lambda_0^2 h^{>}_{2\mathbf{k},\omega} + \lambda_0^3 h^{>}_{3\mathbf{k},\omega} + \cdots . \tag{2.7}$$

Now we write Eq. (2.2) for the slow modes (and a single nonlinearity),

$$G_0^{-1}(\mathbf{k},\omega)h^{<}_{\mathbf{k},\omega} = \eta^{<}_{\mathbf{k},\omega} + \lambda_0 \int_{|\mathbf{q}|<\Lambda/b} \frac{d\mathbf{q}}{(2\pi)^2} \int_{-\infty}^{\infty} \frac{d\Omega}{2\pi} f_i(\mathbf{q},\mathbf{k}) \times \left[h^{<}_{\mathbf{q},\Omega} h^{<}_{\mathbf{k}-\mathbf{q},\omega-\Omega} + 2\, h^{<}_{\mathbf{q},\Omega} h^{>}_{\mathbf{k}-\mathbf{q},\omega-\Omega} + h^{>}_{\mathbf{q},\Omega} h^{>}_{\mathbf{k}-\mathbf{q},\omega-\Omega} \right], \tag{2.8}$$

and replace the height function for fast modes with Eq. (2.7). The resulting equation is quite complicated, and a diagrammatic expansion is useful. Once the whole set of diagrams is determined, we can average out the effect of high frequencies according to the following assumptions:

- The low-frequency components are statistically independent of the high-frequency components.
- Averages involving $h_0^{>}$ can be evaluated using Eq. (2.6) and the statistics of the noise $\eta^{>}$, as G_0 is a deterministic function.
- The noise has zero mean, hence $\langle h_0^{>} \rangle = 0$ and the same result holds for all averages involving an odd number of $h_0^{>}$ factors.
- We drop terms containing higher order products of $h^{<}$, such as $h^{<}h^{<}h^{<}$ because they are irrelevant with respect to $h^{<}h^{<}$ in the hydrodynamic limit [18, 102].

Once the diagrammatic expansion and the average over high frequencies has been carried out, Eq. (2.8) becomes

$$G^{<}(\mathbf{k},\omega)^{-1}h^{<}_{\mathbf{k},\omega} = \eta^{<}_{\mathbf{k},\omega} + \lambda^{<} \int_{|\mathbf{q}|\leq\Lambda/b} \frac{d\mathbf{q}}{(2\pi)^2} \int_{-\infty}^{\infty} \frac{d\Omega}{2\pi} f_i(\mathbf{q},\mathbf{k}) h^{<}_{\mathbf{q},\Omega} h^{<}_{\mathbf{k}-\mathbf{q},\omega-\Omega}, \tag{2.9}$$

which features three *renormalized* quantities:

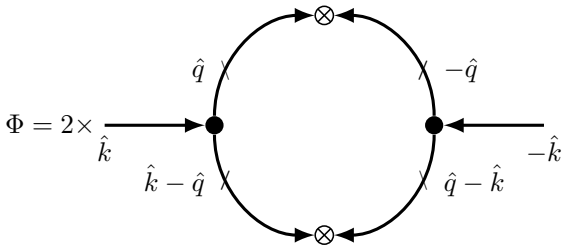

Figure 2.2: Diagram of the noise variance renormalization $\Phi(\mathbf{k},\omega)$. The arrows with vertical bars represent the bare propagators for fast modes.

- A renormalized propagator, given by

$$G^<(\mathbf{k},\omega) = [-\sigma_{\mathbf{k}} - \Sigma(\mathbf{k},0) - i\omega]^{-1}, \tag{2.10}$$

  where $\Sigma(\mathbf{k},0)$ is computed from the diagram in Figure 2.1, and allows us to write a new dispersion relation as a sum of the renormalized parameters. For instance, suppose that the dispersion relation takes the form

$$\sigma_{\mathbf{k}} = \nu k^2 - \mathcal{K} k^4. \tag{2.11}$$

  Then, $\Sigma(\mathbf{k},0)$ can be written as

$$\Sigma(\mathbf{k},0) = \Sigma_\nu k^2 + \Sigma_{\mathcal{K}} k^4, \tag{2.12}$$

  and taking into account Eq. (2.10), we can define two *renormalized* parameters

$$\nu^< = \nu + \Sigma_\nu, \tag{2.13}$$
$$\mathcal{K}^< = \mathcal{K} + \Sigma_{\mathcal{K}}. \tag{2.14}$$

- A renormalized *noise variance* $D^<$, which is computed starting from the equation

$$\langle h^<_{\mathbf{k},\omega} h^<_{-\mathbf{k},-\omega}\rangle = 2DG^<(\mathbf{k},\omega)G^<(-\mathbf{k},-\omega), \tag{2.15}$$

  that leads, with a little algebra, to

$$\langle \eta^<_{\mathbf{k},\omega}\eta^<_{\mathbf{k}',\omega'}\rangle = 2[D + \Phi(\mathbf{k},0)](2\pi)^{d+1}\delta_{\mathbf{k}+\mathbf{k}'}\delta_{\omega+\omega'}, \tag{2.16}$$

  where $\Phi(\mathbf{k},0)$ is the diagram that survives the elimination of fast modes, and is shown in Figure 2.2. The renormalized noise variance will then be given by

$$D^< = D + \Phi(\mathbf{k},0). \tag{2.17}$$

- A renormalized nonlinearity $\lambda^<$, which is computed from the diagrams shown in Figure 2.3. At first order (one loop) in the series expansion, it has been shown that, for the type of nonlinearities we will consider in this work, the contribution of the two diagrams cancels out [104], so that

$$\lambda^< = \lambda_0. \tag{2.18}$$

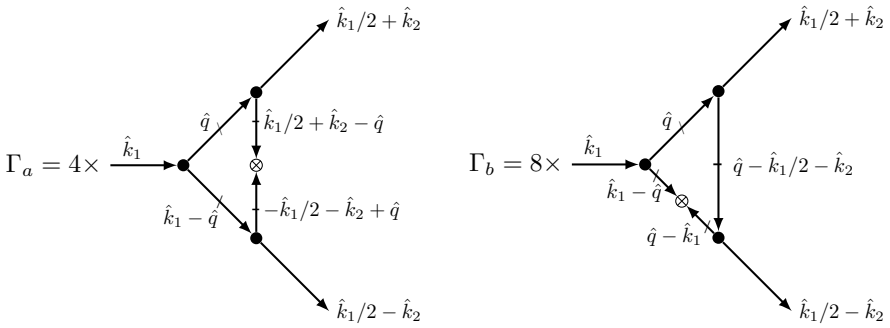

Figure 2.3: Diagram of the vertex renormalization $\Gamma_a(\mathbf{k},\omega)$ and $\Gamma_b(\mathbf{k},\omega)$. The arrows with vertical bars represent the bare propagators for fast modes.

This concludes the *coarse-graining* part of the renormalization procedure.

The next step is to perform a rescaling of the coordinates and fields that restores the value of the wavevector cut-off, which was changed to Λ/b after coarse-graining, to its bare value Λ. In the isotropic case, such rescaling is given by

$$\text{real space: } \begin{cases} \mathbf{r} \to b\tilde{\mathbf{r}} \\ t \to b^z \tilde{t} \\ h \to b^\alpha \tilde{h} \end{cases}, \qquad \text{Fourier space: } \begin{cases} \mathbf{k} \to \tilde{\mathbf{k}}/b \\ \omega \to \tilde{\omega}/b^z \\ h \to b^\alpha \tilde{h} \end{cases}, \tag{2.19}$$

while for anisotropic equations, the rescaling needs also to be anisotropic in the x and y (or k_x and k_y) directions. This procedure is applied to Eq. (2.9) and, after imposing scale invariance and setting $b = e^{\delta l}$, we are able to express the change in the parameters in a differential form. The resulting set of equations is often referred to as the DRG flow, and is an autonomous dynamical system in which the independent variable is l. By defining suitable coupling constants, this flow does not depend explicitly on the critical exponents α and z.

The study of the fixed points and their stability gives insight about the critical behavior of Eq. (2.1) in the hydrodynamic limit. At the fixed points we can calculate the critical exponents by substituting the values of the coupling constants into the equations for the parameters. Moreover, the linear stability of each fixed point gives us information about the true asymptotic behavior displayed by the equation, and about the crossover scaling it may feature.

2.2 Numerical tools: Pseudospectral method

Despite the fact that the DRG analysis usually gives valuable insight about the critical behavior of out-of-equilibrium models, it is very useful to combine such analysis with numerical simulations to obtain a better understanding of the system. This is due to the fact that the renormalization group technique requires approximations and can fail in predicting the correct exponents values. A typical example is the KPZ equation in two dimensions, in which the fixed point belongs to a strong coupling regime, thus outside the scope of perturbative techniques [5, 107]. This makes direct numerical integration an extremely useful tool as a reliable source of precise values for the critical exponents, as well as for studying the preasymptotic behavior of a given model, and provide detailed comparison to e.g. experimental data.

A great number of numerical methods have been proposed for the direct integration of stochastic PDEs. In most cases a straightforward finite-differences (FD) method on a lattice does an excellent job and provides highly precise values for the critical exponents, at least in dimensions of experimental relevance. In this approach one basically approximates the continuous height field, h, by its values on the lattice sites, h_j, and derivatives by differences between neighboring sites. However, these methods have been found to present reliability issues in various cases. For instance, an artifact of FD methods leads in several cases to the appearance of a morphological instability that is not present in the actual continuum equation [108, 109]. Other problems concern the accuracy of the numerical results, that strongly depends on the discretization rules that are chosen. For example, Lam and Shin have shown that a conventional discretization of the KPZ equation in one spatial dimension leads to effective parameter values for its discretized version, that are not consistent with the nominal ones [110].

Given the problems mentioned above, several authors proposed variants based on regularizations of FD [108, 109, 111], or have tried different numerical schemes. Spectral methods are a class of techniques which are widely used in fluid mechanics and in applied mathematics to integrate partial differential equations. These methods work in Fourier space and their strength resides in their exponential convergence for smooth solutions [112]. Let us consider, for simplicity, an equation of the type (1.27), but without the noise term. Such equation is discrete-Fourier transformed in space, giving a system of ODEs

$$\partial_t h_{\mathbf{k}} = \sigma_{\mathbf{k}} h_{\mathbf{k}} + \mathcal{N}[h]_{\mathbf{k}}, \tag{2.20}$$

where $\sigma_{\mathbf{k}}$ is the *linear dispersion relation* and the term $\mathcal{N}_{\mathbf{k}}[h]$ is the Fourier transform of the nonlinear part. However, Eq. (2.20) is difficult to treat numerically, for several reasons. One of them is that the nonlinear term is calculated as a convolution over Fourier modes, which is a very costly operation. To avoid this, *pseudospectral* methods have been introduced. The strength of these techniques resides in the fact that they compute the linear and stochastic terms in Fourier space, while

the nonlinear part is computed in real space as a simple multiplication. In the context of kinetic roughening, such methods were first introduced by Giada, Giacometti, and Rossi [31, 113] for the Kardar-Parisi-Zhang equation. Specifically, the authors proved that such methods perform even better than the improved discretization proposed by Lam and Shin [114].

Another problem arising in the numerical integration of Eq. (2.20) is that the linear term $\sigma_{\mathbf{k}}$ can give rise to a *stiff* system [115]. This means that, due to numerical stability constraints, the time step is forced down to a very small value even when the variation of the solution is very small. For spectral methods, this is due to the fact that the time scale for the $n-$th Fourier mode scales as $\mathrm{O}(n^{-m})$ for large n, where m is the order of the highest spatial derivative, and thus, explicit time-stepping techniques require an extremely small time step in order to be stable. Although implicit schemes with less stringent constraints on the time step are available, they are costly (or unfeasible) to implement in more than two spatial dimensions [116]. In Section 2.2.2 we present an algorithm based on the so-called *integrating factor*, which is able to overcome the difficulties mentioned above. We have employed this method for all the models studied in this thesis.

However, many alternative methods are available in this context. One of the most succesful one is the so called "explicit exponential time differencing" [116, 117], which consist in multiplying equation (2.20) by an exponential term, typically $e^{-\sigma_{\mathbf{k}}t}$, and then integrating it over one time step of length Δt, giving

$$h_{\mathbf{k}}(t+\Delta t) = e^{\sigma_{\mathbf{k}}\Delta t}h_{\mathbf{k}}(t) + e^{\sigma_{\mathbf{k}}\Delta t}\int_0^{\Delta t} e^{-\sigma_{\mathbf{k}}\tau}\mathcal{N}[h(t_n+\tau), t_n+\tau]d\tau. \quad (2.21)$$

All methods of this kind then approximate the integrand on the right hand side in different ways, leading to different truncation errors. These approximations allow to construct generalizations of the most common numerical schemes for ordinary differential equations, such as Euler's or Runge-Kutta's [115]. Recently, implicit pseudospectral methods, such as predictor-corrector, have been also put forward for stochastic PDEs [118].

Many other numerical schemes, in real or Fourier space, are available in order to solve stochastic or deterministic PDEs. Kassam and Trefethen [119] give a summary of the most popular methods for deterministic PDEs, and compare several of them, including the pseudospectral one, for the deterministic Kuramoto-Sivashinsky equation (see Chapter 3). For SPDEs with additive noise like the ones we will study in this work, we refer to [120] and [121] for a review and a discussion of several numerical methods in real and Fourier space. In [122], a pseudospectral method for the Michelson-Sivashinsky equation is compared to a highly accurate method in real space, giving almost identical results.

In general, pseudospectral methods are found to be numerically more stable than finite differences. For this reason, less computational effort is needed in order to reach the hydrodynamic limit of the equations at hand, thus making the estimate of the critical exponents easier. In this work, we will use a pseudospectral

method with integrating factor, combined with an Euler-type approximation for the integrand, as explained in Section 2.2.2.

2.2.1 Pseudospectral method: Basic principles

In this section, we illustrate the basic mathematical concepts for the development of pseudospectral methods. After defining the discrete Fourier transform of a function, we discuss the treatment of nonlinearities and the elimination of the so-called aliasing error by means of the zero-padding technique. More details on this analysis can be found in [123].

The forward and backward Fourier transforms of a d-dimensional periodic function $h(\mathbf{r})$ on a hypercube $\Omega = [0, L]^d$ can be defined as

$$h_{\mathbf{k}} = \frac{1}{L^{d/2}} \int_{\Omega} d\mathbf{r} e^{-i\mathbf{k}\cdot\mathbf{r}} h(\mathbf{r}), \tag{2.22}$$

$$h(\mathbf{r}) = \frac{1}{L^{d/2}} \sum_{\mathbf{n}=-\infty}^{\infty} h_{\mathbf{k}} e^{i\mathbf{k}\cdot\mathbf{r}}, \tag{2.23}$$

or, alternatively,

$$h_{\mathbf{k}} = \frac{1}{L^{d}} \int_{\Omega} d\mathbf{r} e^{-i\mathbf{k}\cdot\mathbf{r}} h(\mathbf{r}), \tag{2.24}$$

$$h(\mathbf{r}) = \sum_{\mathbf{n}=-\infty}^{\infty} h_{\mathbf{k}} e^{i\mathbf{k}\cdot\mathbf{r}}, \tag{2.25}$$

where $\mathbf{k} = 2\pi\mathbf{n}/L$, and $\mathbf{n} = (n_1, n_2, \ldots, n_d)$, with $n_j \in \mathbb{Z}$. In this chapter we will use the second definition, because this is the convention used by most discrete Fourier transform libraries. However, the first definition will be used for the theoretical calculations developed in Chapter 4. These representations require a complete knowledge of $h(\mathbf{r}, t)$ in the whole domain, therefore they are unfeasible for numerical integration purposes and we need to turn to some kind of approximations.

The first approximation consists in truncating the series (2.25) by e.g. setting to zero all the modes such that $|\mathbf{n}| > N/2$,

$$h_N(\mathbf{r}) = \sum_{\mathbf{n}\in\Gamma_N} h_{\mathbf{k}} e^{i\mathbf{k}\cdot\mathbf{r}}, \tag{2.26}$$

where $\Gamma_N = \{(n_1, n_2, \ldots, n_d)| \quad -N/2 \leq n_i \leq N/2 - 1, i = 1, \ldots, d\}$. A second approximation consists in discretizing the real space with N collocation points $\mathbf{r}_j$ in each direction, such that

$$\mathbf{r}_j = \Delta x(j_1, j_2, \ldots, j_d), \tag{2.27}$$

where $\Delta x = L/N$ and $j_i = 0, \ldots, N-1$ for each direction. In this way, the forward Fourier transform (2.24) is now approximated by the discrete transform (DFT) of the function $h_{\mathbf{j}}$ evaluated at the collocation points

$$\hat{h}_{\mathbf{k}} = \mathcal{F}_D[h_{\mathbf{j}}]_{\mathbf{k}} \equiv \frac{1}{N^d} \sum_{\mathbf{j}} h_{\mathbf{j}} e^{-i\mathbf{k}\cdot\mathbf{r}_j}, \tag{2.28}$$

while the inverse discrete transform can be written as

$$h_{\mathbf{j}} = h(\mathbf{r}_j) = \mathcal{F}_D^{-1}[\hat{h}_{\mathbf{k}}]_{\mathbf{j}} = \sum_{\mathbf{n}\in\Gamma_N} \hat{h}_{\mathbf{k}} e^{i\mathbf{k}\cdot\mathbf{r}_j}. \tag{2.29}$$

One can easily compute the approximation error of $\hat{h}_{\mathbf{k}}$ by equating (2.25) with (2.26). Explicitly, in each one of the d independent directions we have

$$h(r_j) = \sum_{n_l=-\infty}^{\infty} h_{k_l} e^{ik_l r_j} = \sum_{n_l=-N/2}^{N/2} e^{ik_l r_j} \left(\sum_{m=-\infty}^{\infty} h_{k_l+mN} \right), \tag{2.30}$$

and comparing with (2.29), we find

$$\hat{h}_{k_l} = \sum_{m=-\infty}^{\infty} h_{k_l+mN}. \tag{2.31}$$

This equation shows that, in any direction, the k-th mode of the DFT of $h_{\mathbf{j}}$ depends on this mode and all the modes which *alias* it on the grid of collocation points $\{\mathbf{r}_j\}$. During the numerical implementation of the pseudospectral (PS) method, we need to take into account this fact, in particular when we compute the non-linear term.

Let us now consider the derivative of a height function in Fourier space. It is easy to see from equation (2.25) that

$$\partial_{x_l} h(\mathbf{r}) = \sum_{\mathbf{n}=-\infty}^{\infty} ik_l h_{\mathbf{k}} e^{i\mathbf{k}\cdot\mathbf{r}}, \tag{2.32}$$

where l refers to any of the possible directions. This equations is approximated by

$$\partial_{x_l} h(\mathbf{r}_j) = \sum_{\mathbf{n}=-N/2}^{N/2} ik_l \hat{h}_{\mathbf{k}} e^{i\mathbf{k}\cdot\mathbf{r}_j}, \tag{2.33}$$

and it is possible to prove that the error in doing such an approximation is of the same order as the one we make in changing $h_{\mathbf{k}}$ to $\hat{h}_{\mathbf{k}}$ [112].

Finally, in general we have to know how to deal with nonlinear terms. Frequently, such terms can be written in real space as a multiplication of two functions u and v

$$w(x) = u(x)v(x). \tag{2.34}$$

The Fourier transform of (2.34) is

$$w_k = \sum_{\substack{m+p=n \\ m,p\in\mathbb{Z}}} u_m v_p, \tag{2.35}$$

where $k = 2\pi n/L$, and u_m and v_p are calculated from (2.24). After approximating u, v, and w by their truncated series of degree $N/2$, equation (2.35) becomes

$$w_k = \sum_{\substack{m+p=n \\ |m|+|p|\leq N/2}} u_m v_p. \tag{2.36}$$

This sum requires a number of operations of order N^2 which, compared with FFT, is computationally too expensive. The main idea of the PS method is to apply the inverse DFT to u and v, compute their product, and use again the DFT to get w. This procedure reads

$$\hat{w}_k = \frac{1}{N}\sum_{j=0}^{N-1} v(r_j)u(r_j)e^{-ikr_j} = \frac{1}{N}\sum_{m,p=-N/2}^{N/2-1}\sum_{j=0}^{N-1} v_m u_p e^{i(2\pi/L)r_j(m+p-n)}. \tag{2.37}$$

Now, using the orthogonality relation

$$\frac{1}{N}\sum_{j=0}^{N-1} e^{ir_j k} = \delta_{n-zN,0} \qquad z\in\mathbb{Z}, \tag{2.38}$$

where $k = 2\pi n/L$, we find

$$\hat{w}_k = \sum_{m,p=-N/2}^{N/2-1} v_m u_p \delta_{(m+p-n)-zN,0} = \sum_{m=-N/2}^{N/2-1}\sum_{z=-1}^{1} v_m u_{n-m+zN}, \tag{2.39}$$

where the range of z arises from the constraint $m, p, n \in [-N/2, N/2-1]$. Splitting the sum in a part corresponding to $z = 0$ and the rest, we get

$$\hat{w}_k = w_k + \sum_{m=-N/2}^{N/2-1} v_m u_{n-m\pm N}, \tag{2.40}$$

the second sum being the aliasing error for the non-linear term. One common technique to remove this error is called zero-padding [112], and it consists in calculating the DFT with a number $M > N$ of modes. The extra modes with $|n| > N/2$ are initially set to zero. Then, equation (2.37) reads

$$\hat{w}_k = \sum_{m=-M/2}^{M/2-1} v_m u_{n-m} + \sum_{m=-M/2}^{M/2-1} v_m u_{n-m\pm M} \tag{2.41}$$

where $n \in [-M/2, M/2-1]$. We now want to choose M such that the second term on the right hand side vanishes. Keeping in mind that we will only use the first N modes of $\hat{w}_k$, and that v_m and u_p are zero for $|m|, |p| \geq N/2$, we get that

$$u_{n-m+M} \neq 0 \qquad \text{for} \quad n - m < \frac{N}{2} - M, \tag{2.42}$$

$$n - m \geq 1 - N \qquad \text{for} \quad n, m \in [-N/2, N/2-1], \tag{2.43}$$

and combining the two conditions, we get

$$u_{n-m+M} \neq 0 \qquad \text{for} \quad 1 - N < \frac{N}{2} - M, \tag{2.44}$$

which implies

$$u_{n-m+M} = 0 \qquad \text{for} \quad M \geq \frac{3}{2}N - 1. \tag{2.45}$$

This tells us that, for the aliasing error to vanish, we need to expand the DFTs to at least $M \geq 3N/2 - 1$ components. This method requires the computation of two FFT of size $3N/2$. A rough estimate of the number of operations required for this method is $(45/4)N \log_2(3N/2)$ [112], which is obviously less than the direct computation of the convolution (2.36).

2.2.2 Pseudospectral method: Integrating factor

The Fourier transform of the SPDE's that will be studied in this work takes the form given by Eq. (2.1). For simplicity, let us consider here an equation with a single nonlinearity,

$$\partial_t h_{\mathbf{k}} = \sigma_{\mathbf{k}} h_{\mathbf{k}} + \mathcal{N}[h]_{\mathbf{k}} + \eta_{\mathbf{k}}, \tag{2.46}$$

with the same conventions as above. The variance of the Fourier transform of the white noise $\eta_{\mathbf{k}}(t)$ turns out to be

$$\langle \eta_{\mathbf{k}}(t) \eta_{\mathbf{k}'}(t') \rangle = \frac{2D}{L^d} \delta_{\mathbf{k}+\mathbf{k}'} \delta(t - t'). \tag{2.47}$$

Considering now the approximation $h_{\mathbf{k}} \approx \hat{h}_{\mathbf{k}}$, equation (2.46) turns into a set of N coupled ordinary differential equations. These equations mantain the original form (2.46), with the only difference that we have reduced the number of modes.

After discretizing time using a time step Δt, one can choose various schemes to integrate this set of equations. A typical simple choice is to use a Euler scheme of first order [124]

$$\hat{h}_{\mathbf{k}}(t + \Delta t) = \hat{h}_{\mathbf{k}}(t) + \Delta t \left[\sigma_{\mathbf{k}} \hat{h}_{\mathbf{k}}(t) + \mathcal{N}[h(t)]_{\mathbf{k}}\right] + \sqrt{\Delta t}\, \hat{\eta}_{\mathbf{k}}(t). \tag{2.48}$$

In this work, we will use a different scheme, called *integrating factor*. This scheme is based on the solution of the linearized version of (2.46) [115, 125]. If we perform the following change of variables

$$\hat{h}_{\mathbf{k}}(t) = e^{\sigma_{\mathbf{k}} t} z_{\mathbf{k}} + e^{\sigma_{\mathbf{k}} t} \int_0^t ds e^{-\sigma_{\mathbf{k}} s} \hat{\eta}_{\mathbf{k}}(s) = e^{\sigma_{\mathbf{k}} t} z_{\mathbf{k}} + G_{\mathbf{k}}(t), \tag{2.49}$$

then, the new field $z_{\mathbf{k}}(t)$ can be expressed in terms of $\hat{h}_{\mathbf{k}}(t)$ as follows

$$z_{\mathbf{k}} = e^{-\sigma_{\mathbf{k}} t}\left(\hat{h}_{\mathbf{k}} - G_{\mathbf{k}}\right), \tag{2.50}$$

and its temporal evolution only depends on the non-linear term,

$$\partial_t z_{\mathbf{k}} = e^{-\sigma_{\mathbf{k}} t}\mathcal{N}[h]_{\mathbf{k}}. \tag{2.51}$$

Now, we use a single-step Euler method to integrate (2.51),

$$z_{\mathbf{k}}(t+\Delta t) = z_{\mathbf{k}}(t) + \Delta t\, e^{-\sigma_{\mathbf{k}} t}\mathcal{N}[h(t)]_{\mathbf{k}}, \tag{2.52}$$

and going back to original variables, we get

$$\begin{aligned}\hat{h}_{\mathbf{k}}(t+\Delta t) &= e^{\sigma_{\mathbf{k}}(t+\Delta t)} z_{\mathbf{k}}(t+\Delta t) + G_{\mathbf{k}}(t+\Delta t) \\ &= e^{\sigma_{\mathbf{k}}\Delta t}\left[\hat{h}_{\mathbf{k}}(t) + \Delta t\,\mathcal{N}[h(t)]_{\mathbf{k}}\right] + g_{\mathbf{k}}(t),\end{aligned} \tag{2.53}$$

where the new noise term is

$$g_{\mathbf{k}}(t) = e^{\sigma_{\mathbf{k}}(t+\Delta t)}\int_t^{t+\Delta t} ds\, e^{-\sigma_{\mathbf{k}} s}\,\hat{\eta}_{\mathbf{k}}(s), \tag{2.54}$$

with variance

$$\langle g_{\mathbf{k}}(t) g_{\mathbf{k}'}(t')\rangle = \left(\frac{2DN^d}{\Delta x^d}\right)\frac{e^{2\sigma_{\mathbf{k}}\Delta t}-1}{\sigma_{\mathbf{k}}}\delta_{\mathbf{k}+\mathbf{k}'}\delta(t-t'). \tag{2.55}$$

Then, the algorithm for the PS integration is as follows:

i) We start from an initial condition, usually a flat interface, $h_{\mathbf{k}}(0) = 0$.

ii) We compute the constant vectors for the numerical scheme, i.e. $\sigma_{\mathbf{k}}$, $e^{\sigma_{\mathbf{k}}\Delta t}$ and the noise variance

$$V_{\mathbf{k}} = \left[\left(\frac{2D}{\Delta x^d}\right)\frac{e^{2\sigma_{\mathbf{k}}\Delta t}-1}{\sigma_{\mathbf{k}}}\right]^{1/2}. \tag{2.56}$$

iii) At each time step, the algorithm performs zero-padding depending on the form of the non-linear term, computes this term in real space, and then Fourier-transforms it. The padding procedure is very dependent on the numerical algorithm which performs the Fourier transform. In our case, the transform has been implemented using the fftw3 library (see website `www.fftw.org`).
An example of nonlinear term is the KPZ nonlinearity $(\nabla h)^2$, which appears in many equations describing surface growth. For such a term, the padding procedure is as follows:

- We start with the interface in Fourier space, $\hat{h}_{\mathbf{k}}$.

- We compute the derivative in each direction in Fourier space, e.g. for the x direction,
$$\partial_x \hat{h}_{\mathbf{k}} = ik_x \hat{h}_{\mathbf{k}}, \tag{2.57}$$
and store the result in a vector (or matrix, if we are in $d = 2$) with M modes, with $M > 3N/2$, where all the modes larger than N are set to zero.
- We compute the backward transform of the derivatives, and we raise the result to the power 2, obtaining, for example in the x direction, a matrix containing a discretized version of $(\partial h/\partial x)^2$. If we work in dimension higher than one, we also have to add the matrices corresponding to derivatives in each direction, obtaining e.g. for $d = 2$, $(\nabla h)^2 = (\partial h/\partial x)^2 + (\partial h/\partial y)^2$, which is the correct expression of the nonlinear term.
- By Fourier transforming the resulting matrix, we obtain a matrix containing an expression of the nonlinear term $\mathcal{N}[h]_{\mathbf{k}}$ in Fourier space, and we can continue with the numerical integration of the equation.

iv) Succesively, the algorithm generates in real space a vector of Gaussian uncorrelated random numbers $u_{\mathbf{r}}$ with unit variance and Fourier transforms it to obtain a vector $u_{\mathbf{k}}$. Since the variance of the transformed vector is now equal to $\langle u_{\mathbf{k}} u_{\mathbf{k}'} \rangle = N^d \delta_{\mathbf{k}+\mathbf{k}'}$, the noise vector $g_{\mathbf{k}}$ of equation (2.53) is obtained by multiplying $V_{\mathbf{k}}$ by $u_{\mathbf{k}}$.

v) The state of the interface is updated according to (2.53). Then, the algorithm jumps back to point (iii) and the integration is carried over until the final time is reached.

3

UNIVERSALITY CLASS OF THE NOISY KS EQUATION

One of the problems we wish to address in this work is the interplay between morphological instabilities and scale invariance. In this chapter we perform a detailed numerical analysis of the stochastic version of the Kuramoto-Sivashinsky equation, also called noisy KS equation. We reach the conclusion that it indeed displays kinetic roughening properties that are in the Kardar-Parisi-Zhang universality class for two dimensional substrates.

3.1 The deterministic and noisy Kuramoto-Sivashinsky equations

The Kuramoto-Sivashinsky equation is a paradigmatic model for chaotic spatially extended systems, arising in a variety of physical contexts, like thin solid films, interfaces between viscous fluids, waves in plasmas and chemical reactions, or combustion fronts [84]. Two versions of this equation can be found in the literature: the *deterministic* KS (dKS) equation,

$$\partial_t h = -\nu\nabla^2 h - \mathcal{K}\nabla^4 h + \frac{\lambda}{2}(\nabla h)^2, \tag{3.1}$$

and the *stochastic* or *noisy* KS (nKS) equation,

$$\partial_t h = -\nu\nabla^2 h - \mathcal{K}\nabla^4 h + \frac{\lambda}{2}(\nabla h)^2 + \eta, \tag{3.2}$$

where $\eta(\mathbf{r}, t)$ is a Gaussian white noise with zero mean and correlations

$$\langle \eta(\mathbf{r}, t)\eta(\mathbf{r}', t')\rangle = 2D\delta(\mathbf{r} - \mathbf{r}')\delta(t - t'). \tag{3.3}$$

Both in (3.1) and (3.2) ν and $\mathcal{K}$ are taken to be positive parameters. Equation (3.1) was originally proposed by Kuramoto [126] in the context of chemical turbulence, and by Sivashinsky [127] for the propagation of a flame front. Equation (3.2), on the other hand, has been proposed more recently for systems in the presence of external fluctuations, like step dynamics in epitaxy [128] and surface erosion by ion beam sputtering [129].

When studied on large domains, both Eqs. (3.1) and (3.2) display a similar behavior, more complex than most of the equations presented in Chapter 1. For relatively short times, the surface shows a pattern, with a characteristic length scale which can be inferred from the power spectral density. At long time and large length scales, the surface becomes scale invariant and displays kinetic roughening, at least for one-dimensional substrates (see Section 3.1.1). An example of the evolution of the surface, the roughness and the power spectral density is given in Figure 3.1. One way to understand this behavior is to write the equations in Fourier space:

$$\partial_t h_{\mathbf{k}}(t) = \sigma_{\mathbf{k}} h_{\mathbf{k}}(t) + \mathcal{N}[h]_{\mathbf{k}}(t) + \eta_{\mathbf{k}}(t), \tag{3.4}$$

where $\mathcal{N}[h]_{\mathbf{k}}(t)$ stands for nonlinear contributions. For Eqs. (3.1) and (3.2), the linear dispersion relation is

$$\sigma_{\mathbf{k}} = \nu|\mathbf{k}|^2 - \mathcal{K}|\mathbf{k}|^4, \tag{3.5}$$

a sketch of which is shown in Figure 3.2. Thus, given that $\nu > 0$, the dispersion relation has a band of unstable modes, i.e. an interval of wave-vectors within which $\sigma_{\mathbf{k}}$ takes only positive values. If we neglect the non-linear term, which is a good approximation at short times, these modes grow exponentially in time, whereas those with a negative value of $\sigma_{\mathbf{k}}$ are smoothed out. Since this interval reaches the $k = 0$ mode, we can infer that such a model displays a Type II stationary instability (see Section 1.4). The Fourier mode $\mathbf{k}_m$ that maximizes the dispersion relation grows exponentially faster than the others, being responsible for the characteristic wavelength of a pattern that ensues.

For longer times, the very same development of the pattern makes local slopes grow, making the non-linear term no longer negligible. The KPZ nonlinearity correlates different wavelengths stabilizing the surface and blurring the pattern. After a crossover time, which can be very long depending on the dimension and the values of the parameters, the surface displays scale invariance.

The fact that the deterministic and noisy KS equations behave so similarly is due to the chaotic nature of Eq. (3.1), which introduces an "intrinsic" noise into the system. This phenomenon has been studied in a rigorous way by Chow and Hwa [130]. In this Reference, the authors constructed an effective stochastic model for the dKS equation in one spatial dimension, belonging to the KPZ universality class. This was achieved by incorporating some previously known statistical properties of the chaotic dynamics [131] into a coarse-graining procedure for the surface height. The fact that the one-dimensional dKS belongs to the KPZ universality class was also confirmed by numerical simulations by Sneppen *et al.* [132]. On the

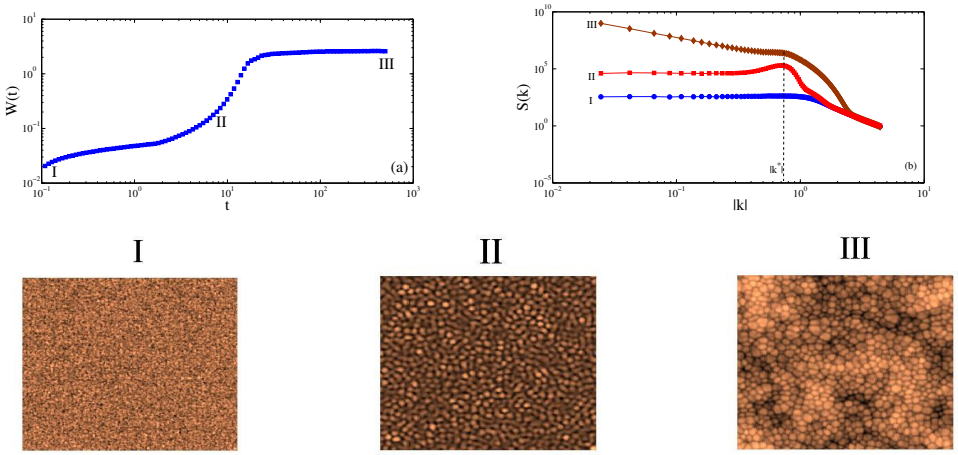

Figure 3.1: Upper panel: Typical behavior of the roughness (a) and the PSD (b) for the two-dimensional noisy Kuramoto-Sivashinsky equation. The power spectral density is shown for three times corresponing to $t = 0.2$ (I), $t = 10$ (II), and $t = 500$ (III). Lower panel: Top view snapshots of the evolution of a surface growing according to the nKS equation for $d = 2$. At short times (I), growth is mostly due to the noise, and the surface is highly disordered; at intermediate times (II), a pattern of "dots" starts to be visible, and the power spectral density exhibits a clear local maximum (see upper panel, b); at long times (III), the surface displays scale invariance. The simulation has been carried out using the following parameters: $L = 256$, $\nu = \mathcal{K} = \lambda = 1$, $D = 0.01$, $\Delta x = 1$, $\Delta t = 0.05$.

other hand, also the noisy KS equation in one spatial dimension has been proven to belong to the KPZ universality class. This has been done by means of direct numerical simulations [133] and dynamic renormalization group analysis [134, 135]. It important to note that this "link" between the deterministic and noisy KS equation is not currently available in higher spatial dimensions.

In spite of their similarities, an important difference exists between equations (3.1) and (3.2), and it concerns their parameter dependence. After the following rescaling

$$\begin{aligned} &\mathbf{r} \to (\mathcal{K}/\nu)^{1/2}\mathbf{r}, \\ &t \to (\mathcal{K}/\nu^2)t, \\ &h(\mathbf{r},t) \to (D/\nu)^{1/2}h(\mathbf{r},t), \end{aligned} \tag{3.6}$$

equation (3.2) can be written as

$$\partial_t h = -\nabla^2 h - \nabla^4 h + \frac{\sqrt{g}}{2}(\nabla h)^2 + \xi, \tag{3.7}$$

where $g = \lambda^2 D/\nu^3$ and the rescaled noise $\xi(\mathbf{r},t)$ has zero mean and correlations

$$\langle \xi(\mathbf{r},t)\xi(\mathbf{r}',t')\rangle = 2\delta(\mathbf{r}-\mathbf{r}')\delta(t-t'). \tag{3.8}$$

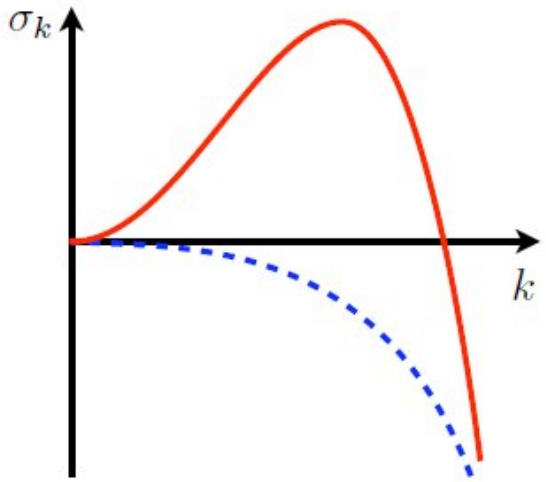

Figure 3.2: Dispersion relations $\sigma_{\mathbf{k}}$ from (3.5) for different values of ν: the blue dashed curve ($\nu < 0$) is stable for every k, whereas the red solid line ($\nu > 0$) has a band of unstable modes.

Thus, we can study the full phase space of the noisy KS equation as a function of only the coupling contant g and the lateral system size L. Note that g has the precise same form as the KPZ coupling [5]. In particular, (3.7) suggests that asymptotic properties do not depend on the sign of λ.

Parameter dependence is even simpler in the deterministic KS equation. In fact, after performing a rescaling analogous to (3.6), equation (3.1) becomes

$$\partial_t h = -\nabla^2 h - \nabla^4 h + (\nabla h)^2, \tag{3.9}$$

with no free parameter apart from the system size L. In this case, the only way to perform simulations that probe the asymptotic behavior of the system is to increase the value of L, which can be numerically demanding. It is precisely in the large domain limit $L \gg 1$ where the dKS equation displays its "turbulent" behavior that makes it a paradigm of spatiotemporal chaos [136].

3.1.1 The controversy on the universality class

It is well established in the literature that the deterministic KS equation, as well as the noisy KS equation in $d = 1$ belong to the Kardar-Parisi-Zhang universality class [20], as borne out from numerical simulations [133] and dynamic renormalization group analysis [134, 135]. In the latter case, this conclusion stems from the fact that, both for the deterministic and noisy KS equations, ν changes sign upon renormalization, becoming positive in the asymptotic state [134, 137]. Since a negative ν is precisely what causes the instability and the formation of a pattern, the system turns stable at long wavelengths and large time-scales. Moreover, at

these scales the term $\nabla^4 h$ becomes irrelevant, the resulting equation being precisely KPZ equation. Other studies are also available for the noisy KS equation in one dimension that, using tools from nonlinear dynamics, also provide evidence that it belongs to the KPZ universality class [138].

However, the two-dimensional case $d = 2$ remains controversial. On the one hand there are opposing claims [139, 140] on the asymptotics of the dKS equation vs that of the 2D KPZ equation. On the other hand, for the nKS equation the dynamic renormalization group approach is inconclusive in $d = 2$, and numerical simulation by Drotar *et al.* [141] suggest non-KPZ asymptotics, contradicting naive expectations based on the RG flow. However, such simulations were carried out in a pre-asymptotic regime. In fact, the authors found two different scaling regimes in terms of the exponent values determined from the behavior of the surface roughness W and the height-difference correlation function G: for short times, the exponents are compatible with the LMBE universality class (see Table 1.1), while for late times, the nKS equation was found to display exponent values for α and β in the ranges $0.25 - 0.28$ and $0.16 - 0.21$, respectively. These values differ substantially from those associated with the KPZ universality class in two dimensions, which are $\alpha_{\text{KPZ}} = 0.39 \pm 0.01$ and $\beta_{\text{KPZ}} = 0.24 \pm 0.01$ [31, 32].

An important remark concerns the numerical scheme used for the integration of Eq. (3.2). Drotar *et al.* chose a standard finite difference discretization for space derivatives. Currently, it is accepted that such a scheme underestimates both the KPZ nonlinearity and the effective coupling g [142, 143]. Thus, a more detailed analysis is needed. In particular, simulations at large values of g and L that are performed with a more reliable numerical scheme could give us more information about the true asymptotics of this equation.

3.2 Simulations of the two-dimensional nKS equation

Simulations have been performed for two-dimensional substrates using the pseudo-spectral numerical scheme described in Chapter 2, which has been successfully used for the numerical integration of local and non-local stochastic equations featuring nonlinearities of the KPZ type.

3.2.1 Parameter dependence of the exponents

We start by considering parameter values of the nKS equation that correspond to relatively small coupling values from $g = 2{\cdot}10^{-2}$ up to $g = 2{\cdot}10^{3}$. We achieve this by tuning λ while keeping the other parameters fixed [see caption of Figure 3.1].

For each parameter set, we measure the global surface roughness W and the power spectral density S as functions of time. By fitting the long time behavior of W prior to saturation and the small $k = |\mathbf{k}|$ behavior of S at the stationary state, we obtain the values of the roughness exponent α and the growth exponent β using the scaling Ansatz (1.32) and (1.40). The results are presented in Figure 3.3. For

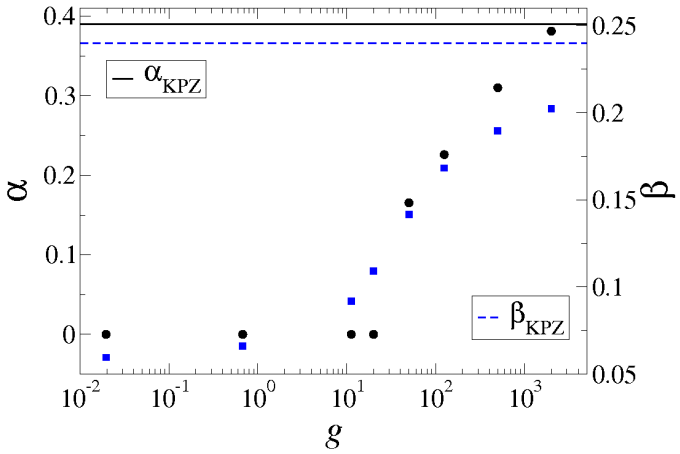

Figure 3.3: Exponent values of the 2D nKS equation as functions of g, in the weak coupling regime. Solid black bullets (ordinates on left vertical axis) provide values for the roughness exponent α; blue squares (ordinates on right vertical axis) provide values of the growth exponent β. The solid black and dashed blue lines indicate our reference values for the exponents of the 2D KPZ equation, $\alpha_{\mathsf{KPZ}} = 0.39$ and $\beta_{\mathsf{KPZ}} = 0.24$, respectively.

$g \lesssim 10$, we find β close to 0 (logarithmic scaling), increasing up to $\beta = 0.20 \pm 0.01$ for $g = 2 \cdot 10^3$. The roughness exponent α is also close to 0 for $g \lesssim 20$, after which it increases, reaching up to $\alpha = 0.39 \pm 0.01$ for $g = 2000$.

Thus, even at small couplings, the equation displays kinetic roughening properties. For $g \lesssim 10$, these are in the two-dimensional Edwards-Wilkinson universality class, as for the 1D nKS case [5, 133, 134]. However, for larger coupling values, the scaling behavior is neither EW nor KPZ, although the value of α for $g = 2000$ seems already reminescent of KPZ behavior. Since EW and KPZ scaling are precisely the two meaningful universality classes that are found through dynamic renormalization group (DRG) analysis, we believe that the intermediate exponent values in Figure 3.3 are to be thought of as non-asymptotic behavior due to the finite system size of our simulations. In order to confirm this interpretation, we need to explore larger coupling and/or system size values, and construct a phase diagram for the equation.

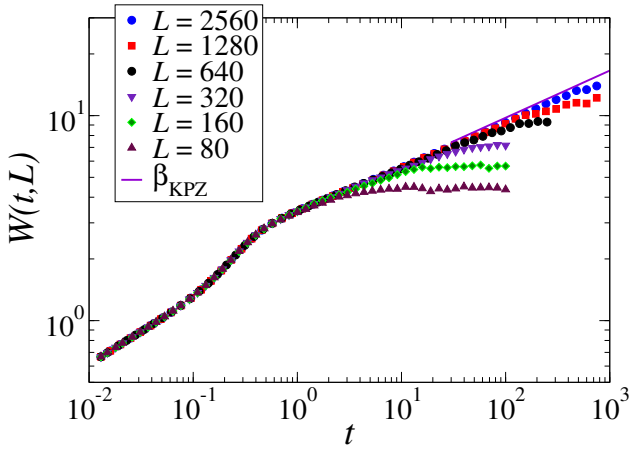

Figure 3.4: Time evolution of the surface roughness for different values of the system size L. For all simulations we use $\nu = 0.1$, $\mathcal{K} = 4$, $\lambda = 20$, $D = 50$, $\Delta x = 1.25$, and $\Delta t = 5 \cdot 10^{-3}$, leading to $g = 2 \cdot 10^7$. Results have been averaged over different numbers of noise realizations: 15 for $L = 2560$, 30 for $L = 1280$, and 100 for the remaing values of L in the legend. The purple solid line is a guide for the eye, and has slope $\beta_{\mathrm{KPZ}} = 0.24$.

3.2.2 Construction of the phase diagram

By increasing the value of g, we have been able to reach an asymptotic state in which the exponents are compatible with those of the 2D KPZ universality class. However, while the roughness exponent α is found to reach a KPZ-compatible value already for moderate values of g and L, the growth exponent β approaches its asymptotic value very slowly. This fact has been also reported in other studies of crossover phenomena within kinetic roughening [144], and may be due to the fact that the roughness is an averaged quantity, as is clear from formula (1.39). This slow-convergence issue for integrated observables will also appear in the study of anisotropic equations in Chapter 4.

Unambiguous assessment of the asymptotic β value is only possible for large g and L, as seen in Figure 3.4, in which the surface roughness is plotted for several system sizes at a fixed large coupling value $g = 2 \times 10^7$. This very long crossover between pre-asymptotic and asymptotic states hinders the possibility to reach the strong coupling KPZ fixed point for small system sizes and small values of g, which applies to the simulations of Drotar *et al.* [141]. In order to analyze the situation in more detail, we have estimated the exponents using a more robust methodology, namely a *data collapse* of the power spectral density. Every simulation can be identified by the values of g and L used; thus, there is a one-to-one correspondence between any simulation and a point in the (g, L) plane (see Figure 3.5). For a given point, we compute the power spectral densities for different (long) times approaching saturation. We then plot the same PSD functions in rescaled variables $k \to kt^{1/z}$ and $S \to Sk^{2\alpha+2}$ using as values for the exponents α and z those of

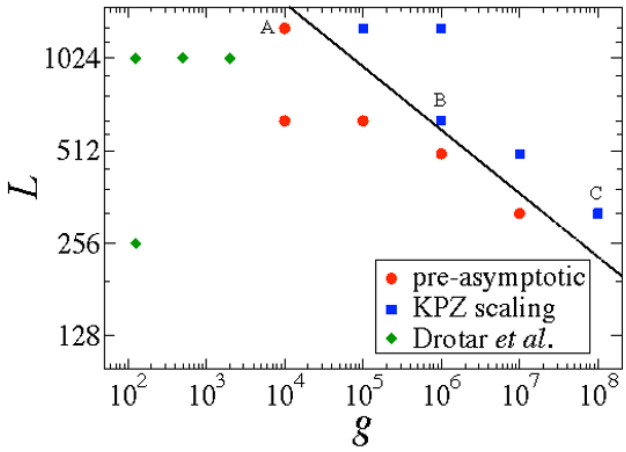

Figure 3.5: Qualitative asymptotic scaling of the nKS equation in (g, L) parameter space. In simulations, $\nu = 0.1$ $\mathcal{K} = 4$, $\Delta x = 1.25$ and $\Delta t = 5 \cdot 10^{-3}$ are fixed, and different values of g have been achieved by tuning λ and D. Red bullets correspond to pre-asymptotic scaling (type i behavior) while blue squares correspond to strong coupling KPZ scaling (type ii and iii behaviors). As examples, the analysis of points A, B, and C is presented in Figure 3.6. Green diamonds are results from [141]. The solid line is a reference fit computed by least squares, separating pre-asymptotic from asymptotic scaling behavior.

the 2D KPZ equation. This provides us with a way of discriminating between pre-asymptotic and asymptotic regimes for each simulation performed. The collapsed PSDs are shown in Figure 3.6. Actually, following this procedure, three types of behavior are seen to occur:

i) Pre-asymptotic regime in which the collapse of the PSD is poor for every value of L in our range (see panels 1a-1b in Figure 3.6, point A in Figure 3.5);

ii) regime in which only the lowest wave-numbers (very large wavelengths) of the PSD collapse with the KPZ exponents (see panels 2a-2b in Figure 3.6, point B in Figure 3.5);

iii) fully developed strong coupling behavior in which KPZ asymptotics is reached immediately after exponential growth (due to the linear instability) of the surface roughness (see panels 3a-3b in Figure 3.6, point C in Figure 3.5).

Note that the scaling behavior for intermediate to large k values is controlled by fixed points other than the KPZ one. For these scales collapse may also be achieved, with pre-asymptotic values of α and z. Within this region, data *do not collapse* using the values of the roughness and dynamic exponent of the Kardar-Parisi-Zhang universality class.

The results of our analysis are summarized in figure 3.5, which is the phase diagram for equation (3.2). In this plot we can see that, for small $g < 10^4$ and

$L \simeq 1024$, we have not been able to reach the KPZ regime (type i behavior). We then find an intermediate region (for $10^5 < g < 10^7$ and $512 \leq L \lesssim 1024$) in which dynamic crossover behavior occurs between the pre-asymptotic regime and the KPZ scaling (type ii behavior). Finally, for $g > 10^7$, 2D KPZ scaling is readily observed even for small systems, $L \simeq 256$ (type iii behavior).

3.3 Conclusions

Our numerical results show that the noisy Kuramoto-Sivashinsky equation is asymptotically in the Kardar-Parisi-Zhang universality class in two space dimensions, confirming previous expectations derived from Dynamic Renormalization Group analysis, and generalizing known results in $d = 1$. We have also observed that crossover effects are substantially stronger for the 2D case than for the 1D case in the sense that, fixing all parameters values including the system size L, the nKS equation can be already in the KPZ asymptotic state for $d = 1$, while only preasymptotic scaling can be measured for $d = 2$. This effect might be due to the particularly strong effect that fluctuations have in one dimension, which may aid the approach to the stationary state for a given parameter set.

Our results can also guide the interpretation of experimental and/or numerical data in which the nKS equation appears as a physical model, such as ion-beam erosion or molecular beam epitaxy, since for such systems at sufficiently large length scales and long times, the 2D KPZ scaling is to be expected.

In the context of the controversy on the universality class of the two-dimensional deterministic KS equation, if an effective description of this equation by an "equivalent" noisy KS equation were achieved as in the 1D case [130], then our result would imply that the asymptotic scaling of the 2D dKS equation is in the 2D KPZ universality class. However, such a link is not yet available for the $d = 2$ case, and in the absence of further progress in that direction the controversy remains an important open question in Nonlinear Science.

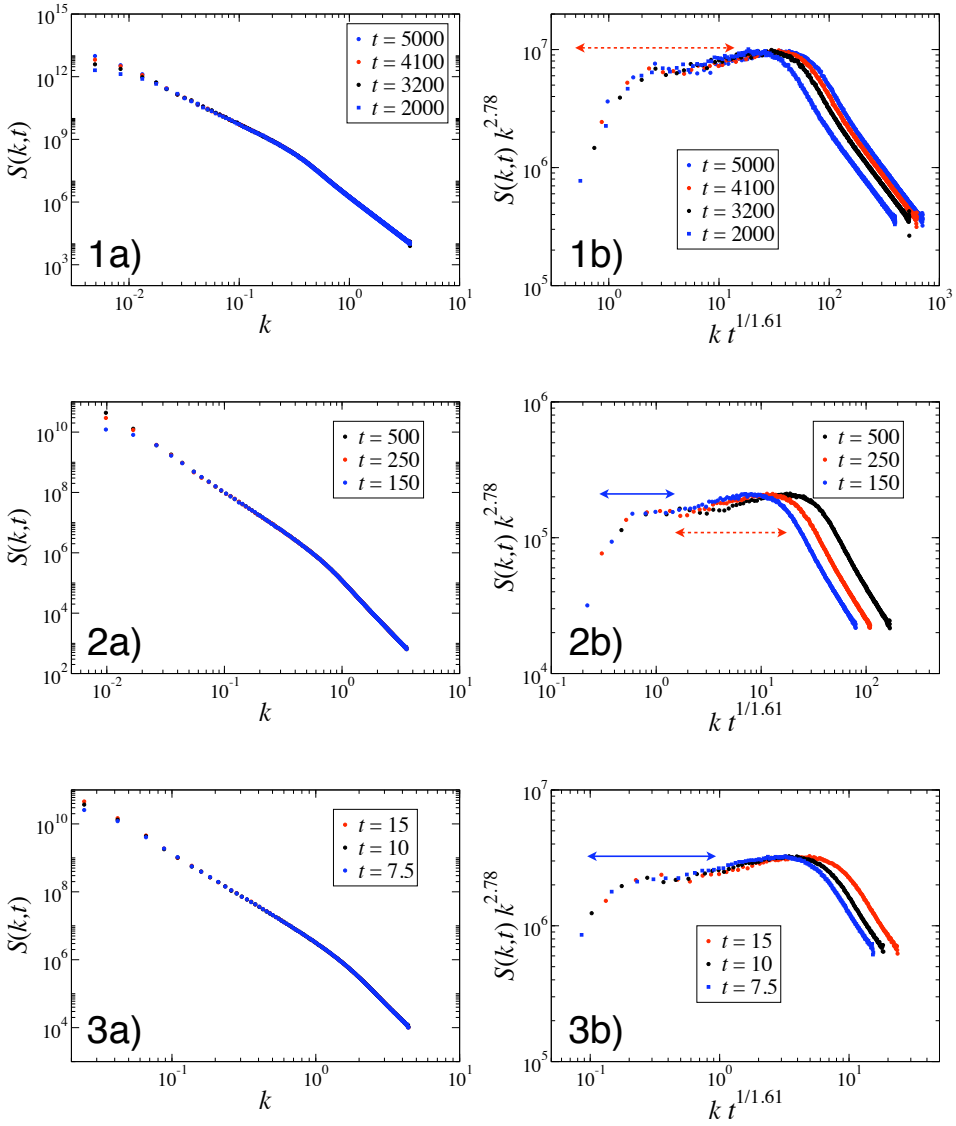

Figure 3.6: Examples of raw PSD data (left column) and their corresponding collapses (right column), for points in the (g, L) plane that are representative of each type of behavior. The plots on the left column [1a), 2a), 3a)] show the PSD vs. wave vector k, for different choices of g and L. Within each panel, the computed PSD are shown for several times, according to the legends. In 1a), $g = 10^4$ and $L = 1280$ (point A in figure 3.5), which is the pre-asymptotic (type i) regime; panel 2a) corresponds to $g = 10^6$ and $L = 640$ (point B in figure 3.5), for which behavior is of type ii; finally, panel 3a) corresponds to $g = 10^8$ and $L = 380$ (point C in figure 3.5) which is in the fully developed aymptotic regime (type iii). On the right column of the figure [panels 1b),2b),3b)], we present the collapsed data for the corresponding panels on the same row. Dashed red arrows indicate regions in which the data do not collapse satisfactorily, while solid blue arrows indicate intervals of k values within which 2D KPZ collapse is satisfactory. The collapse with KPZ exponents is poor in panel 1b); on panel 2b) collapse is good only for the smallest wave numbers, while for larger values of k the quality of collapse deteriorates; finally, panel 3b) shows a collapse in which 2D KPZ asymptotics is reached.

4

ANISOTROPIC EQUATIONS

In Chapter 1 we showed that it is difficult to construct surface growth models where anisotropy constitutes a *relevant* perturbation of the isotropic behavior, i.e. a model which displays strong anisotropy. In this chapter, we begin our systematic analysis of strong anisotropy and strongly anisotropic systems. We start by introducing a generalization of the Family-Vicsek scaling Ansatz that applies to strongly anisotropic surfaces. From this hypothesis, we derive the expected scaling behavior for several observables, focusing on correlation functions in momentum space. We also present relations among the new exponents that will be introduced below.

Next, we test our scaling Ansatz against several systems. We first consider a linear model featuring strong anisotropy and for which our Ansatz actually provides the *exact* solution. Then we consider a nonlinear example, namely the Hwa-Kardar (HK) equation, whose scaling exponents can also be explained using our hypothesis. In the process, we introduce a family of linear (non-local) strongly anisotropic equations, which allows us to construct a *Gaussian approximation* to the HK equation. This approximation will be useful for us in order to elucidate slow convergence properties of some observables, that turn out to be related with small values of the scaling exponents.

4.1 Anisotropic Scaling Ansatz

For a two-dimensional rough interface, a straightforward generalization of the height-difference correlation function that is usually considered for isotropic systems [5],

$$G(r) = \langle [h(\mathbf{r} + \mathbf{r}_0) - h(\mathbf{r}_0)]^2 \rangle, \tag{4.1}$$

is provided by analogous correlation functions along each one of the two independent space directions. Namely,

$$G_x(x) = \langle [h(x_0 + x, y_0) - h(x_0, y_0)]^2 \rangle, \tag{4.2}$$

$$G_y(y) = \langle [h(x_0, y + y_0) - h(x_0, y_0)]^2 \rangle, \tag{4.3}$$

where, as usual, $h(\mathbf{r})$ is the surface height above point $\mathbf{r} = (x, y)$ on a substrate plane, $\mathbf{r}_0 = (x_0, y_0)$ is an arbitrary position, and brackets denote averages over the noise distribution (e.g. independent realizations of the experiment).

While kinetic roughening in an isotropic system implies the simple power-law behavior $G(r) \sim r^{2\alpha}$, where $r = |\mathbf{r}|$ and α is the roughness exponent [5], the expected behavior in the presence of anisotropies is, rather [145],

$$G_x(x) \sim x^{2\alpha_x}, \qquad G_y(y) \sim y^{2\alpha_y}. \tag{4.4}$$

where in principle two different roughness exponents exist, α_x and α_y. We will speak of strong anisotropy (SA) if these exponents take different values in the asymptotic state of the system, while this will be referred to as of weak anisotropy (WA) if they take the same values. Note that in the present discussion we will assume that the surface is at a steady state at which statistical properties are time invariant. Later on, we will consider the time evolution explicitly.

Naturally, real-space correlations are not the only observables one can measure from simulations or from actual experimental data. In the context of surface kinetic roughening, a very important quantity is the two-dimensional power spectral density (PSD) or structure factor of the surface height,

$$S(\mathbf{k}) = \langle |h_{\mathbf{k}}|^2 \rangle, \tag{4.5}$$

where $h_{\mathbf{k}}$ is the space Fourier transform of $h(\mathbf{r}) - \bar{h}$, with $\bar{h}$ being the space average of the height. On the one hand, this function can be easily measured in many experimental setups by using e.g. X-ray diffraction techniques [146]. On the other hand, for theoretical modeling and simulation, it has many advantages over real-space correlation functions, specially in the presence of crossover behavior and/or anomalous scaling, see e.g. [35] and references therein. As will be justified in the next sections, we will hypothesize the following long time, large distance behavior of the PSD for an anisotropic surface,

$$S(\mathbf{k}) = S(k_x, k_y) \sim \frac{1}{k_x^{2\tilde{\alpha}_x} + \nu k_y^{2\tilde{\alpha}_y}}, \tag{4.6}$$

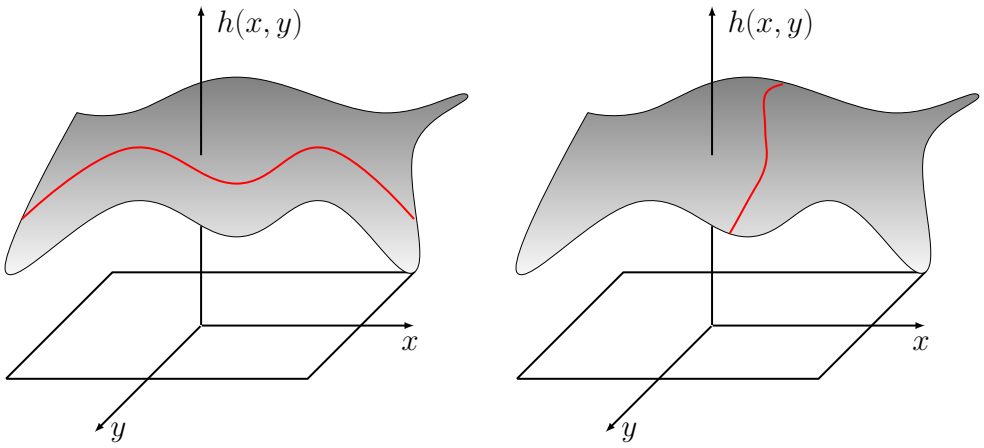

Figure 4.1: Schematic representation of one-dimensional cuts of a surface in the x (left panel) and y (right panel) directions. The Fourier transform of the slice in the x direction is given by Eq. (4.8), while its corresponding power spectrum is given by Eq. (4.7).

where the exponents measured in Fourier space $\tilde{\alpha}_{x,y}$ will be related somehow to the roughness exponents $\alpha_{x,y}$, and ν is a mere constant. Our aim is precisely to elucidate the implications of Eq. (4.6) for the scaling behavior of other observables in the system. Note, Eq. (4.6) is an analogue for non-conserved noise fluctuations of the behavior found in driven-diffusive-systems [147]. In the case of fracture experiments, alternative choices for anisotropic scaling Ansätze are also available. There, either an auxiliary dynamics is postulated [74, 148], or else expansions of observables over appropriate functional bases are performed. These techniques usually exploit the fact that isotropic materials often have anisotropic fracture surfaces only because of the breaking of isotropy by the initial conditions [149, 150].

In general, it is the physical conditions and geometric constraints that dictate the two appropriate directions playing the role of x and y here. For example, under Ion Beam Sputtering at oblique incidence the projection of the ion beam on the target plane naturally fixes them. Likewise, in Molecular Beam Epitaxy of vicinal surfaces, these directions are fixed by the average tilt with respect to the high symmetry orientation, etc. Nevertheless, as will be shown below, under conditions for strong anisotropy any choice of two orthogonal directions will lead to the same set of two different exponents $\tilde{\alpha}_{x,y}$, which guarantees the generality of Ansatz (4.6).

Once a choice of appropriate or convenient orthogonal directions has been made, two rather natural observables are the PSDs $S_x(k_x)$ and $S_y(k_y)$ of corresponding *one-dimensional* profiles. In e.g. thin film experiments, such observables are readily measured using scanning probe microscopies (AFM or STM) [146]. Thus, for instance, considering a fixed value $y = y_0$, one defines

$$S_x(k_x) = \langle h_{y_0}(k_x) h_{y_0}(-k_x) \rangle, \tag{4.7}$$

where $h_{y_0}(k_x)$ is the Fourier transform of the corresponding one-dimensional profile $h(x, y_0)$,

$$h_{y_0}(k_x) = \frac{1}{\sqrt{2\pi}} \int_{-\infty}^{+\infty} dx\, e^{ixk_x} h(x, y_0), \tag{4.8}$$

and in order to simplify the discussion, we have taken the $L \to \infty$ limit, with L being the lateral size of the substrate. We will henceforth work within this limit, and will reconsider this and the following formulas when analyzing finite size effects, see Eqs. (4.54).

It is straightforward to obtain the relation between these observables [the same procedure as applied to $S_x(k_x)$ leads to the definition of $S_y(k_y)$ after exchanging labels $x \leftrightarrow y$] and the two-dimensional PSD. Using (4.8) in (4.7), and substituting $h_{y_0}(k_x)$ by its representation in terms of the two-dimensional Fourier transform $h(k_x, k_y)$,

$$h_{y_0}(k_x) = \frac{1}{\sqrt{2\pi}} \int_{-\infty}^{+\infty} dk_y\, e^{-iy_0k_y} h(k_x, k_y), \tag{4.9}$$

we obtain

$$\begin{aligned} S_x(k_x) &= \frac{1}{2\pi} \int_{-\infty}^{+\infty} dk_y dk'_y\, e^{-iy_0(k_y+k'_y)} \langle h(k_x, k_y) h(-k_x, k'_y) \rangle \\ &= \frac{1}{\pi} \int_0^{\infty} dk_y\, S(k_x, k_y). \end{aligned}$$

The same steps lead to an analogous expression for $S_y(k_y)$; in summary,

$$S_x(k_x) = \frac{1}{\pi} \int_0^{\infty} dk_y\, S(k_x, k_y), \tag{4.10}$$

$$S_y(k_y) = \frac{1}{\pi} \int_0^{\infty} dk_x\, S(k_x, k_y). \tag{4.11}$$

Now, substituting the scaling hypothesis (4.6) into Eqs. (4.10) and (4.11), we derive the following scaling laws for the power spectra of the one-dimensional cuts,

$$S_x(k_x) \sim k_x^{-(2\tilde{\alpha}_x - \zeta)}, \quad S_y(k_y) \sim k_y^{-(2\tilde{\alpha}_y - 1/\zeta)}, \tag{4.12}$$

where $\zeta = \tilde{\alpha}_x/\tilde{\alpha}_y$ is the so-called anisotropy exponent. Strong anisotropy holds whenever $\zeta \neq 1$, whereas $\zeta = 1$ implies weak anisotropy, meaning that the steady state of the system is actually *isotropic*. As shown below [151], Eqs. (4.12) are equivalent to

$$S_x(k_x) \sim k_x^{-(2\alpha_x + 1)}, \quad S_y(k_y) \sim k_y^{-(2\alpha_y + 1)}, \tag{4.13}$$

which provide the natural generalization to the SA case of the scaling behavior of the PSD of 1D cuts of the surface in the isotropic case, in which $\alpha_x = \alpha_y = \alpha$ and $S_{x,y} \sim k_{x,y}^{-(2\alpha+1)}$ [152].

We still have to prove that the anisotropy condition $\zeta \neq 1$ indeed corresponds to $\alpha_x \neq \alpha_y$, for which we need to relate these real-space exponents with their

momentum-space counterparts, $\tilde{\alpha}_{x,y}$. Such a relation is obtained from the definition of $G_{x,y}$, Eqs. (4.2) and (4.3). Inverse transforming Eq. (4.8) we get

$$h(x, y_0) = \frac{1}{\sqrt{2\pi}} \int_{-\infty}^{+\infty} dk_x \, h_{y_0}(k_x) e^{-ik_x x}. \tag{4.14}$$

Using this equation in (4.2), it is easy to see that

$$G_x(x) = \frac{2}{\pi} \int_0^{\infty} dk_x \, [1 - \cos(k_x \, x)] \, S_x(k_x), \tag{4.15}$$

a 1D version of the general 2D relation between the height-difference correlation function and the height structure factor [146]. Now, using the scaling Ansatz for the one-dimensional PSD, Eqs. (4.12), we are able to write the scaling behavior of $G_{x,y}$,

$$G_x(x) \sim x^{2\tilde{\alpha}_x - \zeta - 1}, \qquad G_y(y) \sim y^{2\tilde{\alpha}_y - 1/\zeta - 1}, \tag{4.16}$$

so that

$$2\alpha_x = 2\tilde{\alpha}_x - \zeta - 1, \tag{4.17}$$

$$2\alpha_y = 2\tilde{\alpha}_y - 1/\zeta - 1. \tag{4.18}$$

Eqs. (4.17) and (4.18) lead immediately to Eqs. (4.13) and also to the fact that a single anisotropy exponent is defined, namely,

$$\zeta = \frac{\tilde{\alpha}_x}{\tilde{\alpha}_y} = \frac{\alpha_x}{\alpha_y}. \tag{4.19}$$

In order to incorporate the time dependence into our scaling Ansatz, we consider another important observable, the global surface roughness. In anisotropic systems, it is natural to measure the roughness of slices of the surface along the x and y axes, $W_x(t)$ and $W_y(t)$, respectively. These are simply obtained as the averages of Eqs. (4.2) and (4.3) over all possible values of x_0 and y_0, respectively. As seen in Chapter 1, the Family-Vicsek (FV) dynamic scaling Ansatz [5] that applies to isotropic kinetic roughening is typically formulated in terms of the short and long time behavior for the surface roughness $W^2(t)$, which turns out to be the integral of the PSD [see Eq. (1.39)]. In the SA case, one might expect that a similar behavior would hold for the roughness functions of independent 1D cuts, $W_{x,y}(t)$, but with two different growth exponents, $\beta_x = \alpha_x/z_x$ and $\beta_y = \alpha_y/z_y$. However, it is not difficult to see that these two growth exponents coincide for any value of the anisotropy exponent ζ. To prove this, we consider the effect on the independent and dependent coordinates x, y, h, t under two different anisotropic scale transformations of the space variables. The first rescaling, $\vec{r}_1 \equiv (x_1, y_1, t_1, h_1)$, is performed along the x coordinate with rescaling factor b, while the second one,

$\vec{r}_2 \equiv (x_2, y_2, t_2, h_2)$ is carried out along the y direction with rescaling factor $\tilde{b}$. We obtain

$$\vec{r}_1 = \begin{pmatrix} b\,x \\ b^{\zeta}\,y \\ b^{z_x}\,t \\ b^{\alpha_x}\,h \end{pmatrix}, \qquad \vec{r}_2 = \begin{pmatrix} \tilde{b}^{\tilde{\zeta}}\,x \\ \tilde{b}\,y \\ \tilde{b}^{z_y}\,t \\ \tilde{b}^{\alpha_y}\,h \end{pmatrix}, \tag{4.20}$$

where b and $\tilde{b}$ are positive, but arbitrary otherwise. In these expressions, we have incorporated the shape of the different rescaled coordinates under which scale invariance holds. Notice, in principle one has to allow for a "response" of the time coordinates to a rescaling in space that is anisotropic, namely, $z_x \neq z_y$. Now the hypothesis of scale invariance implies that the same statistical properties hold after we impose any of the two rescalings, $\vec{r}_1$ or $\vec{r}_2$ [75]. In particular, we can equate the two forms of rescaling. For the x and y coordinates, we obtain

$$\begin{cases} b = \tilde{b}^{\tilde{\zeta}} \\ b^{\zeta} = \tilde{b} \end{cases} \Longrightarrow \tilde{\zeta} = \zeta^{-1}. \tag{4.21}$$

Then, by equating the two different ways of rescaling the time variable,

$$b^{z_x} = \tilde{b}^{z_y} \Longrightarrow \tilde{\zeta} = \frac{z_y}{z_x}. \tag{4.22}$$

Finally, from the definition of the growth exponents $\beta_{x,y} = \alpha_{x,y}/z_{x,y}$, and by using (4.21) and (4.22), we obtain

$$\frac{\beta_x}{\beta_y} = \frac{\alpha_x z_y}{z_x \alpha_y} = \zeta\,\tilde{\zeta} = 1, \tag{4.23}$$

indeed implying $\beta_x = \beta_y = \beta$ for any value of ζ. Summarizing, there are only *three independent critical exponents* characterizing a time-dependent SA surface, e.g. α_x, ζ, and z_x, from which all other exponents described in this section can be derived. In particular, the behavior of the roughness of 1D line profiles is

$$W_{x,y} \sim \begin{cases} t^{\beta} & \text{for } t \ll L^{z_{x,y}}, \\ L^{\alpha_{x,y}} & \text{for } t \gg L^{z_{x,y}}, \end{cases} \tag{4.24}$$

with the corresponding values of exponents in terms of the three independent ones. In the next sections we will consider a number of examples for which we will fully verify all the scaling relations derived in this section.

4.2 Linear models

4.2.1 An example: the *2-4* equation

From the examples in Chapter 1, it is not difficult to infer that one possibility to construct a strongly anisotropic equation is by mixing two equations with different scaling exponents, that correspond to different physical phenomena acting along two orthogonal directions. For instance, it is possible to consider a case that combines evaporation-condensation along the x axis and surface diffusion along the y axis. The resulting equation is a mixture of a 1D Edward-Wilkinson (EW) equation [5] along the former direction and a 1D Linear Molecular Beam Epitaxy (LMBE) equation [5] along the latter, namely,

$$\partial_t h = \nu \partial_x^2 h - \mathcal{K} \partial_y^4 h + \eta, \tag{4.25}$$

where we take the parameters ν and $\mathcal{K}$ to be positive. This condition guarantees that the dispersion relation (see below) is always negative, and the equation is *morphologically stable*. We will henceforth call this the *2-4* equation, to recall the order of derivatives acting along each direction. Naturally, Eq. (4.25) is a particular case of a more general linear model in which evaporation-condensation and surface diffusion are fully anisotropic, namely,

$$\partial_t h = \nu_x \partial_x^2 h + \nu_y \partial_y^2 h - \mathcal{K}_{xx} \partial_x^4 h - \mathcal{K}_{xy} \partial_x^2 \partial_y^2 h - \mathcal{K}_{yy} \partial_y^4 h + \eta. \tag{4.26}$$

Equations of this form appear in the context of thin film growth and erosion [77] and have partly been studied along the lines that follow.

The linear nature of Eq. (4.25) allows us to solve it analytically and provides us with a way of checking the anisotropic scaling Ansatz presented in the previous section. To do that, one needs to Fourier transform Eq. (4.25), obtaining

$$\partial_t h_{\mathbf{k}} = \sigma_{\mathbf{k}} h_{\mathbf{k}} + \eta_{\mathbf{k}}, \tag{4.27}$$

where $\sigma_{\mathbf{k}}$ is the dispersion relation,

$$\sigma_{\mathbf{k}} = -(\nu_x k_x^2 + \mathcal{K} k_y^4). \tag{4.28}$$

Given a flat initial condition $h_{\mathbf{k}}(t=0) = 0$, the solution is given by

$$h_{\mathbf{k}}(t) = \int_0^t ds \exp\left[\sigma_{\mathbf{k}}(t-s)\right] \eta_{\mathbf{k}}(s). \tag{4.29}$$

Using this formula, we can compute analytically the two-dimensional PSD,

$$S(\mathbf{k}, t) = \frac{D}{2\pi^2} \left(\frac{e^{2\sigma_{\mathbf{k}} t} - 1}{\sigma_{\mathbf{k}}} \right). \tag{4.30}$$

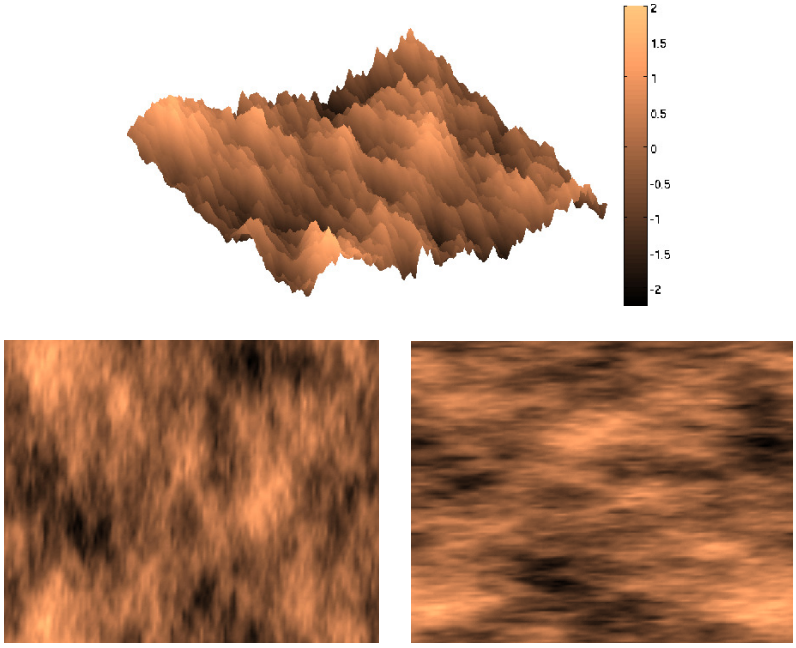

Figure 4.2: Morphology generated by numerical integration of the *2-4* equation, Eq. (4.25). Parameters are given in the main text. Top panel: three-dimensional view. Bottom panels: top views. The right panel has been obtained after rotating the left panel by 90°.

Due to the morphological stability condition, the exponential term vanishes in the $t \to \infty$ limit and Eq. (4.30) reduces trivially to the scaling Ansatz (4.6). Indeed, for a finite system size, it is sufficient to verify the condition

$$t > t_{\rm sat} = \max_{x,y} \left(L^{z_{x,y}} \right) \tag{4.31}$$

in order for the asymptotic form $S(k_x, k_y)$ to approximate reasonably the full time-dependent $S(\mathbf{k}, t)$. Thus, the asymptotic two-dimensional PSD of the *2-4* equation behaves simply as

$$S(k_x, k_y) \sim \left(\nu k_x^2 + \mathcal{K} k_y^4 \right)^{-1}, \tag{4.32}$$

so that $\tilde{\alpha}_x = 1$, $\tilde{\alpha}_y = 2$ and the anisotropic exponent is $\zeta = 1/2$, hence the system displays strong anisotropy as expected. The one-dimensional PSD of cuts along the coordinate axes should scale according to Eqs. (4.12), hence

$$S_x(k_x) \sim k_x^{-3/2}, \qquad S_y(k_y) \sim k_y^{-2}, \tag{4.33}$$

from which we obtain direction-dependent roughness exponents $\alpha_x = 1/4$ and $\alpha_y = 1/2$. Note [77] that these values differ from those of the EW and the LMBE universality classes in 1 and 2 dimensions [5].

As far as the roughness is concerned, as we have seen before the growth exponent β is the same for the two directions. To compute its value, in this case it

suffices to rescale Eq. (4.25) according to the transformation $\vec{r}_1$, see Eq. (4.20). Given the existence of the self-affine solution (4.29), we can impose scale invariance on the rescaled equation,

$$\partial_t h = \nu b^{2-z_x}\partial_x^2 h - \mathcal{K} b^{4\zeta - z_x}\partial_y^4 h + b^{(2\alpha_x - z_x + 1 + \zeta)/2}\eta. \tag{4.34}$$

Namely, one can request coefficients to be b-independent. Thus, substituting the already known exponents $\alpha_x = 1/4$ and $\zeta = 1/2$, we find the dynamic exponents $z_x = 2$ and $z_y = 4$, so that $\beta = 1/8$.

Interestingly, from equations (4.27) and (4.30), it is clear that the *2-4* equation can be seen as a particular case of the following linear model,

$$\partial_t h_{\mathbf{k}}(t) = -(\nu_x |k_x|^n + \nu_y |k_y|^m) h_{\mathbf{k}}(t) + \eta_{\mathbf{k}}(t), \tag{4.35}$$

where n and m are positive real numbers. This defines a two-parameter family of models, which for generic values of n and m is *non-local* and, for $n \neq m$, also strongly anisotropic. By setting $2\tilde{\alpha}_x = n$ and $2\tilde{\alpha}_y = m$, the Ansatz (4.6) provides the long time limit of Eq. (4.30), thus providing an *exact* stationary solution for this family of models.

Numerical simulations of the *2-4* equation

In order to check the analytical results presented in the previous section, we have performed numerical simulations of the *2-4* equation by means of a pseudo-spectral integration algorithm as described in Chapter 2. For these simulations, we have used the following parameters set, $\nu = 1, \mathcal{K} = 100, D = 1, L = 128, \Delta x = 1$, and $\Delta t = 1/2$. An example of the surface morphology that is obtained for long simulation times is provided in Figure 4.2. In order to get a visual impression on the anisotropy of the system, in the same figure we present the same topography after a 90° rotation in the (x, y) plane.

First, we have checked the validity of the asymptotic scaling Ansatz (4.32) for the two-dimensional PSD. In the left panel of Figure 4.3 we present two projections of $S(k_x, k_y)$ along the k_x and k_y axes, together with the analytical solutions, with very good agreement in the asymptotic regime. In this and all remaining figures, simulation data will be provided through symbols, while theoretically expected scaling (whether approximate or exact) will be given as reference lines.

We can moreover verify that the same two exponent values $\tilde{\alpha}_{x,y}$ are actually obtained if one performs any cut of the two-dimensional PSD along any direction in the $\mathbf{k}$-space other than the k_x or k_y axes, see Figure 4.4. However, it turns out that the k_x and k_y directions are the optimal choices in order to obtain a clear-cut scaling behavior. This guarantees that the strongly anisotropic behavior found is not affected by an arbitrary choice of the x, y directions in an associated physical system. Several different choices are shown in Figure 4.4, all of which take the form $S(k\cos\theta, k\sin\theta)$ for different values of the polar angle θ. Thus, e.g. $S(k, 0)$, or $S(0, k)$ in the left panel of Figure 4.3 are just the special cases $\theta = 0$ and $\theta =$

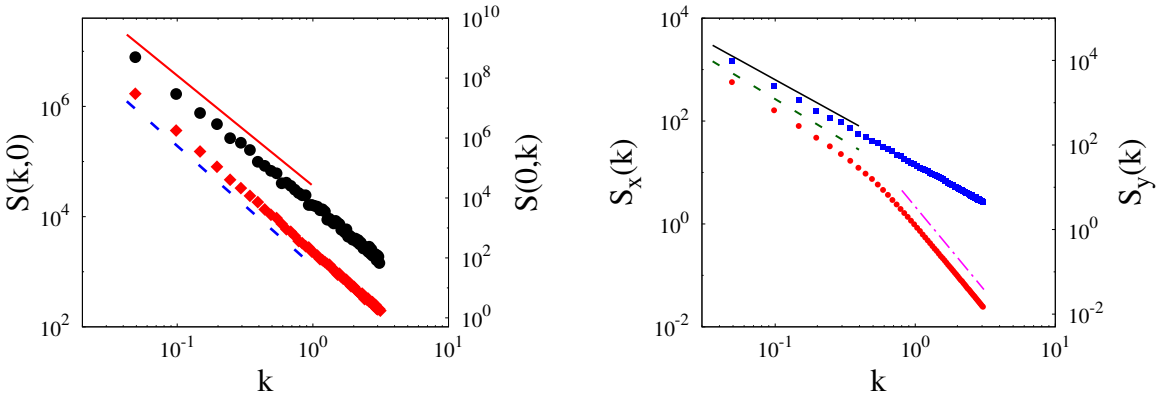

Figure 4.3: Numerical integration of equation (4.25). Parameters are given in the main text. Left panel: One-dimensional projections $S(k,0)$ (black circles, left axis) and $S(0,k)$ (red diamonds, right axis) of the two-dimensional PSD, averaged over 150 different noise realizations. The solid red line is a guide for the eye with slope -2, while the dashed blue line has slope -4. Right panel: PSD of one-dimensional cuts $S_x(k)$ (blue squares, left axis) and $S_y(k)$ (red circles, right axis). The solid black line is a guide for the eye with slope $-3/2$, the dashed green line has slope -2, and the dashed-dot magenta line has slope -4.

$\pi/2$, respectively. For other choices of θ, the scaling behavior of the corresponding cut $S(k\cos\theta, k\sin\theta)$ crosses over between the expected k^{-2} and k^{-4} behaviors, as seen in Figure 4.4. From this point of view $\theta = 0, \pi/2$ allow to elucidate the two existing independent exponents in the most unambiguous way, minimizing finite-size effects, but do not play a more fundamental role.

Further, we have also checked that the one-dimensional PSDs of cuts of the surface along the x and y directions are consistent with Eq. (4.33). In the right panel of Figure 4.3 we see that indeed $S_x(k)$ (left axis) and $S_y(k)$ (right axis) display scaling behavior as predicted by the anisotropic Ansatz. Notice that, for small distances at which dynamics has not yet crossed over to its large scale behavior, $S_y(k_y) \sim k_y^{-4}$, as would correspond for a 1D profile of a 1D LMBE system [5].

Finally, from the full dynamic evolution of the equation we have obtained the value of the growth exponent β. We have checked that this exponent does not depend on the direction chosen for its estimation. In Figure 4.5 we show the roughness of the surface measured along each space direction. As expected, $W_x(t) \sim W_y(t) \sim t^{1/8}$ for times before saturation.

In summary, for the *2-4* equation all the anisotropic scaling relations derived in the previous section are verified both numerically and analytically, thus providing a simple example of a system with strong anisotropy. However, it would be interesting to probe these properties in a non-trivial system in which nonlinearities play a prominent role. The aim of the next section is to perform such type of study for the celebrated example of the Hwa-Kardar equation.

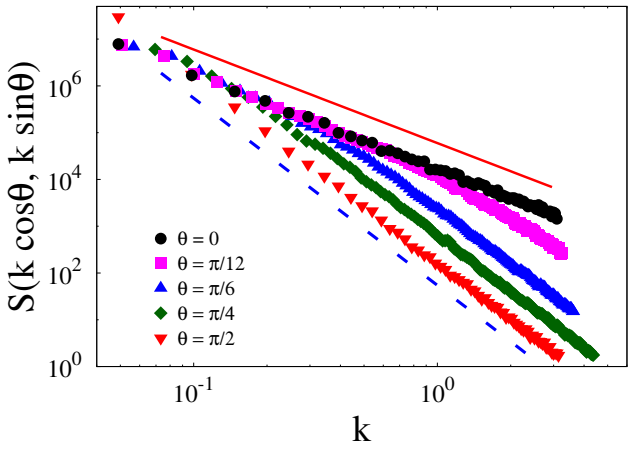

Figure 4.4: One-dimensional cuts $S(k\cos\theta, k\sin\theta)$ of the two-dimensional PSD of surfaces generated by the *2-4* equation (4.25) along oblique directions in $\mathbf{k}$-space, $\theta = 0, \pi/12, \pi/6, \pi/4$, and $\pi/2$, represented as functions of k. Note the expected scalings -2 and -4 are best achieved for θ close to 0 and $\pi/2$, respectively.

4.3 Non-linear models

4.3.1 Running sandpiles and the Hwa-Kardar equation

The Hwa-Kardar equation (HK) was first proposed in [145], in the context of self-organized criticality. More precisely, the aim of this work was to construct a continuum field equation describing the *sandpile* model proposed by Bak, Tang and Wiesenfeld [153] (also called BTW model) in the hydrodynamic limit, in order to extract information about its critical behavior.

In the BTW model, sand grains are added randomly on a square lattice from outside the system; a numerical value, proportional to the height of the local sand column, is associated with each lattice site. It is also possible to define *local slopes* for each site, as the difference between the local height and the height of the neighbouring sites. Whenever a grain hits a lattice site, the local height is incremented by one, and if the local slope crosses a threshold, the sand grains of the colum are distributed among the nearest neighbor columns, until the local slopes come back below the threshold value (see Figure 4.6). It is clear that if one of the neighboring sites also crosses the threshold due to the grains it received from the first site, the phenomenon propagates giving rise to *avalanches*, the behavior of which is of great interest in this context. When an avalanche reaches the boundary of the lattice, the exceeding grains fall out of the system. Many versions of this model can be found in the literature [12]; in the original one [153], the addition of each grain takes place only when the system has relaxed completely; thus, the addition and the transport of grains occur at different time scales. In [145], on the other hand,

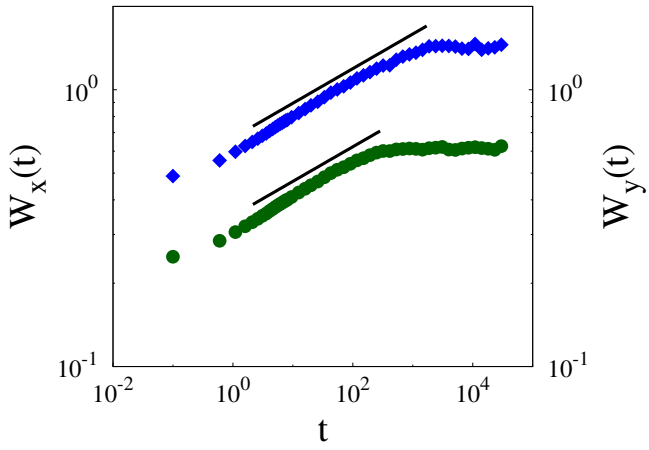

Figure 4.5: Time evolution of the surface roughness functions measured along the two spatial directions, $W_x(t)$ (green circles, left axis) and $W_y(t)$ (blue diamonds, right axis), obtained from numerical integrations of the *2-4* equation (4.25). For visualization purposes, the value of $W_y(t)$ has been artificially offset vertically. The two solid black lines have the same slopes, $1/8$.

the authors focus on the so-called *running* sandpile model, in which sand grains are added according to an external clock, independently of the state of the system.

Since the transport of sand grains occurs only in the direction parallel to gravity, leaving unaffected the direction perpendicular to it, the resulting field equation is inherently anisotropic. The system described is dissipative, since the relaxation mechanism implies a loss of potential energy, and open, since sand is added from the outside and is allowed to escape through the boundaries.

The evolution equation is constructed starting from the properties of the system. The first hypothesis concerns the steady state. Hwa and Kardar assumed that such a state is on average a flat surface, and defined the height $h(\mathbf{r}, t)$ as the deviation from it (see Figure 4.7, right panel). Defining $r_{\parallel}$ and $\mathbf{r}_{\perp}$ as the components of $\mathbf{r}$ parallel and perpendicular to the transport direction, respectively, the system has clearly rotational invariance in $\mathbf{r}_{\perp}$ and translational invariance in both $r_{\parallel}$ and $\mathbf{r}_{\perp}$, but lacks reflection symmetry in $r_{\parallel}$ or h because of the presence of a preferred flow direction. However, there is symmetry under the combined transformation $h \to -h$ and $r_{\parallel} \to -r_{\parallel}$. The presence of this symmetry can be understood by looking at the right panel of Figure 4.7. With respect to the average flat surface, small "bumps" tend to move downhill, while small "voids" will move uphill. Thus, the evolution equation should not change if one interchanges bumps and voids and at the same time the downhill and uphill directions. Mathematically, such a symmetry is expressed precisely as $h \to -h, r_{\parallel} \to -r_{\parallel}$.

Other properties of the system that must be reflected in the equation are conservation laws, and this system displays an important one: excluding the sand that

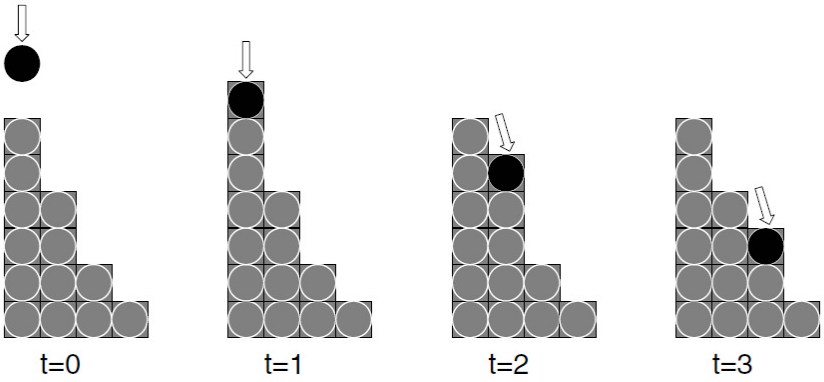

Figure 4.6: Example of one-dimensional sand-pile automaton. The dropped sand grain topples to the next lower level if the local slope $z_j = h(j) - h(j-1)$ is steeper than a critical value z_c (in this example, $z_c = 2$). After the third time step, the sandpile is stable again. The picture has been taken from [154].

is added from outside the system, the relaxation dynamics should not change the number of sand particles.

Taking into account all the properties mentioned above, and including the leading order nonlinearity, Hwa and Kardar proposed the following equation for $h(\mathbf{r}, t)$,

$$\partial_t h = \nu_\parallel \partial_\parallel^2 h + \nu_\perp \nabla_\perp^2 h - \frac{\lambda}{2} \partial_\parallel h^2 + \eta, \tag{4.36}$$

where the first two terms describe the relaxation of the height through diffusive transport, while the nonlinearity accounts for the lack of inversion symmetry and hence is related to the presence of an external driving. In the absence of the noise term ($\eta = 0$), there is a local height-conservation law and a transport current satisfying $\partial_t h + \nabla \cdot \mathbf{J} = 0$, where

$$\mathbf{J} = -\nu_\perp \nabla_\perp h - \nu_\parallel \partial_\parallel h \hat{\mathbf{T}} + \frac{\lambda}{2} h^2 \hat{\mathbf{T}}, \tag{4.37}$$

with $\hat{\mathbf{T}}$ denoting the transport direction, along the parallel coordinate in our case. The noise term η mimics the random addition of sand particles from outside the system, and destroys the overall conservation mentioned above. Note that, as a consequence of noise non-conservation, equation (4.36) is expected to display generic scale invariance [7, 8]. Below, we focus on the two-dimensional version of Eq. (4.36), i.e.

$$\partial_t h = \nu_x \partial_x^2 h + \nu_y \partial_y^2 h - \frac{\lambda}{2} \partial_x h^2 + \eta. \tag{4.38}$$

Although Eq. (4.38) [as well as (4.36)] is nonlinear and cannot be solved analytically, it is a very special system for which the three scaling exponents characterizing its strongly anisotropic behavior are believed to be exactly known, due to the

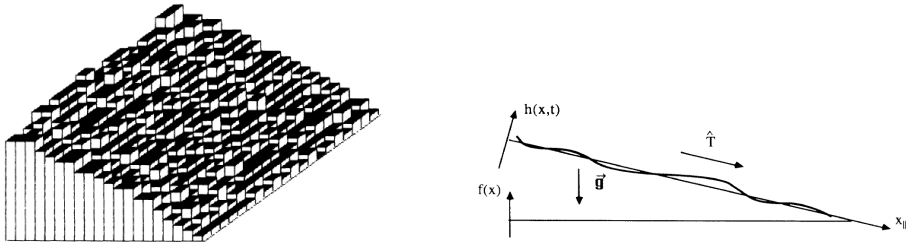

Figure 4.7: Left panel: Typical configuration of a 2D sandpile automata, in which sand is allowed to flow in the direction parallel to gravity. The picture has been taken from [153]. Right panel: Definition of h starting from a continuum description of the 2D sandpile automaton; h is defined as the deviation from a flat steady state sand profile. Gravity drives the sand along the transport direction $\hat{\mathbf{T}}$. The picture has been taken from [145].

occurrence of a sufficient number of symmetries [19, 145]. Specifically, these lead to the following relations among exponents,

$$z_x = 2\zeta, \tag{4.39}$$

$$z_x + \alpha_x = 1, \tag{4.40}$$

$$z_x = 2\alpha_x + \zeta + 1. \tag{4.41}$$

Interestingly, these relations can be easily obtained through a naïve rescaling of equation (4.36) using for instance $\vec{r}_1$ in formula (4.20); in the new coordinate system, the parameters of equation (4.36) are modified in the following way [155],

$$\begin{aligned} &\nu_{\|} \to b^{z_x-2}\nu_{\|}, \\ &\nu_{\perp} \to b^{z_x-2\zeta}\nu_{\perp}, \\ &\lambda \to b^{\alpha_x+z_x-1}\lambda, \\ &D \to b^{z_x-2\alpha_x-\zeta(d-1)-1}D, \end{aligned} \tag{4.42}$$

which immediately lead to equations (4.39)-(4.41), after imposing scale invariance. Usually, the presence of a nonlinearity introduces corrections to equations (4.42), that can be calculated using renormalization group techniques. However, Eq. (4.39) is not modified because the nonlinearity λ, acting only along the x direction, cannot renormalize linear operators that, like the one with coefficient ν_y, act along the perpendicular direction. Eq. (4.40) does not change either, due to a vertex cancellation that is believed to hold to arbitrary order in a perturbative expansion. This is related to a concomitant invariance of the equation under the Galilean transformation

$$\begin{aligned} &r_{\|} \to r_{\|} - \delta\lambda t, \\ &t \to t, \\ &h \to h + \delta, \end{aligned} \tag{4.43}$$

where δ is a parameter and λ is the nonlinearity. Finally, Eq. (4.41) is a hyper-scaling relation (for $d = 2$) [5] deriving from the fact that Eq. (4.38) implements conserved dynamics with non-conserved noise. As mentioned, the three scaling laws Eqs. (4.39)-(4.41) are believed to hold exactly for arbitrary substrate dimension, see [19, 145]. For each value of d, such a non-homogeneous linear system actually has as unique solution the set of three independent exponents that fully characterize the ensuing SA behavior. In our 2D case, such values are

$$\alpha_x = -\frac{1}{5}, \qquad z_x = \frac{6}{5}, \qquad \zeta = \frac{3}{5}. \tag{4.44}$$

The non-linear nature of (4.36) and the fact that the exponents can be calculated analytically, make the HK equation a very good candidate to study the anisotropic scaling Ansatz presented above, specially in view of its strong anisotropy, since $\zeta = 3/5 \neq 1$.

Numerical simulations of the HK equation

From the relation $z_x = \alpha_x/\beta$, we get $\beta = -1/6$. Since the growth exponent is negative, subleading corrections appear in the time evolution of the roughness that complicate the estimation of β from the study of e.g. $W_x(t)$ and $W_y(t)$. However, the scaling relations derived in Section 4.1 allow us to compute

$$\alpha_y = -\frac{1}{3}, \qquad z_y = 2, \tag{4.45}$$

and the values of the momentum-space exponents of the two-dimensional PSD $S(k_x, k_y)$,

$$\tilde{\alpha}_x = \frac{3}{5}, \qquad \tilde{\alpha}_y = 1. \tag{4.46}$$

As for the *2-4* equation, the scaling behavior of the 2D HK equation (4.38) has been verified through pseudo-spectral numerical simulations. In this case, we have used the following parameters set: $\nu_x = \nu_y = 1$, $\lambda = 3$, $D = 1$, $L = 256$, $\Delta x = 1$, $\Delta t = 10^{-2}$. An example of the surface morphology that is obtained for long simulation times is provided in Figure 4.8. In order to get a visual impression on the anisotropy of the system, in the same figure we present the same topography after a 90° rotation in the (x, y) plane. More quantitatively, in the left panel of Figure 4.9 we present the two projections of the two-dimensional PSD $S(k, 0)$ (left axis) and $S(0, k)$ (right axis). Again we clearly observe a scaling behavior like the one predicted by our anisotropic Ansatz, using the exact values given by Eq. (4.46).

However, for the PSDs of 1D cuts of the surface, we find a striking difference. As can be seen in the right panel of Figure 4.9, while the long distance behavior of $S_x(k_x)$ is as expected, this is not the case for the PSD of the one-dimensional cuts along the y direction, $S_y(k)$, that shows an unexpected behavior in the region of small wave-vectors. The discrepancy between the numerical data and our theoretical prediction consists of two different effects:

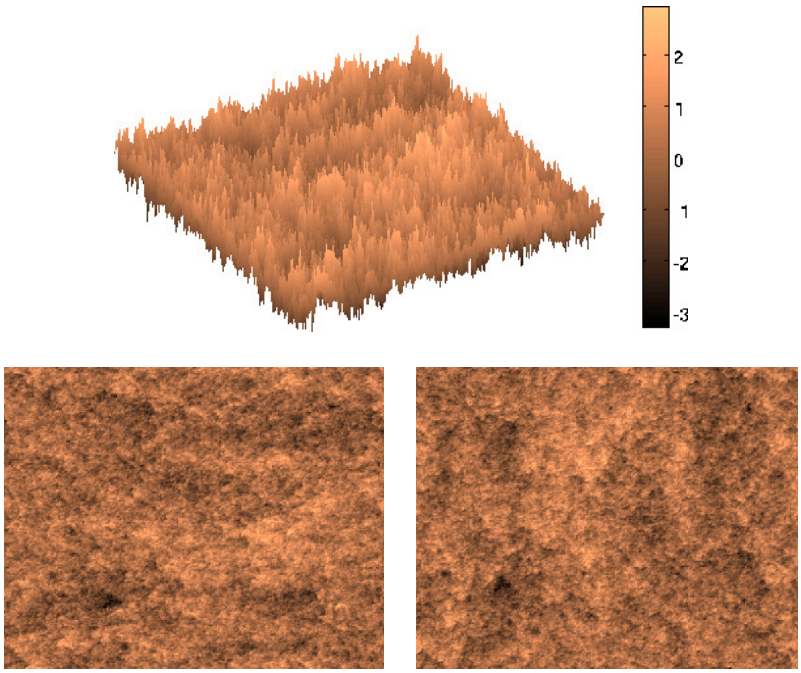

Figure 4.8: Morphology generated by numerical integration of the Hwa-Kardar equation, Eq. (4.38). Parameters are given in the main text. Top panel: three-dimensional view. Bottom panels: top views. The right panel has been obtained after rotating the left panel by 90°.

(i) The value of the PSD for the smallest value of k, i.e. $S_y(2\pi/L)$, behaves quite differently with respect to the other points in the curve, "spoiling" the scaling behavior. Further numerical inspection (not shown) demonstrates that this feature is not due to fluctuations or numerical artifacts.

(ii) Even neglecting the previous point, the scaling behavior of $S_y(k)$ does not resemble in any way the theoretical one given by Eqs. (4.45).

This unexpected behavior of $S_y(k)$ deserves to be studied in more detail since it could have important consequences on the anisotropic scaling Ansatz (4.6). As potential explanations, we can conceive of three possibilities: either the Ansatz needs modifications in the presence of nonlinearities, or the particular values of the exponents induce this behavior, or both the nonlinearity and the exponent values concur in producing it. In order to elucidate this phenomenon, in the next section we construct a linear equation with the same scaling exponents of the HK equation. This non-local Gaussian approximation can be solved analytically and satisfies the anisotropic scaling Ansatz.

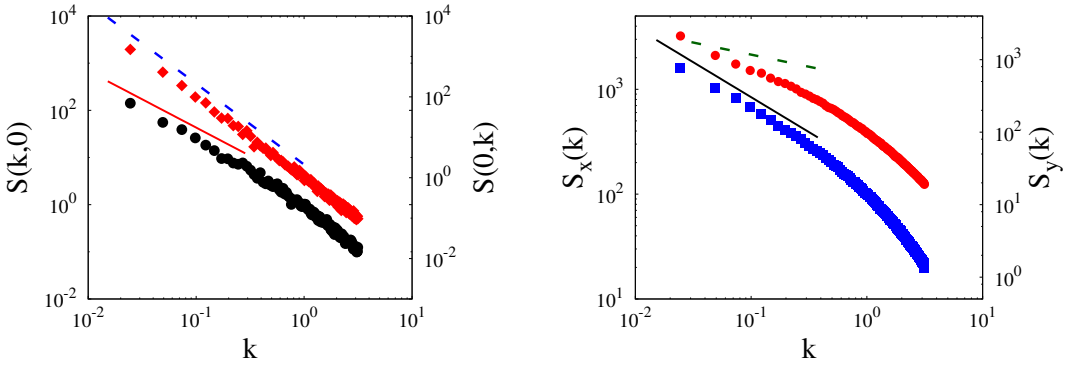

Figure 4.9: Numerical integration of equation (4.38). Left panel: One-dimensional projections $S(k,0)$ (black circles, left axis) and $S(0,k)$ (red diamonds, right axis) of the two-dimensional PSD, averaged over 100 different realizations. The solid red line is a guide for the eye with slope $-6/5$, while the dashed blue line has slope -2. Right panel: PSD of one-dimensional cuts $S_x(k)$ (blue squares, left axis) and $S_y(k)$ (red circles, right axis). The solid black line is a guide for the eye with slope $-3/5$ while the dashed green line has slope $-1/3$. Note that $S_y(k)$ does *not* follow the predicted scaling behavior at small k.

4.3.2 A Gaussian (non-local) approximation for the Hwa-Kardar equation

The fact that the HK asymptotics is in principle determined by three scaling relations allows us to put forward a *linear* equation that shares the same three independent exponents exactly. The key observation appears already in Eq. (4.34) of the previous section. Namely, for an (n,m) equation a rescaling allows to fix all three exponents by requesting statistical invariance. In order to see it, let us rescale Eq. (4.35) for $n = 2\tilde{\alpha}_x$, $m = 2\tilde{\alpha}_y$ and $d = 2$, according to the transformation

$$\begin{aligned} h' &= b^{\alpha_x} h, \\ k'_x &= b^{-1} k_x, \\ k'_y &= b^{-\zeta} k_y, \\ t' &= b^{z_x} t, \end{aligned} \tag{4.47}$$

which is the momentum-space counterpart of $\vec{r}_1$, see Eq. (4.20). Requesting scale invariance, we obtain three relations among the critical exponents, namely,

$$2\tilde{\alpha}_x = z_x, \tag{4.48}$$

$$2\zeta\tilde{\alpha}_y = z_x, \tag{4.49}$$

$$z_x = 2\alpha_x + \zeta + 1. \tag{4.50}$$

From Eqs. (4.17), (4.18), and (4.23), it is straightforward to see that the three relations (4.48)-(4.50) are equivalent to one another, so that only one of them is in-

dependent. Actually, Eq. (4.50) is *hyperscaling*, that holds for any linear equation and is also shared by the HK equation. For a non-conserved nonlinearity (for example, of the KPZ type), the noise term becomes renormalized and a such constraint may not hold. In such a case, the nonlinear equation and its Gaussian approximation would not share the same set of scaling exponents, in contrast with the case considered here.

After these preliminary considerations, it is straightforward to find a (n, m) equation that has the same three independent exponents as the nonlinear HK equation. Thus, we just need to take $n = 2\tilde{\alpha}_x = 6/5$ and $m = 2\tilde{\alpha}_y = 2$. That is, the equation

$$\partial_t h_{\mathbf{k}} = -\left(\nu_x |k_x|^{6/5} + \nu_y |k_y|^2\right) h_{\mathbf{k}} + \eta_{\mathbf{k}}, \tag{4.51}$$

has by construction the exponents given in (4.44). Note that this equation is non-local in space since $n = 6/5$ is not an even integer. Moreover, it is important to stress that Eq. (4.51) is *not* the linearized HK equation. The latter would be obtained by setting λ equal to zero, and therefore both exponents in momentum space would be $2\tilde{\alpha}_x = 2\tilde{\alpha}_y = 2$, corresponding to the simple two-dimensional Edwards-Wilkinson equation [5]. On the other hand, Eq. (4.51) can be considered as a Gaussian approximation of the HK equation, in the sense that it is a variational equation [19] that has the asymptotic Boltzmann height distribution

$$\mathcal{P}\{h\} \propto \exp\left[-\frac{1}{2D}\int \left(\nu_x |k_x|^{6/5} + \nu_y |k_y|^2\right) |\tilde{h}_{\mathbf{k}}|^2 \mathrm{d}\mathbf{k}\right]. \tag{4.52}$$

The fact that accurate approximations of non-linear stochastic equations can be achieved through appropriate Gaussian counterparts is already known. Thus, in equilibrium, the Bogoliubov-Feynman's inequality leads to a variational mean-field approximation that can be applied even to systems for which nonlinearities are non-polynomial in the height field [156, 157], while out of equilibrium the so-called self-consistent expansion (see [90] for an overview with references) allows to account for the scaling exponents of a number of nontrivial systems through an appropriate Gaussian Ansatz.

Numerical simulations of the Gaussian HK equation

Since all the scaling relations that we have derived stem from the two-dimensional PSD, for Eq. (4.51) we expect the behavior of $S_x(k)$ and $S_y(k)$ to be exactly as predicted by (4.12). As before, the numerical simulations have been performed using a pseudospectral scheme, with parameters: $\nu_x = \nu_y = 1$, $D = 1$, $L = 256$, $\Delta x = 1$, $\Delta t = 10^{-2}$. An example of the surface morphology that is obtained for long simulation times is provided in Figure 4.10. Before analyzing the PSD of one-dimensional cuts of the surface, we have checked the behavior of the two-dimensional PSD. In the left panel of Figure 4.11 we plot the projections of the 2D PSD onto the k_x and k_y axes, as in previous cases. The scaling for small k is as expected.

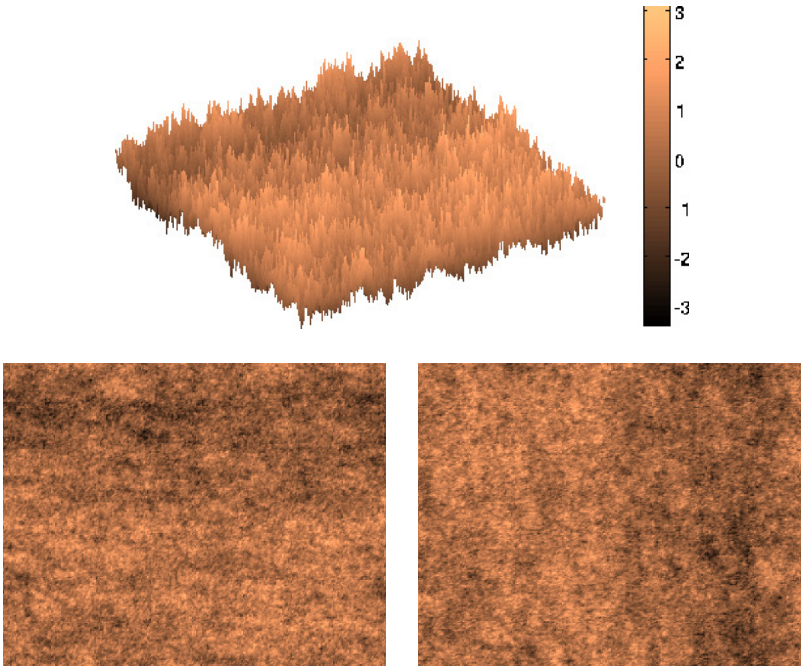

Figure 4.10: Morphology generated by numerical integration of the Gaussian HK equation, Eq. (4.51). Parameters are given in the main text. Top panel: three-dimensional view. Bottom panels: top views. The right panel has been obtained after rotating the left panel by $90°$.

Also $S_x(k)$, reported in the right panel of Figure 4.11 (left axis), behaves as expected. However, the one-dimensional PSD of cuts along the y axis $S_y(k)$ (right axis) displays the same unexpected behavior as for the nonlinear HK equation, the first point being "shifted" above the rest of them, and not adjusting to a straight line with the expected slope. Thus, such type of behavior does not seem due to the scaling Ansatz we are employing since, for a linear equation like (4.51), this simply expresses the exact behavior of the observables in the long time limit. Thus, the behavior of $S_y(k)$ seems, rather, induced by the present exponent values.

In order to clarify this issue, it is important to keep in mind that we are working for a finite system of lateral size $L < \infty$, and with a finite lattice spacing $a = \Delta x \neq 0$. The discrete counterparts of Eqs. (4.10) and (4.11) are

$$\hat{S}_x(k_x) = \frac{1}{L}\left[\hat{S}(k_x,0) + 2\sum_{n_y=1}^{N/2}\hat{S}(k_x,k_y)\right], \tag{4.53}$$

$$\hat{S}_y(k_y) = \frac{1}{L}\left[\hat{S}(0,k_y) + 2\sum_{n_x=1}^{N/2}\hat{S}(k_x,k_y)\right], \tag{4.54}$$

where $N = L/\Delta x = L/a$, and $n_x, n_y = 1, \ldots, N$ are discrete indices so that

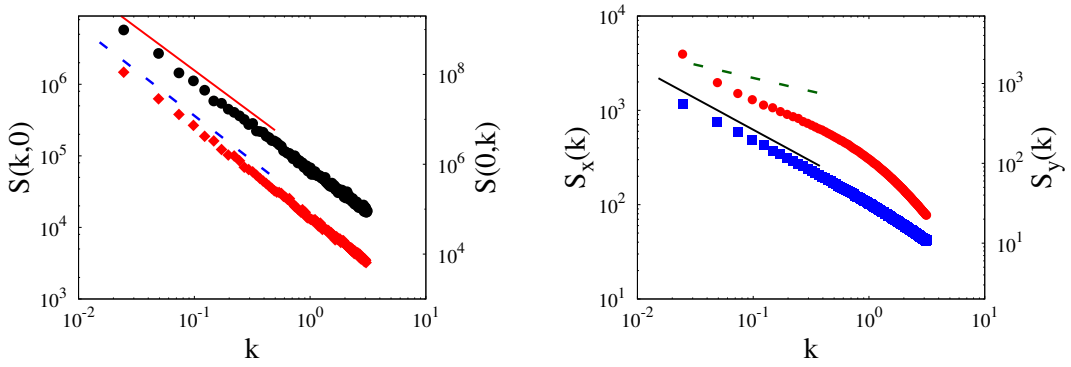

Figure 4.11: Numerical integration of equation (4.51). Left panel: One-dimensional projections $S(k,0)$ (black circles, left axis) and $S(0,k)$ (red diamonds, right axis) of the two-dimensional PSD, averaged over 300 different realizations. The solid red line is a guide for the eye with slope $-6/5$ while the dashed blue line has slope -2. Right panel: PSD of one-dimensional cuts $S_x(k)$ (blue squares, left axis) and $S_y(k)$ (red circles, right axis). The solid black line is a guide for the eye with slope $-2/3$ while the dashed green line has slope $-1/3$. Note that $S_y(k)$ does *not* follow the predicted scaling behavior.

$k_{x,y} = 2\pi n_{x,y}/L$. The hat stresses the discrete nature of these formulas. In the thermodynamic limit (for $L \to \infty$), these two series can be well approximated as

$$\hat{S}_x(k_x) \sim \frac{1}{\pi}\int_0^{\pi/a} dk_y\, S(k_x,k_y) = k_x^{-(2\tilde{\alpha}_x-\zeta)} I(k_x^{\zeta},\tilde{\alpha}_x), \tag{4.55}$$

$$\hat{S}_y(k_y) \sim \frac{1}{\pi}\int_0^{\pi/a} dk_x\, S(k_x,k_y) = k_y^{-(2\tilde{\alpha}_y-1/\zeta)} I(k_y^{1/\zeta},\tilde{\alpha}_y), \tag{4.56}$$

where we have defined

$$I(k,\alpha) = \frac{1}{\pi}\int_0^{\pi/ak} \frac{du}{1+u^{2\alpha}}. \tag{4.57}$$

In case the integral I is finite in the continuum $a \to 0$ limit, the approximations (4.55) and (4.56) hold and we indeed obtain the scaling laws (4.12). However, *depending on the value of the critical exponents* and the numerical parameters employed, convergence of the integrals in (4.55) and (4.56) can be too slow, and a clear-cut scaling may be jeopardized.

In order to verify this issue, we have evaluated the series $\hat{S}_x(k)$ and $\hat{S}_y(k)$ from the known two-dimensional PSD $\hat{S}(k_x,k_y)$ for increasing system size L (at fixed space resolution a). In the left panel of Figure 4.12 we see that the asymptotic scaling is already clear-cut for $\hat{S}_x(k)$ for the L values considered, while for $\hat{S}_y(k)$ it is still far from being seen. However, in the figure one can see that the curves for $\hat{S}_y(k)$ become smoother as L increases, supporting the prediction that, for a

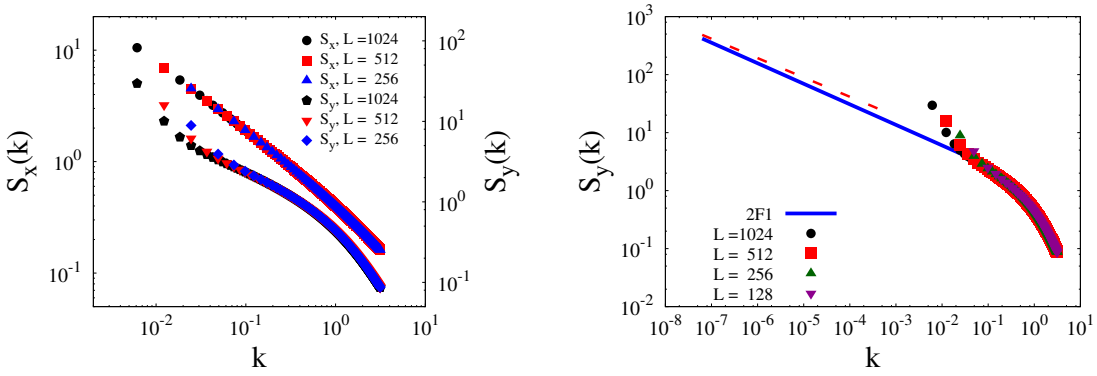

Figure 4.12: Left panel: Discrete 1D PSDs $\hat{S}_x(k)$ (left axis) and $\hat{S}_y(k)$ (right axis) calculated from the sampled two-dimensional PSD $\hat{S}(k_x, k_y)$ of the Gaussian approximation Eq. (4.51) for increasing system size L. Other model parameters are the same as in Figure 4.11. Right panel: Comparison of simulation data for $S_y(k)$ as obtained for Eq. (4.51) in the left panel of Figure 4.12, with the analytical solution of Eq. (4.54) given by Eq. (4.58) (thick blue line). The thin red line corresponds to the asymptotic behavior $S_y(k) \sim k^{-1/3}$.

sufficiently large system size, a well defined scaling behavior could be seen. A further step can be taken by solving the integral in Eq. (4.56) exactly,

$$\lim_{L\to\infty} \hat{S}_y(k_y) \sim k_y^{-2\tilde{\alpha}_y}\, a^{-1}\, {}_2F_1\left(p_1, 1; 1+p_1, p_2\right), \tag{4.58}$$

where ${}_2F_1$ is a hypergeometric function with parameters $p_1 = 1/2\tilde{\alpha}_x$ and $p_2 = -(\pi/a)^{2\tilde{\alpha}_x} k_y^{-2\tilde{\alpha}_y}$. In the right panel of Figure 4.12 we show this approximation of $\hat{S}_y(k_y)$ for a huge system ($L = 10^8$) with lattice cut-off $a = 1$. For the largest system sizes, the asymptotic scaling is clear and agrees perfectly with the one predicted from our scaling Ansatz. In the figure we moreover compare the analytical behavior with the numerical data from simulations of different system sizes. The numerical data indeed tend to adjust to the theoretical curve. This proves that, for the present values of the exponents, the sum (4.54) for $S_y(k_y)$ converges too slowly to the integral (4.58) for any numerically feasible system size. On the other hand, $S_x(k_x)$ displays the asymptotic behavior already at relatively small values of L. Thus, the convergence rate strongly depends on the values of the critical exponents. One way to directly verify this would be to perform numerical simulations with an adequate parameter set, corresponding to a theoretical curve in which the scaling behavior is clear. Unfortunately, as suggested by the right panel of Figure 4.12, this would require a computational effort beyond our capabilities.

These results for the Gaussian approximation of the HK equation support the hypothesis of a similar slow-convergence problem also for the nonlinear HK equation proper. The fact that the behavior of $S_y(k_y)$ for Eqs. (4.38) and (4.51) is qualitatively the same, and the fact that the presence of a nonlinearity usually con-

tributes to slowing the convergence rate of observables, lead us to think that the asymptotic state for HK equation has not been fully reached in our simulations. However, as for its Gaussian approximation, we have not been able to perform a sufficiently large-scale numerical simulation due to the great computational effort required.

The present slow-convergence problem may have important implications for the interpretation of experimental data. As pointed out earlier, many experimental setups are designed to measure the PSD of one-dimensional cuts, but we have shown here that for such integrated quantities there are systems in which the scaling may not be clearly detected. On the other hand, the two-dimensional PSD appears to be a more robust quantity, since it scales correctly already for relatively small values of the system size L and relatively large values of the spatial discretization. We have recently confirmed these expectations in the analysis of experiments on surface erosion by ion-beam sputtering, see Chapter 6.

4.4 Conclusions

In this chapter we have presented a dynamic scaling Ansatz for two-dimensional anisotropic kinetic roughening, that has a form readily applicable to the analysis of simulation or experimental data. The Ansatz incorporates the behavior that characterizes strongly anisotropic linear equations, as has been thoroughly checked via their exact solution and numerical simulations. In this process, we have introduced a family of linear models that display SA while generally being non-local in space. Incidentally, non-local models (incorporating e.g. fractional Laplacians) are lately finding ubiquitous use in equilibrium and non-equilibrium statistical mechanics [158]; see [103, 104, 159] and references therein for the specific context of kinetic roughening.

A natural second step that we have taken in the present chapter has been the validation of our scaling Ansatz against a numerical study of a paradigmatic nonlinear model of SA, and in general of GSI systems, namely, the HK equation for running sand piles. Again, agreement is quite satisfactory (as occurs for some experimental systems [160]), and can be concluded after elucidation of slow convergence properties of certain observables, induced by small critical exponent values. This has required us to formulate and study a linear equation that has the same exact exponents as the HK nonlinear system, and thus can be considered as a Gaussian approximation of the latter. Our results for this representative nontrivial anisotropic system suggest that the scarcity in assessments of anisotropic scaling in practical cases may be related with the occurrence of similar finite size effects.

Methodologically, the previous results can be of interest in the analysis of strongly anisotropic interfaces. On the one hand, we have seen that in the case of systems with conserved dynamics and non-conserved noise it is always possible to tailor a fully dynamical description through an appropriate (n, m) linear equation. Such a procedure to put forward an effective dynamical model may be many times

of interest, if dealing with complex nonlinear systems and/or with the description of simulation and/or experimental data. On the other hand, our analysis has shown the practical convenience of the use of certain observables (e.g. 2D PSD function) over other (e.g. PSD functions of 1D cuts of the 2D surface), provided one can access to data with large enough signal-to-noise ratio. This has actually been recently assessed in the analysis of experimental data from thin-film production [160].

5

STRONG ANISOTROPY IN NONLINEAR EQUATIONS

In Chapter 4, we proposed an Ansatz for anisotropic scaling and tested it against a whole family of linear models. We also considered a well known example of strongly anisotropic equation, namely, the Hwa-Kardar equation, which was susceptible of an accurate approximation through the former. However, it is not difficult to notice that the form of the HK equation is rather peculiar, since nonlinearities in one direction are completely suppressed. This naturally arises the question whether it is possible to construct a fully non-linear strongly anisotropic model, i.e. a model for which a Gaussian approximation of the type explained in Chapter 4 is not feasible. In this chapter, we explore the effect of anisotropic nonlinearities on several well known equations. We separate our analysis into two cases: equations with conserved dynamics and non-conserved noise, and systems whose dynamics is not conserved, but for which a translational symmetry of the field holds. As explained in Chapter 1, such conditions guarantee generic scale invariance. As representative cases for the conserved case, we study the conserved anisotropic KPZ (caKPZ) equation, and we introduce and analyze a generalization of the Hwa-Kardar (gHK) equation. As for the non-conserved case, we reconsider the anisotropic KPZ (aKPZ) equation, and we review and extend some known results. Through the combined use of Dynamic Renormalization Group analysis and direct numerical simulations, we conclude that the occurrence of strong anisotropy in two-dimensional surfaces requires dynamics to be conserved. We find that, moreover, strong anisotropy is not generic in parameter space but requires, rather, specific forms of the terms appearing in the equation of motion, whose justification needs detailed information on the dynamical process that is being modeled in each particular case.

5.1 Conserved dynamics

We start by considering systems for which dynamics are conserved. As explained in Chapter 1, in contrast with non-conserved dynamics, GSI ensues in such a case if noise is non-conserved [7, 8], irrespective of whether the deterministic part of the dynamical equation is or not invariant under arbitrary global changes in the value of the height, $h(\mathbf{r},t) \to h(\mathbf{r},t) + \text{const}$. We thus consider two representative examples: the conserved aKPZ equation, in which such *shift invariance* occurs, and a generalization of the HK equation, in which it does not.

5.1.1 The conserved anisotropic KPZ equation

A conceptually important example of an anisotropic conserved equation with non-conserved noise, which is invariant under arbitrary shifts of the height, is the caKPZ equation. This model has been formulated and studied [83, 161] in the context of non-equilibium growth of epitaxial thin films, specifically for surfaces which are vicinal to a high symmetry surface [44]. The caKPZ equation reads

$$\partial_t h = -\nabla^2 \left[\nu_x \partial_x^2 h + \nu_y \partial_y^2 h + \frac{\lambda_x}{2} (\partial_x h)^2 + \frac{\lambda_y}{2} (\partial_y h)^2 \right] + \eta, \tag{5.1}$$

where a linear first-order derivative term has been omitted, which does not affect our discussion and conclusions [83]. In Eq. (5.1), $\nu_{x,y} > 0$ and $\lambda_{x,y}$ are constant parameters. Note, dynamics are explicitly conserved while noise is not, and the equation only depends on h through its space or time derivatives, so that the equation does not single out any preferred height value. For generic parameter values, the DRG analysis performed in [83, 161] leads to the conclusion that the system shows weak anisotropy (i.e., $\zeta = 1$), displaying the scaling exponents of the isotropic conserved KPZ equation, which reads [33]

$$\partial_t h = -\nabla^2 \left[\nu \nabla^2 h + \frac{\lambda}{2} (\nabla h)^2 \right] + \eta. \tag{5.2}$$

Specifically, for $d = 2$ the scaling exponents of the caKPZ equation are thus predicted to be approximately given through a one-loop DRG analysis [33] (small corrections occur within a two-loop calculation [34]) by $\alpha \simeq 2/3$ and $z \simeq 10/3$. In particular, the change of universality class that occurs in the non-conserved anisotropic KPZ equation when changing the relative signs of the nonlinearities, from non-linear behavior for $\lambda_x \lambda_y > 0$ to linear behavior for $\lambda_x \lambda_y < 0$, does not occur for the caKPZ equation [83, 161].

In order to further discuss the scaling properties of the caKPZ equation, we first consider a similar model that shares with it the behavior just described. Thus, consider the equation

$$\partial_t h = -\nu_x \partial_x^4 h - \nu_y \partial_y^4 h - \frac{\lambda_x}{2} \partial_x^2 (\partial_x h)^2 - \frac{\lambda_y}{2} \partial_y^2 (\partial_y h)^2 + \eta. \tag{5.3}$$

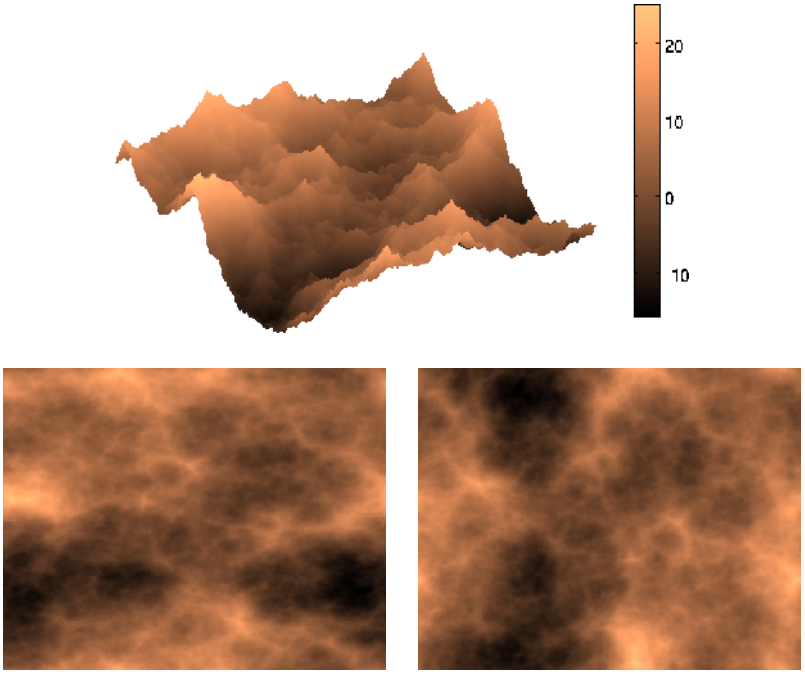

Figure 5.1: Morphology generated by numerical integration of Eq. (5.3) for parameters $\nu_x = \nu_y = 1$, $D = 1$, $\lambda_x = -3$, $\lambda_y = -1$, $L = 256$, $\Delta x = 1$, and $\Delta t = 0.05$. Top panel: three-dimensional view. Bottom panels: top views. The right panel has been obtained after rotating the left panel by $90°$.

The main difference between Eqs. (5.1) and (5.3) is that each term in the latter, e.g. $-\frac{\lambda_x}{2}\partial_x^2(\partial_x h)^2$, is affected by an overall second-order derivative operator with a reduced symmetry as compared to its counterpart in the former, e.g. $-\frac{\lambda_x}{2}\nabla^2(\partial_x h)^2$. Nevertheless, the scaling behavior is not modified, as we have verified by numerical simulations. Specifically, we have integrated Eq. (5.3) by means of a pseudo-spectral integration algorithm as described in Chapter 2. A surface morphology obtained for long simulation times is presented in Figure 5.1. The results of the simulations are presented in Figures 5.2 and 5.3.

Thus, the left and right panels of Figure 5.2 show, respectively, cuts of the 2D PSD function $S(\mathbf{k})$ along the coordinate axes in $\mathbf{k}$-space and 1D PSD functions for cuts of the surface along the x and y directions, $S_{x,y}(k_{x,y})$, for a condition of Eq. (5.3) in which $\lambda_x\lambda_y > 0$. Agreement with asymptotic scaling behavior as in Eqs. (4.6), (4.12), (4.17), and (4.18) for a WA case is very good, using the expected exponents for the isotropic cKPZ equation, $\alpha_x = \alpha_y \simeq 2/3$. Similar agreement is obtained in Figure 5.3 for a condition of Eq. (5.3) in which $\lambda_x\lambda_y < 0$. Therefore, the scaling exponents correspond to those of the isotropic cKPZ equation, irrespective of the relative signs of the nonlinearities, so we can safely say that Eq. (5.3) is in the same universality class as the caKPZ equation, Eq. (5.1).

Having established the previous result, the only possibility for Eq. (5.3), and

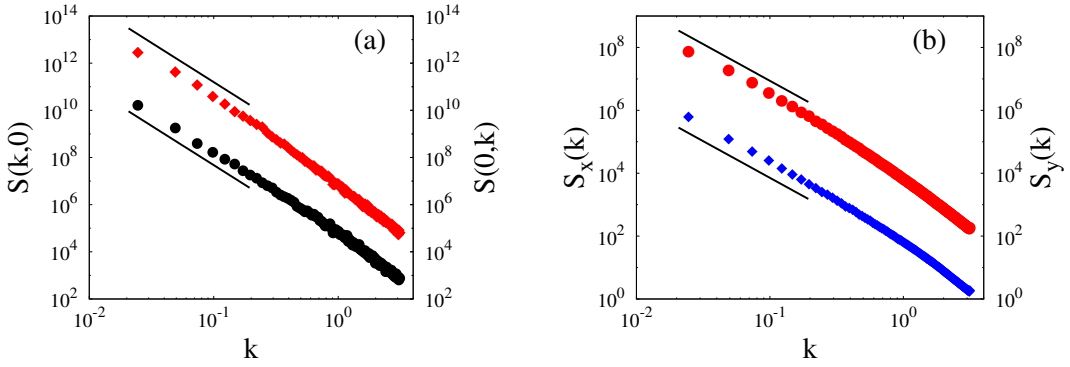

Figure 5.2: Numerical integrations of Eq. (5.3) for parameters $\nu_x = \nu_y = 1$, $D = 1$, $\lambda_x = -3$, $\lambda_y = -1$, $L = 256$, $\Delta x = 1$, and $\Delta t = 0.05$. (a) One-dimensional projections $S(k, 0)$ (black circles, left axis) and $S(0, k)$ (red diamonds, right axis) of the two-dimensional PSD, averaged over 100 different noise realizations. The solid black lines are guides for the eye with slope $-10/3$. (b) PSD of one-dimensional cuts $S_x(k)$ (blue squares, left axis) and $S_y(k)$ (red circles, right axis). The solid black lines are guides for the eye with slope $-7/3$. For visualization purposes, the values of $S(0, k)$ and $S_y(k)$ have been artificially offset vertically.

equivalently for the caKPZ equation, to display strongly anisotropic behavior is that one nonlinearity, say λ_y, is suppressed, but not the other. Hence, we consider equation

$$\partial_t h = -\nu_x \partial_x^4 h - \nu_y \partial_y^4 h - \frac{\lambda_x}{2} \partial_x^2 (\partial_x h)^2 + \eta. \tag{5.4}$$

In a specific physical situation, this implies a non-generic parameter condition, e.g. that the corresponding non-linear contribution to the surface-diffusion current vanishes [5] due to a special parameter choice. This case seems not to have been considered in [83]. Actually, we can benefit from the DRG analysis performed by Kallabis in order to derive expectations for the critical exponents of Eq. (5.4): After the coarse-graining step is performed (full details are available in [161]) as described in Section 2.1, we perform an anisotropic rescaling that restores the original wave-vector cut-off, namely,

$$x \to bx, \qquad y \to b^{\zeta} y, \qquad t \to b^{z_x} t, \qquad h \to b^{\alpha_x} h. \tag{5.5}$$

Using $b = e^{\delta l}$, and taking into account the net modification of the equation parameters after both the coarse-graining and the rescaling transformations, the DRG

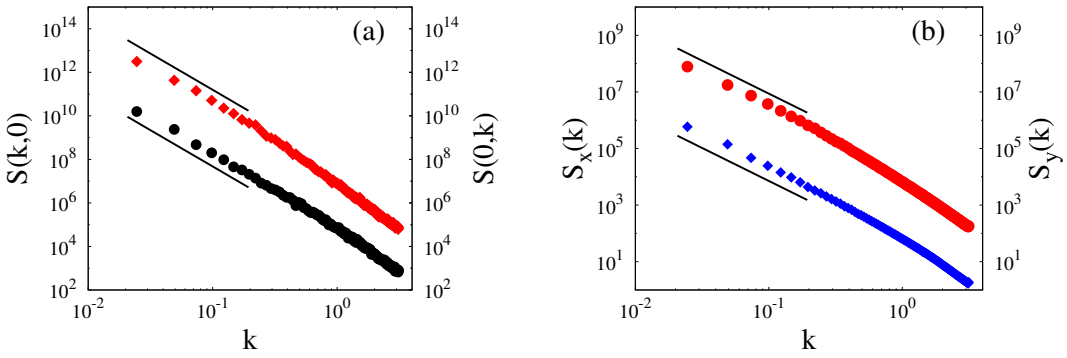

Figure 5.3: Numerical integrations of Eq. (5.3) for parameters as in Figure 5.2, except for $\lambda_x = -3$ and $\lambda_y = 1$. (a) One-dimensional projections $S(k,0)$ (black circles, left axis) and $S(0,k)$ (red diamonds, right axis) of the two-dimensional PSD, averaged over 100 different noise realizations. The solid black lines are guides for the eye with slope $-10/3$. (b) PSD of one-dimensional cuts $S_x(k)$ (blue squares, left axis) and $S_y(k)$ (red circles, right axis). The numerical integrations were performed for the same parameters as in the left panel. The solid black lines are guides for the eye with slope $-7/3$. For visualization purposes, the values of $S(0,k)$ and $S_y(k)$ have been artificially offset vertically.

parameter flow for ν_y, λ_x, and D reads particularly simple, namely,

$$\frac{d\nu_y}{dl} = \nu_y(z_x - 4\zeta), \tag{5.6}$$

$$\frac{d\lambda_x}{dl} = \lambda_x(\alpha_x + z_x - 4), \tag{5.7}$$

$$\frac{dD}{dl} = D(z_x - 2\alpha_x - \zeta - 1), \tag{5.8}$$

which actually coincides with the result of a mere parameter rescaling [5]. The reasons behind such a simplicity are: (i) Given that in Eq. (5.4) $\lambda_y = 0$ to begin with, parameter renormalization can be only due to the remaining nonlinearity λ_x, which does not contribute to k_y^2 order, hence ν_y does not renormalize; (ii) at one-loop order there is a vertex cancellation [104] by which λ_x does not renormalize either; (iii) as standard for conserved equations with non-conserved noise, since the lowest-order non-linear modification of the noise propagator is $\mathrm{O}(k_x^2)$, the variance D is not affected and it does not renormalize either. Finally, the fixed points of the RG flow control the scaling behavior. Thus, setting to zero the right-hand sides of Eqs. (5.6)-(5.8) we obtain

$$z_x = 4\zeta, \tag{5.9}$$

$$\alpha_x + z_x = 4, \tag{5.10}$$

$$z_x = 2\alpha_x + \zeta + 1. \tag{5.11}$$

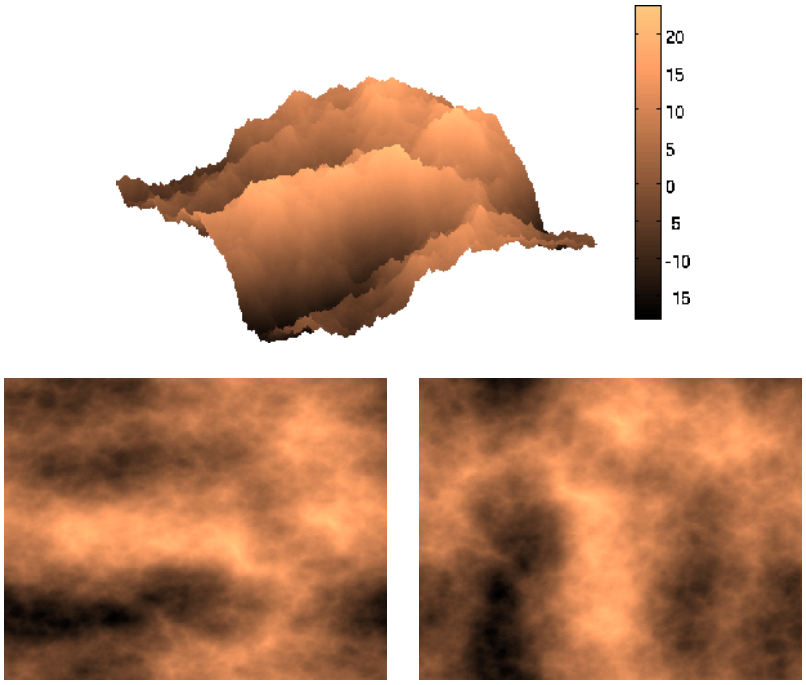

Figure 5.4: Morphology generated by numerical integration of Eq. (5.4) for parameters $\nu_x = \nu_y = 1$, $D = 1$, $\lambda_x = 3$, $L = 256$, $\Delta x = 1$, and $\Delta t = 0.05$. Top panel: three-dimensional view. Bottom panels: top views. The right panel has been obtained after rotating the left panel by $90°$.

These are three non-homogeneous linear equations for three unknowns, whose unique solution does correspond to SA behavior, namely,

$$\alpha_x = 8/11, \qquad z_x = 36/11, \qquad \zeta = 9/11. \tag{5.12}$$

We have performed numerical simulations of Eq. (5.4) in order to verify Eq. (5.12). A surface morphology obtained for long simulation times is presented in Figure 5.4. The results, presented in Figure 5.5, are in good agreement with these SA values of the scaling exponents.

In spite of being strongly anisotropic, the ζ value obtained for Eq. (5.4) is very close to one, so that effectively scaling behavior is not far from a proper weakly anisotropic case. For practical applications, Eq. (5.4), and thus the caKPZ equation with $\lambda_y = 0$, is not the most clear-cut example of strong anisotropy. However, Eqs. (5.9)-(5.11) give us a way to construct an equation similar to (5.4), but with a tunable anisotropy exponent ζ. In wave-vector space, such an equation can be written as

$$\partial_t h_{\mathbf{k}} = -(\nu_x |k_x|^{2n+2} + \nu_y |k_y|^{2m}) h_{\mathbf{k}} - \frac{\lambda_x}{2} |k_x|^{2n} \mathcal{F}[(\partial_x h)^2] + \eta_{\mathbf{k}}, \tag{5.13}$$

where $\mathcal{F}[\cdot]$ denotes space Fourier transform, and n and m are positive *real* numbers. Notice, Eq. (5.4) corresponds simply to the particular choice $n = 1$ and $m = 2$.

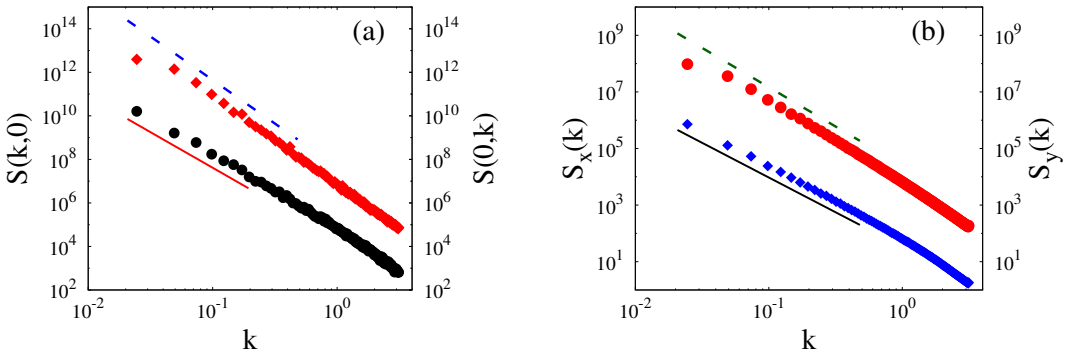

Figure 5.5: Numerical integrations of Eq. (5.4) for parameters $\nu_x = \nu_y = 1$, $D = 1$, $\lambda_x = 3$, $L = 256$, $\Delta x = 1$, and $\Delta t = 0.05$. (a) One-dimensional projections $S(k,0)$ (black circles, left axis) and $S(0,k)$ (red diamonds, right axis) of the two-dimensional PSD, averaged over 100 different noise realizations. The solid red line and the dashed blue line are guides for the eye with slopes $-36/11$ and -4 respectively. (b) PSD of one-dimensional cuts $S_x(k)$ (blue squares, left axis) and $S_y(k)$ (red circles, right axis). The solid black line and the dashed green line are guides for the eye with slopes $-27/11$ and $-25/9$, respectively. For visualization purposes, the values of $S(0,k)$ and $S_y(k)$ have been artificially offset vertically.

In exactly the same form as for Eq. (5.9), it is not difficult to derive the following scaling relations for Eq. (5.13),

$$\alpha_x + z_x = 2(n+1), \tag{5.14}$$
$$z_x = 2m\zeta, \tag{5.15}$$
$$z_x = 2\alpha_x + 1 + \zeta, \tag{5.16}$$

whose solution provides the following values of the exponents, as functions of n and m,

$$\alpha_x = \frac{4nm + 2m - 2n - 2}{6m - 1}, \qquad z_x = 2m\frac{4n+5}{6m-1}, \qquad \zeta = \frac{4n+5}{6m-1}. \tag{5.17}$$

Indeed, Eqs. (5.17) reduce to Eqs. (5.9)-(5.11) for $n = 1$ and $m = 2$. The advantage is that now we can make different choices for (n, m) in such a way that ζ is far from unity and SA behavior is enhanced. Note, a result such as Eq. (5.17) is remarkable, as it provides the solution for the scaling exponents of a two-parameter family of non-linear equations. Actually, the symmetries leading to it circumvent the generation under renormalization of additional lower-order terms in the equation of motion, which would otherwise be expected. In principle, note that we have derived Eq. (5.17) under the one-loop DRG approximation. An analogous result was obtained for the HK equation in [145, 155], where it was argued to hold at any order in the DRG loop expansion. Again, it is due to the symmetries of the

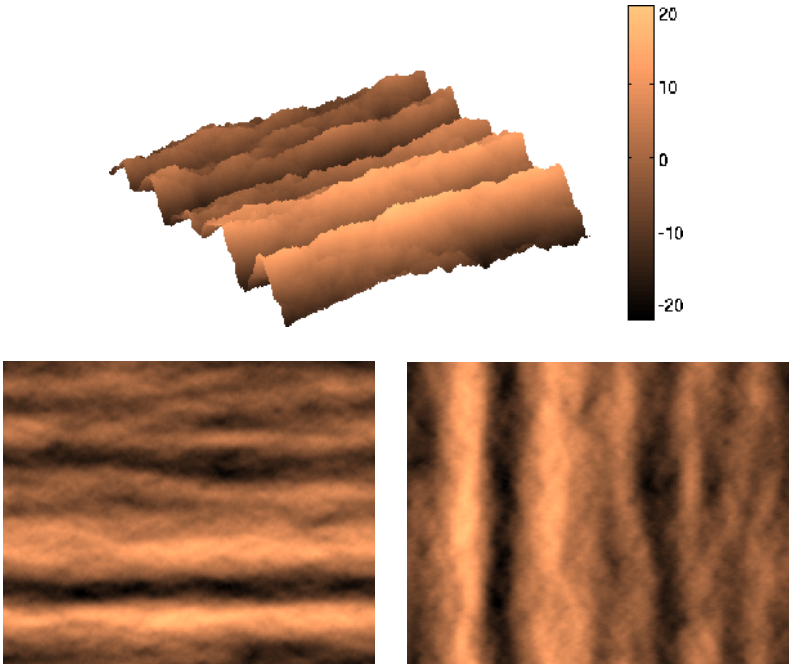

Figure 5.6: Morphology generated by numerical integration of Eq. (5.13) for for $n = 1/2$, $m = 3$, and parameters $\nu_x = \nu_y = 1$, $D = 1$, $\lambda_x = 2$, $L = 256$, $\Delta x = 1$, and $\Delta t = 0.05$. Top panel: three-dimensional view. Bottom panels: top views. The right panel has been obtained after rotating the left panel by $90°$.

system as discussed above, leading to the three scaling relations among exponents. In the case of the HK equation proper, this even allows to approximate it very accurately by a *linear* equation with the exact same scaling exponents [160], as seen in Chapter 4.

As a specific example, we have performed numerical simulations of Eq. (5.13) with $n = 1/2$ and $m = 3$ in order to compare with the expected scaling exponents, which are

$$\alpha_x = \frac{9}{17}, \qquad z_x = \frac{42}{17}, \qquad \zeta = \frac{7}{17}. \tag{5.18}$$

A surface morphology obtained for long simulation times is presented in Figure 5.6. The results, presented in Figure 5.7 indeed agree with these exponents values. Notice in this case full saturation of correlations along the y direction has not been achieved for our longest simulation times, hence the k_y-independent behavior of $S(0, k_y)$ and $S_y(k_y)$ at small arguments.

As a summary of the results in this section, we conclude that strong anisotropy is indeed feasible for conserved equations with non-conserved noise which are invariant under global shifts of the height field. However, this requires the suppression of nonlinearities along one of the substrate directions, which is a non-generic parameter condition. Notice, under such a constraint the equation cannot possibly

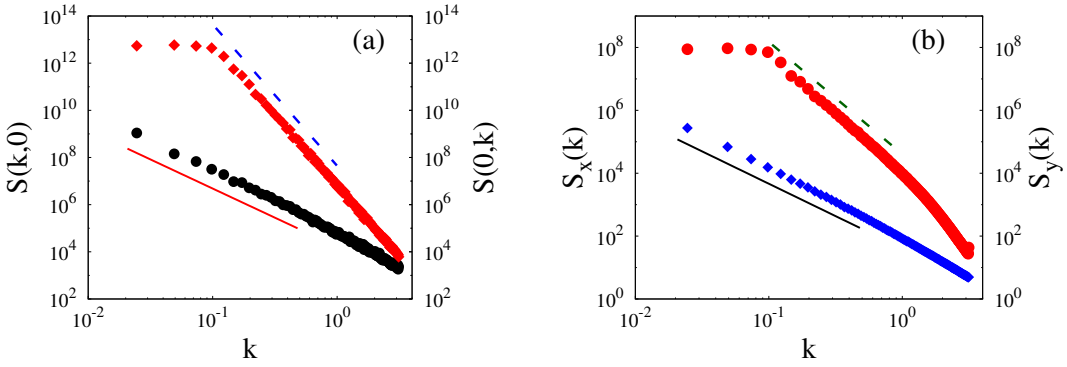

Figure 5.7: Numerical integrations of Eq. (5.13) for $n = 1/2$, $m = 3$, and parameters $\nu_x = \nu_y = 1$, $D = 1$, $\lambda_x = 2$, $L = 256$, $\Delta x = 1$, and $\Delta t = 0.05$. (a) One-dimensional projections $S(k, 0)$ (black circles, left axis) and $S(0, k)$ (red diamonds, right axis) of the two-dimensional PSD, averaged over 100 different noise realizations. The solid red line and the dashed blue line are guides for the eye with slopes $-42/17$ and -6 respectively. (b) PSD of one-dimensional cuts $S_x(k)$ (blue squares, left axis) and $S_y(k)$ (red circles, right axis). The solid black line and the dashed green line are guides for the eye with slopes $-35/17$ and $-25/7$, respectively. For visualization purposes, the values of $S(0, k)$ and $S_y(k)$ have been artificially offset vertically.

be brought into isotropic form by any simple combination of coordinate rotations and/or rescalings in the substrate plane.

5.1.2 The generalized HK equation

In Chapter 4 we considered the Hwa-Kardar equation, which was originally proposed to describe the interface dynamics of a running-sandpile model, in the context of self-organized criticality [145, 155]. For a two-dimensional substrate such as we are currently considering, this equation reads

$$\partial_t h = \nu_x \partial_x^2 h + \nu_y \partial_y^2 h - \frac{\lambda_x}{2} \partial_x h^2 + \eta. \tag{5.19}$$

In the original formulation [145, 155], the linear terms model the relaxation of the height of the sand-pile through diffusive transport, whereas the nonlinearity accounts for the lack of inversion symmetry in the x direction, being related to the presence of the external driving provided by the influx of sand. This is assumed to occur along the x axis, which is an example of a non-generic condition for nonlinearities, as discussed in the previous section. The noise term η in Eq. (5.19) mimics the random addition of sand particles from outside the system, thus being non-conserved. This leads to GSI properties, in spite of the fact that the HK equation depends explicitly on h, and not only on its derivatives [8]. In particular, as we

have discussed in Section 4.3 SA occurs, with scaling exponents

$$\alpha_x^{\rm HK} = -\frac{1}{5}, \quad z_x^{\rm HK} = \frac{6}{5}, \quad \zeta^{\rm HK} = \frac{3}{5}. \tag{5.20}$$

Note that the negative values of $\alpha_{x,y}$ actually imply subdominant (logarithmic) behavior for observables in real space, such as e.g. the surface roughness [5]. As discussed in detail in Chapter 4 and Reference [160], it also leads to slow convergence even for observables in Fourier space, but which are integrals of the 2D PSD function, such as $S_{x,y}(k_{x,y})$. We will meet again this type of behavior in some specific examples to be discussed below.

In view of the results of the previous section, a natural question is whether the different behavior of the HK under global shifts of the height, as compared to e.g. the caKPZ equation, could allow for the occurrence of strong anisotropy, even for more generic parameter conditions such that, e.g., the non-linear part of the equation could be brought into an isotropic form via appropriate coordinate transformations in the substrate plane. In order to elucidate this possibility, we generalize the HK equation into

$$\partial_t h = \nu_x \partial_x^2 h + \nu_y \partial_y^2 h + \nu_{xy} \partial_{xy}^2 h - \frac{\lambda_x}{2} \partial_x h^2 - \frac{\lambda_y}{2} \partial_y h^2 + \eta, \tag{5.21}$$

which will be henceforth referred to as the gHK equation. Indeed, the original HK equation simply corresponds to the particular case of Eq. (5.21) in which $\lambda_x \neq 0$ while $\lambda_y = \nu_{xy} = 0$. The term proportional to ν_{xy} has been introduced for technical reasons, as will become clear next.

In order to derive analytical insight into the critical behavior of the gHK equation, we apply to it the DRG procedure described in Chapter 2. The flow equations for the renormalization of the parameters of the gHK equation read

$$\frac{d\nu_x}{dl} = \nu_x \left(z_x - 2 - \Sigma_{\nu_x} \right), \tag{5.22}$$

$$\frac{d\nu_{xy}}{dl} = \nu_{xy} (z_x - \zeta - 1 - \Sigma_{\nu_{xy}}), \tag{5.23}$$

$$\frac{d\nu_y}{dl} = \nu_y \left(z_x - 2\zeta - \Sigma_{\nu_y} \right), \tag{5.24}$$

$$\frac{d\lambda_x}{dl} = \lambda_x (\alpha_x + z_x - 1), \tag{5.25}$$

$$\frac{d\lambda_y}{dl} = \lambda_y (\alpha_x + z_x - \zeta), \tag{5.26}$$

$$\frac{dD}{dl} = D(z_x - 2\alpha_x - \zeta - 1). \tag{5.27}$$

where Σ_{ν_x}, Σ_{ν_y} and $\Sigma_{\nu_{xy}}$ are functions of $\nu_{x,y}$ and $\lambda_{x,y}$ which are provided in Appendix A.2, together with further details on the derivation of Eqs. (5.22)-(5.27). From Eqs. (5.22)-(5.24) note that for the gHK equation, even if the term with bare parameter ν_{xy} were initially zero, it is in principle generated by the coarse-graining

procedure. This is due to the fact that $\Sigma_{\nu_{xy}}$ has a prefactor of $1/\nu_{xy}$, see Eq. (A.30), so that the term $\nu_{xy}\Sigma_{\nu_{xy}}$ in the flux equation for ν_{xy} will not generically vanish, even when $\nu_{xy}=0$. This is the reason why we have incorporated it to the definition of Eq. (5.21), in order to correctly take it into account in the DRG analysis.

We can write down an equivalent DRG flow which does not depend explicitly on α_x and z_x through the identification of natural couplings in the system, such as, e.g.

$$g=\frac{\lambda_x^2 D}{16\pi^2\Lambda^2\nu_x^3},\qquad r_\nu=\frac{\nu_y}{\nu_x},\quad f_\nu=\frac{\nu_{xy}}{\nu_x},\qquad r_\lambda=\frac{\lambda_y}{\lambda_x}. \tag{5.28}$$

Thus, we get

$$\frac{dr_\lambda}{dl}=r_\lambda\,(1-\zeta), \tag{5.29}$$

$$\frac{df_\nu}{dl}=f_\nu\left[1-\zeta+\Sigma_{\nu_x}-\Sigma_{\nu_{xy}}\right], \tag{5.30}$$

$$\frac{dr_\nu}{dl}=r_\nu\left[2\,(1-\zeta)+\Sigma_{\nu_x}-\Sigma_{\nu_y}\right], \tag{5.31}$$

$$\frac{dg}{dl}=g\left[3-\zeta+3\,\Sigma_{\nu_x}\right]. \tag{5.32}$$

HK equation as a particular case

The behavior of the original HK equation, which corresponds to $r_\lambda=f_\nu=0$, can be readily obtained from the above DRG results, see details in Appendix A.2.1. The non-trivial part of the flow reduces in this case to

$$\frac{dr_\nu}{dl}=2r_\nu(1-\zeta)-g\left[\frac{3\zeta+(7+\zeta)r_\nu+5r_\nu^2}{(1+r_\nu)^2}+5\sqrt{r_\nu}\tan^{-1}(\sqrt{r_\nu})+\frac{3\zeta}{\sqrt{r_\nu}}\tan^{-1}\left(\frac{1}{\sqrt{r_\nu}}\right)\right], \tag{5.33}$$

$$\frac{dg}{dl}=g(3-\zeta)-\frac{3g^2}{r_\nu}\left[\frac{3\zeta+(7+\zeta)r_\nu+5r_\nu^2}{(1+r_\nu)^2}+5\sqrt{r_\nu}\tan^{-1}(\sqrt{r_\nu})+\frac{3\zeta}{\sqrt{r_\nu}}\tan^{-1}\left(\frac{1}{\sqrt{r_\nu}}\right)\right]. \tag{5.34}$$

The fixed points of Eq. (5.34) are either $g=0$ or

$$g=g^*\equiv\frac{3-\zeta}{3}r_\nu\left[\frac{3\zeta+(7+\zeta)r_\nu+5r_\nu^2}{(1+r_\nu)^2}+5\sqrt{r_\nu}\tan^{-1}(\sqrt{r_\nu})+\frac{3\zeta}{\sqrt{r_\nu}}\tan^{-1}\left(\frac{1}{\sqrt{r_\nu}}\right)\right]^{-1}. \tag{5.35}$$

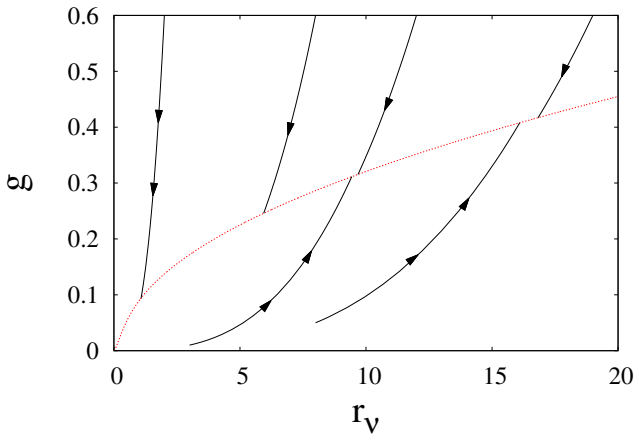

Figure 5.8: Numerical integration of the DRG flow for the gHK equation (5.21) in the HK limiting case $r_\lambda = f_\nu = 0$, Eqs. (5.31)-(5.32). The solid black lines are flow trajectories, while the dashed red line is the manifold of fixed points of the flow.

If $g = 0$, Eq. (5.31) implies $\zeta = 1$, see Eq. (5.33). In contrast, setting $g = g^*$ requires $\zeta = 3/5$ in order to yield a fixed point for Eqs. (5.31)-(5.32) [note Eqs. (5.29)-(5.30) hold automatically since we have set $\nu_{xy} = \lambda_y = 0$]. Moreover, in this case a manifold of fixed points actually exists in (r_ν, g) parameter space, described by the equation obtained once we set $\zeta = 3/5$ in Eq. (5.35), namely,

$$g = \frac{4}{5} r_\nu \left[\frac{9 + 38 r_\nu + 25 r_\nu^2}{5(1+r_\nu)^2} + 5\sqrt{r_\nu}\tan^{-1}(\sqrt{r_\nu}) + \frac{9}{5\sqrt{r_\nu}}\tan^{-1}\left(\frac{1}{\sqrt{r_\nu}}\right)\right]^{-1}.$$

In order to explore the stability of this family of fixed points, we have numerically integrated the flux (5.31)-(5.32) for $\nu_{xy} = \lambda_y = 0$. The result is shown in Figure 5.8, where it is clear that all the fixed points on the manifold are attractive, illustrating how GSI occurs in this system. This is in stark contrast with the role of RG fixed points in equilibrium critical systems, which are unstable due to the relevance of temperature perturbations. Moreover, each point on the manifold corresponds to the *same* set of scaling exponents, which are obtained by going back to Eqs. (5.22)-(5.27), and plugging in the values of g^* and ζ. The resulting exponents have the expected values for the HK equation, namely Eq. (5.20).

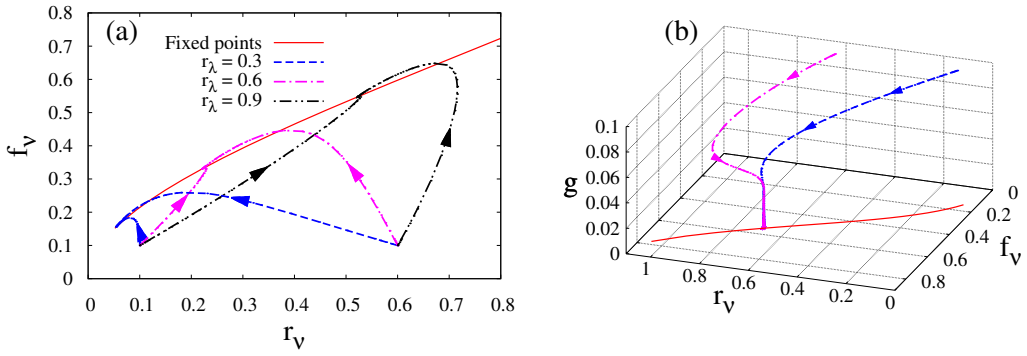

Figure 5.9: Numerical integration of the DRG flow for the gHK equation (5.21) in the case $\zeta = 1$ [Eqs. (5.30)-(5.32)]. (a) Projection on the (r_ν, f_ν) plane for two initial conditions, $(r_\nu, f_\nu, g) = (0.1, 0.1, 0.1), (0.6, 0.1, 0.1)$, and several values of r_λ in each case, as indicated in the legend. The solid red line is the manifold of fixed points, parametrized by r_λ. (b) Three-dimensional view of two flow trajectories for $r_\lambda = 1$ and the same two initial conditions as in the left panel. Again, the solid red line is the manifold of fixed points.

Full generalized HK equation

In the case of the full gHK equation, it is clear from Eq. (5.29) that if $r_\lambda \neq 0$, then $\zeta = 1$ at the RG fixed point, leading to *isotropic asymptotic behavior*. In Appendix A.2.2, we explicitly provide the three remaining DRG flow equations, Eqs. (5.30)-(5.32) in this case. By numerically exploring the parameter space, for $0.3 \leq r_\lambda \leq 1.2$ we have found a non-trivial manifold of fixed points, which can actually be seen as a line parametrized by the value of r_λ. All points on this manifold share the scaling exponents values

$$\alpha_x = -\frac{1}{3}, \qquad z_x = \frac{4}{3}, \qquad \zeta = 1. \tag{5.36}$$

In Figure 5.9 we show the numerical integration of the DRG flow for r_λ within this range. Similar considerations can be made as those provided for Figure 5.8.

However, we have not been able to find a similar set of fixed points for other values of r_λ. Due to the strong non-linear character of the equations that one needs to solve (see Appendix A.2), it is uncertain whether this is due to lack of convergence of the numerical scheme we have employed to integrate the DRG flow equations, or to an artifact of the approximations made within our DRG approach itself. Nevertheless, one would expect such fixed points to also exist and correspond to exponent values as given in Eq. (5.36). In order to verify this conjecture, we have performed direct numerical simulations of the full gHK equation using the same pseudo-spectral scheme as above. We have paid particular attention to a potential change of scaling behavior due to a relative change in the signs of the nonlinearities λ_x and λ_y. A surface morphology obtained for long simulation times is presented

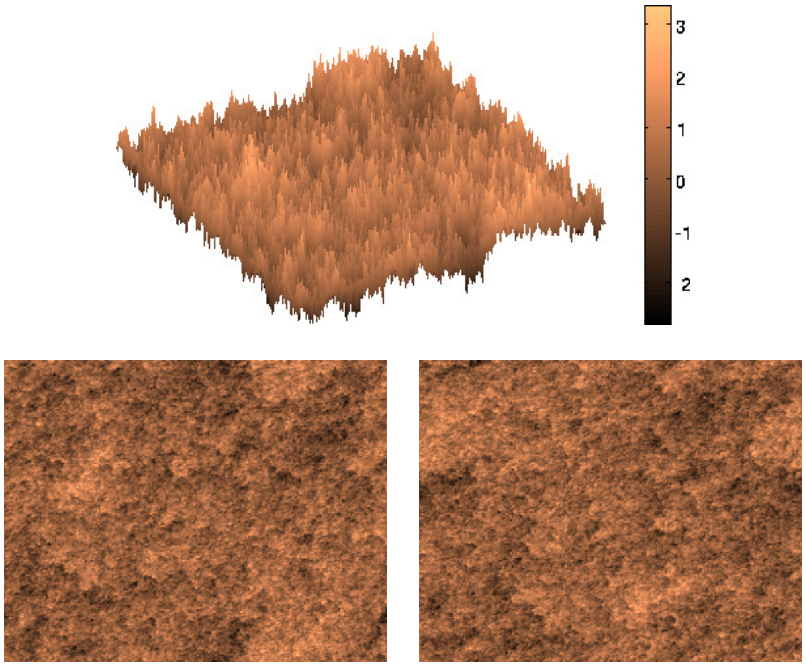

Figure 5.10: Morphology generated by numerical integration of Eq. (5.21) for parameters $\nu_x = \nu_y = 1$, $\nu_{xy} = 0$, $D = 1$, $\lambda_x = 1$, $\lambda_y = 2$ (so that $r_\lambda > 0$), $L = 256$, $\Delta x = 1$, and $\Delta t = 0.01$. Top panel: three-dimensional view. Bottom panels: top views. The right panel has been obtained after rotating the left panel by $90°$.

in Figure 5.10. As is clear from the left panels of Figures 5.11 and 5.12, in the hydrodynamic limit the equation displays the expected isotropic exponent values, Eq. (5.36), irrespective of such a relative sign, analogous in this sense to the caKPZ equation.

Looking at the right panels of Figures 5.11 and 5.12, the analytical predictions for the one-dimensional PSDs apparently do not agree with the results from numerical simulations. A very similar phenomenon has been found and studied for the HK equation in [160, Figs. 9 through 11], as we have seen in Chapter 4. In that case, the discrepancy was due to finite size effects for the system sizes employed in the numerical simulation of the equation, and we believe that a similar phenomenon is taking place here. It is worth mentioning that such a lack of convergence seems more pronounced for the PSD of cuts along the y direction than for cuts along the x direction, probably related with the value of λ_y, which is larger in absolute value than λ_x in both cases.

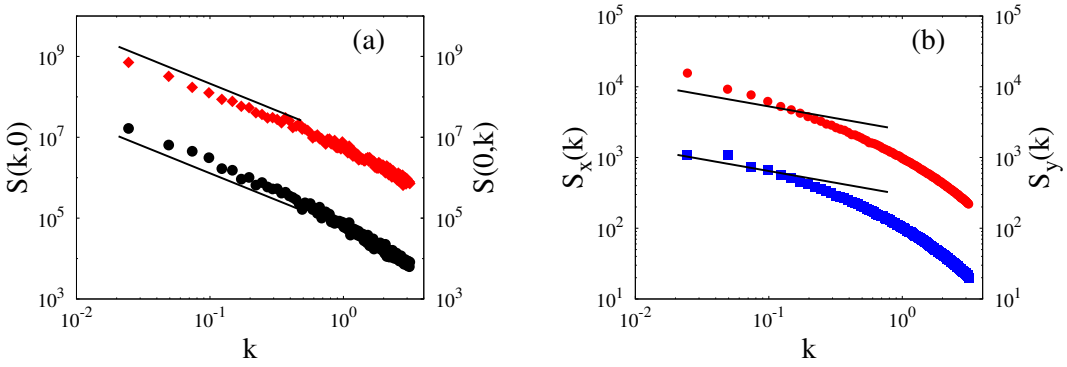

Figure 5.11: Numerical integrations of the gHK equation, Eq. (5.21), for parameters $\nu_x = \nu_y = 1$, $\nu_{xy} = 0$, $D = 1$, $\lambda_x = 1$, $\lambda_y = -2$ (so that $r_\lambda < 0$), $L = 256$, $\Delta x = 1$, and $\Delta t = 0.01$. (a) One-dimensional projections $S(k, 0)$ (black circles, left axis) and $S(0, k)$ (red diamonds, right axis), averaged over 50 different noise realizations. The solid black lines are guides for the eye with slope $-4/3$. (b) PSD of one-dimensional cuts $S_x(k)$ (blue squares, left axis) and $S_y(k)$ (red circles, right axis). The solid black lines are guides for the eye with slope $-1/3$. For visualization purposes, the values of $S(0, k)$ and $S_y(k)$ have been artificially offset vertically.

5.2 Non-conserved dynamics

After the previous results, it is natural to ponder whether strongly anisotropic behavior can actually occur for GSI systems with non-conserved dynamics. The prime representative of them is the aKPZ equation [79], namely,

$$\partial_t h = \nu_x \partial_x^2 h + \nu_y \partial_y^2 h + \frac{\lambda_x}{2}(\partial_x h)^2 + \frac{\lambda_y}{2}(\partial_y h)^2 + \eta. \tag{5.37}$$

This equation was studied in detail in the seminal paper [79]. The main result was that the scaling behavior is always isotropic, changing from linear Edwards-Wilkinson (EW) type to non-linear KPZ type as a function of the nonlinearities having opposite or the same signs, respectively. However, the case in which only one of the nonlinearities is zero remained basically unexplored. Our results above suggest that it might lead to SA behavior, and for this reason we will revisit the DRG analysis in [79], complementing it with direct numerical simulations of the equation. Moreover, while detailed calculations are available for the caKPZ system [161], this is not the case of Eq. (5.37). For this reason we provide details of our analysis in Appendix A.3.

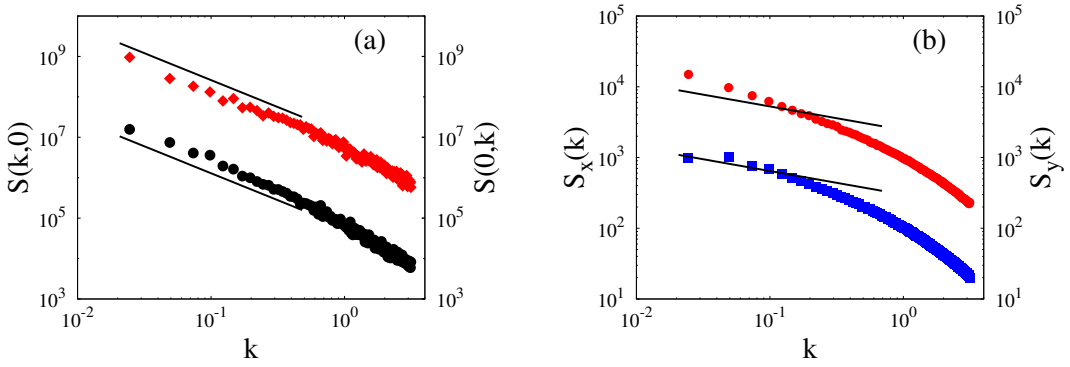

Figure 5.12: Numerical integrations of the gHK equation, Eq. (5.21), for parameters $\nu_x = \nu_y = 1$, $\nu_{xy} = 0$, $D = 1$, $\lambda_x = 1$, $\lambda_y = 2$ (so that $r_\lambda > 0$), $L = 256$, $\Delta x = 1$, and $\Delta t = 0.01$. (a) One-dimensional projections $S(k,0)$ (black circles, left axis) and $S(0,k)$ (red diamonds, right axis) of the two-dimensional PSD, averaged over 50 different noise realizations. The solid black lines are guides for the eye with slope $-4/3$. (b) PSD of one-dimensional cuts $S_x(k)$ (blue squares, left axis) and $S_y(k)$ (red circles, right axis). The solid black lines are guides for the eye with slope $-1/3$. For visualization purposes, the values of $S(0,k)$ and $S_y(k)$ have been artificially offset vertically.

5.2.1 DRG analysis of the anisotropic KPZ equation

In the case of Eq. (5.37), the DRG flow equations read in general

$$\frac{d\nu_x}{dl} = \nu_x(z_x - 2 - \Sigma_{\nu_x}), \qquad \frac{d\nu_y}{dl} = \nu_y(z_x - 2\zeta - \Sigma_{\nu_y}), \tag{5.38}$$

$$\frac{d\lambda_x}{dl} = \lambda_x(z_x + \alpha_x - 2), \qquad \frac{d\lambda_y}{dl} = \lambda_y(z_x + \alpha_x - 2\zeta), \tag{5.39}$$

$$\frac{dD}{dl} = D(z_x - 2\alpha_x - \zeta - 1 + \Phi_D), \tag{5.40}$$

where functions Σ_{ν_x}, Σ_{ν_y}, and Φ_D are reported in Appendix A.3, together with the main steps in their calculation. From Eq. (5.39) we immediately see that, if both nonlinearities are non-zero, $\lambda_x\lambda_y \neq 0$, a fixed point can be attained only for a weakly anisotropic system, that is $\zeta = 1$. By introducing the following couplings,

$$r_\nu = \frac{\nu_y}{\nu_x}, \qquad r_\lambda = \frac{\lambda_y}{\lambda_x}, \qquad g = \frac{\lambda_x^2 D}{32\pi^2\nu_x^3}, \tag{5.41}$$

we again obtain a renormalization flow that is independent of α_z and z_x, specifically,

$$\frac{dr_\nu}{dl} = 2r_\nu(1-\zeta)\left\{1 - g\left[\frac{3+r_\nu}{(1+r_\nu)^2} - A_{\zeta,r_\nu} + \frac{r_\lambda}{r_\nu}\left(\frac{4}{1+r_\nu} + \frac{r_\lambda}{r_\nu}\left(A_{\zeta,r_\nu} + \frac{1+3r_\nu}{(1+r_\nu)^2}\right)\right)\right]\right\}, \tag{5.42}$$

$$\frac{dr_\lambda}{dl} = 2r_\lambda(1-\zeta), \tag{5.43}$$

$$\frac{dg}{dl} = g(1-\zeta)\left\{1 - g\left[\frac{13+3r_\nu}{(1+r_\nu)^2} - 3A_{\zeta,r_\nu} + \frac{r_\lambda}{r_\nu}\left(8A_{\zeta,r_\nu} + \frac{16r_\nu+8}{(1+r_\nu)^2} + \frac{r_\lambda}{r_\nu}\left(3A_{\zeta,r_\nu} + \frac{3+5r_\nu}{(1+r_\nu)^2}\right)\right)\right]\right\}, \tag{5.44}$$

where we have introduced the auxiliary function (proportional to the one defined in [79])

$$A_{\zeta,r_\nu} = \frac{\tan^{-1}\sqrt{r_\nu} + \zeta\tan^{-1}\sqrt{1/r_\nu}}{(\zeta-1)\sqrt{r_\nu}}. \tag{5.45}$$

Without loss of generality, we can consider only the cases $r_\lambda \neq 0$ and $r_\lambda = 0$ (a zero λ_x, i.e. $r_\lambda = \infty$, is not taken into account due to the symmetry of the aKPZ equation with respect to an exchange in the spatial coordinates $x \leftrightarrow y$). For $r_\lambda \neq 0$, the fixed points of the set of Eqs. (5.42)-(5.44) must satisfy the condition $\zeta = 1$ (weak anisotropy), the only terms different from zero being those proportional to $(1-\zeta)A_{1,r_\nu} = -\pi/2\sqrt{r_\nu}$, so that the non-trivial part of the flow (5.42)-(5.44) becomes

$$\frac{dr_\nu}{dl} = g\pi\sqrt{r_\nu}\left[\left(\frac{r_\lambda}{r_\nu}\right)^2 - 1\right], \tag{5.46}$$

$$\frac{dg}{dl} = 4\pi\frac{g^2}{\sqrt{r_\nu}}\left(\frac{r_\lambda}{r_\nu} + \frac{3}{8}\left[\left(\frac{r_\lambda}{r_\nu}\right)^2 - 1\right]\right). \tag{5.47}$$

The fixed points of this set of equations need to belong to the manifold $(r_\nu^*, r_\lambda^*, g^*, \zeta) = (r_\nu, r_\lambda, 0, 1)$ with $r_\nu > 0$. Beyond the trivial solution $(0, r_\lambda, 0, 1)$ (see below), which corresponds to EW behavior, two submanifolds of $(r_\nu, r_\lambda, 0, 1)$ provide non-trivial fixed points. Indeed, by equating (5.46) to zero we have $r_\lambda = \pm r_\nu$, and fixed points $(r_\nu, \pm r_\nu, 0, 1)$, while from Eq. (5.47) we obtain the two solutions $r_\lambda = r_\nu/3, -3r_\nu$, i.e. $(r_\nu, r_\nu/3, 0, 1)$ and $(r_\nu, -3r_\nu, 0, 1)$. Nevertheless, difficulties arise when we try to compute the stability of these points. In fact, the stability matrix has three elements equal to zero for $g = 0$. Even though a more refined analysis is possible, the RG flow can be more conveniently studied through numerical integration of Eqs. (5.46) and (5.47). In Figure 5.13 we show results of such a study. If we take a bare parameter condition such that $r_\lambda < 0$ (dashed

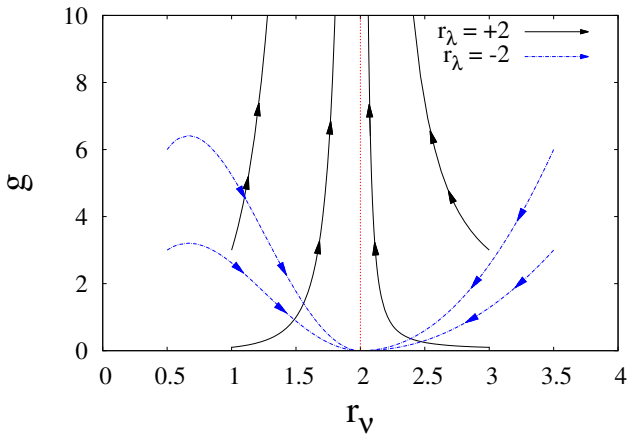

Figure 5.13: Numerical intergation of the DRG Flow for the aKPZ equation (5.37) for the case $\zeta = 1$ [Eqs. (5.46)-(5.47)]. The solid black lines correspond to the case of positive r_λ, while the dashed blue lines correspond to $r_\lambda < 0$.

blue lines), the flow is attracted by the fixed point at the origin, namely, scaling behavior is WA and linear, scaling exponents being those of the EW equation in 2+1 dimensions, namely, $\alpha_x = \alpha_y = 0$ (logarithmic) and $z_x = z_y = 2$ [5]. In contrast, for bare parameter choices such that $r_\lambda > 0$ (solid black lines in Figure 5.13) the RG flow lines move towards unbounded values for g. This is a manifestation of the occurrence of WA non-linear KPZ scaling, which is well-known not to lead to a finite fixed point in 2+1 dimensions [5]. Thus, as expected, Wolf's results are recovered through the numerical integration of the RG flow.

Once the well-known results for the aKPZ equation have been retrieved, we focus next in the case of strong anisotropy $\zeta \neq 1$. From Eq. (5.43) we immediately obtain $r_\lambda = 0$ at the fixed points, so that the DRG flow equations reduce to

$$\frac{dr_\nu}{dl} = 2r_\nu(1-\zeta)\left[1 - g\left(\frac{3+r_\nu}{(1+r_\nu)^2} - A_{\zeta,r_\nu}\right)\right], \tag{5.48}$$

$$\frac{dg}{dl} = g(1-\zeta)\left[1 - g\left(\frac{13+3r_\nu}{(1+r_\nu)^2} - 3A_{\zeta,r_\nu}\right)\right]. \tag{5.49}$$

In order to find the fixed points for Eqs. (5.48)-(5.49), we need to set their right hand sides to zero. This gives us several possible solutions, which we proceed to analyze. Considering Eq. (5.48), zeros are obtained setting $r_\nu = r_\nu^* = 0$ or $g = g_1^* = \left[(3+r_\nu)(1+r_\nu)^{-2} - A_{\zeta,r_\nu}\right]^{-1}$. However:

(a) When $r_\nu = 0$, Eq. (5.49) cannot be set to zero. This is due to the fact that one of the terms within the equation, namely,

$$g^2\left[\tan^{-1}\left(r_\nu^{1/2}\right) + \zeta\tan^{-1}\left(r_\nu^{-1/2}\right)\right] r_\nu^{-1/2}, \tag{5.50}$$

does not have a well defined limit as a two-variable function for $(r_\nu, g) \to (0,0)$.

(b) Substituting g_1^* into Eq. (5.49), we get

$$A_{\zeta,r_\nu} = \frac{5+r_\nu}{(1+r_\nu)^2}, \tag{5.51}$$

which gives us the possible values of r_ν and ζ corresponding to g_1^*. However, it is not difficult to see that Eq. (5.51) leads to $g_1^* = -(1+r_\nu)^2/2 < 0$, which is not a physically acceptable value.

Hence, the formal zeros of Eq. (5.48) provided by $r_\nu = 0$ and $g = g_1^*$ are both to be discarded. On the other hand, if we start out with Eq. (5.49), we obtain zeros for $g = 0$ and $g = g_2^* = \left[(13+3r_\nu)(1+r_\nu)^{-2} - 3A_{\zeta,r_\nu}\right]^{-1}$. Then:

(a) By substituting $g = 0$ into Eq. (5.48) we get

$$\frac{dr_\nu}{dl} = 2r_\nu(1-\zeta), \tag{5.52}$$

which implies that the line $g = 0$, $r_\nu > 0$ is a separatrix for the RG flow. One could then argue that the point $g = 0$, $r_\nu = 0$ is indeed a fixed point, but strictly speaking this is not true due to the ill-definiteness of the flow at the origin, as discussed above.

(b) If we substitute $g = g_2^*$ into Eq. (5.48), we again obtain Eq. (5.51), and therefore no physically acceptable fixed points.

A final possibility to find a meaningful fixed point of the flow is to set $\zeta = 1$, which would correspond to isotropic asymptotic behavior. Eqs. (5.48)-(5.49) then become

$$\frac{dr_\nu}{dl} = -\pi g\sqrt{r_\nu}, \qquad \frac{dg}{dl} = -\frac{3\pi}{2}\frac{g^2}{\sqrt{r_\nu}}. \tag{5.53}$$

As it turns out, these equations can be exactly solved, giving

$$r_\nu(l) = \frac{r_0^{3/2}}{\sqrt{r_0}+\pi g_0 l}, \qquad g(l) = \frac{g_0 r_0^{3/4}}{(\sqrt{r_0}+\pi g_0 l)^{3/2}}, \tag{5.54}$$

where $r_0 = r_\nu(0)$ and $g_0 = g(0)$ are the initial conditions (bare parameter values). This exact solution tells us that the flow moves towards the point $r_\nu = 0$, $g = 0$, which is only reached in infinite "time", i.e. for $l \to \infty$. Moreover, Eqs. (5.54) can be simply restated as

$$g(l) = g_0 \left[\frac{r_\nu(l)}{r_0}\right]^{3/2}, \tag{5.55}$$

implying that g vanishes faster than r_ν in this limit.

The latter result actually allows us to rationalize the behavior of the RG flow, Eqs. (5.42)-(5.44), for the anisotropic condition $\zeta \neq 1$, $r_\lambda = 0$, as obtained through numerical integration of the corresponding Eqs. (5.48)-(5.49). In Figure 5.14 we

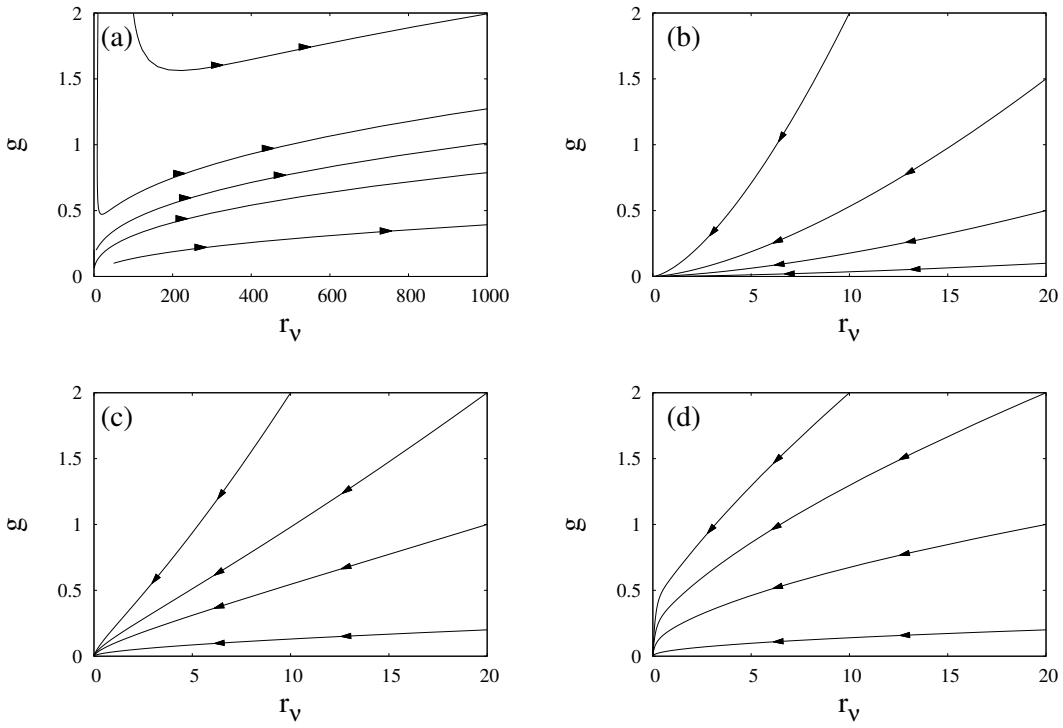

Figure 5.14: Numerical integration of the DRG flow for the aKPZ equation (5.37) for the case $r_\lambda = 0$ [Eqs. (5.48)-(5.49)], and different values of the anisotropy exponent, (a) $\zeta = 1/2$, (b) $\zeta = 1$, (c) $\zeta = 3/2$, and (d) $\zeta = 5$.

show such type of results for different values of ζ. Obviously, $\zeta = 1$ [see Figure 5.14(b)] constitutes a natural reference case for which, as we have just seen, the RG flow is both well-defined at, and attracted by, the origin, where scaling behavior is isotropic, EW-type. Even though this point cannot be reached by the RG flow at finite l for other values of ζ, for which no finite fixed points otherwise exist, it still plays an important role. Thus, as can be seen in Figure 5.14(a), for $\zeta < 1$ the origin seems to repel the flow lines, which evolve towards arbitrarily large values of (r_ν, g). This behavior may be an artifact of the approximations made in the DRG analysis, as suggested by further results. Namely, $\zeta > 1$ is seen in Figure 5.14(c),(d) to reverse the stability of the origin. Now it attracts the RG trajectories, which flow into it for infinite l, indicating asymptotic isotropic EW behavior. We have checked that it is the latter behavior, rather than the unbounded growth of r_ν and g obtained for $\zeta < 1$, which seems to actually occur for the aKPZ equation under the present type of conditions. Specifically, we have performed direct numerical simulations of the aKPZ equation, Eq. (5.37), for a case in which one of the nonlinearities is "suppressed", $\lambda_y = 0$. A surface morphology obtained for long simulation times is presented in Figure 5.15, while the results for the power spectral densities are shown in Figure 5.16. Actually, The same numeri-

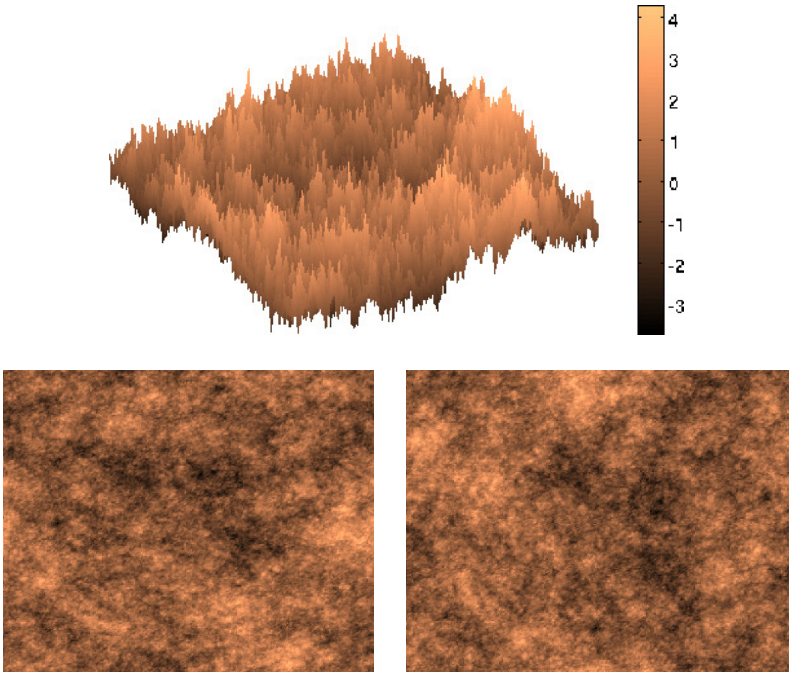

Figure 5.15: Morphology generated by numerical integration of Eq. (5.37) for parameters $\nu_x = \nu_y = 1$, $D = 1$, $\lambda_x = 3$, $\lambda_y = 0$, $L = 256$, $\Delta x = 1$, and $\Delta t = 0.01$. Top panel: three-dimensional view. Bottom panels: top views. The right panel has been obtained after rotating the left panel by $90°$.

cal simulation scheme has also allowed us to also check for the aKPZ equation (not shown), the change of universality class as a function of the relative signs of the nonlinearities when both are non-zero. As can be seen in the figures, the behavior of correlation functions is well-reproduced by isotropic EW exponents, namely, $\alpha = 0$ (logarithmic) and $z = 2$. This is consistent with the effective g coupling renormalizing to zero much faster than r_ν, so that at large length scales the system is effectively behaving as an anisotropic EW equation, for which the scaling is well-known to be of the WA type [160].

5.3 Conclusions

The previous sections have allowed us to assess the non-genericity of strong anisotropy for surfaces displaying generic scale invariance and non-linear effects. Thus, for non-conserved dynamics, strong anisotropy simply does not occur, even for special conditions under which only one of the nonlinearities is suppressed. On the other hand, for systems with conserved dynamics, strong anisotropy can be obtained, and even whole families of equations can be formulated which display this property, such as Eq. (5.13). However, both in the presence and in the absence of

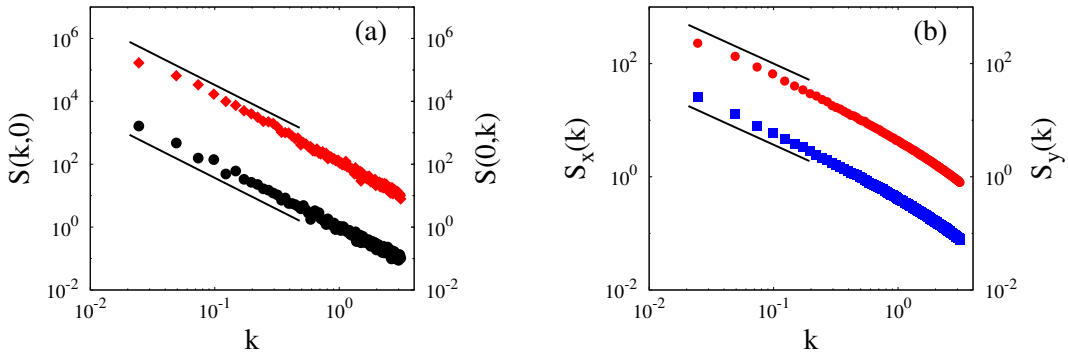

Figure 5.16: Numerical integrations of the aKPZ equation, Eq. (5.37), for parameters $\nu_x = \nu_y = 1$, $D = 1$, $\lambda_x = 3$, $\lambda_y = 0$, $L = 256$, $\Delta x = 1$, and $\Delta t = 0.01$. (a) One-dimensional projections $S(k, 0)$ (black circles, left axis) and $S(0, k)$ (red diamonds, right axis), averaged over 50 different noise realizations. The solid black lines are guides for the eye with slope -2. (b) PSD of one-dimensional cuts along the x direction, $S_x(k)$ (blue squares, left axis), and along the y direction, $S_y(k)$ (red circles, right axis). The solid black lines are guides to the eye with slope -1. For visualization purposes, the values of $S(0, k)$ and $S_y(k)$ have been artificially offset vertically.

the shift symmetry $h \to h + \text{const.}$, this seems only possible for "incomplete" equations in which only one of the nonlinearities is suppressed.

Overall for the type of systems that we have studied here and in Chapter 4, one can conclude that, if the part of the interface equation which is most relevant for the scaling behavior (e.g. non-linear vs linear terms, or surface tension vs surface diffusion, etc.) can be rewritten in an isotropic form using coordinate transformations, such as rotations or a mere rescaling (in which rescaling factors are *positive*), then the system will display *weak anisotropy*. Actually, this is a sufficient condition for weak anisotropy, but is not necessary: One also obtains weak anisotropy for example in the anisotropic KPZ equation when the coefficients of the nonlinearities have different signs. Note that a rescaling in such a situation still preserves the difference in sign between the two nonlinear terms.

But in order to obtain strong anisotropy, one further needs conserved dynamics, combined with special parameter cancellations such that, e.g. $\lambda_x \neq 0$ while $\lambda_y = 0$. In general, conditions of this type depend critically on details of the dynamics that is being described, acting as special constraints, and are in this sense non-generic in parameter space. Hence, they cannot be obtained from simple-minded derivations of the equations of motion based on symmetries and conservation laws.

Naturally, there are formulations of the interface equation, such as the original one by Hwa and Kardar, in which this type of special conditions becomes natural, as imposed by the geometry of the external driving fields and/or relaxation mechanisms (e.g. the direction of sand transport, etc.). Beyond driven diffusive systems or models of self-organized criticality, such type of constraints also appear for in-

stance in solidification fronts [163], the dynamics of localized structures [164] in plasmas [165] and in fluid propagation [166], the evolution of driven flux lines in superconductors [167], or the effect of shear on interface fluctuations [168]. Still, such type of constraints leading to "incomplete" equations are not to be expected in many other systems. Consider for instance epitaxial growth systems [79, 81] in which lattice anisotropies are expected to lead to different values of, say, λ_x and λ_y. In general, the physics is limited to inducing different values in the equation parameters, but not necessarily to exact cancellations of specific ones.

Additionally, we have to note an implicit assumption that we have made in our analysis. This is the fact that the interface equation is morphologically stable, in the sense that the deterministic terms tend to smooth out surface inhomogeneities. However, many natural contexts for the occurrence of spatial anisotropies are actually systems in which patterns emerge (convection rolls, ripples under ion beam sputtering, etc.), some of which correspond to references just quoted [81,163–166]. Formation of this type of structures requires morphological instabilities to occur, which suggests pattern-forming systems as a potential context for non-trivial strongly anisotropic behavior. Note, pattern-forming behavior (i.e. the emergence of a spatial structure from an homogeneous system) is to some extent the opposite interfacial property to generic scale invariance, since the former is characterized by the predominance of a characteristic length scale (namely, the pattern periodicity), which is absent in the latter. Nevertheless, studies are already available [105,106] in which a highly non-trivial interplay occurs between instability and anisotropy, and in which the difference between scale invariance (kinetic roughening, or surface generic scale invariance) and its opposite property (pattern formation) is a matter of space and time scales [32, 128]. The anisotropic Kuramoto-Sivashinsky equation [81, 105, 106, 134] is a natural example, albeit itself being possibly confined to weak anisotropy. Thus, we believe an interesting avenue for further studies of the occurrence of strong anisotropy in generic scale invariant systems is related with anisotropic models of pattern formation that are compatible with kinetic roughening at the appropriate scales.

6

STRONG ANISOTROPY IN EXPERIMENTAL SYSTEMS

In this chapter we show that the scaling analysis presented in Chapter 4 does provide a consistent description of the anisotropic kinetic roughening properties of actual experimental surfaces. We present an analysis of experimental data produced through erosion of silicon targets by Ion Beam Sputtering at low to intermediate ion energies [72, 73]. After a brief historical review of the most relevant experimental results and theoretical modeling in this context, we focus our attention on two experimental sets, one that is morphologically stable and a second one which is unstable. We show that in both cases strong anisotropy ensues, verifying the anisotropic scaling Ansatz proposed in Chapter 4.

6.1 Ion Beam Sputtering

In 1962, Navez *et al.* [169] showed that, by bombarding a glass sample with a beam of ionized air, new surface morphologies could be produced depending mainly on the incidence angle θ of the beam onto the substrate. More precisely, wavelike structures (ripples) were found to appear, the distance between them setting a characteristic length scale for the system. For incidence angles close to $\theta = 0^\circ$ the ripples aligned perpendicular to the ion beam direction, while they became parallel to it when the beam reached the surface at grazing incidence, i.e. $\theta \approx 90^\circ$. Some of the morphologies obtained by Navez *et al.* are presented in Figure 6.1. Since the first experimental observations it was found that, whenever a substrate was irradiated by ions with energy around 1 KeV, part of the material was ejected from the surface. The incident ions lose energy due to collisions with the nuclei and electrons of the atoms in the substrate, in such a way that superficial atoms are ejected (sputtered) whenever they receive enough energy to break the bonds with

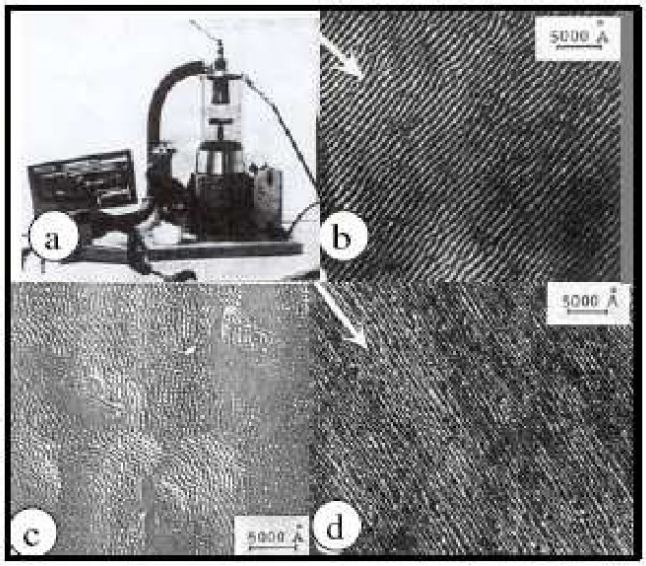

Figure 6.1: Experiment by Navez, Sella, and Chaperot [169] on glass. (a) Experimental setup. The sample is bombarded with ionized air at 4 keV for six hours. (b) Morphology after bombarding with incidence angle $\theta = 30^\circ$. The arrow indicates the projection of the beam onto the substrate. The ensuing ripple structure is perpendicular to it. (c) Morphology at normal incidence. (d) Morphology at $\theta = 80^\circ$. The ripples are now parallel to the projection of the ion beam direction. The picture has been taken from [124].

their neighbors.

This type of systems have recently gained considerable interest, both experimentally [72] and theoretically [73], the main reason being the promising applicability of the (nano) pattern produced to a wide variety of technological applications, such as microelectronic device fabrication [170] or magnetic data storage [171]. Indeed, nowadays this technique constitutes a basic tool in surface analysis, depth profiling, sputter cleaning, micromachining and sputter deposition. Perhaps the largest community of users of this technique is in the thin film and semiconductor fabrication areas, sputter erosion being routinely used for etching patterns that are important in the production of integrated circuits and device packaging. However, while the associated pattern formation holds great promise for low-cost and large-area applications, its specific use for the design of new materials and bottom-up manufacturing processes is at present hampered by our incomplete knowledge of the underlying mechanisms of self-organization. Thus, in order to understand these kinds of systems, it is of paramount importance to develop theoretical models, as well as to improve and increase the amount of experimental data available.

Although a comprehensive review of experimental data and theoretical models for IBS systems is beyond the scope of this thesis, it is useful to summarize some

of the most important results in this field. To this end, we will henceforth focus on experiments performed on amorphous targets, like glass, or on materials that become amorphous upon ion bombardment, like monocrystaline semiconductors such as silicon [172, 173]. In principle sputter erosion may have different effects on the surface depending on many factors, such as incident ion energy, mass of the ion, angle of incidence, substrate temperature and material composition. However, experiments have assessed some sort of "universal" features for the patterns that develop under fairly generic experimental conditions [73].

One of the most interesting aspects of systems that undergo IBS is the dependence of the type of pattern with the angle of incidence and the energy of the ions. Historically, a picture similar to the one presented by Navez was believed to be quite generic; these experiments, as mentioned above, found an isotropic pattern (dots or holes) at normal incidence, followed by ripples oriented perpendicular to the projection of the ion beam onto the substrate when $\theta < \theta^*$. Then, for θ greater than the "critical" value θ^*, a ripple structure also formed, but this time it was oriented parallel to the ion beam projection.

It was only 40 years later, with the work by Ozaydin *et al.* [174], that key role in the formation of the pattern was hypothesized to be played by accidental codeposition of metallic *impurities* onto the substrate. Interesting consequences have been derived from this fact, as it seems that the concentration and type of impurities can be tuned in order to control the type of morphology (holes, dots, ripples) that develops [175–177]. Such an observation also called for an improvement of the experimental setups in order to control the contamination levels, and for a reexamination of previous experimental results, that were presumably obtained for contaminated samples. Since then, experiments have been performed so as to prevent such effects [177, 178], and the picture emerging from them is quite different. Specifically, it has been shown that *no* pattern forms below a critical angle of incidence θ_c. For $\theta > \theta_c$, a ripple structure forms, which is oriented perpendicular to the ion beam projection, while at grazing incidence (typically $\theta > 80^\circ$) the ripple structure rotates by 90°. All of this seems to be quite independent on the energy of the ions (although this point has also been recently challenged in the case of Germanium substrates [179]) and quite general, at least for Si and similar semiconductor targets. However, the actual value of θ_c seems to depend on the type of ions chosen. Also depending on this, it may be possible to observe a rough surface also at grazing incidence instead of a rotation of the ripples [180]. Naturally, nowadays a lot of effort is being put into a better characterization of the morphologies that emerge in these systems, and into developing experimental setups and *in-situ* measuring that prevent any contamination of the sample, as well as to control the exact amount of impurities that are deposited onto the substrate during erosion.

In view of the huge and continuing amount of experimental data available, the theoretical modeling of IBS surface nanopatterning also appears to be a field in constant evolution. Since the formation of a pattern is quite a slow process ($\simeq 1$ s) compared to processes associated with collision cascades or with surface diffu-

sion ($\simeq$ 1 ps), this phenomenon remains beyond reach for microscopic approaches like Molecular Dynamics or kinetic Monte Carlo [22, 181]. On the other hand, descriptions through continuum equations such as the ones introduced in the previous Chapters appear as a natural choice in order to account for the main properties of these systems. The universality of the phenomena, in the sense of their occurrence for a wide choice of experimental conditions, adds credit to applicability of these type of models. Historically, the work that paved the way for further continuum modeling of IBS surface nanopatterns is due to Bradley and Harper [76]. There, it is assumed that the local surface velocity is proportional to the total deposited energy due to ion bombardment, and that such energy follows a Gaussian distribution, according to Sigmund's theory of sputtering [182]. It is not difficult to see, by geometrical considerations, that the latter assumption causes an instability due to different erosion rates for surface troughs and crests, the former being eroded faster than the latter. Thus, the small slope approximation leads to the following linear equation for the evolution of the height of the surface,

$$\partial_t h = -\nu_x \partial_x^2 h - \nu_y \partial_y^2 h - \mathcal{K} \nabla^4 h, \tag{6.1}$$

where $\nu_{x,y}$ are positive constants that depend on phenomenological parameters such as flux, average ion energy, average penetration depth, etc. , while the last term on the r.h.s. accounts for *thermal* surface diffusion, as described by Mullins [183]. The negative sign in front of the second derivatives gives rise to the morphological instability mentioned above, in such a way that dots form for normal incidence and ripples form for any $\theta > 0$. This equation also predicts correctly the rotation of the ripples that was found in the first IBS experiments.

It is however clear that Eq. (6.1) cannot be a complete description of the process, since it predicts exponential blow-up of the surface height. An improvement to this model can be achieved by introducing nonlinear effects. Since Eq. (6.1) was obtained by using a small slope expansion for h, it is sufficient to go to one further order in such expansion [129] in order to obtain

$$\partial_t h = -\nu \nabla^2 h - \mathcal{K} \nabla^4 h + \lambda (\nabla h)^2 + \eta, \tag{6.2}$$

where also a noise term has been added to account for fluctuations in the ion beam flux, and the surface diffusion constant, $\mathcal{K}$, depends both on the temperature and the ion flux. Equation (6.2) is the noisy Kuramoto-Sivashinsky equation studied in Chapter 3. This equation displays a morphological instability in which a preferred wavelength is selected, followed by a kinetic roughening regime which we have shown to be in the KPZ universality class [32]. Although a transition from ordered patterns to kinetic roughening is quite common in IBS experiments, an unambiguous assessment of the KPZ exponents in this type of systems has not been obtained so far. Moreover, the generically expected and technologically appealing case in which well ordered dots or ripples form remains far from the description by the KS equation proper. An improved ordering of surface structures is obtained by going to a higher nonlinear order in the Bradley-Harper type expansion [184], obtaining

$$\partial_t h = -\nu \nabla^2 h - \mathcal{K} \nabla^4 h + \lambda_1 (\nabla h)^2 + \lambda_2 \nabla^2 (\nabla h)^2, \tag{6.3}$$

which indeed produces well ordered structures but for which a cancellation mode exists [see Section 1.3.4] that is linearly unstable. This means that the surface amplitude blows up exponentially, as a result of which the continuum description breaks down.

Interestingly, it is possible to derive a similar equation starting from a two-field "hydrodynamic" model. The idea for its derivation comes from the important observation that a thin amorphous layer on top of the crystalline bulk forms under irradiation [172]. This allows one to construct a model where the surface height h is coupled to the density R of species, that are subject to transport *within* the amorphous layer [185, 186],

$$\partial_t h = -\Gamma_{ex} + \Gamma_{ad}, \tag{6.4}$$

$$\partial_t R = (1-\phi)\Gamma_{ex} - \Gamma_{ad} + D\nabla^2 R. \tag{6.5}$$

Here, Γ_{ex} (Γ_{ad}) are rates of excavation (addition) from (to) the crystalline bulk that are derived from constitutive laws, and ϕ controls the amount of local redeposition. The approximation of slow evolution for the field R leads to the following effective equation for h [185],

$$\partial_t h = -\nu\nabla^2 h - \mathcal{K}\nabla^4 h + \lambda_1(\nabla h)^2 - \lambda_2\nabla^2(\nabla h)^2, \tag{6.6}$$

where the sign of the last term on the right hand side frees Eq. (6.6) from cancellation modes. Equation (6.6) leads to a short range order of the nanodots and intermediate coarsening properties, and it compares quite favorably to experiments on Si targets [187]. Equation (6.6) also displays kinetic roughening properties in its asymptotic state, probably also in the KPZ universality class, although both numerical (due to the presence of long crossovers) and analytical confirmations are missing at the moment.

An important aspect of IBS systems that we have not mentioned so far, is the fact that, for incidence angles greater than zero, they are inherently anisotropic. In fact, it is natural to think that the projection of the ion beam onto the substrate and the direction perpendicular to it have different properties concerning, for instance, the transport of material. In order to describe this, anisotropic versions of the KPZ and nKS equations have been proposed. These models present a richer dynamical behavior of the morphology. An anisotropic version of Eq. (6.6) is also available [186], that reads

$$\begin{aligned}\partial_t h = \gamma\partial_x h + \sum_{i=x,y}\left[-\nu_i\partial_i^2 h + \lambda_{1i}(\partial_i h)^2 + \Omega_i\partial_i^2\partial_x h + \xi_i(\partial_x h)(\partial_i^2 h)\right] \\ + \sum_{i,j=x,y}\left\{-\mathcal{K}_{ij}\partial_i^2\partial_j^2 h - \lambda_{2ij}\partial_i^2(\partial_j h)^2\right],\end{aligned} \tag{6.7}$$

where, again, coefficients are functions of physical parameters. This equation also leads to non-uniform ripple transport and coarsening, and to a good qualitative

comparison with some experiments [22]. It is also supposed to display kinetic roughening, although a comprehensive study has not been provided yet.

After the experimental works of Madi *et al.* [178] that established the absence of pattern formation for small incidence angle, it is clear that BH-type expansions cannot account for such behavior, unless additional relaxation mechanism are invoked [186]. Recently, another approach has been proposed, which focuses on the dynamics of the amorphous layer and describes it as a viscous flow using approximations of the Navier-Stokes equation [30]. This hydrodynamical model seems promising in describing the transition from flat to patterned surface depending on the incidence angle θ. As for the two-field model, it is also possible to formulate an equation for the evolution of the surface height, in the limit of small thickness of the amorphous layer.

In the remainder of this chapter, we present experimental data from ion beam sputtering that, according to our analysis, not only display kinetic roughening, but also strong anisotropy. Although this fact needs a deeper validation and deserves to be studied in more detail, we believe that the emergence of strong anisotropy in systems of this kind calls for the development of alternative descriptions. This is due to the fact that the most studied continuous models of ion beam erosion do not display strong anisotropy, their dynamics being non-conserved (see Chapter 4). However, the hydrodynamic model mentioned above seems promising in this direction.

6.2 Experiments

We consider two different sets of experimental data; the first one corresponds to a *clean* experiment, meaning that any contamination source has been carefully avoided during the sputtering process [180]. By working at grazing incidence, the authors obtained a rough interface instead of the expected ripple structure aligned with the projection of the ion beam onto the substrate. We will show that such a rough structure actually displays strong anisotropy.

The second set of experimental data was obtained with simultaneous (intentional) codeposition of metallic impurities onto the substrate, giving rise to an instability that produces ripple-like structures [188]. In these experiments the type of ion is different and the angle of incidence is lower than for the stable case. Also in this case, it is possible to find a range of scales within which scale invariance (i.e. kinetic roughening) occurs. We will show that the scaling exponents are different if measured along different directions, thus confirming the presence of strong anisotropy also in this case.

In each section below, the analysis of the experimental data and the verification of the scaling Ansatz presented in Chapter 4, has been carried out following the next steps:

(i) For each experimental condition, the irradiation dose guarantees that the surface has reached a steady state (as reflected in the time independence of

the correlation functions measured).

(ii) A single sample is scanned (by Scanneling Tunneling Microscopy or Atomic Force Microscopy) using different resolutions, and over regions of different sizes, which we will call windows. These scans provide us with different images (matrices) of the same sample.

(iii) For each matrix, we compute two quantities: the two- dimensional Power Spectral Density $S(k_x, k_y)$, and the PSDs of one-dimensional cuts of the surface, $S_{x,y}(k_{x,y})$. The 2D PSD is then averaged over all the images we have. For the 1D PSDs, we also perform averages over all the lines and columns of each matrix, respectively.

(iv) Next, we consider the projections $S(k_x, 0)$ and $S(0, k_y)$ of the two-dimensional PSD onto the k_x and k_y axes. According to our Ansatz, these profiles should scale as power laws of $k_{x,y}$ with exponents $2\tilde{\alpha}_x$ and $2\tilde{\alpha}_y$, respectively, that are estimated by fits over appropriate scaling ranges.

(v) Using formulas (4.17) and (4.18), we compute real-space roughness exponents $\tilde{\alpha}_{x,y}$ and, through Eq. (4.12) we predict the scaling behavior for the one-dimensional PSDs.

(vi) Finally, we verify if the one-dimensional PSDs indeed scale in a form that is consistent with the two-dimensional PSD, as required by our scaling theory.

6.3 Morphologically stable case

6.3.1 Experimental setup

For the morphologically stable condition that we will study, the experiments have been carried out by the group in Reference [180] at "Universität zu Köln", Germany. The experiments were conducted in a scanning tunneling microscopy (STM) apparatus with a base pressure below 1×10^{-10} mbar [180]. The system is equipped with a differentially pumped fine focus ion source. The fine focus ion beam exposed only the sample and thus impurity effects were avoided. A Si(100) sample was irradiated at room temperature with 2 keV Kr^+ ions at an ion incidence angle $\theta = 81^\circ$ with the surface normal. The reproducibility of the angle is better than 0.5°, the error of the angle's absolute value being 1°. The sample was exposed to an ion fluence of 2×10^{22} ions m^{-2}, with an average ion flux of 3×10^{17} ions m^{-2} s^{-1}. The flux is specified here for the sample plane. It was controlled by a Faraday cup movable to the sample position. After ion exposure, the samples were imaged *in situ* by STM. A representative image is shown in Figure 6.2.

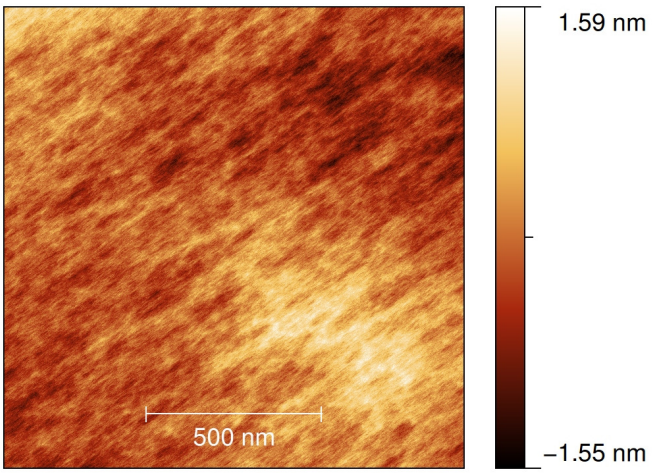

Figure 6.2: STM top view of the surface morphology for the contamination-free sample. Image size is 1.3×1.3 μm^2.

6.3.2 Results

Superficial naked-eye inspection of Figure 6.2 already suggests the existence of a long-wave corrugation which does not seem particularly ordered, but does have a preferred orientation that coincides with the projection of the ion-beam onto the substrate plane. Actually, this is taken into account in the analysis of the topography. Specifically, the ion beam comes from the lower left corner with an angle of 35° to the x axis. After rotating the images so that the ion-beam projection coincides with the x (horizontal) axis, rectangular regions have been cut out from the original figures and provide the data for our analysis, as detailed in Table 6.1 together with size and resolution of each sample window considered.

Projections of the two dimensional PSD along the k_x and k_y axes are presented in the left panel of Figure 6.3. These plots have been obtained after averaging the $S(\mathbf{k})$ functions obtained for different window sizes, to improve statistics. Note that power-law behavior takes place for length scales that are larger than approximately 6 nm, while for shorter distances (larger corresponding values of k) different behavior is obtained. Thus, we will restrict our analysis in this case to the small k range, thus indeed facing the properties of the long-wavelength corrugation just mentioned. By performing a fit over the small wave-vector region in the left panel of Figure 6.3, we estimate the values of the momentum-space roughness exponents to be

$$\begin{aligned} 2\tilde{\alpha}_x &= 2.66 \pm 0.02, \\ 2\tilde{\alpha}_y &= 1.80 \pm 0.02, \\ \zeta &= 1.48 \pm 0.02, \end{aligned} \tag{6.8}$$

where error bars come from statistical uncertainty in the fits. Hence, strong an-

Index	Before (nm^2)	After (nm^2)	Δx (nm/pixel)
I	1800×1600	1757.2×632.2	1.8595
II	1200×1190	1115.6×500.1	1.2410
III	600×600	557.36×250.88	0.6179
IV	301×301	279.71×125.86	0.3100
V	150×150	139.16×62.85	0.1548
VI	70×70	65.04×29.27	0.0774
VII	40×40	37.15×16.72	0.0391
VIII	20×20	18.39×8.28	0.0193

Table 6.1: Original size of the window (second column), size of the rectangular region extracted from the rotated image (third column), and resolution used (fourth column), for the morphologically stable system.

isotropy occurs, since $\zeta \neq 1$. The corresponding exponents characterizing the power-law decays of the 1D PSD functions should be

$$2\alpha_x + 1 = 1.18 \pm 0.02, \tag{6.9}$$
$$2\alpha_y + 1 = 1.12 \pm 0.02. \tag{6.10}$$

Using these values in Eqs. (4.13), the scaling behavior of $S_y(k_y)$ extracted from our Ansatz agrees well with experimental data as shown in the right panel of Figure 6.3, while such an agreement is not reached in the case of $S_x(k_x)$. In order to understand this disagreement, note first that in the present system both real-space exponents are quite close to being effectively zero, in view of the statistical fluctuations in the data. In the context of critical phenomena and kinetic roughening this would be associated with logarithmic (rather than proper power-law) behavior for the real space correlation functions [5, 42]. As we have seen in Chapter 4, such small values of the roughness exponents may lead to slow convergence issues for integrated quantities like the one-dimensional PSDs, thus hindering a clear-cut scaling for such observables.

On the other hand, as we can see in the right panel of Figure 6.3, the scaling behavior predicted by the simple power law $S_x(k_x) \sim k_x^{-(2\alpha_x+1)}$ has not been reached by the experimental data, especially for the smallest wave-vector values. This inconsistency seems reminescent of the slow convergence issue we found in Chapter 4 for the Hwa-Kardar equation. There, we have seen that for small numerical values of the exponents $\tilde{\alpha}_{x,y}$, integrals such as Eqs. (4.10)-(4.11) converge slowly to their asymptotic properties, in the sense that non-negligible corrections occur to the leading terms $k^{-(2\alpha_{x,y}+1)}$ in a small $k_{x,y}$ expansion [see Eqs. (4.55)-(4.56)].

As seen in Chapter 4, it is possible to investigate this issue by introducing a Gaussian approximation to the system, i.e. a continuum model with the same scaling exponents as measured in (6.8), and analyze for it the behavior of the 1D PSD

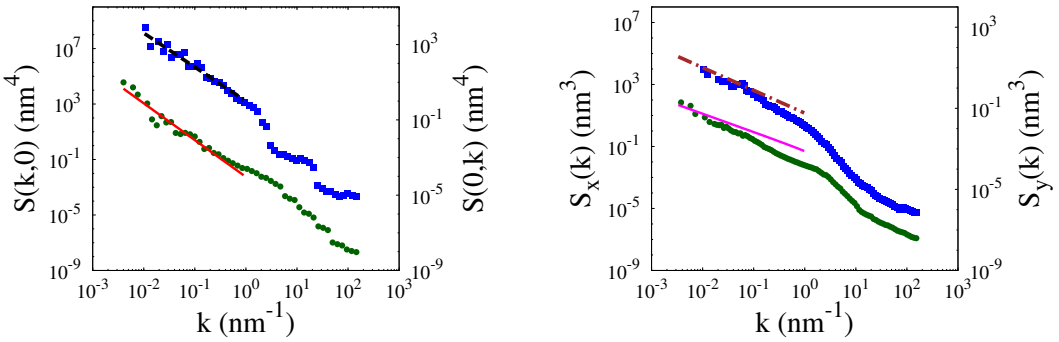

Figure 6.3: Experimental results for the contamination free sample, averaged over eight windows. Left panel: One-dimensional projections $S(k,0)$ (green circles, left axis) and $S(0,k)$ (blue squares, right axis) of the two-dimensional PSD. The solid red and dashed black lines are fits obtained by least squares, the resulting exponents being $2\tilde{\alpha}_x \simeq 2.66$ and $2\tilde{\alpha}_y \simeq 1.80$. These lines correspond to the exact stationary behavior of Eq. (6.11) for $\nu_x = 178$, $\nu_y = 0.99$, and $D = 1$. Right panel: PSD of one-dimensional cuts $S_x(k)$ (green circles, left axis) and $S_y(k)$ (blue squares, right axis). The solid magenta line and the dot-dashed brown line correspond to Eq. (4.13) with values given by Eq. (6.10), and are *not* fits to the data. Rather, they have been computed using Eqs. (4.10) and (4.11) for Eq. (6.11) with $\nu_x = 178$, $\nu_y = 0.99$, and $D = 1$. The raw data are given in Appendix B.

functions. Thus, as a proxy for the scaling behavior of the present experimental data, the resulting equation for the Fourier components of the height field, $h_{\mathbf{k}}(t)$, takes the form

$$\partial_t h_{\mathbf{k}} = -(\nu_x |k_x|^{2.66} + \nu_y |k_y|^{1.80}) h_{\mathbf{k}} + \eta_{\mathbf{k}}. \tag{6.11}$$

Note that (6.11) is again a particular case of Eq. (4.35) that we have introduced in Chapter 4, and therefore it follows the scaling Ansatz (4.6) *exactly*, with exponents given by (6.8). Actually, the power-law fits in the left panel of Figure 6.3 are the exact stationary behavior of Eq. (6.11), provided we use $\nu_x = 178$, $\nu_y = 0.99$, and $D = 1$, with nm and s for space and time units, respectively. Once this is the case, the behavior of the 1D PSD functions for Eq. (6.11) follows without the possibility of further fits, and is shown in the right panel of Figure 6.3. As we see, there is good quantitative agreement with experimental data for $S_y(k_y)$, while in the case of $S_x(k_x)$ the experimental data overshoot the theoretical curve at small k_x values. The resemblance of this behavior to the one we presented in Chapter 4 for the Hwa-Kardar equation and its Gaussian approximation, makes us believe that the true asymptotic behavior of this system is reached at larger length scales than the ones which have been experimentally assessed. Note, we are not claiming that Eq. (6.11) provides the description of the full dynamics of the experimental system. They do both share the same asymptotic behavior, which is possible even if the

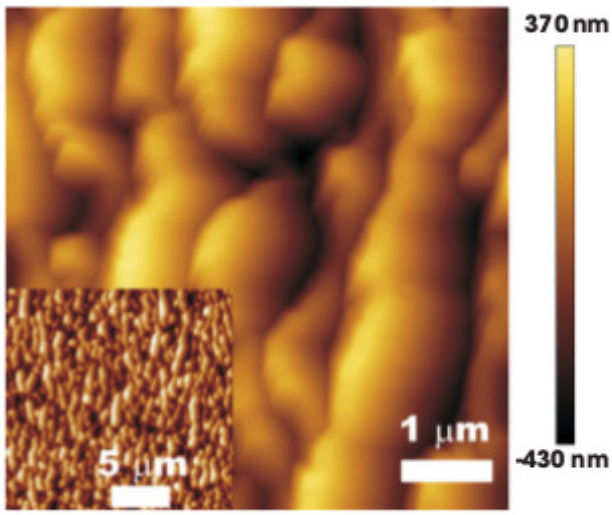

Figure 6.4: AFM top view of the morphology of Si(100) irradiated for 8 h with 40 keV Ar^+ ions and concurrent Fe codeposition. Image size is 6×6 μm^2.

"true" dynamical equation for this system is a different, even nonlinear, one [160].

An interesting physical conclusion for the modeling of IBS problems stems from the fact that Eq. (6.11) preserves the average value of the height field along the system evolution, since $\langle h_{\mathbf{k}=\mathbf{0}}(t)\rangle = \langle \bar{h}(t)\rangle = \text{const}$. This suggests in particular that erosive mechanisms [72, 73], which do not preserve this quantity, are negligible under the present experimental conditions. This conclusion agrees with recent experimental results for similar systems, see, e.g., Reference [178] and references therein.

6.4 Morphologically unstable case

6.4.1 Experimental setup

The irradiation experiments in the morphologically unstable case have been performed by the team of Reference [188], at "Instituto de Ciencia de Materiales" in Madrid, Spain in collaboration with "Instituto Tecnológico e Nuclear" in Lisbon, Portugal and the "Institute of Ion Beam Physics and Materials Research" in Dresden, Germany.

The experiments were performed with a 40 keV Ar^+ beam extracted from a Danfysik 1090 ion implanter with a base pressure of 5×10^{-6} mbar. The ions impinged on the single-crystal Si(100) targets (1×1 cm^2) at $60° \pm 5°$ with respect to the surface normal with a current density of $18\,\mu$A cm^{-2} in the sample plane. A steel plate (1.5 mm high) placed adjacent to the Si target acted simultaneously as

Index	Linear Size (μm)	Δx (μm)
I	160	0.3125
II	160	0.3125
III	100	0.1953
IV	100	0.1953
V	60	0.1172
VI	60	0.1172
VII	20	0.0391

Table 6.2: Linear size and resolution used for each sample window in the morphologically unstable system.

Fe source and sample holder. To obtain homogeneous irradiation, the focused beam was scanned with a magnetic $x - y$ sweeping system in such way that both the Si surface and the steel target were bombarded. The irradiation time was eight hours. The resulting surface morphology was imaged *ex-situ* by AFM operating in the dynamic mode with Nanoscope IIIa equipment (Veeco©). Silicon cantilevers, with a nominal radius r of 8nm and opening angle smaller than 52°, were employed. A representative topography is shown in Figure 6.4. The projection of the ion beam coincides with the x (horizontal) axis in the Figure.

6.4.2 Results

Although from the physical point of view the present system is perhaps more complex (due to the not well understood role of impurities in the nanopatterning process), the occurrence of strong anisotropy seems in principle clear cut. We employ the same procedure as above, with windows sizes and resolution given by Table 6.2 After computing the two-dimensional PSD, we show its two projections $S(k_x, 0)$ and $S(0, k_y)$ in the left panel of Figure 6.5. Both plots appearing in the latter figure immediately suggest the existence of a characteristic length scale around 800–900 nm, above which no proper scaling takes place. We associate this scale with the wavelength of the pattern that develops under these experimental conditions. Nevertheless, at smaller scales (larger k values) power-law behavior appears that is different in the k_x and k_y directions, as described by exponent values

$$2\tilde{\alpha}_x = 5.81 \pm 0.06, \tag{6.12}$$

$$2\tilde{\alpha}_y = 3.74 \pm 0.2, \tag{6.13}$$

$$\zeta = 1.55 \pm 0.01, \tag{6.14}$$

which are obtained by least squares. Note that $\zeta \neq 1$. Thus, according to Eqs. (4.12), exponents characterizing the power-law decay of the 1D PSD functions should be

$$2\alpha_x + 1 = 4.26 \pm 0.14, \qquad 2\alpha_y + 1 = 3.10 \pm 0.2. \tag{6.15}$$

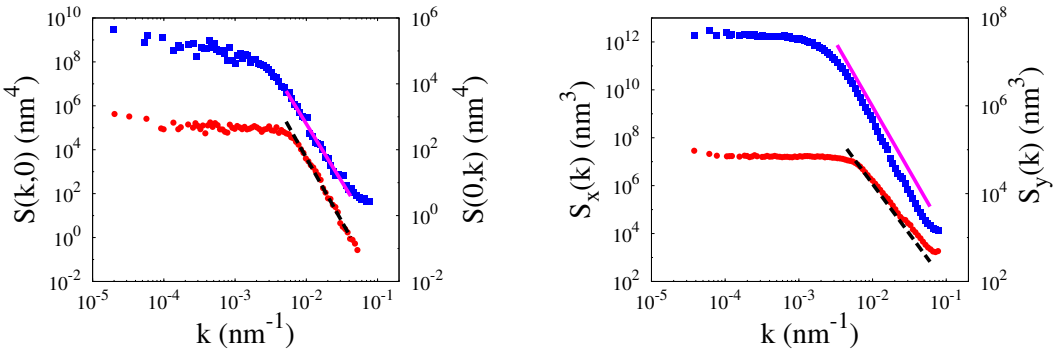

Figure 6.5: Experimental results for the samples illustrated in Figure 6.4, after an average over seven windows. Left panel: One-dimensional projections $S(k,0)$ (red circles, left axis) and $S(0,k)$ (blue squares, right axis) of the two-dimensional PSD. The black dashed line and the solid magenta line are fits obtained by least squares, the resulting exponents being $2\tilde{\alpha}_x \simeq 5.81$ and $2\tilde{\alpha}_y \simeq 3.74$. Right panel: PSD of one-dimensional cuts $S_x(k)$ (red circles, left axis) and $S_y(k)$ (blue squares, right axis). The black dashed line and the solid magenta line correspond to Eqs. (4.13), with exponents values given by Eq. (6.15). The raw data are given in Appendix B.

Using these values in Eqs. (4.13), the agreement with the experimental data obtained for the one-dimensional PSDs for the corresponding range in k is very good, as shown in the right panel of Figure 6.5.

The appearance of scaling behavior at length scales *below* the one associated with the morphological instability suggests as a cause the influence of the average shape (ripple) associated with it, rather than kinetic roughening, similar to the case of mound formation in epitaxial growth on high symmetry surfaces [189]. In order to explore this possibility, we have generated artificial topographies made up by an array of semi-ellipsoids that are placed off their ordered positions by a random error (see Figure 6.6). The interplay between disorder and the smooth shape of the basic motif does give rise to power law behavior of 2D and 1D PSD functions below the corresponding characteristic sizes. This situation is similar to the one investigated by Oliveira and Aarão Reis in [190, 191], where the authors studied the effects of the grain shape on the roughness exponent for several surfaces. However, the scaling exponents we find for our artificially generated topographies do *not* fulfill the relations expected within our scaling Ansatz. Specifically, from the linear fits presented in the left panel of Figure 6.7 we obtain the following exponent values,

$$2\tilde{\alpha}_x = 2.22, \qquad 2\tilde{\alpha}_y = 1.81 \Rightarrow \zeta = 1.23. \tag{6.16}$$

These would imply a scaling of the one dimensional PSDs of controlled by the exponents

$$2\alpha_x + 1 = 0.99, \qquad 2\alpha_y + 1 = 1, \tag{6.17}$$

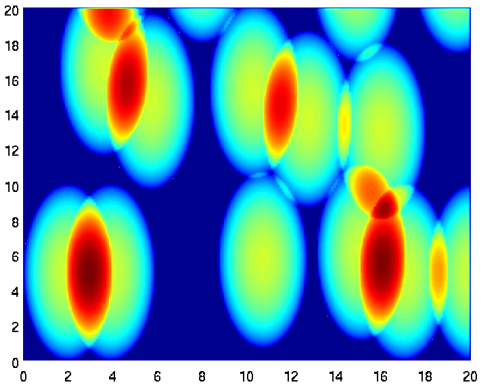

Figure 6.6: Synthetic surface morphology made up by an array of 3×7 identical semi-ellipsoids. Each of them conforms to the shape given by $(x/a)^2 + (y/b)^2 + (z/c)^2 = 1$ for $a = 2$, $b = 5$, and $c = 10$. The typical lateral scales a, b correspond to wave-vector values $k_x^* = \pi/2$ and $k_y^* = \pi/5$, respectively. The center of each semi-ellipsoid has been misplaced with respect to its regular position by a random deviation $(\delta x, \delta y)$ such that $|\delta x| \leq a/2$ and $|\delta y| \leq b/2$. If two semi-ellipsoids overlap in some region, the surface height above that region is the sum of those of each ellipsoid, thus providing some disorder in height.

which are obviously different from the actual scaling behavior, as is clear from the right panel of Figure 6.7. Rather, scaling in these cases seems related with the smooth geometry of the basic pattern [192], combined with fluctuations in its space arrangement. This constitutes a sort of "proof of principle" that the effects of the grain shape can lead to (anisotropic) scaling for the power spectral density without necessarily meaning that the system displays anisotropic kinetic roughening. One can only assume this if all the scaling relations that stem from the scaling hypothesis are verified, as it happens for our experimental data. It would be interesting, however, to explore in more detail the effects of anisotropic grains on the scaling behavior of a morphology, and perform a similar analysis to the one in References [190, 191] in this case.

We thus suggest strongly anisotropic kinetic roughening at submicron scales (above which scale invariance is lost) to account for the present experimental system features. To some extent, such a behavior is complementary to the one that is typical of e.g. the Kuramoto-Sivashinsky system [73]. In such a model, as seen in Chapter 3, a small-scale pattern becomes disordered at sufficiently large scales at which kinetic roughening occurs [32]. Although in terms of the latter class of systems it may look somewhat peculiar, the behavior found for the experiments just analyzed is again readily obtained in appropriate simple model systems. Thus, one

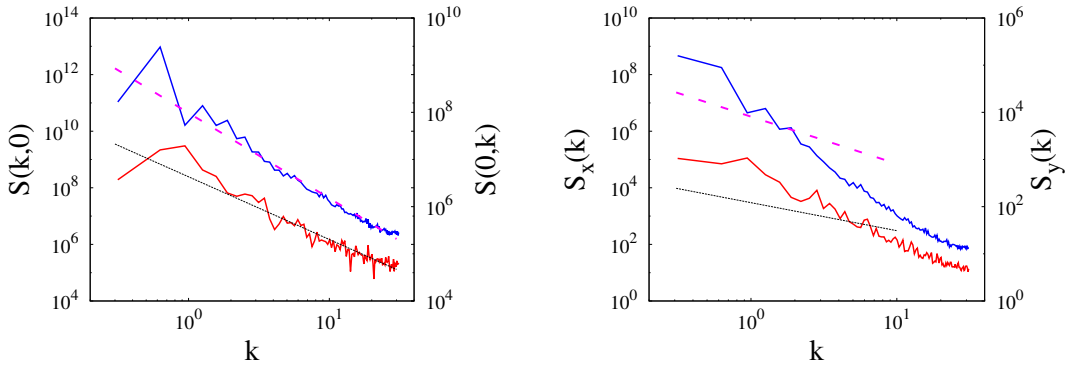

Figure 6.7: PSD functions for the topography displayed in Figure 6.6. Left panel: one-dimensional projections $S(k_x, 0)$ (left axis, solid red line) and $S(0, k_y)$ (right axis, solid blue line) of the two-dimensional PSD. The solid black line and magenta dashed line are linear fits, with values of the exponents given by Eq. (6.16). Right panel: PSDs of one-dimensional cuts of the sample $S_x(k_x)$ (left axis, solid red line) and $S_y(k_y)$ (right axis, solid blue line). The solid black line and magenta dashed line are reference lines with slopes given by Eq. (6.17).

can generalize, e.g. Eq. (4.25) to

$$\partial_t h = -\mu h + \nu_x \partial_x^2 h - \nu_y \partial_y^4 h + \eta, \tag{6.18}$$

where the linear term with coefficient $\mu > 0$ accounts for a physical mechanism (e.g., a wetting layer) that favors a specific value of the height (say, $h = 0$). For Eq. (6.18), at $t \to \infty$ one can exactly obtain $S(k_x, k_y) \sim (\mu + \nu_x k_x^2 + \nu_y k_y^4)^{-1}$. This implies that $S(k_x, k_y)$ does *not* scale with $k_{x,y}$ (but, rather, becomes a constant) for the largest length scales (smallest $k_{x,y}$ values), thus breaking scale invariance at such large scales. However, kinetic roughening precisely as in Eq. (4.6) does still occur for (large) $k_{x,y}$ values whose contribution to $S(k_x, k_y)$ dominates over μ. While we are not saying that Eq. (6.18) describes the experiments just analyzed, we believe the latter may correspond to a situation that is qualitatively captured by this example. Currently there is a large effort to pursue a more quantitative description of IBS experiments in the presence of metallic contamination that takes into account these type of effects, see Reference [193] and references therein.

6.5 Conclusions

In this Chapter we have verified a scaling Ansatz for strongly anisotropic kinetic roughening properties in two experimental systems. First of all, our results provide a consistent experimental assessment of such type of behavior, which calls for the development of theoretical models that can describe in detail the observed experimental properties. This would add to an improved knowledge of the phenomena governing the specific systems considered, as well as to our understanding of driven systems in general. From a more practical point of view, our work illustrates several forms of occurrence of strong anisotropy, both in the absence and in the presence of morphological instabilities, and at (sufficiently large) scales that remain either above or below a privileged (pattern) size.

Generally speaking, even in the absence of typical length scales, it is important to keep in mind that our scaling Ansatz applies only in a hydrodynamic limit. Therefore, in actual physical systems, effects due to finite-size and/or finite-space resolution of measurement techniques could hinder a clear-cut scaling of the correlation functions, thus preventing the observation of a consistent behavior between the one and two-dimensional PSDs. As we have seen in Chapter 4 by means of analytical arguments and numerical simulations, this "slow convergence" issue appears to be more pronounced for integrated quantities, such as the one-dimensional PSDs.

Thus, the two-dimensional PSD, conveniently averaged over several samples (or windows of the same sample), appears to be a more reliable observable in order to assess anisotropic scaling. However, in experiments it is seldom possible to have a sufficient number of samples over which to perform such an average, and the two-dimensional PSD frequently appears too noisy to extract reliable values of the exponents. On the other hand, the one-dimensional PSDs have a higher signal-to-noise ratio due to the fact that, for each window, they are averaged over all the rows or columns of the matrix. For this reason, despite the fact that they are more sensitive to finite size effects, such quantities do indeed provide relevant information about surface features.

We can hypothesize that this type of complication may have hindered a more frequent observation of anisotropic scaling in the literature. We hope that, once the analysis has been clarified, the identification of this challenging type of behavior becomes simplified and we can thus understand it better. Perhaps an analogy can be drawn with the case of anomalous scaling. This is a type of kinetic roughening behavior that was usually associated with large values of the roughness exponent, that induced many wrong assessments of scaling behavior both in experiments and models [35]. Incidentally, such "anomalous" values usually introduced slow convergence properties in correlation functions. Once anomalous scaling was identified and systematized [194–196], it has been indeed assessed in different thin-film experimental systems, from, e.g., electrochemical deposition [197] to chemical vapor deposition [198], metal dissolution [199], etc. We can only hope for a parallel development regarding strong anisotropy in the near future.

CONCLUSIONS AND OUTLOOK

In this Thesis we have shown how continuum modeling can provide a great amount of information about surface growth processes in many out-of-equilibrium systems, in particular under conditions for scale invariance. Specifically, we have considered surfaces displaying generic scale invariance (kinetic roughening) and the interplay between this property and two other phenomena, namely the onset of instabilities that lead to pattern formation, and the presence of anisotropy. We have seen that both phenomena lead to non-trivial dynamics and scaling properties.

As for the first problem, we have considered the noisy Kuramoto-Sivashinsky equation, the behavior of which was yet to be completely understood in $d = 2$. By means of large-scale numerical simulations, we have shown that it belongs to the two-dimensional Kardar-Parisi-Zhang universality class, confirming previous expectations based on renormalization group calculations that had not been verified, and improving upon previous numerical approaches. We have also pointed out the role of crossover effects in preventing the true asymptotic behavior from emerging, and we have discussed the implications of our results within the controversy on the universality class of the deterministic Kuramoto-Sivashinsky equation.

In the context of the study of anisotropic surfaces, we have put forward an anisotropic scaling Ansatz expressed in terms of observables in momentum space, like the two-dimensional PSD and the power spectral densities of one dimensional cuts of the surfaces. Despite being equivalent to other proposals that can be found in the literature for the correlation functions in real space, our Ansatz is specifically tailored for two-dimensional surfaces, and is more readily applicable to experimental systems or numerical simulations of related continuum or discrete models. We have verified the consistency of our Ansatz by means of numerical simulations of two strongly anisotropic equations, one linear (the 2-4 equation) and another one nonlinear (the Hwa-Kardar equation), obtaining good agreement with our theoretical predictions. Nevertheless, our results show that finite size effects may play an important role in hindering a clear-cut scaling behavior for some observables. In this process, we also have introduced a family of linear models that display strong anisotropy, while generally being non local in space. We have seen how these models could provide useful (Gaussian) approximations of nonlinear equations with conserved dynamics and non-conserved noise. The fact that a nonlinear equation may be approximated by a linear one is highly non trivial, and requires

certain scaling relations among exponents to be verified in both equations. The importance of such approximations lies in the existence of exact analytical solutions for linear equations. This allows, for instance, to test results obtained from simulations of the nonlinear model, in the regime of validity of the approximation considered. In the study of the Hwa-Kardar equation, the introduction of a Gaussian approximation has been of a fundamental importance in order to explain the anomalous behavior of some observables at small wave vectors, which was due to finite size effects. We also note that the analytical and numerical study has been possible by working in Fourier space. In fact, on the one hand it would be difficult to construct such an approximation in real space, due to its non local nature. On the other hand, the pseudospectral method integrates equations directly in Fourier space, and its implementation for non-local equations is straightforward. Moreover, the computational time required for the integration of linear models is much smaller than for nonlinear ones, thus allowing to increase the signal-to-noise ratio considerably.

We have then extended our analysis to fully nonlinear continuum models, for which the Gaussian approximation mentioned above fails. Our aim was to identify which features of a given continuum equation would give rise to strongly anisotropic scaling. We have thus considered several anisotropic extensions of paradigmatic models displaying generic scale invariance, with conserved and non-conserved dynamics. By means of numerical simulations and dynamic renormalization group analysis, we were able to conclude that, at least for morphologically stable equations with quadratic nonlinearities and non-conserved noise, strong anisotropy may only occur when the dynamics is conserved. Moreover, we have seen that strong anisotropy arises only when one nonlinearity is suppressed, thus implying that such a phenomenon is non-generic in parameter space.

Finally, we have studied several morphologies obtained from Ion Beam Sputtering experiments. Such systems are inherently anisotropic because the projection of the ion beam onto the substrate sets up a preferred direction for the dynamics of the material. Moreover, under certain experimental conditions the morphologies produced are rough, thus making these systems good candidates for displaying strong anisotropy. By using the anisotropic scaling Ansatz, we were able to reasonably confirm the presence of strong anisotropy, both in the morphologically stable and in the unstable cases. As for the case of the Hwa-Kardar equation, we found that finite size effects may play a major role for some observables, namely the one dimensional power spectral densities. These results suggest that a correct estimate of the exponents should be performed on more robust quantities such as the two-dimensional power spectral density, whenever a good signal-to-noise ratio can be obtained. It is important to notice that, to date, not many reports are available that undoubtedly assess strong anisotropy in experiments. Some promising data in this sense are given in Reference [151] for an ion beam erosion experiment. There, a silicon sample was irradiated at incidence angle $\theta = 67^\circ$ with respect to the surface normal using Ar^+ ions with an average kinetic energy of 500 eV

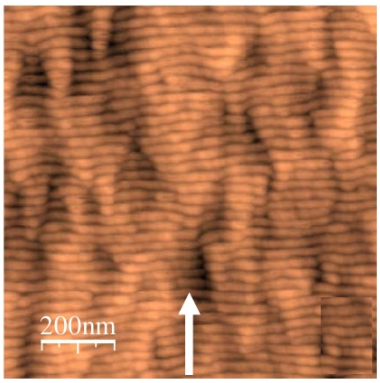

Figure 1: Morphology obtained for a silicon sample irradiated with 500 eV Ar^+ ions, at incidence angle $\theta = 67°$. The arrow indicates the projection of the ion beam direction onto the substrate. The picture has been taken from [151].

(Figure 1), and the resulting morphologies were studied. The authors observed different values of the scaling exponents for the one-dimensional power spectral densities measured along two orthogonal substrate directions (see Figure 2). In the context of Ion Beam Sputtering experiments, several other reports are also available that similarly suggest strongly anisotropic kinetic roughening, but do not confirm such behavior beyond any doubt. We believe that the results of this Thesis provide a well defined theoretical framework, as well as a set of procedures to analyze experimental morphologies and extract the correct scaling exponents, in the strongly anisotropic case.

Future work

In view of the results of this Thesis, one can conceive of several research lines to follow, that would be interesting to explore in order to improve the understanding of the phenomena addressed here.

In the context of the study of the Kuramoto-Sivashinsky equation, it would be interesting to perform large-scale numerical simulations of the *deterministic* case in two spatial dimensions, in order to confirm the expectations that it also belongs to the Kardar-Parisi-Zhang universality class. It is important to take into account that, in this case, the only free parameter is the size L of the system. Thus, the strong coupling regime would be presumably reached at very high values of L, and numerical simulations may be extremely time-consuming. An improvement over the pseudospectral numerical scheme could be useful in this situation. For instance, an exponential time-differencing algorithm combined with a Runge-Kutta time stepping could at least improve precision of our results. It would be interesting to explore other numerical schemes, perhaps exploiting parallel computing, that could considerably decrease the integration time.

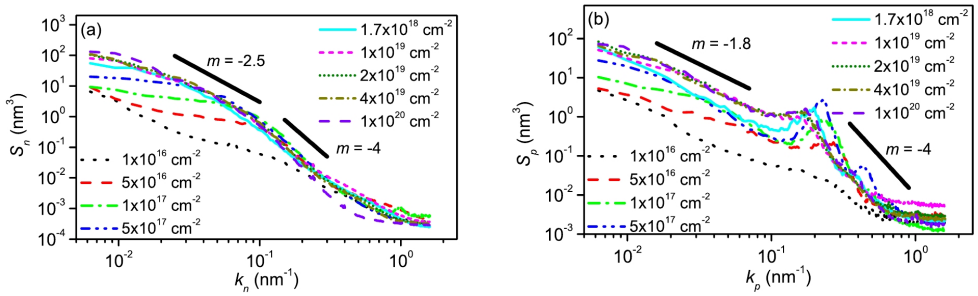

Figure 2: One-dimensional power spectral densities for a silicon sample irradiated with 500 eV Ar^+ ions, at incidence angle $\theta = 67°$, in the direction normal (left panel) and parallel (right panel) to the projection of the ion beam onto the substrate. Note, the value of the scaling exponents at small values of k is different for the two directions. The picture has been taken from [151].

For the noisy Kuramoto-Sivashinsky equation in two substrate dimensions, a refinement over the phase diagram presented in Figure 3.5 may be possible. In order to do this, a detailed study of the crossover is needed, analogously to the analysis by Sneppen *et al.* [132] for the one-dimensional deterministic case. However, the latter is based on several analytical results regarding the universal amplitudes and saturation time for the Kardar-Parisi-Zhang equation in one dimension, that are not currently available for the two-dimensional case. Nevertheless, some recent results by Halpin-Healy and collaborators [64] seem promising in identifying universal quantities for the Kardar-Parisi-Zhang universality class in two dimensions, beyond the values of the critical exponents. These results could help us estimate, or even predict analytically, the shape of the transition line between the weak and strong coupling regimes in the phase diagram of Figure 3.5. The same analysis could also be carried out for the deterministic case, after a confirmation of its universality class is provided.

From a theoretical point of view, it would also be interesting to continue the study of anisotropic equations, and more precisely the search for conditions for strong anisotropy. We plan to relax some hypothesis we have made in the present study, in order to obtain more general results, and test the range of validity of our conclusions. One possibility is to consider two different nonlinearities in the x and y directions, one conserved and the other one non-conserved. Preliminary results suggest that this could also give rise to strong anisotropy.

As mentioned above, introducing a Gaussian approximation to a given nonlinear model, whenever possible, may provide very valuable information on the system at hand. This clearly goes way beyond anisotropic equations, and can in principle be applied to a great variety of nonlinear models. It would be interesting to compare the dynamics of some nonlinear model and its approximation, in order to check the range of validity of the latter. Such an approximation may be

useful also when dealing with actual experimental data, since it provides a simple linear model of the system at hand, accounting for the observed scaling exponents. Also in this case, it would be useful to compare the dynamics of such a model with the evolution of the experimental morphologies. Such a comparison may provide information not only on the range of validity of the approximation, but also on identifying those physical mechanism that are not universal, but rather are specific of the system considered.

As far as the experiments are concerned, as mentioned above several reports on alleged strong anisotropy are available, but the lack of a well defined theoretical framework prevented a clear-cut observation of this phenomenon. Moreover, continuum (nonlinear) models are still lacking for many of these experimental situations, such as, for instance, the system studied in Reference [151]. Thus, it would be useful to re-examine those experimental data in view of the more complete understanding of strong anisotropy provided by the results of this Thesis.

Another interesting issue concerns the interplay between morphological instabilities and strong anisotropy. As mentioned above, in the present work we have only studied morphologically stable anisotropic equations, whereas our analysis of the interplay between kinetic roughening and pattern formation only concerned an isotropic model, the noisy Kuramoto-Sivashinsky equation. Thus, it would be interesting to perform an analysis of the equations studied in Chapter 5 and related ones, in the morphologically unstable case. Despite the analytical and numerical difficulties that would arise in this case, this would lead to a better understanding of the phenomenon of kinetic roughening, and may result into a better description of several experimental systems. Actually, a similar analysis has already been performed for the anisotropic Kuramoto-Sivashinsky equation [105], where the authors showed that the behavior of the model under renormalization leads to a nontrivial dynamics for the ensuing pattern, namely a rotation of the ripples. However, such model is not strongly anisotropic, and a similar study on strongly anisotropic equations would be interesting.

Recently, there have been several advances in the study of the probability distribution functions for the two-dimensional Kardar-Parisi-Zhang equation [64, 65]. These studies attempt to generalize the known results in one dimension for the statistics of fluctuations of this paradigmatic model, to one higher spatial dimension. It would be interesting to apply this kind of analysis to other models, and especially to study the effect of (strong) anisotropy on the probability distribution functions for the fluctuations.

We also plan to apply the anisotropic scaling analysis to other anisotropic surfaces, in order to identify novel "anisotropic" universality classes that could help construct models for this kind of systems. Examples are given by discrete models of deposition, with directional dependent attachment and/or relaxation rules, or in the context of crack formation, where anisotropies indeed play a fundamental role. Other examples are given by epitaxial growth, solidification fronts, etc.

Finally, it is well known that different types of noise, such as quenched dis-

order, play a relevant role in several situations, such as e.g. crack propagation in heterogeneous materials [74], fluid flow in porous media, etc., in which they induce peculiar kinetic roughening properties. Thus, a further possibility for future research would be to study the interplay between anisotropy and different types of disorder.

RESUMEN EN CASTELLANO

Esta tesis se centra en fenómenos de invariancia de escala genérica en modelos de crecimiento de superficies. Concretamente, hemos considerado sistemas fuera de equilibrio que presentaran desorden a grandes escalas espaciales y temporales (rugosidad cinética), y que estuvieran descritos por ecuaciones continuas. El objetivo de la tesis ha sido utilizar métodos propios de la mecánica estadística para estudiar la interacción de este tipo de sistemas con otros dos fenómenos: la aparición de inestabilidades morfológicas que dan lugar a la formación de patrones, y la presencia de anisotropía.

En cuanto al primer problema, hemos considerado un ejemplo paradigmático de ecuación que presente invariancia de escala genérica e inestabilidades morfológicas, la ecuación de Kuramoto-Siashinsky. Hasta la fecha, el comportamiento asintótico de este modelo no se había entendido completamente. De hecho, existe una controversia acerca de cual sea la clase de universalidad a la que este modelo pertenece en dos dimensiones. Utilizando simulaciones numéricas de grande escala, hemos comprobado que esta ecuación en dos dimensiones pertenece a la clase de universalidad de Kardar-Parisi-Zhang.

Sucesivamente, nos hemos centrado en modelos que presenten invariancia de escala genérica, cuyos exponentes críticos sean distintos cuando se miden en direcciones distintas del sustrato. Cuando eso ocurre, decimos que el sistema presenta *anisotropía fuerte*. A pesar de la presencia generalizada de anisotropía en sistemas naturales, hasta el momento se había dedicado relativamente poca atención a este fenómeno. Eso se debe probablemente al hecho de que los modelos mas estudiados en este ámbito no presentan anisotropía fuerte, aunque la forma de la ecuación sea en algunos casos completamente anisótropa. Después de introducir un marco teórico para el estudio de modelos fuertemente anisótropos, hemos comprobado nuestra hipótesis a través de simulaciones numéricas de distintas ecuaciones que presentaran anisotropía fuerte. Sucesivamente, hemos llevado a cabo un estudio numérico y analítico de otros modelos, con el objetivo de encontrar condiciones para la aparición de anisotropía fuerte. Encontramos que este fenómeno ocurre en presencia de una dinámica conservada, siempre que la ecuación tenga una forma bastante especifica. Finalmente, hemos presentado evidencias experimentales de la aparición de anisotropía fuerte, a través de una análisis de datos de experimentos de erosión iónica en distintas condiciones experimentales.

La memoria se ha dividido en seis capítulos, cada uno con sus propias conclusiones. Hemos recogido en apéndices los detalles de los cálculos y los resultados menores. En el capitulo final hemos resumido nuestras conclusiones desde una perspectiva unificada y hemos presentado posibles lineas de investigación futura.

En el primer capitulo, hemos introducido la mayoría de los conceptos utilizados a lo largo de la tesis. Después de un breve resumen sobre el concepto de invariancia de escala (genérica) en equilibrio y fuera del equilibrio, nos hemos centrado en modelos de crecimiento de superficies descritos por ecuaciones de Langevin. Hemos definido las observables que caracterizan el proceso de crecimiento, y hemos descrito su comportamiento típico para sistemas isótropos. Sucesivamente, hemos introducido el concepto de clases de universalidad y algunos importantes resultados en este ámbito, y hemos presentado algunas consideraciones sobre el escalado anisótropo de superficies. En la ultima sección del capitulo, mencionamos el fenómeno de las inestabilidades morfológicas y formación de patrones en el contexto de modelos de crecimiento.

En el segundo capitulo, hemos presentado las herramientas numéricas y analíticas utilizadas en la memoria. Concretamente, hemos introducido y discutido el grupo de renormalización dinámico, y hemos presentado el esquema pseudoespectral para la integración numérica de ecuaciones estocásticas.

En el tercer capitulo, hemos llevado a cabo un estudio numérico detallado de la ecuación de Kuramoto-Sivashinsky con ruido, en dos dimensiones espaciales. En la primera parte del capitulo, hemos introducido el modelo y hemos discutido su relevancia y sus propiedades fundamentales; en la segunda parte, hemos presentado la controversia sobre su clase de universalidad. En la ultima parte, hemos descrito nuestros resultados numéricos en detalle, y hemos presentados argumentos solidos que prueban que este modelo se encuentra en la clase de universalidad de Kardar-Parisi-Zhang. Los contenidos de este capitulo han sido publicados en (1).

En el cuarto capitulo, hemos empezado el estudio de modelos anisótropos. Hemos presentado una hipótesis para el escalado anisótropo que generaliza la de Family-Vicsek, valida para superficies isótropas. Sucesivamente, hemos comprobado nuestra hipótesis a través de simulaciones numéricas de dos ecuaciones anisótropas, una lineal y otra no lineal, y hemos obtenido un buen acuerdo con nuestras predicciones teóricas. A lo largo de este proceso, hemos introducido una familia de modelos lineales fuertemente anisótropos. Los resultados obtenidos han llevado a la identificación de observables cuyo comportamiento de escala no es el esperado, debido a efectos de tamaño finito y a la discretización utilizada. Los resultados de este análisis han sido publicados en (2).

En el quinto capitulo, hemos explorado la interacción entre las no-linealidades y la anisotropia fuerte, a través de un estudio numérico y analítico de varios modelos. En la primera parte del capitulo, hemos considerado ecuaciones con dinámica conservada, mientras que en la segunda parte hemos estudiado una ecuación con dinámica no conservada. En ambos casos, hemos presentado los resultados de la integración numérica directa, y del análisis de grupo de renormalización. Hemos

encontrado anisotropia fuerte solamente en casos con dinámica conservada y para valores no genéricos de los parámetros. Este análisis ha sido publicado en (3).

En el sexto capitulo, hemos aplicado la hipótesis de escalado anisótropo presentada en el cuarto capitulo, a morfologías obtenidas a través de experimentos de bombardeo iónico. Después de un breve resumen sobre esta técnica experimental y sus modelizaciones teóricas, hemos considerado dos situaciones experimentales: una correspondiente a un experimento "limpio", en el que se había evitado contaminación de las muestras, y otra en la que la deposición simultanea de impurezas diera lugar a inestabilidades morfológicas. En ambos casos hemos observado distintos exponentes críticos en las dos direcciones del sustrato, y hemos encontrado un acuerdo satisfactorio con las predicciones teóricas. Los contenidos de este capitulo han sido publicados en (4).

Artículos publicados

(1) M. Nicoli, E. Vivo, and R. Cuerno, "Kardar-Parisi-Zhang asymptotics for the two-dimensional noisy Kuramoto-Sivashinsky equation," Physical Review E, vol. 82, p. 045202(R), 2010.

(2) E. Vivo, M. Nicoli, and R. Cuerno, "Strong anisotropy in two-dimensional surfaces with generic scale invariance: Gaussian and related models," Physical Review E, vol. 86, p. 051611, 2012.

(3) E. Vivo, M. Nicoli, and R. Cuerno. "Strong anisotropy in two-dimensional surfaces with generic scale invariance: Nonlinear effects." Physical Review E, vol. 89, p. 042407, 2014.

(4) E. Vivo, M. Nicoli, M. Engler, T. Michely, L. Vázquez, and R. Cuerno, "Strong anisotropy in surface kinetic roughening: Analysis and experiments," Physical Review B, vol. 86, p. 245427, 2012.

A

DRG CALCULATIONS FOR ANISOTROPIC EQUATIONS

A.1 Isotropic vs. Anisotropic momentum shell

An issue that seems to be overlooked in previous DRG studies of anisotropic equations concerns the shape of the momentum shell. As explained in Chapter 2, the correction to the bare parameters can be expressed as integrals of certain combinations of the bare propagators over a region of high wave vectors $\mathbf{k}$, provided that they do not exceed the cut-off Λ. In two dimensions this means that the momentum shell is square. However, for isotropic equations this region can be usually approximated by a spherical one, due to the symmetries of the integrand. The actual and approximated momentum shell are shown in Figure A.1. When dealing with anisotropic equations, one actually needs to define a *rectangular* momentum shell, as depicted in Figure A.2. This is due to the fact that in this case the correct form of the rescaling is anisotropic as well, being given for instance by Eq. (4.20). In the context of the Forster-Nelson-Stephen scheme, such a rescaling should restore the original value of the cut-off Λ after coarse graining. It is then straightforward to see that the shape of the momentum shell is indeed given by the one in Figure A.2.

Once the correct form of the momentum shell is recognized, another issue concerns the symmetry of the integrands that appear in the renormalization procedure. Thus, as explained below, for the generalized Hwa-Kardar equation it has been necessary to compute integrals over the first and third quadrant of Figure A.2, while in the case of the anisotropic Kardar-Parisi-Zhang equation, the higher symmetry of the integrands allowed us to consider only the first quadrant for integration.

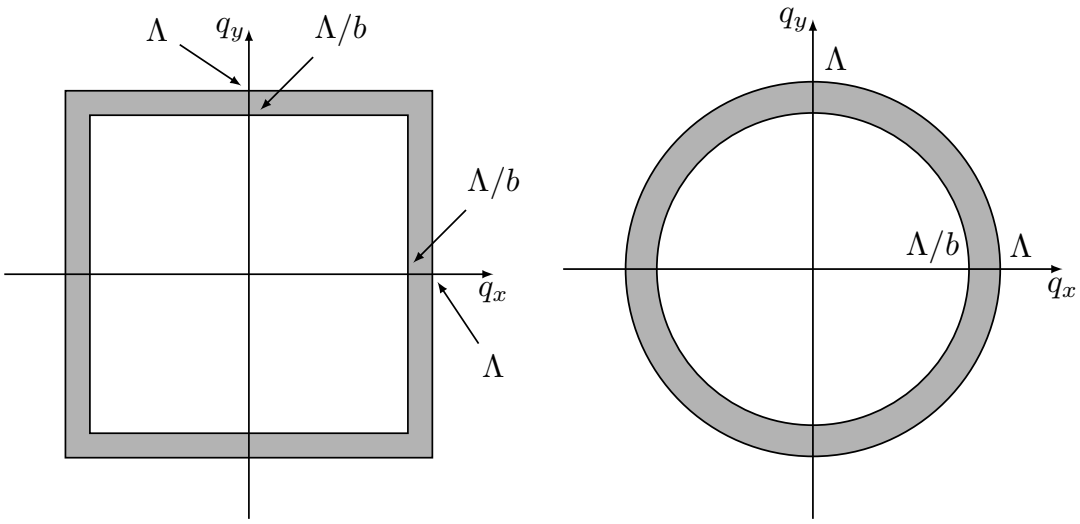

Figure A.1: Two-dimensional shell in the wave vector plane. The left panel shows the actual square shell with the explicit dependence on the two components of the wave vector $\mathbf{q}$. The right panel depicts the spherical approximation used for isotropic equations. The fast modes are shown in grey and the slow modes in white.

A.2 Dynamic Renormalization Group analysis of the generalized Hwa-Kardar equation

The diagrammatic expansion of the integrals that contribute to the renormalization of the bare propagator of the gHK equation is sketched in Figure A.3, where we use standard notation for the nonlinearities involved [102]. Note, there being two different vertices with couplings $\lambda_{x,y}$, both indices l, m take as values the two spatial variables x, y, leading to four different contributions, $\Sigma_{xx}, \Sigma_{xy}, \Sigma_{yx}$, and Σ_{yy}. After the usual symmetrization of the integration variables $(\mathbf{q}, \Omega) \to (\mathbf{j} + \mathbf{k}/2, \Omega + \omega/2)$, we get

$$\Sigma_{lm}(\mathbf{k},\omega) = -2\lambda_l\lambda_m D \int^{>} \frac{d\mathbf{j}}{(2\pi)^2} \int \frac{d\Omega}{2\pi}\, k_l \left(\frac{k_m}{2} - j_m\right) \times \left|G_0\left(\frac{\hat{k}}{2} + \hat{j}\right)\right|^2 G_0\left(\frac{\hat{k}}{2} - \hat{j}\right), \tag{A.1}$$

where $G_0\big(\hat{k}\big)$ is short-hand notation for the bare propagator

$$G_0\big(\hat{k}\big) = \left[\nu_x k_x^2 + 2\nu_{xy} k_x k_y + \nu_y k_y^2 - i\omega\right]^{-1}. \tag{A.2}$$

An expansion to first order in $k_x/j_x, k_y/j_y \ll 1$ leads to

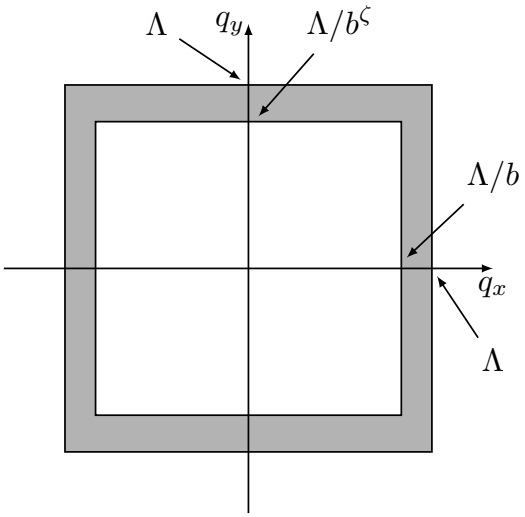

Figure A.2: Two-dimensional shell in the wave vector plane for anisotropic equations. Note that this coincides with the left panel of Figure A.1 only when the anisotropy exponent $\zeta = 1$. The fast modes are shown in grey and the slow modes in white.

$$\lim_{\omega\to 0}\left|G_0\left(\hat{k}/2+\hat{j}\right)\right|^2 \sim \frac{1}{\Delta^2+\Omega^2}\left[1-\frac{2\Delta}{\Delta^2+\Omega^2}\right.$$
$$\left.\times\left(\nu_x j_x k_x+\nu_y j_y k_y+\nu_{xy} j_y k_x+\nu_{xy} j_x k_y\right)\right], \quad \text{(A.3)}$$

$$\lim_{\omega\to 0} G_0\left(\hat{k}/2-\hat{j}\right) \sim \frac{1}{\Delta+i\Omega}\left[1+\frac{1}{\Delta+i\Omega}\right.$$
$$\left.\times\left(\nu_x j_x k_x+\nu_y j_y k_y+\nu_{xy} j_y k_x+\nu_{xy} j_x k_y\right)\right], \quad \text{(A.4)}$$

where $\Delta = \nu_x j_x^2 + 2\nu_{xy} j_x j_y + \nu_y j_y^2$. Using these results in Eq. (A.1) and after integration over the frequency variable Ω, we retain terms up to second order in the components of $\mathbf{k}$, to get

$$\Sigma_{lm}(\mathbf{k},0) = -\frac{\lambda_l\lambda_m D}{16\pi^2}\int^{>}\frac{d\mathbf{j}}{\Delta^2}\left[k_l k_m+\frac{2}{\Delta}k_l j_m\right.$$
$$\left.\times\left(\nu_x k_x j_x+\nu_y k_y j_y+\nu_{xy} j_y k_x+\nu_{xy} j_x k_y\right)\right]. \quad \text{(A.5)}$$

Considering all possible combinations for $l, m = x, y$, we obtain the coarse-grained propagator, $\Sigma = \Sigma_{xx} + \Sigma_{xy} + \Sigma_{yx} + \Sigma_{yy}$, where

$$\Sigma_{xx}(\mathbf{k},0) = -\frac{\lambda_x^2 D}{16\pi^2}\int^{>}\frac{d\mathbf{j}}{\Delta^2}\left\{\left[1+\frac{2}{\Delta}\left(\nu_x j_x^2+\nu_{xy} j_x j_y\right)\right]k_x^2\right.$$
$$\left.+\frac{2}{\Delta}\left(\nu_y j_x j_y+\nu_{xy} j_x^2\right)k_x k_y\right\}, \quad \text{(A.6)}$$

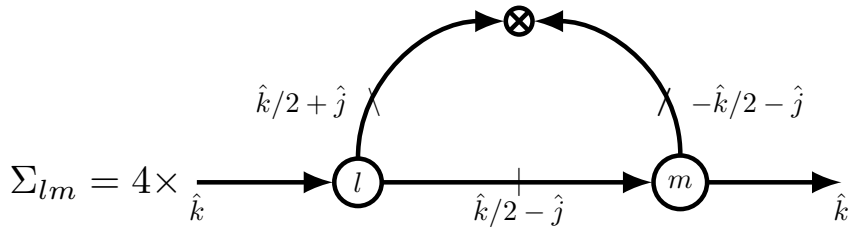

Figure A.3: Generic diagrammatic representation of the four different contributions Σ_{xx}, Σ_{xy}, Σ_{yx}, and Σ_{yy} to the renormalization of the propagator $G(\mathbf{k},\omega)$ of the gHK and the aKPZ equations. For each equation the exact meaning of the solid lines differ, see Eq. (A.1) for the former and Eq. (A.38) for the latter.

$$\Sigma_{xy}(\mathbf{k},0) = -\frac{\lambda_x\lambda_y D}{16\pi^2}\int^{>}\frac{d\mathbf{j}}{\Delta^2}\left\{\frac{2}{\Delta}\Big(\nu_x j_x j_y + \nu_{xy} j_y^2\Big)k_x^2 + \left[1+\frac{2}{\Delta}\Big(\nu_y j_y^2 + \nu_{xy} j_x j_y\Big)\right]k_x k_y\right\}, \tag{A.7}$$

$$\Sigma_{yx}(\mathbf{k},0) = -\frac{\lambda_x\lambda_y D}{16\pi^2}\int^{>}\frac{d\mathbf{j}}{\Delta^2}\left\{\frac{2}{\Delta}\Big(\nu_y j_x j_y + \nu_{xy} j_x^2\Big)k_y^2 + \left[1+\frac{2}{\Delta}\Big(\nu_x j_x^2 + \nu_{xy} j_x j_y\Big)\right]k_x k_y\right\}, \tag{A.8}$$

$$\Sigma_{yy}(\mathbf{k},0) = -\frac{\lambda_y^2 D}{16\pi^2}\int^{>}\frac{d\mathbf{j}}{\Delta^2}\left\{\left[1+\frac{2}{\Delta}\Big(\nu_y j_y^2 + \nu_{xy} j_x j_y\Big)\right]k_y^2 + \frac{2}{\Delta}\Big(\nu_x j_x j_y + \nu_{xy} j_y^2\Big)k_x k_y\right\}. \tag{A.9}$$

The next step is to calculate the $\mathbf{k}$-contributions to these integrals induced by the dependence on the wave-vector components of the integration limits that define the rectangular momentum-shell which is being integrated out. Due to the lack of symmetry of the function Δ with respect to j_x and j_y, we cannot use only the first quadrant of the momentum shell to find them. Rather, it is convenient to expand Eqs. (A.6)-(A.9) in the limit $\delta l \to 0$. This allows us to rewrite each contribution Σ_{lm} to the renormalization of the propagator in a simpler form. In fact, for any function $f(j_x, j_y)$ appearing in the integrand of Eq. (A.5), its integral decomposes into four terms, namely,

$$\int^{>} d\mathbf{j}\, f(j_x,j_y) = \int_{\Lambda/b}^{\Lambda} dj_x f_x(j_x) + \int_{-\Lambda}^{-\Lambda/b} dj_x f_x(j_x) + \int_{\Lambda/b^\zeta}^{\Lambda} dj_y f_y(j_y) + \int_{-\Lambda}^{-\Lambda/b^\zeta} dj_y f_y(j_y), \tag{A.10}$$

where the associated single-variable functions f_x and f_y are simply given by

$$f_x(j_x) = \int_{-\Lambda}^{\Lambda} ds\, f(j_x, s), \tag{A.11}$$

$$f_y(j_y) = \int_{-\Lambda}^{\Lambda} ds\, f(s, j_y). \tag{A.12}$$

By expanding perturbatively Eq. (A.10) for $b = e^{\delta l} \to 1$ we obtain the general result

$$\int^{>} d\mathbf{j}\, f(j_x, j_y) \sim [f_x(\Lambda) + f_x(-\Lambda) + \zeta f_y(\Lambda) + \zeta f_y(-\Lambda)]\, \Lambda\, \delta l. \tag{A.13}$$

For the specific functions appearing in Eq. (A.5), it is easy to verify that $f_{x,y}(\Lambda) = f_{x,y}(-\Lambda)$, so that, in this particular case,

$$\int^{>} d\mathbf{j}\, f(j_x, j_y) \sim 2\,[f_x(\Lambda) + \zeta f_y(\Lambda)]\, \Lambda\, \delta l. \tag{A.14}$$

Then it is convenient to express the general contribution to the coarse-grained propagator in the following way

$$\Sigma_{lm}(\mathbf{k}, 0) = -\frac{\lambda_l \lambda_m D}{8\pi^2} \left[\int_{-\Lambda}^{\Lambda} ds\, \frac{N_{lm}(\Lambda, s)}{\Delta_y^3(s)} + \zeta \int_{-\Lambda}^{\Lambda} ds\, \frac{N_{lm}(s, \Lambda)}{\Delta_x^3(s)} \right] \Lambda \delta l, \tag{A.15}$$

where

$$\Delta_x(s) = \Delta(s, \Lambda) = \nu_x s^2 + 2\nu_{xy} \Lambda s + \nu_y \Lambda^2, \tag{A.16}$$

$$\Delta_y(s) = \Delta(\Lambda, s) = \nu_x \Lambda^2 + 2\nu_{xy} \Lambda s + \nu_y s^2, \tag{A.17}$$

$$N_{lm}(j_x, j_y) = \Big(\nu_x j_x^2 + 2\nu_{xy} j_x j_y + \nu_y j_y^2\Big) k_l k_m + 2\Big(\nu_x j_x j_m + \nu_{xy} j_y j_m\Big) k_l k_x + 2\Big(\nu_y j_y j_m + \nu_{xy} j_x j_m\Big) k_l k_y. \tag{A.18}$$

Only six integrals need to be evaluated in order to cast Eq. (A.15) into a form that can be used in our further analysis, namely,

$$J_i^x = \int_{-\Lambda}^{\Lambda} ds\, s^i / \Delta_x^3(s), \tag{A.19}$$

$$J_i^y = \int_{-\Lambda}^{\Lambda} ds\, s^i / \Delta_y^3(s), \tag{A.20}$$

for $i = 0, 1, 2$. At this stage of the calculation it is practical to leave them unspecified, hence

$$\Sigma_{xx}(\mathbf{k}, 0) = -\frac{\lambda_x^2 D\Lambda}{8\pi^2}\Big\{\Big[3\nu_x\left(\zeta J_2^x + \Lambda^2 J_0^y\right) + 4\nu_{xy}\Lambda\left(\zeta J_1^x + J_1^y\right) + \nu_y\left(\zeta\Lambda^2 J_0^x + J_2^y\right)\Big]k_x^2 + 2\Big[\nu_{xy}\left(\zeta J_2^x + \Lambda^2 J_0^y\right) + \nu_y\Lambda\left(\zeta J_1^x + J_1^y\right)\Big]k_x k_y\Big\}\delta l, \tag{A.21}$$

$$\Sigma_{xy}(\mathbf{k}, 0) = -\frac{\lambda_x\lambda_y D\Lambda}{8\pi^2}\Big\{\Big[\nu_x\left(\zeta J_2^x + \Lambda J_0^y\right) + 4\nu_{xy}\Lambda\left(\zeta J_1^x + J_1^y\right) + 3\nu_y\left(\zeta\Lambda^2 J_0^x + J_2^y\right)\Big]k_x k_y + 2\Big[\nu_{xy}\left(\zeta\Lambda^2 J_0^x + J_2^y\right) + \nu_x\Lambda\left(\zeta J_1^x + J_1^y\right)\Big]k_x^2\Big\}\delta l, \tag{A.22}$$

$$\Sigma_{yx}(\mathbf{k}, 0) = -\frac{\lambda_x\lambda_y D\Lambda}{8\pi^2}\Big\{\Big[3\nu_x\left(\zeta J_2^x + \Lambda^2 J_0^y\right) + 4\nu_{xy}\Lambda\left(\zeta J_1^x + J_1^y\right) + \nu_y\left(\zeta\Lambda^2 J_0^x + J_2^y\right)\Big]k_x k_y + 2\Big[\nu_{xy}\left(\zeta J_2^x + \Lambda^2 J_0^y\right) + \nu_y\Lambda\left(\zeta J_1^x + J_1^y\right)\Big]k_y^2\Big\}\delta l, \tag{A.23}$$

$$\Sigma_{yy}(\mathbf{k}, 0) = -\frac{\lambda_y^2 D\Lambda}{8\pi^2}\Big\{\Big[\nu_x\left(\zeta J_2^x + \Lambda^2 J_0^y\right) + 4\nu_{xy}\Lambda\left(\zeta J_1^x + J_1^y\right) + 3\nu_y\left(\zeta\Lambda^2 J_0^x + J_2^y\right)\Big]k_y^2 + 2\Big[\nu_{xy}\left(\zeta\Lambda^2 J_0^x + J_2^y\right) + \nu_x\Lambda\left(\zeta J_1^x + J_1^y\right)\Big]k_x k_y\Big\}\delta l. \tag{A.24}$$

Using the definitions of the couplings $g, f_\nu, r_\nu, r_\lambda$ provided in Eq. (5.28) of the main text and performing a change of variables, the integrals in Eq. (A.20) can be expressed as

$$J_i^x = \frac{1}{\nu_x^3\Lambda^2} J_i(1, r_\nu), \tag{A.25}$$

$$J_i^y = \frac{1}{\nu_x^3\Lambda^2} J_i(r_\nu, 1), \tag{A.26}$$

where

$$J_i(a, b) = \int_{-1}^{+1} \frac{s^i\, ds}{(as^2 + 2f_\nu s + b)^3}. \tag{A.27}$$

After some algebra, we can make these integrals explicit in term of the couplings,

$$J_0(a,b) = \frac{1}{8(ab-f_\nu^2)^2}\Bigg\{(a+f_\nu)\frac{2(ab-f_\nu^2)+3a(a+2f_\nu+b)}{(a+2f_\nu+b)^2} + (a-f_\nu)\frac{2(ab-f_\nu^2)+3a(a-2f_\nu+b)}{(a-2f_\nu+b)^2} + \frac{3a^2}{\sqrt{ab-f_\nu^2}}\left[\tan^{-1}\left(\frac{a+f_\nu}{\sqrt{ab-f_\nu^2}}\right)+\tan^{-1}\left(\frac{a-f_\nu}{\sqrt{ab-f_\nu^2}}\right)\right]\Bigg\},$$

$$J_1(a,b) = -\frac{1}{8(ab-f_\nu^2)^2}\Bigg\{\frac{2(ab-f_\nu^2)(f_\nu+b)}{(a+2f_\nu+b)^2}+\frac{3f_\nu(a+f_\nu)}{a+2f_\nu+b} + \frac{2(ab-f_\nu^2)(f_\nu-b)}{(a-2f_\nu+b)^2}+\frac{3f_\nu(a-f_\nu)}{a-2f_\nu+b} + \frac{3af_\nu}{\sqrt{ab-f_\nu^2}}\left[\tan^{-1}\left(\frac{a+f_\nu}{\sqrt{ab-f_\nu^2}}\right)+\tan^{-1}\left(\frac{a-f_\nu}{\sqrt{ab-f_\nu^2}}\right)\right]\Bigg\},$$

$$J_2(a,b) = \frac{1}{8(ab-f_\nu^2)^2}\Bigg\{\frac{2(a-b)\left[ab(a+b)^2+2(a^2+4ab+b^2)f_\nu^2-16f_\nu^4\right]}{\left[(a+b)^2-4f_\nu^2\right]^2} + \frac{2f_\nu^2+ab}{\sqrt{ab-f_\nu^2}}\left[\tan^{-1}\left(\frac{a+f_\nu}{\sqrt{ab-f_\nu^2}}\right)+\tan^{-1}\left(\frac{a-f_\nu}{\sqrt{ab-f_\nu^2}}\right)\right]\Bigg\}.$$

It is now convenient to write the contributions to the coarse-grained propagator by gathering together the various terms, according to which parameter they renormalize in the original gHK equation,

$$\Sigma = \Sigma_{xx}+\Sigma_{xy}+\Sigma_{yx}+\Sigma_{yy} \approx \left(\Sigma_{\nu_x}\nu_x k_x^2+2\Sigma_{\nu_{xy}}\nu_{xy}k_xk_y+\Sigma_{\nu_y}\nu_y k_y^2\right)\delta l. \quad \text{(A.28)}$$

Using Eq. (5.28) of the main text, the functions on the right-hand side of Eq. (A.28) read

$$\Sigma_{\nu_x} = -2g\Big\{3\left[\zeta J_2(1,r_\nu)+J_0(r_\nu,1)\right] + 2\left(r_\nu+2f_\nu\right)\left[\zeta J_1(1,r_\nu)+J_1(r_\nu,1)\right] + \left(r_\nu+2f_\nu r_\lambda\right)\left[\zeta J_0(1,r_\nu)+J_2(r_\nu,1)\right]\Big\}, \quad \text{(A.29)}$$

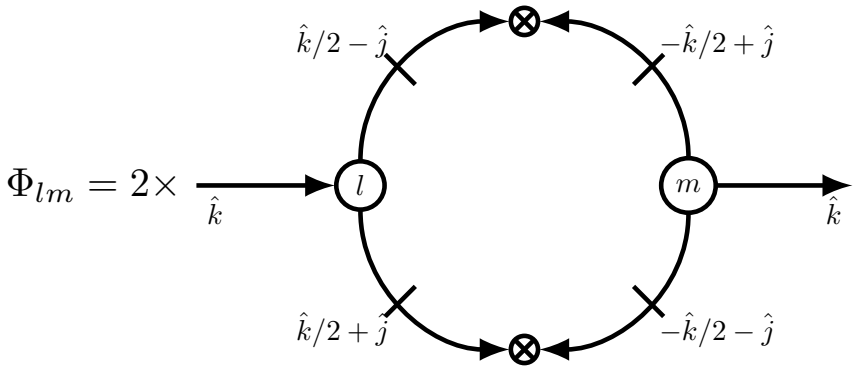

Figure A.4: Generic diagrammatic representation of the four different contributions Φ_{xx}, Φ_{xy}, Φ_{yx}, and Φ_{yy} to the renormalization of the noise variance $2D$ for the gHK and the aKPZ equations. For each equation the exact meaning of the solid lines differ, see Eq. (A.32) for the former and Eq. (A.54) for the latter.

$$\begin{aligned}\Sigma_{\nu_{xy}} = -\frac{g}{f_\nu}\Big\{ & 2\left(f_\nu + 2r_\lambda\right)\Big[\zeta J_2(1,r_\nu) + J_0(r_\nu,1)\Big] \\ & + \left(2r_\nu + 8r_\lambda f_\nu + r_\lambda^2\right)\Big[\zeta J_1(1,r_\nu) + J_1(r_\nu,1)\Big] \\ & + r_\lambda(4r_\nu + r_\lambda f_\nu)\Big[\zeta J_0(1,r_\nu) + J_2(r_\nu,1)\Big]\Big\}, \end{aligned} \tag{A.30}$$

$$\begin{aligned}\Sigma_{\nu_y} = -2\frac{g r_\lambda}{r_\nu}\Big\{ & \left(r_\lambda + 2f_\nu\right)\Big[\zeta J_2(1,r_\nu) + J_0(r_\nu,1)\Big] \\ & + 2\left(r_\nu + 2f_\nu r_\lambda\right)\Big[\zeta J_1(1,r_\nu) + J_1(r_\nu,1)\Big] \\ & + 3r_\lambda r_\nu\Big[\zeta J_0(1,r_\nu) + J_2(r_\nu,1)\Big]\Big\}, \end{aligned} \tag{A.31}$$

so that the coarse-grained propagator can be finally written as

$$G_0^<(\mathbf{k},\omega) = \Big[\nu_x\left(1-\Sigma_{\nu_x}\delta l\right)k_x^2 + 2\nu_{xy}\left(1-\Sigma_{\nu_{xy}}\delta l\right)k_x k_y + \nu_y\left(1-\Sigma_{\nu_y}\delta l\right)k_y^2 - i\omega\Big]^{-1}.$$

Hence, the coarse-grained surface tension parameters are $\nu_x^< = \nu_x(1-\Sigma_{\nu_x}\delta l)$, $\nu_{xy}^< = \nu_{xy}(1-\Sigma_{\nu_{xy}}\delta l)$, and $\nu_y^< = \nu_y(1-\Sigma_{\nu_y}\delta l)$. After rescaling as in Eq. (5.5), the corresponding flow equations become Eqs. (5.22)-(5.24).

The renormalization of the noise variance is calculated from the standard diagram shown in Figure A.4. Due to the existence of two different vertices, four different contributions occur, analogously to the renormalization of the propagator.

In the symmetric momentum variable $\mathbf{j}$ they read, to leading order,

$$\Phi_{lm}(\mathbf{k},\omega) = \lambda_l \lambda_m D^2 k_l k_m \int^{>} \frac{d\mathbf{j}}{(2\pi)^2} \int \frac{d\Omega}{2\pi} \left| G_0\left(\frac{\hat{k}}{2} + \hat{j}\right)\right|^2 \times \left| G_0\left(\frac{\hat{k}}{2} - \hat{j}\right)\right|^2 . \tag{A.32}$$

Since all contributions given by Eq. (A.32) are proportional to $k_l k_m$, they can be neglected in the limit $k_{x,y} \to 0$. Hence, the coefficient D is not renormalized to all orders of the perturbation series, and its flow equation is simply given by Eq. (5.27). Finally, the one-loop contributions to the renormalization of the nonlinearities $\lambda_{x,y}$ cancel out [104], giving rise to Eq. (5.25)-(5.26), thus completing the DRG flow for the gHK equation.

A.2.1 Standard HK equation

The RG flow for the standard HK equation is retrieved from the one derived for the gHK equation by setting $f_\nu = 0$ and $r_\lambda = 0$. In this case the J_i integrals, Eq. (A.27), reduce to

$$J_0(a,b) = \frac{1}{8b^2}\left[\frac{6a+10b}{(a+b)^2} + \frac{6}{\sqrt{ab}}\tan^{-1}\left(\sqrt{\frac{a}{b}}\right)\right], \tag{A.33}$$

$$J_2(a,b) = \frac{1}{8ab}\left[\frac{2(a-b)}{(a+b)^2} + \frac{2}{\sqrt{ab}}\tan^{-1}\left(\sqrt{\frac{a}{b}}\right)\right], \tag{A.34}$$

whereas J_1 is identically equal to zero. The condition $r_\lambda = 0$ implies $\lambda_y = 0$, so that $\Sigma_{xy} = \Sigma_{yx} = \Sigma_{yy} = 0$. The condition $f_\nu = 0$ implies $\nu_{xy} = 0$, so that in this case Σ_{xx} does not generate ν_{xy} under coarse-graining, provided its bare value is zero.

A.2.2 gHK equation for $\zeta = 1$

If $\zeta = 1$, the functions intervening in the RG flow of the gHK equation simplify somewhat. Thus,

$$\begin{aligned} J_2(1,r_\nu) + J_0(r_\nu,1) = \frac{1}{8(r_\nu - f_\nu^2)^2}\Bigg\{ & \frac{4f_\nu^2(5r_\nu - 1) - 2r_\nu(1 + 4r_\nu + 3r_\nu^2)}{4f_\nu^2 - (1+r_\nu)^2} \\ & + \frac{3r_\nu^2}{\sqrt{r_\nu - f_\nu^2}}\left[\tan^{-1}\left(\frac{r_\nu + f_\nu}{\sqrt{r_\nu - f_\nu^2}}\right) + \tan^{-1}\left(\frac{r_\nu - f_\nu}{\sqrt{r_\nu - f_\nu^2}}\right)\right] \\ & + \frac{2f_\nu^2 + r_\nu}{\sqrt{r_\nu - f_\nu^2}}\left[\tan^{-1}\left(\frac{1 + f_\nu}{\sqrt{r_\nu - f_\nu^2}}\right) + \tan^{-1}\left(\frac{1 - f_\nu}{\sqrt{r_\nu - f_\nu^2}}\right)\right]\Bigg\}, \end{aligned}$$

$$J_1(1,r_\nu)+J_1(r_\nu,1)=\frac{1}{8(r_\nu-f_\nu^2)^2}\Bigg\{\frac{2f_\nu(3-8f_\nu^2+2r_\nu+3r_\nu^2)}{4f_\nu^2-(1+r_\nu)^2}$$
$$-\frac{3f_\nu r_\nu}{\sqrt{r_\nu-f_\nu^2}}\left[\tan^{-1}\left(\frac{r_\nu+f_\nu}{\sqrt{r_\nu-f_\nu^2}}\right)+\tan^{-1}\left(\frac{r_\nu-f_\nu}{\sqrt{r_\nu-f_\nu^2}}\right)\right]$$
$$-\frac{3f_\nu}{\sqrt{r_\nu-f_\nu^2}}\left[\tan^{-1}\left(\frac{1+f_\nu}{\sqrt{r_\nu-f_\nu^2}}\right)+\tan^{-1}\left(\frac{1-f_\nu}{\sqrt{r_\nu-f_\nu^2}}\right)\right]\Bigg\},$$
$$J_0(1,r_\nu)+J_2(r_\nu,1)=\frac{1}{8(r_\nu-f_\nu^2)^2}\Bigg\{\frac{4f_\nu^2(5-r_\nu)-2r_\nu(4+r_\nu)-6}{4f_\nu^2-(1+r_\nu)^2}$$
$$+\frac{2f_\nu^2+r_\nu}{\sqrt{r_\nu-f_\nu^2}}\left[\tan^{-1}\left(\frac{r_\nu+f_\nu}{\sqrt{r_\nu-f_\nu^2}}\right)+\tan^{-1}\left(\frac{r_\nu-f_\nu}{\sqrt{r_\nu-f_\nu^2}}\right)\right]$$
$$+\frac{3}{\sqrt{r_\nu-f_\nu^2}}\left[\tan^{-1}\left(\frac{1+f_\nu}{\sqrt{r_\nu-f_\nu^2}}\right)+\tan^{-1}\left(\frac{1-f_\nu}{\sqrt{r_\nu-f_\nu^2}}\right)\right]\Bigg\}.$$

These formulae can be employed in order to rewrite the flow of the couplings, which reads

$$\frac{dr_\nu}{dl}=-\frac{g}{(r_\nu-f_\nu^2)^2}\Bigg\{\frac{p_{r1}(r_\lambda)}{4f_\nu^2-(1+r_\nu)^2}$$
$$+\frac{p_{r2}(r_\lambda)}{4\sqrt{r_\nu-f_\nu^2}}\left[\tan^{-1}\left(\frac{1+f_\nu}{\sqrt{r_\nu-f_\nu^2}}\right)+\tan^{-1}\left(\frac{1-f_\nu}{\sqrt{r_\nu-f_\nu^2}}\right)\right]$$
$$+\frac{p_{r3}(r_\lambda)}{4\sqrt{r_\nu-f_\nu^2}}\left[\tan^{-1}\left(\frac{r_\nu+f_\nu}{\sqrt{r_\nu-f_\nu^2}}\right)+\tan^{-1}\left(\frac{r_\nu-f_\nu}{\sqrt{r_\nu-f_\nu^2}}\right)\right]\Bigg\},\quad\text{(A.35)}$$
$$\frac{df_\nu}{dl}=\frac{g}{2(r_\nu-f_\nu^2)^2}\Bigg\{\frac{p_{f1}(r_\lambda)}{4f_\nu^2-(1+r_\nu)^2}$$
$$-\frac{p_{f2}(r_\lambda)}{4\sqrt{r_\nu-f_\nu^2}}\left[\tan^{-1}\left(\frac{1+f_\nu}{\sqrt{r_\nu-f_\nu^2}}\right)+\tan^{-1}\left(\frac{1-f_\nu}{\sqrt{r_\nu-f_\nu^2}}\right)\right]$$
$$-\frac{p_{f3}(r_\lambda)}{4\sqrt{r_\nu-f_\nu^2}}\left[\tan^{-1}\left(\frac{r_\nu+f_\nu}{\sqrt{r_\nu-f_\nu^2}}\right)+\tan^{-1}\left(\frac{r_\nu-f_\nu}{\sqrt{r_\nu-f_\nu^2}}\right)\right]\Bigg\},\quad\text{(A.36)}$$

$$\frac{dg}{dl} = 2g + \frac{3g^2}{(r_\nu - f_\nu^2)^2}\Bigg\{ \frac{p_{g1}}{4f_\nu^2 - (1+r_\nu)^2} - \frac{p_{g2}(r_\lambda)}{4\sqrt{r_\nu - f_\nu^2}}\left[\tan^{-1}\left(\frac{1+f_\nu}{\sqrt{r_\nu - f_\nu^2}}\right) + \tan^{-1}\left(\frac{1-f_\nu}{\sqrt{r_\nu - f_\nu^2}}\right)\right] - \frac{p_{g3}(r_\lambda)}{4\sqrt{r_\nu - f_\nu^2}}\left[\tan^{-1}\left(\frac{r_\nu + f_\nu}{\sqrt{r_\nu - f_\nu^2}}\right) + \tan^{-1}\left(\frac{r_\nu - f_\nu}{\sqrt{r_\nu - f_\nu^2}}\right)\right]\Bigg\}, \quad \text{(A.37)}$$

with

$$\begin{aligned}
p_{r1}(r_\lambda) &= \left(f_\nu^2 - r_\nu\right)\left[16f_\nu^2 - (r_\nu+1)(3r_\nu+5)\right] r_\lambda^2 \\
&\quad - f_\nu\left[2f_\nu^2(r_\nu^2 - 4r_\nu - 1) + r_\nu^3 + 2r_\nu^2 + 5r_\nu\right] r_\lambda \\
&\quad - r_\nu\left[16f_\nu^4 + 8r_\nu f_\nu^3 - (5r_\nu^2 + 24r_\nu + 3)f_\nu^2\right. \\
&\quad \left. -(3r_\nu^3 + 2r_\nu^2 + 3r_\nu)f_\nu + 5r_\nu^3 + 8r_\nu^2 + 3r_\nu\right], \\
p_{r2}(r_\lambda) &= 10(f_\nu^2 - r_\nu)r_\lambda^2 + 2f_\nu(5r_\nu - 2f_\nu^2)r_\lambda + 6r_\nu(r_\nu - f_\nu r_\nu - f_\nu^2), \\
p_{r3}(r_\lambda) &= 6r_\nu(f_\nu^2 - r_\nu)r_\lambda^2 + 2f_\nu r_\nu(r_\nu + 2f_\nu^2)r_\lambda + 2r_\nu^2(5r_\nu - 3f_\nu r_\nu - 5f_\nu^2), \\
p_{f1}(r_\lambda) &= f_\nu(f_\nu^2 - r_\nu)(1 - r_\nu)r_\lambda^2 + \left[f_\nu^4(4r_\nu - 52) + f_\nu^2(10r_\nu^2 + 56r_\nu + 14)\right. \\
&\quad \left. -8r_\nu(r_\nu^2 + 2r_\nu + 1)\right] r_\lambda + 2f_\nu\left[8f_\nu^3(r_\nu + 2f_\nu) - f_\nu^2(5r_\nu^2 + 23r_\nu + 4)\right. \\
&\quad \left. -f_\nu r_\nu(3r_\nu^2 + 2r_\nu + 3) + r_\nu(5r_\nu^2 + 7r_\nu + 4)\right], \\
p_{f2}(r_\lambda) &= 4(7f_\nu^2 - 4r_\nu)r_\lambda + 4f_\nu(4r_\nu - 3f_\nu r_\nu - 4f_\nu^2), \\
p_{f3}(r_\lambda) &= 2f_\nu(r_\nu - f_\nu^2)r_\lambda^2 + 4(-4r_\nu^2 + 5f_\nu^2 r_\nu + 2f_\nu^4)r_\lambda \\
&\quad + 4f_\nu r_\nu(5r_\nu - 3f_\nu r_\nu - 5f_\nu^2), \\
p_{g1}(r_\lambda) &= r_\lambda\left[2f_\nu^3(r_\nu - 5) + f_\nu(r_\nu^2 + 4r_\nu + 3)\right] + 8f_\nu^3(r_\nu + 2f_\nu) \\
&\quad - f_\nu^2(5r_\nu^2 + 24r_\nu + 3) - f_\nu r_\nu(3r_\nu^2 + 2r_\nu + 3) + r_\nu(5r_\nu^2 + 8r_\nu + 3), \\
p_{g2}(r_\lambda) &= 6f_\nu r_\lambda + 6(r_\nu - f_\nu r_\nu - f_\nu^2), \\
p_{g3}(r_\lambda) &= 2f_\nu(2f_\nu^2 + r_\nu)r_\lambda + 2r_\nu(5r_\nu - 3f_\nu r_\nu - 5f_\nu^2).
\end{aligned}$$

A.3 Dynamic Renormalization Group analysis of the anisotropic Kardar-Parisi-Zhang equation

For the aKPZ equation, the diagrammatic expansion of the integrals that contribute to the renormalization of the bare propagator can be also sketched using general notation as shown in Figure A.3. Again $l, m = x, y$ in all possible combinations, leading to four different contributions, which will be denoted $\Sigma_{xx}, \Sigma_{xy}, \Sigma_{yx}$, and Σ_{yy}, as in the gHK case. Naturally, the values of these differ for each equation; we hope the context will hinder any potential ambiguity, as we are providing separate discussions for the two equations. After the usual symmetrization of the integration variables $(\mathbf{q}, \Omega) \to (\mathbf{j} + \mathbf{k}/2, \Omega + \omega/2)$, these contributions read

$$\Sigma_{lm}(\mathbf{k},\omega) = 2\lambda_l\lambda_m D \int^{>} \frac{d\mathbf{j}}{(2\pi)^2} \int \frac{d\Omega}{2\pi} \left(j_l^2 - \frac{k_l^2}{4}\right)\left(\frac{k_m}{2} + j_m\right) k_m \times \left|G_0\left(\frac{\hat{k}}{2} + \hat{j}\right)\right|^2 G_0\left(\frac{\hat{k}}{2} - \hat{j}\right), \tag{A.38}$$

where again $G_0(\hat{k})$ is short-hand notation for the bare propagator, which now reads

$$G_0(\hat{k}) = \left[\nu_x k_x^2 + \nu_y k_y^2 - i\omega\right]^{-1}. \tag{A.39}$$

An expansion to first order in $k_x/j_x, k_y/j_y \ll 1$ leads to

$$\lim_{\omega\to 0}\left|G_0\left(\hat{k}/2 + \hat{j}\right)\right|^2 \sim \frac{1}{\Delta^2 + \Omega^2}\left[1 - \frac{2\Delta}{\Delta^2 + \Omega^2} \times\left(\nu_x j_x k_x + \nu_y j_y k_y\right)\right], \tag{A.40}$$

$$\lim_{\omega\to 0} G_0\left(\hat{k}/2 - \hat{j}\right) \sim \frac{1}{\Delta + i\Omega}\left[1 + \frac{1}{\Delta + i\Omega}\left(\nu_x j_x k_x + \nu_y j_y k_y\right)\right]. \tag{A.41}$$

where $\Delta = \nu_x j_x^2 + \nu_y j_y^2$. Using these results in Eq. (A.38) and after integration over the frequency variable Ω, to second order in the components of $\mathbf{k}$ we get

$$\Sigma_{lm}(\mathbf{k},0) = \frac{\lambda_l\lambda_m D}{16\pi^2}\int^{>}\frac{d\mathbf{j}}{\Delta^2}\left[j_l^2 k_m^2 - \frac{2}{\Delta}k_m j_l^2 j_m\left(\nu_x k_x j_x + \nu_y k_y j_y\right)\right].$$

Considering all possible combinations for $l, m = x, y$, we obtain the coarse-grained propagator, $\Sigma = \Sigma_{xx} + \Sigma_{xy} + \Sigma_{yx} + \Sigma_{yy}$. We now take into account that the momentum shell is symmetric with respect to j_x and j_y; hence, contributions from odd functions cancel out in these integrals, leading to

$$\Sigma_{xx}(\mathbf{k},0) = \frac{\lambda_x^2 D}{16\pi^2}\int^{>}\frac{d\mathbf{j}}{\Delta^2}\left(j_x^2 - \frac{2}{\Delta}\nu_x j_x^4\right)k_x^2, \tag{A.42}$$

$$\Sigma_{xy}(\mathbf{k},0) = \frac{\lambda_x\lambda_y D}{16\pi^2}\int^{>}\frac{d\mathbf{j}}{\Delta^2}\left(j_x^2 - \frac{2}{\Delta}\nu_y j_x^2 j_y^2\right)k_y^2, \tag{A.43}$$

$$\Sigma_{yx}(\mathbf{k},0) = \frac{\lambda_x\lambda_y D}{16\pi^2}\int^{>}\frac{d\mathbf{j}}{\Delta^2}\left(j_y^2 - \frac{2}{\Delta}\nu_x j_x^2 j_y^2\right)k_x^2, \tag{A.44}$$

$$\Sigma_{yy}(\mathbf{k},0) = \frac{\lambda_y^2 D}{16\pi^2}\int^{>}\frac{d\mathbf{j}}{\Delta^2}\left(j_y^2 - \frac{2}{\Delta}\nu_y j_y^4\right)k_y^2. \tag{A.45}$$

As in the gHK case, the next step is to calculate the contributions to these integrals induced by the $\mathbf{k}$-dependence of the integration limits defining the momentum shell. Now we can split the momentum integrals in only two parts,

$$\begin{aligned}
\int^{>}\frac{d\mathbf{j}}{4\Delta^2}\left(j_x^2 - \frac{2}{\Delta}\nu_x j_x^4\right) &= \int_{\Lambda/b}^{\Lambda} dj_x \int_0^{\Lambda} dj_y \left(\frac{j_x^2}{\Delta^2} - 2\nu_x\frac{j_x^4}{\Delta^3}\right) \\
&\quad + \int_{\Lambda/b^\zeta}^{\Lambda} dj_y \int_0^{\Lambda} dj_x \left(\frac{j_x^2}{\Delta^2} - 2\nu_x\frac{j_x^4}{\Delta^3}\right) \\
&= \int_{\Lambda/b}^{\Lambda} dj_x\, j_x^2\left(I_{02}^y - 2\nu_x j_x^2 I_{03}^y\right) \\
&\quad + \int_{\Lambda/b^\zeta}^{\Lambda} dj_y\left(I_{22}^x - 2\nu_x I_{43}^x\right), \\
\int^{>}\frac{d\mathbf{j}}{4\Delta^2}\left(j_x^2 - \frac{2}{\Delta}\nu_y j_x^2 j_y^2\right) &= \int_{\Lambda/b}^{\Lambda} dj_x\, j_x^2\left(I_{02}^y - 2\nu_y I_{23}^y\right) \\
&\quad + \int_{\Lambda/b^\zeta}^{\Lambda} dj_y\left(I_{22}^x - 2\nu_y j_y^2 I_{23}^x\right), \\
\int^{>}\frac{d\mathbf{j}}{4\Delta^2}\left(j_y^2 - \frac{2}{\Delta}\nu_x j_x^2 j_y^2\right) &= \int_{\Lambda/b}^{\Lambda} dj_x\left(I_{22}^y - 2\nu_x j_x^2 I_{23}^y\right) \\
&\quad + \int_{\Lambda/b^\zeta}^{\Lambda} dj_y\, j_y^2\left(I_{02}^x - 2\nu_x I_{23}^x\right), \\
\int^{>}\frac{d\mathbf{j}}{4\Delta^2}\left(j_y^2 - \frac{2}{\Delta}\nu_y j_y^4\right) &= \int_{\Lambda/b}^{\Lambda} dj_x\left(I_{22}^y - 2\nu_y I_{43}^y\right) \\
&\quad + \int_{\Lambda/b^\zeta}^{\Lambda} dj_y\, j_y^2\left(I_{02}^x - 2\nu_y j_y^2 I_{03}^x\right),
\end{aligned}$$

where the values of the integrals

$$I_{ij}^x = \int_0^{\Lambda} ds\, s^i(\nu_x s^2 + \nu_y j_y^2)^{-j}, \tag{A.46}$$

$$I_{ij}^{y} = \int_0^{\Lambda} ds\, s^i (\nu_x j_x^2 + \nu_y s^2)^{-j}, \tag{A.47}$$

are provided in Table A.1. The remaining integrals are solved perturbatively for $\delta l \to 0$, using that $\Lambda/b = \Lambda e^{-\delta l} \sim \Lambda(1-\delta l)$, and $\Lambda/b^{\zeta} \sim \Lambda(1-\zeta\delta l)$. We thus get

$$\Sigma_{xx}(\mathbf{k},0) = \frac{\lambda_x^2 D}{16\pi^2\nu_x}(\zeta-1)\left[\frac{3\nu_x+\nu_y}{(\nu_x+\nu_y)^2} - B_{\nu_x,\nu_y,\zeta}\right] k_x^2\delta l, \tag{A.48}$$

$$\Sigma_{xy}(\mathbf{k},0) = \frac{\lambda_x\lambda_y D}{16\pi^2\nu_x}(\zeta-1)\left[B_{\nu_x,\nu_y,\zeta} - \frac{3\nu_x+\nu_y}{(\nu_x+\nu_y)^2}\right] k_y^2\delta l, \tag{A.49}$$

$$\Sigma_{yx}(\mathbf{k},0) = \frac{\lambda_x\lambda_y D}{16\pi^2\nu_y}(\zeta-1)\left[B_{\nu_x,\nu_y,\zeta} + \frac{\nu_x+3\nu_y}{(\nu_x+\nu_y)^2}\right] k_x^2\delta l, \tag{A.50}$$

$$\Sigma_{yy}(\mathbf{k},0) = \frac{\lambda_y^2 D}{16\pi^2\nu_y}(1-\zeta)\left[\frac{\nu_x+3\nu_y}{(\nu_x+\nu_y)^2} + B_{\nu_x,\nu_y,\zeta}\right] k_y^2\delta l, \tag{A.51}$$

where

$$B_{\nu_x,\nu_y,\zeta} = \frac{\tan^{-1}\left(\sqrt{\nu_y/\nu_x}\right) + \zeta\tan^{-1}\left(\sqrt{\nu_x/\nu_y}\right)}{(\zeta-1)\,(\nu_x\nu_y)^{1/2}}. \tag{A.52}$$

At this stage of the calculation it is convenient to gather the factors together, according to the parameter in the original aKPZ equation which they renormalize. We thus introduce functions $\Sigma_{\nu_{x,y}}$ through $\Sigma_{\nu_x}\delta l\,\nu_x k_x^2 \equiv \Sigma_{xx}(\mathbf{k},0) + \Sigma_{yx}(\mathbf{k},0)$ and $\Sigma_{\nu_y}\delta l\,\nu_y k_y^2 \equiv \Sigma_{xy}(\mathbf{k},0) + \Sigma_{yy}(\mathbf{k},0)$, so that the coarse-grained propagator reads

$$G_0^{<}(\mathbf{k},\omega) = \left[\nu_x\left(1-\Sigma_{\nu_x}\delta l\right)k_x^2 + \nu_y\left(1-\Sigma_{\nu_y}\delta l\right)k_y^2 - i\omega\right]^{-1}. \tag{A.53}$$

Hence, the coarse-grained surface tension parameters are $\nu_x^{<} = \nu_x(1-\Sigma_{\nu_x}\delta l)$ and $\nu_y^{<} = \nu_y(1-\Sigma_{\nu_y}\delta l)$. After rescaling as in Eq. (5.5), the corresponding flow equations become Eqs. (5.38).

The renormalization of the noise variance is again calculated from the standard diagram in Figure A.4. Similar considerations apply as in the case of the gHK equation. However, now noise does renormalize non-trivially. Indeed, in the symmetric momentum variable $\mathbf{j}$, the contributions to the coarse-grained noise variance read

$$\Phi_{lm}(\mathbf{k},\omega) = \lambda_l\lambda_m D^2 \int^{>} \frac{d\mathbf{j}}{(2\pi)^2}\int\frac{d\Omega}{2\pi}\left(\frac{k_l^2}{4}-j_l^2\right)\left(\frac{k_m^2}{4}-j_m^2\right) \times\left|G_0\left(\frac{\hat{k}}{2}+\hat{j}\right)\right|^2\left|G_0\left(\frac{\hat{k}}{2}-\hat{j}\right)\right|^2, \tag{A.54}$$

I_{02}	$\frac{1}{2a}\left(\frac{\tan^{-1}\left(\Lambda\sqrt{b/a}\right)}{\sqrt{ab}}+\frac{\Lambda}{a+b\Lambda^2}\right)$
I_{22}	$\frac{1}{2b}\left(\frac{\tan^{-1}\left(\Lambda\sqrt{b/a}\right)}{\sqrt{ab}}-\frac{\Lambda}{a+b\Lambda^2}\right)$
I_{03}	$\frac{1}{8a^2}\left(\frac{3\tan^{-1}\left(\Lambda\sqrt{b/a}\right)}{\sqrt{ab}}+\frac{\Lambda(5a+3b\Lambda^2)}{(a+b\Lambda^2)^2}\right)$
I_{23}	$\frac{1}{8ab}\left(\frac{3\tan^{-1}\left(\Lambda\sqrt{b/a}\right)}{\sqrt{ab}}+\frac{\Lambda(b\Lambda^2-a)}{(a+b\Lambda^2)^2}\right)$
I_{43}	$\frac{1}{8b^2}\left(\frac{3\tan^{-1}\left(\Lambda\sqrt{b/a}\right)}{\sqrt{ab}}-\frac{\Lambda(3a+5b\Lambda^2)}{(a+b\Lambda^2)^2}\right)$

Table A.1: Definite integrals $I_{ij}=I^x_{ij}$, Eq. (A.46), for $a=\nu_y j_y^2$ and $b=\nu_x$, and $I_{ij}=I^y_{ij}$, Eq. (A.47), for $a=\nu_x j_x^2$ and $b=\nu_y$.

where $l,m=x,y$ in all four possible combinations. Taking into account that in the perturbative expansion of Φ_{lm} we only have to retain the zeroth order contribution in $\mathbf{k}$ components, and that

$$\lim_{\omega\to 0}\left|G_0\left(\hat{k}/2-\hat{j}\right)\right|^2\sim\frac{1}{\Delta^2+\Omega^2}, \tag{A.55}$$

after the integration in the frequency variable Ω, we obtain

$$\Phi_{lm}(\mathbf{k},0)\sim\frac{\lambda_l\lambda_m D^2}{16\pi^2}\int^{>}d\mathbf{j}\,\frac{j_l^2 j_m^2}{\Delta^3}. \tag{A.56}$$

The four contributions are calculated as

$$\begin{aligned}
\Phi_{xx}(\mathbf{k},0)&=\frac{\lambda_x^2 D^2}{16\pi^2}\int^{>}d\mathbf{j}\,\frac{j_x^4}{\Delta^3}\\
&=\frac{\lambda_x^2 D^2}{4\pi^2}\left[\int_{\Lambda/b}^{\Lambda}dj_x\,j_x^4 I^y_{03}+\int_{\Lambda/b^\zeta}^{\Lambda}dj_y\,I^x_{43}\right]\\
&\sim\frac{\lambda_x^2 D^2}{32\pi^2\nu_x^2}(\zeta-1)\left[3B_{\nu_x,\nu_y,\zeta}-\frac{5\nu_x+3\nu_y}{(\nu_x+\nu_y)^2}\right]\delta l,
\end{aligned} \tag{A.57}$$

$$\begin{aligned}
\Phi_{xy}(\mathbf{k},0)=\Phi_{yx}(\mathbf{k},0)&=\frac{\lambda_x\lambda_y D^2}{16\pi^2}\int^{>}d\mathbf{j}\,\frac{j_x^2 j_y^2}{\Delta^3}\\
&=\frac{\lambda_x\lambda_y D^2}{4\pi^2}\left[\int_{\Lambda/b}^{\Lambda}dj_x\,j_x^2 I^y_{23}+\int_{\Lambda/b^\zeta}^{\Lambda}dj_y\,j_y^2 I^x_{23}\right]
\end{aligned}$$

$$\sim \frac{\lambda_x \lambda_y D^2}{32\pi^2 \nu_x \nu_y}(\zeta - 1)\left[B_{\nu_x,\nu_y,\zeta} + \frac{\nu_x - \nu_y}{(\nu_x + \nu_y)^2}\right]\delta l, \tag{A.58}$$

$$\begin{aligned}\Phi_{yy}(\mathbf{k},0) &= \frac{\lambda_y^2 D^2}{16\pi^2}\int^{>} d\mathbf{j}\,\frac{j_y^4}{\Delta^3} \\ &= \frac{\lambda_y^2 D^2}{4\pi^2}\left[\int_{\Lambda/b}^{\Lambda} dj_x\, I_{43}^{y} + \int_{\Lambda/b^\zeta}^{\Lambda} dj_y\, j_y^4 I_{03}^{x}\right] \\ &\sim \frac{\lambda_y^2 D^2}{32\pi^2 \nu_y^2}(\zeta - 1)\left[3B_{\nu_x,\nu_y,\zeta} + \frac{3\nu_x + 5\nu_y}{(\nu_x + \nu_y)^2}\right]\delta l,\end{aligned} \tag{A.59}$$

and finally

$$\Phi(\mathbf{k},0) = \sum_{l,m=x,y}\Phi_{lm}(\mathbf{k},0) = \frac{D^2}{32\pi^2}(\zeta - 1)\left[3B_{\nu_x,\nu_y,\zeta}\left(\frac{\lambda_x^2}{\nu_x^2} + \frac{2\lambda_x\lambda_y}{3\nu_x\nu_y} + \frac{\lambda_y^2}{\nu_y^2}\right)\right.$$
$$\left. + \left(\frac{\lambda_y^2(3\nu_x + 5\nu_y)}{\nu_y^2(\nu_x + \nu_y)^2} + \frac{2\lambda_x\lambda_y(\nu_x - \nu_y)}{\nu_x\nu_y(\nu_x + \nu_y)^2} - \frac{\lambda_x^2(5\nu_x + 3\nu_y)}{\nu_x^2(\nu_x + \nu_y)^2}\right)\right]\delta l.$$

Note this function is $\mathbf{k}$-independent, hence it implies a non-trivial effect of coarse-graining in the noise variance for the aKPZ equation. By introducing a function Φ_D through $\Phi_D D\delta l \equiv \Phi(\mathbf{k},0)$, the coarse-grained noise variance is $D^< = D(1 + \Phi_D \delta l)$. After rescaling as in Eq. (5.5), the corresponding flow equation becomes Eq. (5.40). Finally, the one-loop contributions to the renormalization of the nonlinearities $\lambda_{x,y}$ cancel out [104], giving rise to Eq. (5.39), thus completing the DRG flow for the aKPZ equation.

B

POWER SPECTRAL DENSITY DATA

In what follows, we present the raw data for the one and two-dimensional PSDs, both for the unstable and the stable case, and we discuss in detail the procedure to perform the average, resulting into Figsures 6.3 and 6.5.

Obviously, if all sample windows spanned the same interval in wave-vectors k, with the same step $\mathrm{d}k$, then performing the average of the PSDs would be straightforward. However, since, as explained in Chapter 6, we deal with windows of different sizes and measured with different resolutions, we have chosen another method to average them. Namely, for each data set, we have performed the following operations:

i) We first determine the range of k values that is spanned by all the PSDs.
ii) We then divide this interval in a number of bins, n.
iii) For each bin, we have chosen its middle point in k as representative.
iv) We have computed the average of all the points in each bin, and assigned the resulting value to the representative point in k.

The result is obviously dependent on the value of n chosen for each data set. For small values of n, the resulting average would have a poor resolution, and a scaling analysis would be impossible. On the other hand, large values of n would result into a very high resolution for the average, but the signal-to-noise ratio would be low, thus affecting the reliability of our estimate for the exponents.

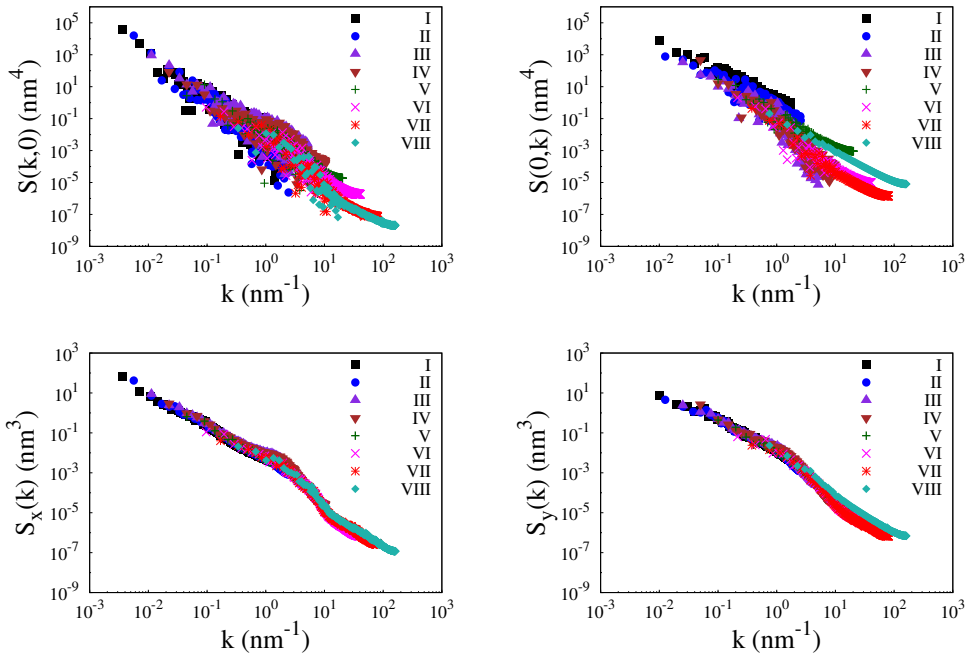

Figure B.1: Raw data for the morphologically stable case. Upper panel: one-dimensional projections, $S(k,0)$ and $S(0,k)$, of the two-dimensional PSDs, for each sample window. Lower panel: PSDs of one-dimensional cuts of the sample, $S_x(k)$ and $S_y(k)$, for each sample window. The legend refers to the number of the window (see Table 6.1).

B.1 Morphologically stable case

We start by considering the morphologically stable case. Figure B.1 provides the raw data for the PSDs. High frequency data ($k > 10$ nm^{-1}) have not been employed for the scaling analysis. Specifically, the upper panel of Figure B.1 shows the raw data for the projections of the two-dimensional PSD, whose average, carried out using n bins, results into the left panel of Figure 6.3. The lower panel displays the one-dimensional PSDs, their average being provided in the right panel of Figure 6.3.

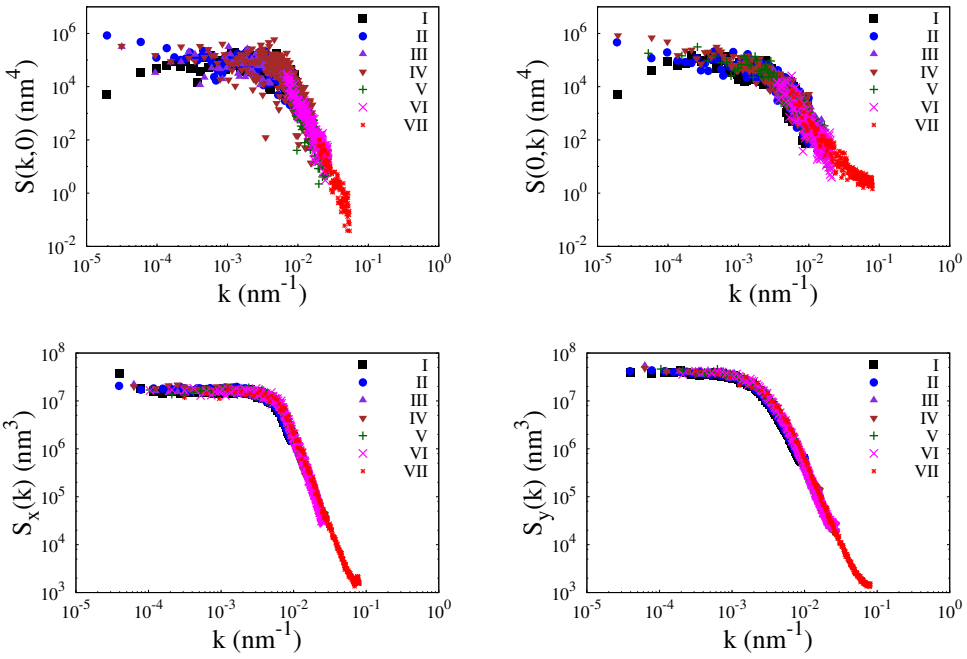

Figure B.2: Raw data for the morphologically unstable case. Upper panel: one-dimensional projections $S(k,0)$ and $S(0,k)$ of the two-dimensional PSDs, for each sample window. Lower panel: PSDs of one-dimensional cuts of the sample $S_x(k)$ and $S_y(k)$, for each sample window. The legend refers to the number of the window (see Table 6.2).

B.2 Morphologically unstable case

Next we consider the morphologically unstable case. In Figure B.2 we show the raw data for the PSDs. High frequency data ($k > 10^{-2}$ nm^{-1}) have not been employed for the scaling analysis. Specifically, the upper panel of Figure B.2 shows data for the projections of the two-dimensional PSDs, whose average, performed with n bins, provides the left panel of Figure 6.5. The one dimensional PSDs are displayed in the lower panel of Figure B.2, and their average (n bins) gives rise to the right panel of Figure 6.5.

REFERENCES

[1] S. A. Safran, *Statistical Thermodynamics of Surfaces, Interfaces, and Membranes*. Boulder, CO.: Westview Press, 2003.
Cited on page III.

[2] M. Kléman, *Soft Matter Physics: An Introduction*, ser. Partially ordered systems. New York: Springer, 2003.
Cited on page III.

[3] D. L. Allara, "A perspective on surfaces and interfaces," *Nature*, vol. 437, p. 638, 2005.
Cited on page III.

[4] U. Landman, "Materials by numbers: Computations as tools of discovery," *Proceedings of the National Academy of Sciences*, vol. 102, p. 6671, 2005.
Cited on page III.

[5] A. L. Barabási and H. Stanley, *Fractal Concepts in Surface Growth*. Cambridge: Cambridge University Press, 1995.
Cited on pages III, 1, 7, 8, 10, 11, 13, 14, 27, 33, 44, 46, 52, 55, 57, 58, 60, 65, 68, 78, 79, 84, 92, and 107.

[6] B. B. Mandelbrot, *The Fractal Geometry of Nature*. San Francisco: W.H. Freeman, 1982.
Cited on page III.

[7] G. Grinstein, "Generic scale invariance in classical nonequilibrium systems," *Journal of Applied Physics*, vol. 69, p. 5441, 1991.
Cited on pages III, 2, 6, 7, 8, 9, 63, and 76.

[8] G. Grinstein, "Generic scale invariance and self-organized criticality," in *Scale Invariance, Interfaces and Nonequilibrium Dynamics*, A. McKane, M. Droz, J. Vannimenus, and D. Wolf, Eds. New York: Plenum Press, 1995.
Cited on pages III, 2, 6, 7, 8, 9, 63, 76, and 83.

[9] N. Goldenfeld, *Lectures on Phase Transitions and the Renormalization Group*. Addison-Wesley, 1993.
Cited on pages IV, 1, 2, 3, 4, 5, 6, 20, and 28.

[10] J. J. Binney, N. J. Dowrick, J. Fisher, and M. E. J. Newman, *The Theory of Critical Phenomena: An Introduction to the Renormalization Group*. Oxford: Oxford University Press, 1992.
Cited on pages 1, 5, and 28.

[11] D. Belitz, T. R. Kirkpatrick, and T. Vojta, "How generic scale invariance influences quantum and classical phase transitions," *Reviews of modern physics*, vol. 77, p. 579, 2005.
Cited on page 2.

[12] H. J. Jensen, *Self-organized Criticality: Emergent Complex Behavior in Physical and Biological Systems*, ser. Cambridge lecture notes in physics. Cambridge ; New York: Cambridge University Press, 1998, no. 10.
Cited on pages 2 and 61.

[13] G. Pruessner, *Self-organised Criticality: Theory, Models, and Characterisation*. Cambridge ; New York: Cambridge University Press, 2012.
Cited on page 2.

[14] V. Frette, K. Christensen, A. Malthe-Sørenssen, J. Feder, T. Jøssang, and P. Meakin, "Avalanche dynamics in a pile of rice," *Nature*, vol. 379, p. 49, 1996.
Cited on page 2.

[15] K. Christensen and N. R. Moloney, *Complexity and Criticality*. London: Imperial College Press, 2000.
Cited on pages 2 and 5.

[16] J. P. Sethna, *Statistical Mechanics: Entropy, Order Parameters, and Complexity*. Oxford: Oxford Univeristy Press, 2006.
Cited on page 2.

[17] J. S. Langer, "An introduction to the kinetics of first-order phase transitions," in *Solids far from equilibrium*, C. Godrèche, Ed., p. 297. Cambridge: Cambridge University Press, 1991.
Cited on page 3.

[18] S. Ma, *Modern Theory of Critical Phenomena*, ser. Advanced book classics. Cambridge, Mass: Perseus Pub, 2000.
Cited on pages 6 and 30.

[19] M. Kardar, *Statistical Physics of Fields*. Cambridge: Cambridge University Press, 2007.
Cited on pages 7, 8, 64, 65, and 68.

[20] J. Krug, "Origins of scale invariance in growth processes," *Advances in Physics*, vol. 46, p. 139, 1997.
Cited on pages 7, 16, and 44.

[21] C. Haselwandter and D. Vvedensky, "Multiscale theory of fluctuating interfaces: Renormalization of atomistic models," *Physical Review Letters*, vol. 98, p. 046102, 2007.
Cited on pages 8 and 28.

[22] R. Cuerno, M. Castro, J. Muñoz-García, R. Gago, and L. Vázquez, "Universal non-equilibrium phenomena at submicrometric surfaces and interfaces," *The European Physical Journal Special Topics*, vol. 146, p. 427, 2007.
Cited on pages 8, 102, and 104.

[23] A. Corral and A. Díaz-Guilera, "Symmetries and fixed point stability of stochastic differential equations modeling self-organized criticality," *Physical Review E*, vol. 55, p. 2434, 1997.
Cited on page 8.

[24] M. Kardar, G. Parisi, and Y.-C. Zhang, "Dynamic scaling of growing interfaces," *Physical Review Letters*, vol. 56, p. 889, 1986.
Cited on pages 9 and 16.

[25] M. Schwartz and E. Perlsman, "Upper critical dimension of the Kardar-Parisi-Zhang equation," *Physical Review E*, vol. 85, p. 050103(R), 2012.
Cited on page 9.

[26] T. Kloss, L. Canet, and N. Wschebor, "Nonperturbative renormalization group for the stationary Kardar-Parisi-Zhang equation: scaling functions and amplitude ratios in 1+1, 2+1, and 3+1 dimensions," *Physical Review E*, vol. 86, p. 051124, 2012.
Cited on pages 9 and 28.

[27] K. A. Takeuchi, M. Sano, T. Sasamoto, and H. Spohn, "Growing interfaces uncover universal fluctuations behind scale invariance," *Scientific Reports*, vol. 1, p. 1, 2011.
Cited on page 10.

[28] F. Family and T. Vicsek, *Dynamics of Fractal Surfaces*. World Scientific, 1991.
Cited on page 11.

[29] J. G. Moreira, J. K. L. d. Silva, and S. O. Kamphorst, "On the fractal dimension of self-affine profiles," *Journal of Physics A: Mathematical and General*, vol. 27, p. 8079, 1994.
Cited on page 11.

[30] M. Castro and R. Cuerno, "Hydrodynamic approach to surface pattern formation by ion beams," *Applied Surface Science*, vol. 258, p. 4171, 2012.
Cited on pages 13 and 104.

[31] L. Giada, A. Giacometti, and M. Rossi, "Pseudospectral method for the Kardar-Parisi-Zhang equation," *Physical Review E*, vol. 65, p. 036134, 2002.
Cited on pages 14, 34, and 45.

[32] M. Nicoli, E. Vivo, and R. Cuerno, "Kardar-Parisi-Zhang asymptotics for the two-dimensional noisy Kuramoto-Sivashinsky equation," *Physical Review E*, vol. 82, p. 045202(R), 2010.
Cited on pages 14, 45, 97, 102, and 112.

[33] Z.-W. Lai and S. Das Sarma, "Kinetic growth with surface relaxation: Continuum versus atomistic models," *Physical Review Letters*, vol. 66, p. 2348, 1991.
Cited on pages 14 and 76.

[34] H. Janssen, "On critical exponents and the renormalization of the coupling constant in growth models with surface diffusion," *Physical Review Letters*, vol. 78, p. 1082, 1997.
Cited on pages 14 and 76.

[35] R. Cuerno and L. Vázquez, "Universality issues in surface kinetic roughening of thin solid films," in *Advances in Condensed Matter and Statistical Physics*, E. Korutcheva and R. Cuerno, Eds., p. 237. New York: Nova Science Publishers, 2004.
Cited on pages 14, 52, and 114.

[36] E. Medina, T. Hwa, M. Kardar, and Y. Zhang, "Burgers equation with correlated noise: Renormalization-group analysis and applications to directed polymers and interface growth," *Physical Review A*, vol. 39, p. 3053, 1989.
Cited on page 14.

[37] Y.-C. Zhang, "Growth anomaly and its implications," *Physica A: Statistical Mechanics and its Applications*, vol. 170, p. 1, 1990.
Cited on page 14.

[38] K. Lauritsen, "Growth equation with a conservation law," *Physical Review E*, vol. 52, p. R1261, 1995.
Cited on page 14.

[39] E. Flekkøy and D. Rothman, "Fluctuating fluid interfaces," *Physical Review Letters*, vol. 75, p. 260, 1995.
Cited on page 15.

[40] J. López and M. Rodríguez, "Lack of self-affinity and anomalous roughening in growth processes," *Physical Review E*, vol. 54, p. R2189, 1996.
Cited on page 15.

[41] M. Nicoli, R. Cuerno, and M. Castro, "Dimensional fragility of the Kardar–Parisi–Zhang universality class," *Journal of Statistical Mechanics: Theory and Experiment*, vol. 2013, p. P11001, 2013.
Cited on pages 15 and 18.

[42] M. Henkel, H. Hinrichsen, and S. Lübeck, *Non-equilibrium Phase Transitions. Vol. 1*. Dordrecht: Kluwer Academic Publishers, 2008.
Cited on pages 15 and 107.

[43] K. A. Takeuchi and M. Sano, "Universal fluctuations of growing interfaces: Evidence in turbulent liquid crystals," *Physical Review Letters*, vol. 104, p. 230601, 2010.
Cited on page 16.

[44] C. Misbah, O. Pierre-Louis, and Y. Saito, "Crystal surfaces in and out of equilibrium: A modern view," *Reviews of Modern Physics*, vol. 82, p. 981, 2010.
Cited on pages 16, 18, 20, and 76.

[45] M. Matsushita, J. Wakita, H. Itoh, I. Ràfols, T. Matsuyama, H. Sakaguchi, and M. Mimura, "Interface growth and pattern formation in bacterial colonies," *Physica A: Statistical Mechanics and its Applications*, vol. 249, p. 517, 1998.
Cited on page 16.

[46] T. Kwon, A. Hopkins, and S. O'Donnell, "Dynamic scaling behavior of a growing self-affine fractal interface in a paper-towel-wetting experiment," *Physical Review E*, vol. 54, p. 685, 1996.
Cited on page 16.

[47] T. Engøy, K. Måløy, A. Hansen, and S. Roux, "Roughness of two-dimensional cracks in wood," *Physical Review Letters*, vol. 73, p. 834, 1994.
Cited on page 16.

[48] L. Miettinen, M. Myllys, J. Merikoski, and J. Timonen, "Experimental determination of KPZ height-fluctuation distributions," *The European Physical Journal B*, vol. 46, p. 55, 2005.
Cited on page 16.

[49] J. Krug, P. Meakin, and T. Halpin-Healy, "Amplitude universality for driven interfaces and directed polymers in random media," *Physical Review A*,

vol. 45, p. 638, 1992.
Cited on page 16.

[50] T. Kriecherbauer and J. Krug, "A pedestrian's view on interacting particle systems, KPZ universality and random matrices," *Journal of Physics A: Mathematical and Theoretical*, vol. 43, p. 403001, 2010.
Cited on page 17.

[51] J. Baik, P. Deift, and K. Johansson, "On the distribution of the length of the longest increasing subsequence of random permutations," *Journal of the American Mathematical Society*, vol. 12, p. 1119, 1999.
Cited on page 17.

[52] K. Johansson, "Shape fluctuations and random matrices," *Communications in mathematical physics*, vol. 209, p. 437, 2000.
Cited on page 17.

[53] C. A. Tracy and H. Widom, "Level-spacing distributions and the Airy kernel," *Communications in Mathematical Physics*, vol. 159, p. 151, 1994.
Cited on page 17.

[54] M. Prähofer and H. Spohn, "Statistical self-similarity of one-dimensional growth processes," *Physica A: Statistical Mechanics and its Applications*, vol. 279, p. 342, 2000.
Cited on page 17.

[55] M. Prähofer and H. Spohn, "Universal distributions for growth processes in 1+1 dimensions and random matrices," *Physical Review Letters*, vol. 84, p. 4882, 2000.
Cited on page 17.

[56] M. Prähofer and H. Spohn, "Scale invariance of the PNG droplet and the Airy process," *Journal of statistical physics*, vol. 108, p. 1071, 2002.
Cited on page 17.

[57] I. Corwin, "The Kardar–Parisi–Zhang equation and universality class," *Random Matrices: Theory and Applications*, vol. 01, p. 1130001, 2012.
Cited on page 17.

[58] L. Bertini and G. Giacomin, "Stochastic Burgers and KPZ equations from particle systems," *Communications in Mathematical Physics*, vol. 183, p. 571, 1997.
Cited on page 17.

[59] T. Sasamoto and H. Spohn, "One-dimensional Kardar-Parisi-Zhang equation: An exact solution and its universality," *Physical Review Letters*, vol. 104, p. 230602, 2010.
Cited on page 17.

[60] G. Amir, I. Corwin, and J. Quastel, "Probability distribution of the free energy of the continuum directed random polymer in 1 + 1 dimensions," *Communications on Pure and Applied Mathematics*, vol. 64, p. 466, 2011.
Cited on page 17.

[61] P. Calabrese and P. Le Doussal, "Exact solution for the Kardar-Parisi-Zhang equation with flat initial conditions," *Physical Review Letters*, vol. 106, p. 250603, 2011.
Cited on pages 17 and 27.

[62] K. A. Takeuchi and M. Sano, "Evidence for geometry-dependent universal fluctuations of the Kardar-Parisi-Zhang interfaces in liquid-crystal turbulence," *Journal of Statistical Physics*, vol. 147, p. 853, 2012.
Cited on page 18.

[63] T. Halpin-Healy, "(2+1)-dimensional directed polymer in a random medium: Scaling phenomena and universal distributions," *Physical Review Letters*, vol. 109, p. 170602, 2012.
Cited on page 18.

[64] T. Halpin-Healy and G. Palasantzas, "Universal correlators and distributions as experimental signatures of (2 + 1)-dimensional Kardar-Parisi-Zhang growth," *Europhysics Letters*, vol. 105, p. 50001, 2014.
Cited on pages 18, 118, and 119.

[65] R. A. L. Almeida, S. O. Ferreira, T. J. Oliveira, and F. D. A. A. Reis, "Universal fluctuations in the growth of semiconductor thin films," *Physical Review B*, vol. 89, p. 045309, 2014.
Cited on pages 18 and 119.

[66] S. H. Davis, *Theory of Solidification*, ser. Cambridge monographs on mechanics. Cambridge: Cambridge University Press, 2001.
Cited on page 18.

[67] C. Schelling, G. Springholz, and F. Schäffler, "Kinetic growth instabilities on vicinal Si(001) surfaces," *Physical Review Letters*, vol. 83, p. 995, 1999.
Cited on page 18.

[68] M. Sato and M. Uwaha, "Pattern formation in the instability of a vicinal surface by the drift of adatoms," *Physical Review E*, vol. 60, p. 7120, 1999.
Cited on page 18.

[69] A. D. Verga, "Anisotropic dynamics of a vicinal surface under the meandering step instability," *Physical Review B*, vol. 80, p. 174115, 2009.
Cited on page 18.

[70] A. Ballestad, B. Ruck, M. Adamcyk, T. Pinnington, and T. Tiedje, "Evidence from the surface morphology for nonlinear growth of epitaxial GaAs films," *Physical Review Letters*, vol. 86, p. 2377, 2001.
Cited on page 18.

[71] A. Ballestad, B. Ruck, J. Schmid, M. Adamcyk, E. Nodwell, C. Nicoll, and T. Tiedje, "Surface morphology of GaAs during molecular beam epitaxy growth: Comparison of experimental data with simulations based on continuum growth equations," *Physical Review B*, vol. 65, p. 205302, 2002.
Cited on pages 18 and 19.

[72] W. L. Chan and E. Chason, "Making waves: Kinetic processes controlling surface evolution during low energy ion sputtering," *Journal of Applied Physics*, vol. 101, p. 121301, 2007.
Cited on pages 18, 99, 100, and 109.

[73] J. Muñoz-García, L. Vázquez, R. Cuerno, J. A. Sánchez-García, M. Castro, and R. Gago, "Self-organized surface nanopatterning by ion beam sputtering," in *Towards Functional Nanomaterials*, Z. M. Wang, Ed., p. 323. New York: Springer US, 2009.
Cited on pages 18, 99, 100, 101, 109, and 112.

[74] D. Bonamy and E. Bouchaud, "Failure of heterogeneous materials: A dynamic phase transition?" *Physics Reports*, vol. 498, p. 1, 2011.
Cited on pages 18, 53, and 120.

[75] R. Pastor-Satorras and D. Rothman, "Scaling of a slope: The erosion of tilted landscapes," *Journal of statistical physics*, vol. 93, p. 477, 1998.
Cited on pages 19 and 56.

[76] R. M. Bradley and J. M. E. Harper, "Theory of ripple topography induced by ion bombardment," *Journal of Vacuum Science and Technology A*, vol. 6, p. 2390, 1988.
Cited on pages 20 and 102.

[77] Y. Zhao, G. Wang, and T. Lu, "Anisotropy in growth-front roughening," *Physical Review B*, vol. 58, p. 13909, 1998.
Cited on pages 20, 57, and 58.

[78] U. C. Täuber and E. Frey, "Universality classes in the anisotropic Kardar-Parisi-Zhang model," *Europhysics Letters*, vol. 59, p. 655, 2002.
Cited on page 21.

[79] D. Wolf, "Kinetic roughening of vicinal surfaces," *Physical Review Letters*, vol. 67, p. 1783, 1991.
Cited on pages 21, 89, 91, and 97.

[80] R. da Silveira and M. Kardar, "Nonlinear stochastic equations with calculable steady states," *Physical Review E*, vol. 68, p. 046108, 2003.
Cited on page 21.

[81] M. Rost and J. Krug, "Anisotropic Kuramoto-Sivashinsky equation for surface growth and erosion," *Physical Review Letters*, vol. 75, p. 3894, 1995.
Cited on pages 21 and 97.

[82] A. Barabási, M. Araujo, and H. Stanley, "Three-dimensional Toom model: Connection to the anisotropic Kardar-Parisi-Zhang equation," *Physical Review Letters*, vol. 68, p. 3729, 1992.
Cited on page 21.

[83] H. Kallabis, "Conserved growth on vicinal surfaces," *Journal of Physics A: Mathematical and General*, vol. 31, p. L581, 1998.
Cited on pages 22, 76, and 78.

[84] M. Cross and H. Greenside, *Pattern Formation and Dynamics in Nonequilibrium Systems*. Cambridge: Cambridge University Press, 2009.
Cited on pages 22, 23, 24, and 41.

[85] S. Facsko, "Formation of ordered nanoscale semiconductor dots by ion sputtering," *Science*, vol. 285, p. 1551, 1999.
Cited on page 23.

[86] B. Ziberi, F. Frost, T. Höche, and B. Rauschenbach, "Ripple pattern formation on silicon surfaces by low-energy ion-beam erosion: Experiment and theory," *Physical Review B*, vol. 72, p. 235310, 2005.
Cited on page 23.

[87] R. Gago, L. Vázquez, R. Cuerno, M. Varela, C. Ballesteros, and J. M. Albella, "Production of ordered silicon nanocrystals by low-energy ion sputtering," *Applied Physics Letters*, vol. 78, p. 3316, 2001.
Cited on page 23.

[88] D. R. Reichman and P. Charbonneau, "Mode-coupling theory," *Journal of Statistical Mechanics: Theory and Experiment*, vol. 2005, p. P05013, 2005.
Cited on page 28.

[89] P.-M. Lam and F. Family, "Mode-coupling theory and simulations results for the "running-sandpile" model of self-organized criticality," *Physical Review E*, vol. 47, p. 1570, 1993.
Cited on page 28.

[90] M. Schwartz and E. Katzav, "The ideas behind self-consistent expansion," *Journal of Statistical Mechanics: Theory and Experiment*, vol. 2008, p.

P04023, 2008.
Cited on pages 28 and 68.

[91] K. Wilson, "The renormalization group and the ε expansion," *Physics Reports*, vol. 12, p. 75, 1974.
Cited on page 28.

[92] K. G. Wilson, "Renormalization group methods," *Advances in Mathematics*, vol. 16, p. 170, 1975.
Cited on page 28.

[93] L. Pietronero, A. Vespignani, and S. Zapperi, "Renormalization scheme for self-organized criticality in sandpile models," *Physical Review Letters*, vol. 72, p. 1690, 1994.
Cited on page 28.

[94] C. Castellano, A. Gabrielli, M. Marsili, M. Muñoz, and L. Pietronero, "High dimensional behavior of the Kardar-Parisi-Zhang growth dynamics," *Physical Review E*, vol. 58, p. R5209, 1998.
Cited on page 28.

[95] P. Martin, E. Siggia, and H. Rose, "Statistical dynamics of classical systems," *Physical Review A*, vol. 8, p. 423, 1973.
Cited on page 28.

[96] H.-K. Janssen, "On a lagrangean for classical field dynamics and renormalization group calculations of dynamical critical properties," *Zeitschrift für Physik B Condensed Matter*, vol. 23, p. 377, 1976.
Cited on page 28.

[97] C. De Dominicis, "Techniques de renormalisation de la théorie des champs et dynamique des phénomènes critiques," *Le Journal de Physique Colloques*, vol. 37, pp. C1–247, 1976.
Cited on page 28.

[98] H. Janssen, "Field-theoretic method applied to critical dynamics," in *Dynamical Critical Phenomena and Related Topics*, C. Enz, Ed., p. 25. Springer Berlin Heidelberg, 1979, vol. 104.
Cited on page 28.

[99] L. Canet, H. Chaté, B. Delamotte, and N. Wschebor, "Nonperturbative renormalization group for the Kardar-Parisi-Zhang equation," *Physical Review Letters*, vol. 104, p. 150601, 2010.
Not cited.

[100] J. Zinn-Justin, *Quantum Field Theory and Critical Phenomena*, ser. International series of monographs on physics. Oxford : New York:

Clarendon Press ; Oxford University Press, 2002, no. 113.
Cited on page 28.

[101] D. Forster, D. Nelson, and M. Stephen, "Large-distance and long-time properties of a randomly stirred fluid," *Physical Review A*, vol. 16, p. 732, 1977.
Cited on page 28.

[102] W. D. McComb, *The Physics of Fluid Turbulence*. Oxford: Oxford University Press, 1992.
Cited on pages 28, 30, and 126.

[103] M. Nicoli, M. Castro, and R. Cuerno, "Kinetic roughening in a realistic model of non-conserved interface growth," *Journal of Statistical Mechanics: Theory and Experiment*, vol. 2009, p. P02036, 2009.
Cited on pages 28 and 72.

[104] M. Nicoli, R. Cuerno, and M. Castro, "Dynamical renormalization group study for a class of non-local interface equations," *Journal of Statistical Mechanics: Theory and Experiment*, vol. 2011, p. P10030, 2011.
Cited on pages 28, 31, 72, 79, 133, and 140.

[105] A. Keller, M. Nicoli, S. Facsko, and R. Cuerno, "Dynamic effects induced by renormalization in anisotropic pattern forming systems," *Physical Review E*, vol. 84, p. 015202, 2011.
Cited on pages 28, 97, and 119.

[106] A. Keller, M. Nicoli, S. Facsko, and R. Cuerno, "Erratum: Dynamic effects induced by renormalization in anisotropic pattern forming systems [Phys. Rev. E 84, 015202(R) (2011)]," *Physical Review E*, vol. 85, p. 029905, 2012.
Cited on pages 28 and 97.

[107] T. Halpin-Healy and Y. Zhang, "Kinetic roughening phenomena, stochastic growth, directed polymers and all that." *Physics Reports*, vol. 254, p. 215, 1995.
Cited on page 33.

[108] C. Dasgupta, S. Das Sarma, and J. Kim, "Controlled instability and multiscaling in models of epitaxial growth," *Physical Review E*, vol. 54, p. 4552, 1996.
Cited on page 33.

[109] C. Dasgupta, J. Kim, M. Dutta, and S. Sarma, "Instability, intermittency, and multiscaling in discrete growth models of kinetic roughening," *Physical Review E*, vol. 55, p. 2235, 1997.
Cited on page 33.

[110] C. Lam and F. Shin, "Anomaly in numerical integrations of the Kardar-Parisi-Zhang equation," *Physical Review E*, vol. 57, p. 6506, 1998.
Cited on page 33.

[111] V. G. Miranda and F. D. A. Aarão Reis, "Numerical study of the Kardar-Parisi-Zhang equation," *Physical Review E*, vol. 77, p. 031134, 2008.
Cited on page 33.

[112] C. Canuto, M. Y. Hussaini, A. Quarteroni, and T. A. Zang, *Spectral Methods: Evolution to Complex Geometries and Applications to Fluid Dynamics*. Springer Verlag, 2007.
Cited on pages 33, 36, 37, and 38.

[113] A. Giacometti and M. Rossi, "Pseudospectral approach to inverse problems in interface dynamics," *Physical Review E*, vol. 63, p. 046102, 2001.
Cited on page 34.

[114] C. Lam and F. Shin, "Improved discretization of the Kardar-Parisi-Zhang equation," *Physical Review E*, vol. 58, p. 5592, 1998.
Cited on page 34.

[115] S. Cox and P. Matthews, "Exponential time differencing for stiff systems," *Journal of Computational Physics*, vol. 176, p. 430, 2002.
Cited on pages 34 and 38.

[116] R. Holland, "Finite-difference time-domain (FDTD) analysis of magnetic diffusion," *IEEE Transactions on Electromagnetic Compatibility*, vol. 36, p. 32, 1994.
Cited on page 34.

[117] C. Schuster, A. Christ, and W. Fichtner, "Review of FDTD time-stepping schemes for efficient simulation of electric conductive media," *Microwave and Optical Technology Letters*, vol. 25, p. 16, 2000.
Cited on page 34.

[118] R. Gallego, "Predictor–corrector pseudospectral methods for stochastic partial differential equations with additive white noise," *Applied Mathematics and Computation*, vol. 218, p. 3905, 2011.
Cited on page 34.

[119] A.-K. Kassam and L. N. Trefethen, "Fourth-order time-stepping for stiff PDEs," *SIAM Journal on Scientific Computing*, vol. 26, p. 1214, 2005.
Cited on page 34.

[120] A. Jentzen and P. E. Kloeden, "Overcoming the order barrier in the numerical approximation of stochastic partial differential equations

with additive space-time noise," *Proceedings of the Royal Society A: Mathematical, Physical and Engineering Sciences*, vol. 465, p. 649, 2009.
Cited on page 34.

[121] A. Jentzen and P. Kloeden, "Taylor expansions of solutions of stochastic partial differential equations with additive noise," *The Annals of Probability*, vol. 38, p. 532, 2010.
Cited on page 34.

[122] V. Karlin, V. Maz'ya, and G. Schmidt, "High accuracy periodic solutions to the Sivashinsky equation," *Journal of Computational Physics*, vol. 188, p. 209, 2003.
Cited on page 34.

[123] R. Toral and P. Colet, *Stochastic Numerical Methods: An Introduction for Scientists*. Weinheim, Bergstr: Wiley-VCH, 2014.
Cited on page 35.

[124] J. Muñoz-Garcia, "Invariancia de escala y formación de patrones en la erosión de superficies," Ph.D. dissertation, Universidad Carlos III de Madrid, Leganés, Madrid, 2007.
Cited on pages 38 and 100.

[125] M. Nicoli, "Quantitative approach to unstable nonconserved growth with fluctuations," Ph.D. dissertation, Universidad Carlos III de Madrid, Leganés, Madrid, 2009.
Cited on page 38.

[126] Y. Kuramoto and T. Yamada, "Pattern formation in oscillatory chemical reactions," *Progress of Theoretical Physics*, vol. 56, p. 724, 1976.
Cited on page 42.

[127] G. Sivashinsky, "Nonlinear analysis of hydrodynamic instability in laminar flames–I. Derivation of basic equations," *Acta Astronautica*, vol. 4, p. 1177, 1977.
Cited on page 42.

[128] A. Karma and C. Misbah, "Competition between noise and determinism in step flow growth," *Physical Review Letters*, vol. 71, p. 3810, 1993.
Cited on pages 42 and 97.

[129] R. Cuerno and A.-L. Barabási, "Dynamic scaling of ion-sputtered Surfaces," *Physical Review Letters*, vol. 74, p. 4746, 1995.
Cited on pages 42 and 102.

[130] C. C. Chow and T. Hwa, "Defect-mediated stability: an effective hydrodynamic theory of spatiotemporal chaos," *Physica D: Nonlinear*

Phenomena, vol. 84, p. 494, 1995.
Cited on pages 42 and 49.

[131] P. Manneville, "Statistical properties of chaotic solutions of a one-dimensional model for phase turbulence," *Physics Letters A*, vol. 84, p. 129, 1981.
Cited on page 42.

[132] K. Sneppen, J. Krug, M. Jensen, C. Jayaprakash, and T. Bohr, "Dynamic scaling and crossover analysis for the Kuramoto-Sivashinsky equation," *Physical Review A*, vol. 46, p. R7351, 1992.
Cited on pages 42 and 118.

[133] R. Cuerno, H. Makse, S. Tomassone, S. Harrington, and H. Stanley, "Stochastic model for surface erosion via ion sputtering: Dynamical evolution from ripple morphology to rough morphology," *Physical Review Letters*, vol. 75, p. 4464, 1995.
Cited on pages 43, 44, and 46.

[134] R. Cuerno and K. Lauritsen, "Renormalization-group analysis of a noisy Kuramoto-Sivashinsky equation," *Physical Review E*, vol. 52, p. 4853, 1995.
Cited on pages 43, 44, 46, and 97.

[135] K. Ueno, H. Sakaguchi, and M. Okamura, "Renormalization-group and numerical analysis of a noisy Kuramoto-Sivashinsky equation in 1+1 dimensions," *Physical Review E*, vol. 71, p. 046138, 2005.
Cited on pages 43 and 44.

[136] P. Manneville, "Liapounov exponents for the Kuramoto-Sivashinsky model," in *Macroscopic Modeling of Turbulent Flows*, O. Pironneau, Ed., p. 319. Berlin: Springer, 1985, no. 230.
Cited on page 44.

[137] V. Yakhot, "Large-scale properties of unstable systems governed by the Kuramoto-Sivashinksi equation," *Physical Review A*, vol. 24, p. 642, 1981.
Cited on page 44.

[138] M. Pradas, D. Tseluiko, S. Kalliadasis, D. T. Papageorgiou, and G. A. Pavliotis, "Noise induced state transitions, intermittency, and universality in the noisy Kuramoto-Sivashinksy equation," *Physical Review Letters*, vol. 106, 2011.
Cited on page 45.

[139] C. Jayaprakash, F. Hayot, and R. Pandit, "Universal properties of the two-dimensional Kuramoto-Sivashinsky equation," *Physical Review Letters*, vol. 71, p. 12, 1993.
Cited on page 45.

[140] I. Procaccia, M. Jensen, V. L'vov, K. Sneppen, and R. Zeitak, "Surface roughening and the long-wavelength properties of the Kuramoto-Sivashinsky equation," *Physical Review A*, vol. 46, p. 3220, 1992.
Cited on page 45.

[141] J. Drotar, Y. Zhao, T. Lu, and G. Wang, "Numerical analysis of the noisy Kuramoto-Sivashinsky equation in 2+1 dimensions," *Physical Review E*, vol. 59, p. 177, 1999.
Cited on pages 45, 47, and 48.

[142] R. Gallego, M. Castro, and J. López, "Pseudospectral versus finite-difference schemes in the numerical integration of stochastic models of surface growth," *Physical Review E*, vol. 76, p. 051121, 2007.
Cited on page 45.

[143] H. S. Wio, J. A. Revelli, R. R. Deza, C. Escudero, and M. S. de La Lama, "Discretization-related issues in the Kardar-Parisi-Zhang quation: Consistency, galilean-invariance violation, and fluctuation-dissipation relation," *Physical Review E*, vol. 81, p. 066706, 2010.
Cited on page 45.

[144] M. Siegert, "Determining exponents in models of kinetic surface roughening," *Physical Review E*, vol. 53, p. 3209, 1996.
Cited on page 47.

[145] T. Hwa and M. Kardar, "Dissipative transport in open systems: An investigation on self-organized criticality," *Physical Review Letters*, vol. 62, p. 1813, 1989.
Cited on pages 52, 61, 64, 65, 81, and 83.

[146] Y. Zhao, G.-C. Wang, and T.-M. Lu, *Characterization of Amorphous and Crystalline Rough Surfaces: Principles and Applications*. San Diego: Academic Press, 2001.
Cited on pages 52, 53, and 55.

[147] B. Schmittmann and R. K. P. Zia, "Statistical mechanics of driven diffusive systems," in *Phase Transitions and Critical Phenomena*, C. Domb and J. L. Lebowitz, Eds., p. 1. London: Academic Press, 2000, vol. 17.
Cited on page 53.

[148] L. Ponson, D. Bonamy, and E. Bouchaud, "Two-dimensional scaling properties of experimental fracture surfaces," *Physical Review Letters*, vol. 96, p. 035506, 2006.
Cited on page 53.

[149] E. Bouchbinder, I. Procaccia, and S. Sela, "Disentangling scaling properties in anisotropic fracture," *Physical Review Letters*, vol. 95, p. 255503, 2005.
Cited on page 53.

[150] E. Bouchbinder, I. Procaccia, and S. Sela, "Statistical physics of fracture surfaces morphology," *Journal of Statistical Physics*, vol. 125, p. 1025, 2006.
Cited on page 53.

[151] A. Keller, R. Cuerno, S. Facsko, and W. Möller, "Anisotropic scaling of ripple morphologies on high-fluence sputtered silicon," *Physical Review B*, vol. 79, p. 115437, 2009.
Cited on pages 54, 116, 117, 118, and 119.

[152] A. Hansen, J. Schmittbuhl, and G. Batrouni, "Distinguishing fractional and white noise in one and two dimensions," *Physical Review E*, vol. 63, p. 062102, 2001.
Cited on page 54.

[153] P. Bak, C. Tang, and K. Wiesenfeld, "Self organized criticality," *Physical Review A*, vol. 38, p. 364, 1988.
Cited on pages 61 and 64.

[154] M. J. Aschwanden, *Self-organized Criticality in Astrophysics : The Statistics of Nonlinear Processes in the Universe*. Springer, 2011.
Cited on page 63.

[155] T. Hwa and M. Kardar, "Avalanches, hydrodynamics, and discharge events in models of sandpiles," *Physical Review A*, vol. 45, p. 7002, 1992.
Cited on pages 64, 81, and 83.

[156] Y. Saito, *Statistical Physics of Crystal Growth*. Singapore: World Scientific, 1996.
Cited on page 68.

[157] E. Moro and R. Cuerno, "Variational mean-field study of a continuum model of crystalline tensionless surfaces," *Physical Review E*, vol. 63, p. 036104, 2001.
Cited on page 68.

[158] M. Henkel and M. J. F. Pleimling, *Non-equilibrium Phase Transitions. Vol. 2*. Dordrecht: Springer, 2010.
Cited on page 72.

[159] M. Nicoli, R. Cuerno, and M. Castro, "Unstable nonlocal interface dynamics," *Physical Review Letters*, vol. 102, p. 256102, 2009.
Cited on page 72.

[160] E. Vivo, M. Nicoli, and R. Cuerno, "Strong anisotropy in two-dimensional surfaces with generic scale invariance: Gaussian and related models," *Physical Review E*, vol. 86, p. 051611, 2012.
Cited on pages 72, 73, 82, 84, 88, 95, and 109.

[161] H. Kallabis, Ph.D. dissertation, Universität Duisburg, Juel-Bericht 3484, Forschungzentrum Jülich, 1997.
Cited on pages 76, 78, and 89.

[162] M. Nicoli, M. Castro, and R. Cuerno, "Unified moving-boundary model with fluctuations for unstable diffusive growth," *Physical Review E*, vol. 78, p. 021601, 2008.
Not cited.

[163] A. Golovin and S. Davis, "Effect of anisotropy on morphological instability in the freezing of a hypercooled melt," *Physica D: Nonlinear Phenomena*, vol. 116, p. 363, 1998.
Cited on page 97.

[164] S. Toh, H. Iwasaki, and T. Kawahara, "Two-dimensionally localized pulses of a nonlinear equation with dissipation and dispersion," *Physical Review A*, vol. 40, p. 5472, 1989.
Cited on page 97.

[165] E. Kuznetsov, A. Rubenchik, and V. Zakharov, "Soliton stability in plasmas and hydrodynamics," *Physics Reports*, vol. 142, p. 103, 1986.
Cited on page 97.

[166] E. A. Demekhin, E. N. Kalaidin, S. Kalliadasis, and S. Y. Vlaskin, "Three-dimensional localized coherent structures of surface turbulence: Model validation with experiments and further computations," *Physical Review E*, vol. 82, p. 036322, 2010.
Cited on page 97.

[167] T. Hwa, "Nonequilibrium dynamics of driven line liquids," *Physical Review Letters*, vol. 69, p. 1552, 1992.
Cited on page 97.

[168] A. Bray, A. Cavagna, and R. Travasso, "Interface fluctuations, Burgers equations, and coarsening under shear," *Physical Review E*, vol. 65, p. 016104, 2001.
Cited on page 97.

[169] M. Navez, C. Sella, and D. Chaperot, "Investigation of the attack on glass by ion bombardment," *Comptes Rendus de l'Académie des Sciences*, vol. 254, p. 240, 1962.
Cited on pages 99 and 100.

[170] V. K. Smirnov, D. S. Kibalov, O. M. Orlov, and V. V. Graboshnikov, "Technology for nanoperiodic doping of a metal oxide semiconductor field-effect transistor channel using a self-forming wave-ordered structure," *Nanotechnology*, vol. 14, p. 709, 2003.
Cited on page 100.

[171] T. Bobek, N. Mikuszeit, J. Camarero, S. Kyrsta, L. Yang, M. Niño, C. Hofer, L. Gridneva *et al.*, "Self-organized hexagonal patterns of independent magnetic nanodots," *Advanced Materials*, vol. 19, p. 4375, 2007.
Cited on page 100.

[172] H. Gnaser, *Low-energy Ion Irradiation of Solid Surfaces*, ser. Springer tracts in modern physics. New York: Springer, 1999.
Cited on pages 101 and 103.

[173] R. Cuerno, M. Castro, J. Muñoz-García, R. Gago, and L. Vázquez, "Nanoscale pattern formation at surfaces under ion-beam sputtering: A perspective from continuum models," *Nuclear Instruments and Methods in Physics Research Section B: Beam Interactions with Materials and Atoms*, vol. 269, p. 894, 2011.
Cited on page 101.

[174] G. Ozaydin, A. S. Özcan, Y. Wang, K. F. Ludwig, H. Zhou, R. L. Headrick, and D. P. Siddons, "Real-time x-ray studies of Mo-seeded Si nanodot formation during ion bombardment," *Applied Physics Letters*, vol. 87, p. 163104, 2005.
Cited on page 101.

[175] H. Hofsäss and K. Zhang, "Surfactant sputtering," *Applied Physics A*, vol. 92, p. 517, 2008.
Cited on page 101.

[176] J. A. Sánchez-García, L. Vázquez, R. Gago, A. Redondo-Cubero, J. M. Albella, and Z. Czigány, "Tuning the surface morphology in self-organized ion beam nanopatterning of Si(001) via metal incorporation: From holes to dots," *Nanotechnology*, vol. 19, p. 355306, 2008.
Cited on page 101.

[177] S. Macko, F. Frost, B. Ziberi, D. F. Förster, and T. Michely, "Is keV ion-induced pattern formation on Si(001) caused by metal impurities?" *Nanotechnology*, vol. 21, p. 085301, 2010.
Cited on page 101.

[178] C. S. Madi, E. Anzenberg, K. F. Ludwig, and M. J. Aziz, "Mass redistribution causes the structural richness of ion-irradiated surfaces," *Physical Review Letters*, vol. 106, p. 066101, 2011.
Cited on pages 101, 104, and 109.

[179] M. Teichmann, J. Lorbeer, B. Ziberi, F. Frost, and B. Rauschenbach, "Pattern formation on Ge by low energy ion beam erosion," *New Journal of Physics*, vol. 15, p. 103029, 2013.
Cited on page 101.

[180] S. Macko, F. Frost, M. Engler, D. Hirsch, T. Höche, J. Grenzer, and T. Michely, "Phenomenology of iron-assisted ion beam pattern formation on Si(001)," *New Journal of Physics*, vol. 13, p. 073017, 2011.
Cited on pages 101, 104, and 105.

[181] D. D. Vvedensky, "Multiscale modelling of nanostructures," *Journal of Physics: Condensed Matter*, vol. 16, p. R1537, 2004.
Cited on page 102.

[182] P. Sigmund, "A mechanism of surface micro-roughening by ion bombardment," *Journal of Materials Science*, vol. 8, p. 1545, 1973.
Cited on page 102.

[183] W. W. Mullins, "Theory of thermal grooving," *Journal of Applied Physics*, vol. 28, p. 333, 1957.
Cited on page 102.

[184] T. Kim, C.-M. Ghim, H. Kim, D. Kim, D. Noh, N. Kim, J. Chung, J. Yang *et al.*, "Kinetic roughening of ion-sputtered Pd(001) surface: Beyond the Kuramoto-Sivashinsky model," *Physical Review Letters*, vol. 92, p. 246104, 2004.
Cited on page 102.

[185] J. Muñoz-García, R. Cuerno, and M. Castro, "Coupling of morphology to surface transport in ion-beam-irradiated surfaces: Normal incidence and rotating targets," *Journal of Physics: Condensed Matter*, vol. 21, p. 224020, 2009.
Cited on page 103.

[186] J. Muñoz-García, R. Cuerno, and M. Castro, "Coupling of morphology to surface transport in ion-beam irradiated surfaces: Oblique incidence," *Physical Review B*, vol. 78, p. 205408, 2008.
Cited on pages 103 and 104.

[187] J. Muñoz-García, R. Gago, L. Vázquez, J. A. Sánchez-García, and R. Cuerno, "Observation and modeling of interrupted pattern coarsening: Surface nanostructuring by ion erosion," *Physical Review Letters*, vol. 104, p. 026101, 2010.
Cited on page 103.

[188] A. Redondo-Cubero, R. Gago, F. J. Palomares, A. Mücklich, M. Vinnichenko, and L. Vázquez, "Nanopatterning dynamics on Si(100) during oblique 40-keV Ar^+ erosion with metal codeposition: Morphological and compositional correlation," *Physical Review B*, vol. 86, p. 085436, 2012.
Cited on pages 104 and 109.

[189] T. Michely, *Islands, Mounds and Atoms*. Berlin: Springer-Verlag Berlin, 2013.
Cited on page 111.

[190] T. J. Oliveira and F. D. A. Aarão Reis, "Effects of grains' features in surface roughness scaling," *Journal of Applied Physics*, vol. 101, p. 063507, 2007.
Cited on pages 111 and 112.

[191] T. J. Oliveira and F. D. A. Aarão Reis, "Roughness exponents and grain shapes," *Physical Review E*, vol. 83, 2011.
Cited on pages 111 and 112.

[192] P. Keblinski, "Comment on "Columnar growth and kinetic roughening in electrochemical deposition"," *Physical Review Letters*, vol. 71, p. 805, 1993.
Cited on page 112.

[193] R. M. Bradley, "Producing ripple topographies by ion bombardment with codeposition of impurities: A curvature-dependent sputter yield is not required," *Physical Review B*, vol. 85, p. 115419, 2012.
Cited on page 113.

[194] J. López, M. Rodríguez, and R. Cuerno, "Superroughening versus intrinsic anomalous scaling of surfaces," *Physical Review E*, vol. 56, p. 3993, 1997.
Cited on page 114.

[195] J. Ramasco, J. López, and M. Rodríguez, "Generic dynamic scaling in kinetic roughening," *Physical Review Letters*, vol. 84, p. 2199, 2000.
Cited on page 114.

[196] J. López, M. Castro, and R. Gallego, "Scaling of local slopes, conservation laws, and anomalous roughening in surface growth," *Physical Review Letters*, vol. 94, p. 166103, 2005.
Cited on page 114.

[197] W. Schwarzacher, "Kinetic roughening of electrodeposited films," *Journal of Physics: Condensed Matter*, vol. 16, p. R859, 2004.
Cited on page 114.

[198] A. Yanguas-Gil, J. Cotrino, A. Barranco, and A. González-Elipe, "Influence of the angular distribution function of incident particles on the microstructure and anomalous scaling behavior of thin films," *Physical Review Letters*, vol. 96, p. 236101, 2006.
Cited on page 114.

[199] P. Córdoba-Torres, T. Mesquita, I. Bastos, and R. Nogueira, "Complex dynamics during metal dissolution: From intrinsic to faceted anomalous

scaling," *Physical Review Letters*, vol. 102, p. 055504, 2009.
Cited on page 114.